Observation of the Microenvironment Around CO_2 Reduction Electrodes *via* Fluorescent Confocal Laser-Scanning Microscopy

Thesis by
Annette Ellen Böhme

In Partial Fulfillment of the Requirements for the
degree of
Doctor of Philosophy

CALIFORNIA INSTITUTE OF TECHNOLOGY
Pasadena, California

2024
Defended April 2nd, 2024

Annette Ellen Böhme
ORCID: 0000-0003-1109-3428

ACKNOWLEDGEMENTS

First and foremost, I want to thank my advisor Harry Atwater. I truly admire how he juggles so many responsibilities but manages to remain incredibly enthusiastic about science. At the same time, he is a genuinely nice person and the most encouraging advisor anyone could wish for. I always felt like Harry appreciated and respected my work and that is invaluable.

Second, I would like to thank my committe members, Bill Goddard, Julia Greer, and Shane Ardo. I had the opportunity to collaborate with Shane and his students Cassidy and Rohit and I learned a lot from them. Shane is so enthusiastic and never runs out of ideas for the next cool project. It was a joy to work with him and I especially appreciated the opportunity to tour his labs at UC Irvine.

I was very lucky to have an amazing mentor, Alex Welch, over the first few months of my PhD. We spent countless hours in the lab together as Alex taught me about CO_2 reduction and pH imaging with confocal microscopy but just as importantly, she also showed me that it is possible to be a truly happy scientist. Next, I want to thank Aidan Fenwick. I'm not a chemist and I am so glad that Aidan answered my countless electrochemistry questions. I deeply respect his expertise and thank him for all his measurements and advice. I learned so much from both Alex and Aidan, on a professional as well as on a personal level.

I'd like to thank the students that I was lucky enough to mentor. Cristian spent a summer helping me with the measurements presented in Chapter 8. I am very impressed by how hard he worked and so proud about how much he learned. César agreed to continue applying confocal imaging to electrochemical applications. I really enjoyed working with him over the past months and I'm so excited to see where the journey takes him.

There are so many other people in the Atwater group that helped me get through my PhD with their scientific advice but also with their friendship and kindness. Eowyn, who shares my love for the outdoors and the environment. Lucy, who (together with Cory) introduced me to backpacking in California. Marianne, my amazing workout buddy. Rachel, who was so helpful when I bought a confocal microscope. Emily, Ellis, Megan, Zack, Phil, Julie, Aisulu, Andy, Catherine, Lily, John, Lior, Ramon, Prachi, Susana, Jared, and Fabian all made my daily life better with their advice, hands-on help in the lab, or through enjoyable conversations.

Other members of the Caltech community I would like to thank are Weixuan Nie who led the project about CO_2 reduction in acidic electrolyte (Chapter 7), Nick Watkins, Shaoyang Lin, Giada Spigiolon, and Nathan Dellaska.

Collaborators outside of Caltech that I want to acknowledge are the dedicated and talented simulation specialists Justin Bui and Alex King, as well as Calton Kong and Yanwei Lum.

I am lucky that I found great friends who made my adventure in California so much more enjoyable: The amazing Jillian and David, Rob, Kim, Tara, Golsa, Sahangi, and Hannah. A huge thanks to the Caltech Triathlon club that is such a welcoming and supportive community, especially Ryan, Lauren, Marianne, Andreas, William, Stephanie, Miles, Angus, Matthias, Leonie, Jess, Han, Joy, and Carina. I really enjoyed yelling at them during track practice and the workouts and races made my daily life so much better.

I want to thank the whole Farmington crew: Jenny, Marc, Yannik, Matthias, Lukas, Chris, Tobi, Carsten, Lukas, Irina, and Robin. I truly don't think that I would have embarked on this adventure without their enthusiastic encouragement and am grateful that they all believed that I could do this.

Finally, I want to thank my friends back in Germany: Andrea, Frank, Sarah, Nicole, Matze, Amelie, Kirill, and Martin all made the long trip to California to visit me. Also thanks to Ina, Sonja, Verena, Anja, Mario, Pascal, and Tim.

I am grateful that I have a very loving family. My parents always support me in all my endeavors, no matter how far away from home they lead me. My sister is the kindest person I know and I think the world would be a better place if everyone had a big sister like her.

The most important person in my life is Simon. I am so lucky that I found a partner who lets me chase my dreams no matter where they lead me, who always puts my well-being before his, who loves and supports me unconditionally, and is always up for an adventure. I can't wait to marry him.

ABSTRACT

Electrochemical carbon dioxide reduction (CO_2R) is compelling because it enables the storage of renewable energy in the form of chemical bonds and offers the possibility to make carbon-based chemicals and fuels from a sustainable feedstock. A solid understanding of and control over the local microenvironment in and around CO_2R electrodes is crucial to optimize the device performance.

In this work, we develop and refine a technique to observe the microenvironment around CO_2R electrodes via fluorescent confocal laser scanning microscopy with three-dimensional sub-micrometer spatial as well as temporal resolution. We combine two fluorescent pH probes, DHPDS and APTS, to resolve the local pH value around operando CO_2R electrodes. The pH plays an important role in determining the CO_2R activity and selectivity. In a first step, we image the local pH value in and around CO_2R GDEs with a random pattern of trenches and find that the pH is locally enhanced inside trenches. This effect becomes more pronounced for narrower trenches, reaching a maximum at a trench width of 5 μm. With the help of multiphysics simulations we can show that the high pH inside trenches is closely related to an enhanced C_{2+} Faradaic efficiency. We harness this effect and fabricate CO_2R GDEs with tailored patterns of holes and trenches that allow a more systematic study of the influence of various micromorphology geometry parameters. We confirm experimentally that narrow holes and trenches exhibit a locally enhanced CO_2R selectivity and determine the most beneficial geometry parameters. We further use the developed technique to investigate the influence of a GDE's pore size on the local pH and with it, on the CO_2R selectivity. We observe that CO_2 transport is slower through smaller pores which can lead to switching of the reaction pathway and significantly alter the selectivity. We further investigate the importance of the microenvironment pH for CO_2R in acidic bulk electrolytes with the result that a non-acidic microenvironment pH, that can be reached at sufficiently high current densities, is required for the onset of CO_2R. Finally, we aim to extend the sensing capabilities and detect the local CO concentration in electrochemical devices but identify several challenges, including the probe reduction at the cathode.

Overall, we utilized fluorescent confocal laser-scanning microscopy to observe the microenvironment around CO_2R electrodes and correlate it with the CO_2R performance to gain a better mechanistic understanding of CO_2R and inform the design of future CO_2R electrodes.

PUBLISHED CONTENT AND CONTRIBUTIONS

[1] A. J. Welch, A. Q. Fenwick, **A. E. Böhme**, H.-Y. Chen, I. Sullivan, X. Li, J. S. DuChene, C. Xiang, and H. A. Atwater. "Operando Local pH Measurement within Gas Diffusion Electrodes Performing Electrochemical Carbon Dioxide Reduction". In: *J. Phys. Chem. C* 125 (2021), pp. 20896–20904. DOI: https://doi.org/10.1021/acs.jpcc.1c06265.
A.E.B. assisted with and performed pH imaging experiments as well as conceptualized, designed, performed, and analyzed all COMSOL Multiphysics simulations.

[2] **A. E. Böhme**, J. C. Bui, A. Q. Fenwick, R. Bhide, C. N. Feltenberger, A. J. Welch, A. J. King, A. T. Bell, A. Z. Weber, S. Ardo, and H. A. Atwater. "Direct Observation of the Local Microenvironment in Inhomogeneous CO_2 Reduction Gas Diffusion Electrodes via Versatile pOH Imaging". In: *Energy Environ. Sci.* 16 (2023), pp. 1783–1795. DOI: https://doi.org/10.1039/D2EE02607D.
A.E.B. contributed to the conceptualization of the study and performed dye calibration and all pOH imaging experiments as well as data analysis.

[3] **A. E. Böhme***, A. Q. Fenwick*, and H. A. Atwater. "Probing the Effect of Intentionally Tailored Gas Diffusion Electrode Micromorphology Geometries on Enhancing the Selectivity of CO_2 Reduction". In: *in preparation* (2024).
A.E.B. conceptualized the study, fabricated all samples, performed dye calibration, pH imaging experiments and data analysis as well as performed and analyzed multiphysics simulations.

[4] **A. E. Böhme***, S. Bin Dolmanan*, Z. Fan*, A. J. King, A. Q. Fenwick, A. D. Handoko, W. R. Leow, A. Z. Weber, X. Ma, E. Khoo, H. A. Atwater, and Y. Lum. "Local Microenvironment Tuning Induces Switching between Electrochemical CO_2 Reduction Pathways". In: *J. Mater. Chem. A* 11 (2023), pp. 13493–13501. DOI: https://doi.org/10.1039/D3TA02558F.
A.E.B. designed, performed and analyzed all pH imaging and confocal microscopy experiments.

[5] **A. E. Böhme***, W. Nie*, M. H. Hicks, H. A. Atwater, T. Agapie, and J. C. Peters. "Electrochemical CO_2 Reduction in Acidic Electrolytes is Enabled by an Increase in the Microenvironment pH". In: *in preparation* (2024).
A.E.B. designed and conducted confocal laser-scanning microscopy measurements, related pH imaging and data analysis.

[6] **A. E. Böhme**, A. J. Welch, R. Bhide, C. N. Feltenberger, S. Ardo, and H. A. Atwater. "Reversible Excited-State Photoacids and Photobases as Dynamic Fluorescence Sensors of Local pH". 63/332,540. California Institute of Technology. Non-provisional patent application. Apr. 19, 2023.

A.E.B. reduced the idea to practice via the demonstration that the excited-state photobase APTS can be used as a dynaminc sensor of local pH in electrochemical systems.

* These authors contributed equally to this work.

TABLE OF CONTENTS

LIST OF ILLUSTRATIONS

LIST OF TABLES

Chapter 1

INTRODUCTION

1.1 The Role of CO_2 Reduction in the Mitigation of Climate Change

Climate change is one of the greatest threats facing humanity today. Many disasterous events like species extinction, floods, wildfires, drought, heat waves, and other extreme weather events can be connected to it. This is accompanied by a plethora of humanitarian problems like hunger, unaccessible drinking water, loss of homes, health crises, and mass migration. This is happening today, all around the globe, and the problem is expected to become more and more severe over the course of the next few years and decades [1–6].

One of the main driving forces of climate change is the rising level of greenhouse gases in the atmosphere. One of the most prominent greenhouse gases is carbon dioxide (CO_2) that results for example from burning fossil fuels, industrial processes, or from agriculture [7, 8].

The levels of CO_2 in the atmosphere have been rising since the beginning of industrialization due to increasing emissions [9] (Fig. 1.1). Scientists agree that to mitigate the worst effects of climate change, it is necessary to keep the average temperature increase below 1.5 °C [10]. To reach this goal, net-zero and even net-negative CO_2 emissions are required before the end of this century [9, 11].

To reach this goal, a globally coordinated effort is required [1]. Various different strategies can and must contribute to this effort. It is necessary to transform the energy sector to predominantly use sustainable energy sources like solar or wind. Industries that are responsible for large amounts of carbon emissions should be electrified wherever possible, e.g., in the short-distance transportation sector. Another important contribution can be the capture and utilization of CO_2 (CCU) via CO_2 reduction (CO_2R), a very promising route to make sustainable products like chemicals or aviation fuels that are otherwise connected to large amounts of CO_2 emissions.

Fig. 1.2 proposes a strategy to reach net-zero carbon emissions in the US by 2050. This includes the transformation of the energy sector, e.g., by using solar or wind power instead of fossil fuels, the decarbonization of transportation and

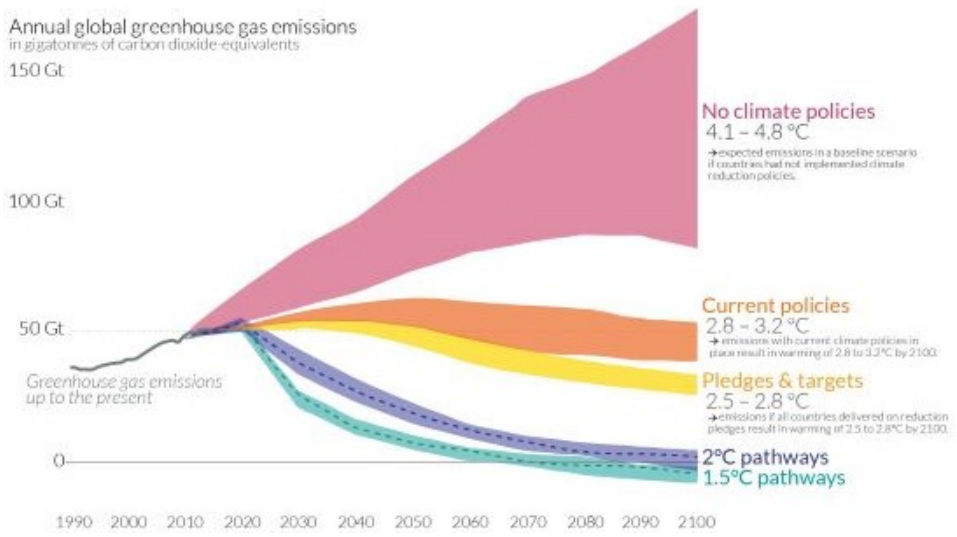

Figure 1.1: Annual greenhouse gas emissions in gigatons of CO_2 equivalents as a function of time from 1990 until 2020 as well as different future warming scenarios until 2100 relative to pre-industrial temperatures. To reach the 1.5 °C goal, net-zero or even net-negative greenhouse gas emissions are required before the end of the century. Adapted from [9].

industry, electrification, the use of low carbon fuels like hydrogen and the reduction of the emission of non-CO_2 greenhouse gases like methane. In addition to reducing emissions, carbon capture, utilization, and storage (CCUS) can play a major role [8].

It is possible to capture CO_2 from flue gas, from the atmosphere, or from ocean water via various techniques and this is a very active area of research [13–17]. Various carbon capture plants of different scales and sizes are already in operation [18–21]. The captured CO_2 can be sequestered for long-term storage, for example in geological features [13, 14, 16]. Alternatively, CO_2 can be transformed into long-lived carbon-based products such as concrete or into short-lived products such as plastics, chemical precursors, or fuels. Products that are already produced on an industrial scale from CO_2 include CO_2-cured concrete or urea and methanol [8].

The focus of this work is the reduction of CO_2 to short-lived products. Making short-lived products from CO_2 is compatible with a net-zero carbon emission strategy. It allows the production of carbon-based products without the use of fossil fuels and with minimal CO_2 emissions. Assuming that the CO_2 that is used as a feedstock is captured from the air or ocean and that the energy used comes from sustainable sources (e.g., solar), it is possible to close the carbon cycle and take as much CO_2

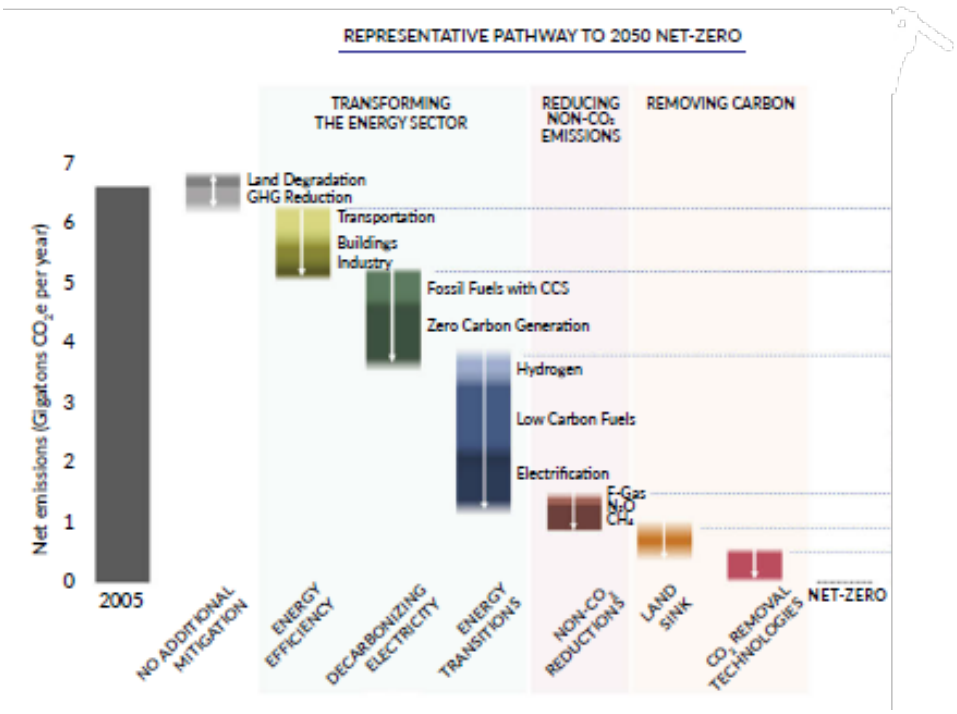

Figure 1.2: A proposed strategy to reach net-zero greenhouse gas emissions in the US by 2050. This includes improved energy efficiency, decarbonizing electricity, energy transitions, non-CO_2 reduction of species other than CO_2, land sinks, and CO_2 removal. Adapted from [8] and [12].

out of the atmosphere as is released at the end of the lifecycle of a short-lived carbon product, e.g., when fuel is burned. This is illustrated in Fig. 1.3.

Importantly, CO_2R is a very promising route to make carbon-neutral products that are otherwise very challenging to decarbonize. It can be used to make carbon-neutral chemicals from a sustainable feedstock and decarbonize the chemical industry [22]. Further, it is a step on the route towards sustainable aviation fuels, an industry that is very challenging to electrify [23, 24].

In addition, CO_2R presents an intriguing possibility for long-term energy storage in the form of chemical bonds [25, 26]. This is necessary since many sustainable energy sources like solar or wind are intermittent. Present energy storage technologies like batteries or pumped hydro are limited and either lack long-term storage capacities or require specific landscape features and large areas [27, 28]. Sustainable fuels reduced from CO_2 are both energy-dense and long-lasting.

There have been many encouraging advances in the field of electrochemical CO_2R since the first systematic study of CO_2R was performed by Hori et al. in 1985

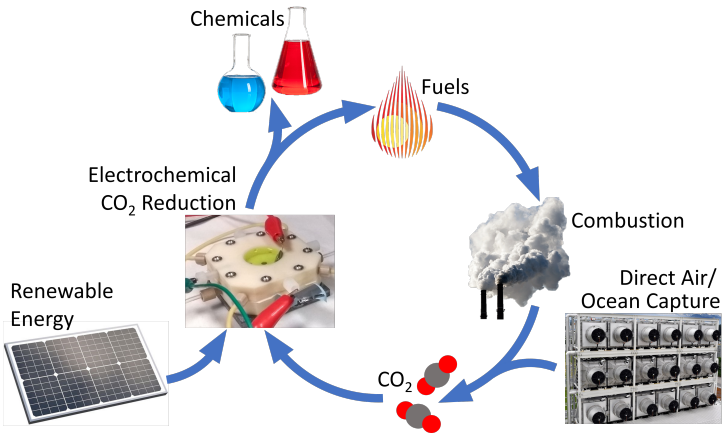

Figure 1.3: Simplified schematic representation of a closed carbon cycle. CO_2 is being reduced electrochemically to chemicals and fuels with CO_2, water and renewable energy as input. The combustion of fuels releases CO_2, which can be captured from the air or ocean to be used as a feedstock for electrochemical CO_2 reduction.

[29]. However, the process is highly complex and still not fully understood. Many challenges remain that, as of now, inhibit the wide-spread adaption of the technique [30–32]. This includes the higher cost as well as higher energy requirement for products made via CO_2R compared to products made from fossil carbon materials [8].

The aim of this work is to develop a tool to better investigate CO_2R electrodes, to gain a better mechanistic understanding of CO_2R processes and to improve the CO_2R efficiency and selectivity through electrode engineering to pave the road towards a wide-spread application of this important technique.

1.2 Electrochemical CO_2 Reduction

Electrochemical CO_2R only requires the application of an electrical bias which is in contrast to photochemical or thermochemical CO_2R that include the input of photons or heat. A very basic CO_2R setup consists of an aqueous electrolyte that is saturated with CO_2, an anode and a cathode. This is schematically depicted in Fig. 1.4. If an adequate potential is applied, CO_2 can be reduced at the cathode surface.

Usually, a three-electrode setup with a reference electrode is used. This allows to measure the voltage at the working electrode with reference to a stable, well known electrode potential. In this work, we use a silver/silver chloride (Ag/AgCl) reference electrode. At the same time, the current can be controlled and measured between

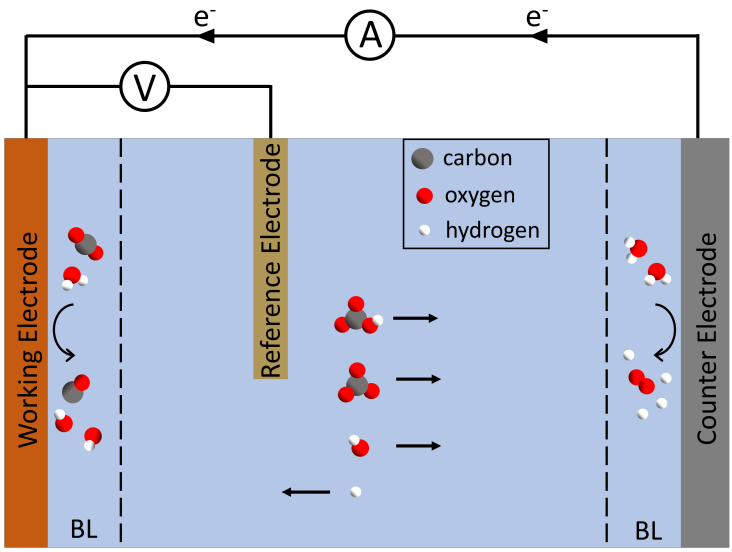

Figure 1.4: Schematic of a basic CO_2R setup, consisting of a working electrode (cathode), a counter electrode (anode), a reference electrode and an aqueous electrolyte. The current is measured between the working and counter electrodes. The reference electrode is necessary to measure the voltage at the working electrode on a known scale. The dotted lines indicate the boundary layers (BLs) in the vicinity of the anode and cathode. CO_2 is reduced to hydrocarbons (e.g., CO) at the cathode and water is reduced to oxygen at the anode. Arrows indicate in which direction different molecules diffuse.

the working electrode (cathode) and the counter electrode (anode) [33]. In this work, a platinum mesh is used as the anode because it is very stable and has a low overpotential [34]. The boundary layer (BL) indicates the region around electrodes within which the concentrations of different species are different from their bulk concentration. The BL is typically tens of micrometers to 100 micrometers thick [35].

1.2.1 Reaction Mechanisms of Electrochemical CO_2 Reduction

CO_2R can proceed at the cathode surface if a suitable catalyst material is chosen and a negative enough potential is applied. In more acidic electrolyte conditions, a proton is consumed during CO_2R, resulting in water (H_2O) as a byproduct (see Table 1.1). In more basic conditions, CO_2 uses H_2O as the proton source, resulting in hydroxide (OH^-) as a byproduct (see Table 1.2). The formation of various different carbon-based products is possible, ranging from carbon monoxide (CO) to complex multicarbon (C_{2+}) products [36–41].

Table 1.1: A selection of common CO_2R reactions in more acidic conditions with their equilibrium potentials. RHE refers to the reversible hydrogen electrode.

CO_2 Reduction Reaction	**Product**	**E^0** (V vs. RHE)
$CO_2 + 2H^+_{(aq)} + 2e^- \longrightarrow CO_{(g)} + H_2O_{(l)}$	Carbon Monoxide	-0.10
$CO_2 + 2H^+_{(aq)} + 2e^- \longrightarrow HCOOH_{(aq)}$	Formic Acid	-0.12
$CO_2 + 6H^+_{(aq)} + 6e^- \longrightarrow CH_3OH_{(aq)} + H_2O_{(l)}$	Methanol	0.03
$CO_2 + 8H^+_{(aq)} + 8e^- \longrightarrow CH_{4(g)} + 2H_2O_{(l)}$	Methane	0.17
$2CO_2 + 12H^+_{(aq)} + 12e^- \longrightarrow C_2H_5OH_{(aq)} + 3H_2O_{(l)}$	Ethanol	0.09
$2CO_2 + 12H^+_{(aq)} + 12e^- \longrightarrow C_2H_{4(g)} + 4H_2O_{(l)}$	Ethylene	0.08
$3CO_2 + 18H^+_{(aq)} + 18e^- \longrightarrow C_3H_6OH(aq) + 5H_2O_{(l)}$	Propanol	0.10

Table 1.2: A selection of common CO_2R reactions in more basic conditions with their equilibrium potentials. RHE refers to the reversible hydrogen electrode.

CO_2 Reduction Reaction	**Product**	**E^0** (V vs. RHE)
$CO_2 + H_2O_{(l)} + 2e^- \longrightarrow CO_{(g)} + 2OH^-_{(aq)}$	Carbon Monoxide	-0.11
$CO_2 + H_2O_{(l)} + 2e^- \longrightarrow HCOO^-_{(aq)} + OH^-_{(aq)}$	Formate	-0.02
$CO_2 + 5H_2O_{(l)} + 6e^- \longrightarrow CH_3OH^-_{(aq)} + 6OH^-_{(aq)}$	Methanol	0.03
$CO_2 + 6H_2O_{(l)} + 8e^- \longrightarrow CH_{4(g)} + 8OH^-_{(aq)}$	Methane	0.17
$2CO_2 + 9H_2O_{(l)} + 12e^- \longrightarrow C_2H_5OH_{(aq)} + 12OH^-_{(aq)}$	Ethanol	0.08
$2CO_2 + 8H_2O_{(l)} + 12e^- \longrightarrow C_2H_{4(aq)} + 12OH^-_{(aq)}$	Ethylene	0.07
$3CO_2 + 13H_2O_{(l)} + 18e^- \longrightarrow C_3H_7OH_{(aq)} + 18OH^-_{(aq)}$	Propanol	0.09

Another important reaction that takes place at the cathode is the hydrogen evolution reaction (HER, see reactions 1 and 2 with 1 favored in acidic conditions and 2 favored in basic conditions). HER is unwanted since it diminishes the efficiency and selectivity of the CO_2R [42–44].

$$2\,H^+_{(aq)} + 2\,e^- \longrightarrow H_{2(g)}, \qquad E^0 = 0 \text{ V vs. RHE} \qquad \{1\}$$

$$2\,H_2O_{(l)} + 2\,e^- \longrightarrow H_{2(g)} + 2\,OH^-_{(aq)}, \qquad E^0 = 0 \text{ V vs. RHE} \qquad \{2\}$$

At the anode, on the other hand, the oxygen evolution reaction (OER, reaction 3) takes place [45].

$$2\,H_2O_{(l)} \longrightarrow O_{2(g)} + 4\,H^+_{(aq)} + 4\,e^-, \qquad E^0 = 1.23 \text{ V vs. RHE} \qquad \{3\}$$

When comparing the equilibrium potentials for different products in tables 1.1 and 1.2, it becomes evident that they are all very similar. The close spacing between

the equilibrium potentials is one reason why performing CO_2R selectively is very difficult since merely tuning the applied potential does not allow to tune the product selectivity. Further, the equilibrium potential of the parasitic HER (reactions 1 and 2) is close to the equilibrium potentials of different CO_2R products. In an aqueous electrolyte, the concentration of water molecules is significantly higher than that of CO_2 molecules (max. 33 mM [46]) and it is therefore a challenge to selectively perform CO_2R over HER.

In addition, specifically the CO_2R reactions to more complex carbon-based molecules, including C_{2+} products, involve multiple protons, electrons and CO2 molecules. Consequently, the reaction pathway can be complicated with several reaction intermediates. It can therefore be difficult to find one single catalyst that is capable to sustain all these intermediates [34].

1.2.2 Catalyst Considerations

Different parameters can influence the performance of a CO_2R device and the interplay between these dictates the CO_2R activity and selectivity. It is important to understand the influence of each parameter. One of the most important factors is the choice of catalyst material [29, 41, 47]. The CO_2R performance of a catalyst mainly depends on its adsorption energy for the HER intermediate H^* and the CO_2R intermediates $COOH^*$ and CO^* (* indicates that a species is adsorbed) [47].

Fig. 1.5 (a) displays the binding energy for H^* and for CO^* on different metals. Most transition metals (marked in red) have a negative H^* binding energy which makes them good HER catalysts and therefore unsuitable for CO_2R. At the same time, these metals bind CO very strongly which means that the catalyst becomes "poisoned" since CO occupies all catalytic sites. Catalysts that are marked in blue and yellow have a positive H^* binding energy which makes them worse HER catalysts. Their binding energy to CO is positive which means that CO is quickly released from the catalyst surface and these materials are unable to make multicarbon products. Copper, marked with cyan color is the only catalyst material known to date that can make complex multicarbon products. Its moderate binding energy to CO allows for the further reduction of CO to higher-order carbon products like ethanol or ethylene [47].

Fig. 1.5 (b) shows the CO_2R current density, a good property to compare CO_2R activity for different catalysts, at -0.8 V vs. RHE, as a function of the CO binding strength. It displays a volcano-shaped trend. Gold exhibits the highest CO_2R

current density and therefore, CO_2R activity. Catalyst materials with a lower CO binding energy like silver and zinc are characterized by a slower CO_2 activation which explains the lower CO_2R activity. Metals with a higher CO binding energy, including platinum, nickel and copper, have such a negative CO binding energy that the slow CO desorption limits the CO_2R activity [48].

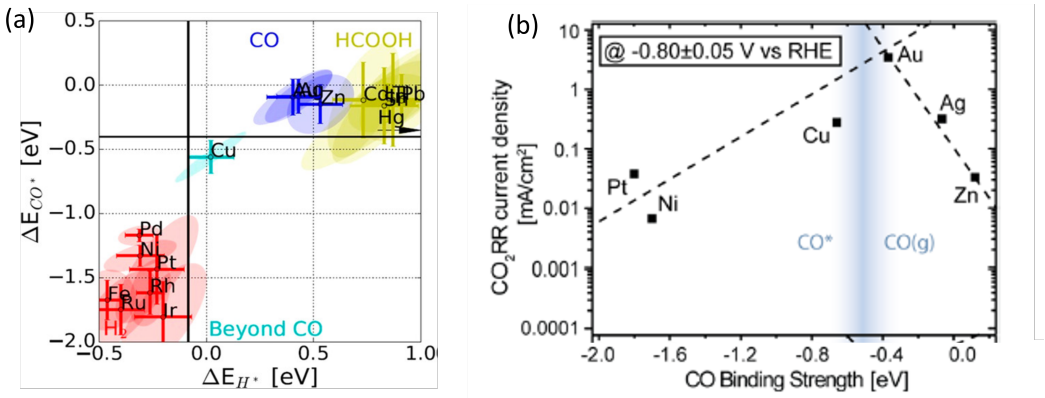

Figure 1.5: (a) Categorization of different metals by binding energy to H^* (x-axis) and CO^* (y-axis). Red color denotes materials that have a major Faradaic efficiency (FE) towards H_2, blue towards CO and yellow towards formic acid. Copper (cyan) forms its own group that can make multicarbon products. Adapted from [47]. (b) Volcano plot of the CO_2R partial current density at -0.8 V vs. RHE for different catalyst materials as a function of the CO binding energy. Gold exhibits the highest CO_2R current density. Adapted from [48]

Even though gold possesses a superior CO_2R activity, (compare Fig. 1.5 (b)) it is limited by the fact that it almost exclusively makes CO as a product (compare Fig. 1.5 (a)). Copper, while having a slightly lower CO_2R activity than gold, is the only catalyst that has the ability to make complex multicarbon products. This feature makes copper one of the most actively studied CO_2R catalysts [41, 49, 50] and the catalyst of choice in most chapters of this work.

1.2.3 Gas Diffusion Electrodes (GDEs)

There are two possibilities how CO_2 can be delivered to the cathode surface. The first is the dissolution of CO_2 in the electrolyte. This is usually done by bubbling gaseous CO_2 through the electrolyte until it is saturated with CO_2. The equilibrium concentration of CO_2 in the electrolyte depends on the temperature, pressure, and salinity of the electrolyte and reaches 33 mM in an aqueous electrolyte under ambient conditions [46]. The other CO_2 delivery method is the use of gas diffusion electrodes (GDEs) that allow the transportation of CO_2 in the gas phase.

The first system, schematically depicted in Fig. 1.6 (a), is easier to implement experimentally as well as easier to understand. However, it is limited by the solubility of CO_2 in water and mass transfer limitations that restrict the rate of CO_2 consumption. As a consequence, only low current densities up to 30 $\frac{\text{mA}}{\text{cm}^2}$ in magnitude can be achieved [51].

Following this observation, scientists developed gas-fed, porous GDEs, see Fig. 1.6 (b), that allow the transport of CO_2 molecules in the gas phase directly to the catalyst-electrolyte interface. They typically consist of a macroporous layer that provides mechanical stability and is usually 100 - 500 μm thick. This is topped with a thinner (usually 50 - 100 μm) microporous layer that is often treated with a hydrophobic substance, e.g., polytetrafluoroethylene (PTFE). The microporous layer is coated with a thin catalyst layer that is typically hundreds of nanometers thick. Gaseous CO_2 can be fed to the GDE from the backside through a gas chamber.

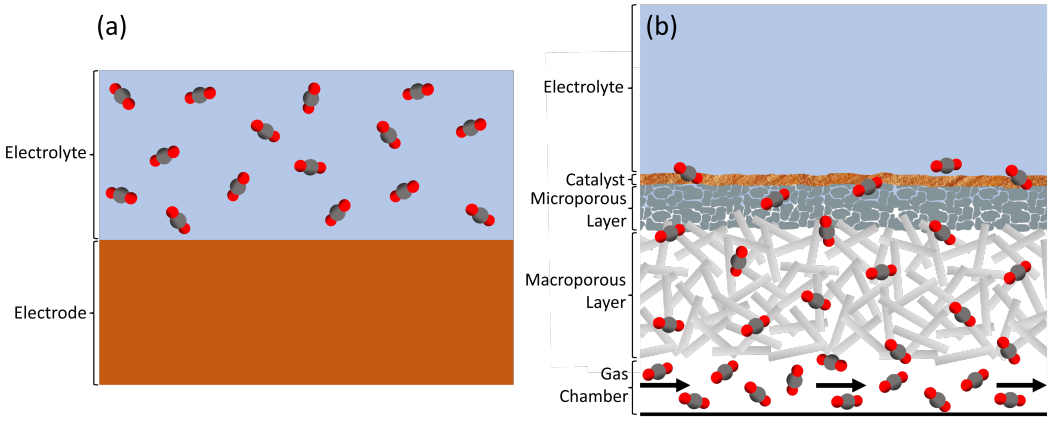

Figure 1.6: (a) Schematic representation of a solid CO_2R electrode. CO_2 is dissolved in an aqueous electrolyte that is in contact with the electrode.(b) A CO_2R GDE, consisting of a macroporous layer, a microporous layer and a catalyst that is in contact with the electrolyte. Gaseous CO_2 is fed from the backside of the GDE through a gas chamber. Schematic not to scale.

It is important that a GDE system is set up such that the GDE is not flooded since that would prevent the effective transport of gaseous CO_2. On the other hand, the catalyst also must not be dry as aqueous electrolyte is required as a proton donor for CO_2R and an electric connection between cathode and anode is required. To create stable wetted conditions, the pressures of the electrolyte and the gaseous CO_2 must be carefully balanced [35, 52].

The development of GDEs for CO_2R has been a milestone in enhancing the CO_2R performance. CO_2R current densities higher in magnitude than 1 $\frac{mA}{cm^2}$ have been demonstrated [53] and the Faradaic efficiency towards multicarbon products like ethylene can be improved with the use of a GDE.

However, CO_2R GDEs are highly complex systems and difficult to investigate. They are still not perfectly understood and not stable, selective and efficient enough to be widely applied on an industrial scale [30–32]. A deep understanding of the mechanisms that dictate the CO_2R performance of a GDE and how it can be optimized is urgently needed. This work aims to address these issues.

1.2.4 Electrochemical Cell Design

Fig. 1.4 schematically depicts the setup of a very simple electrochemical CO_2R cell. Multiple factors need to be taken into consideration when designing an electrochemical cell.

The first is the CO_2 delivery method. If a GDE is used and CO_2 is to be fed in the gas phase, a gas chamber at the back side of the GDE (cathode) must be included.

The next consideration is the inclusion of an ion exchange membrane. Such a membrane is often placed between the cathode and anode to prevent the crossover of reduced liquid products to the anode where they could be oxidized as well as the crossover of dissolved O_2 to the cathode. Anion exchange membranes (AEMs) block cations but allow the free transport of anions while cation exchange membranes (CEMs) block anions but allow the free transport of cations. Bipolar membranes (BPMs) consist of an AEM and a CEM layer and can maintain a distinct pH value on either side of the membrane.

Another cell design parameter to pay attention to is the cell resistance. It is important to place the reference electrode close to the cathode to minimize the resistance between cathode and the reference electrode. Further, to reduce the cell resistance, the anode and cathode should be placed as close together as possible without causing mass transfer limitations. Membranes, particularly BPMs, increase the cell resistance. To obtain a uniform voltage profile across the cathode, a parallel plate configuration can be used.

Compression cells, consisting of a gas chamber in case a GDE is used, a cathode, a catholyte chamber with a reference electrode, an ion exchange membrane, an anolyte chamber as well as an anode allow to reliably and reproducibly set up a parallel plate configuration and are commonly used. In most cases, the compression

cell is oriented vertically such that gas bubbles that form at the cathode and anode during cell operation can easily detach and leave the cell.

However, some applications require a different cell design. This is the case if the cell is not designed to maximize the electrochemical CO_2R performance but to be compatible with characterization techniques like scanning electrochemical microscopy (SECM) [54, 55], surface-enhanced Raman spectroscopy (SERS) [56], electrochemical atomic force microscopy (EC-AFM) [57] or surface-enhanced infrared spectroscopy (SEIRAS) [58].

This work focuses on the characterization of CO_2R cathodes with laser-scanning confocal microscopy (CLSM) and as a consequence, the electrochemical cell design that is predominantly used in this work is optimized for this technique (see Fig. 2.1 (a), Fig. 2.2 and Fig. 3.2). The main constraining factor is that in order to investigate processes at the cathode, the microscope's objective must have a direct line of sight to the cathode. As a consequence, the cell does not contain an ion exchange membrane and the cathode is not placed parallel to the anode but at the side. Further, the cell is oriented horizontally and is open at the top to allow the use of a water immersion objective.

1.3 The Role of the Local pH/ pOH Value for CO_2 Reduction

The local pH and pOH values are very important parameters that significantly influence the CO_2R selectivity and activity.

The pOH value is defined as

$$\mathrm{pOH} = -\log_{10}(a_{OH^-}) \tag{1.1}$$

and the pH value as

$$\mathrm{pH} = -\log_{10}(a_{H^+}) \tag{1.2}$$

with a_{OH^-} the OH^- (hydroxide) activity and a_{H^+} the H^+ (proton) activity. In many cases, the hydroxide and proton activity can be approximated as the concentration. If the system is in equilibrium,

$$\mathrm{pH} + \mathrm{pOH} = \mathrm{pK_w}, \tag{1.3}$$

with pK_w = 14 under ambient conditions. In equilibrium, the pH can be directly calculated from the pOH and vice versa [59].

1.3.1 Carbonate and Bicarbonate Equilibria

In an electrochemical device, it is important to distinguish the bulk pH and the local pH profile within the boundary layer around the anode and cathode.

The pH in the bulk and everywhere in an electrolyte with pH ≥ 5 is influenced by the dissolution of CO_2 molecules. CO_2 participates in bulk equilibrium reactions and partially reacts to carbonate (CO_3^{2-}) and bicarbonate (HCO_3^-)via the equilibrium reactions 4 - 7. k_1 - k_4 are the forward rate constants.

$$CO_{2(aq)} + H_2O \rightleftharpoons H^+ + HCO_3^-, \qquad k_1 = 3.61 \cdot 10^{-2} \frac{1}{s} \qquad \{4\}$$

$$HCO_3^- \rightleftharpoons H^+ + CO_3^{2-}, \qquad k_2 = 59.44 \frac{1}{s} \qquad \{5\}$$

$$CO_{2(aq)} + OH^- \rightleftharpoons HCO_3^-, \qquad k_3 = 2.23 \cdot 10^3 \frac{L}{mol\ s} \qquad \{6\}$$

$$HCO_3^- + OH^- \rightleftharpoons H_2O + CO_3^{2-}, \qquad k_4 = 6 \cdot 10^9 \frac{L}{mol\ s} \qquad \{7\}$$

Reactions 6 and 7 are schematically depicted in Fig. 1.7 (a). As can be seen in this figure and reactions 4 - 7, the reaction of CO_2 to carbonate and bicarbonate creates protons or consumes hydroxides which leads to a decrease in pH or an increase in pOH as per equations 1.1 and 1.2.

Further, water dissociates to protons and hydroxides everywhere in the electrolyte according to reaction 8 with k_w the forward rate constant.

$$H_2O \rightleftharpoons H^+ + OH^-, \qquad k_w = 1.4 \cdot 10^{-3} \frac{mol}{L\ s} \qquad \{8\}$$

Fig. 1.7 (c) displays the concentrations of CO_2, carbonate, bicarbonate, protons and potassium ions as a funtion of pH in a potassium bicarbonate solution [51]. While the concentration of CO_2 never exceeds 33 mM at ambient conditions, it decreases rapidly for pH values > 9.2 because the equilibrium shifts towards bicarbonate and carbonate. This further motivates the use of GDEs that allow the delivery of CO_2 in the gas phase without relying on the solubility of CO_2 in an aqueous electrolyte.

1.3.2 Charge Transfer Reactions

Hydroxides and protons are not only involved in the carbonate and bicarbonate equilibrium reactions discussed above, they also play an important role in the charge-transfer reactions of CO_2R and HER as per tables 1.1 and 1.2. The reduction of CO_2 to CO with a GDE in more basic conditions, leading to the creation of two hydroxides, is schematically depicted in Fig. 1.7 (b). For both CO_2R to uncharged

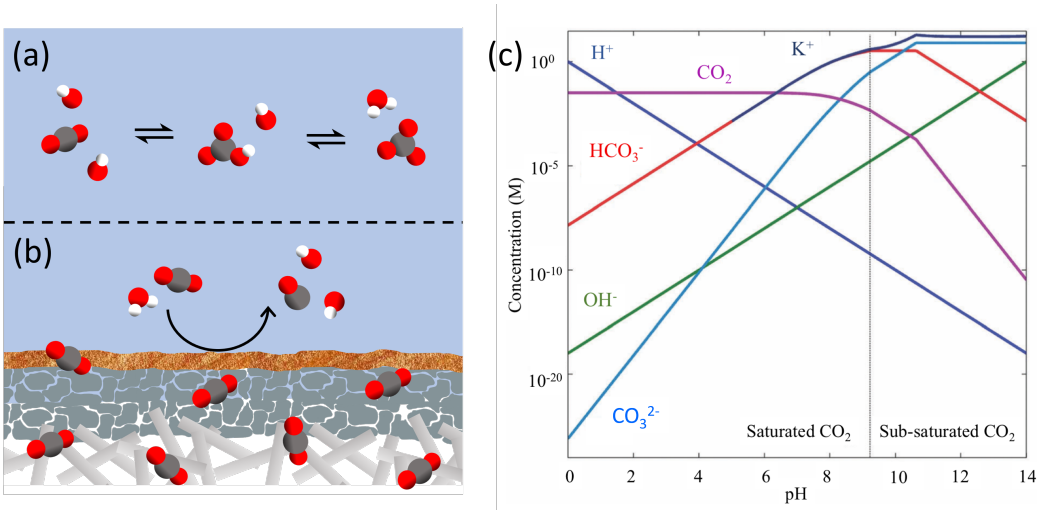

Figure 1.7: Equilibrium and charge-transfer reactions around a CO_2R GDE and the influence of pH on dissolved species. (a) Schematic representation of the bulk equilibrium reactions of CO_2 to carbonate and bicarbonate. (b) Schematic of the reduction of CO_2 to CO with a GDE. (c) Concentrations of CO_2, carbonate, bicarbonate, protons and potassium ions as a function of pH in a potassium bicarbonate solution at atmospheric pressure and room temperature. Adapted from [51].

products (Tables 1.1 and 1.2) as well as for HER (reaction 1 and 2), one proton is consumed or one hydroxide is created for each electron involved. As a result, the local pH value within the boundary layer around the cathode is expected to increase (and the pOH decrease) if the current density is sufficiently negative.

If a GDE is used, CO_2 diffuses into the the electrolyte through the pores of the GDE where it will react to bicarbonate and carbonae according to equilibrium reactions 4 - 7 which leads to an acidification and therefore decrease in local pH (increase in local pOH) as discussed above. The effects of pH increase due to charge transfer reactions and pH decrease due to carbonate and bicarbonate reactions are therefore in competition. Consequentially, a high local pH around a GDE indicated the presence of CO_2R and HER charge transfer reactions.

Furthermore, it has been shown that the local pH and pOH themselves can significantly influence the CO_2R selectivity and reactivity. Several reports demonstrated that a high pH or low pOH has the potential to suppress the parasitic HER [58, 60] as well as shift the CO_2R selectivity towards multicarbon products [60–63]. This is believed to be the case because high hydroxide concentrations suppress the formation of H_2 via HER as well as single carbon products but it does not affect the partial multicarbon product current density. Consequently, the Faradaic efficiency

towards multicarbon products is increased at a given current density for high pH/ low pOH [31, 63].

1.3.3 Techniques to Measure the Local pH Value

Since the local pH and pOH play such a vital role for CO_2R, its determination can both provide mechanistic information and allow for the optimization of CO_2R devices.

Various theoretical models have been developed that aim to simulate the local pH/pOH close to the surface of a cathode performing CO_2R [35, 64, 65]. While insightful, it is almost impossible to accurately represent all parameters that influence the electrochemical environment in a model. It is therefore much more revealing if theoretical studies are combined with experimental measurements of the pH/ pOH around CO_2R electrodes. As has been established above, there is a difference between the bulk pH and the local pH within the boundary layer around a CO_2R cathode. Further, the pH varies within the boundary layer as a function of proximity to the cathode. If the electrode is not homogeneous, the local pH value can also vary as a function of the lateral position along the electrode. It is therefore not sufficient to use a pH meter and measure the bulk pH value but it is necessary to locally resolve the pH value within the boundary layer.

Various techniques have been proposed that allow to measure the local pH value in different electrochemical applications. These are summarized in Table 1.3. The methods can be categorized into optical techniques (fluorescence microscopy, SEIRAS, SERS), scanning probe techniques (SECM,SICM) as well as RRDE [66].

All the techniques summarized in Table 1.3 have advantages and disadvantages. RRDE offers the possibility to perform pH measurements under defined mass transport conditions which is particularly useful for mechanistic studies. However, it lacks lateral resolution. Scanning techniques like SECM and SICM possess superior spatial resolution along the sample surface and additionally provide information about the sample topography. They further offer temporal resolution and allow to study a wide pH range. A major drawback is that the probe significantly alters the fluid dynamics. Further, while it is possible to resolve a 3D curved electrode surface, no information is obtained about the pH in the electrolyte at a distance from the electrode surface. SEIRAS and SERS can resolve the pH value in small volumes around the electrode surface with good lateral and time resolution. However, they lack vertical resolution and are unable to resolve larger macroscopic samples [66].

Table 1.3: Methods to measure the local pH value in electrochemical applications and a comparison of the characteristics of each technique. Spatial resolution in x-y means parallel to the electrode surface, in z perpendicular to the electrode surface. In parts adapted from [34].

Technique	**References**	**Cell Requirements**	**Spatial Resolution**	**Temporal Resolution**	**Chemical Perturbation**	**Fluids Dynamics Perturbation**	**Sensing Capacity**
Fluorescent Microscopy	[67–78]	Compatible w. objective	3D, 250 nm in x-y, 500 nm in z	milliseconds to seconds, depends on probing volume	Yes	Yes	pH, pOH, potentially species concentrations
Surface-enhanced Infrared Spectroscopy (SEIRAS)	[58, 79–81]	ATR crystal	No	picoseconds to seconds	No	No	CO_2, HCO_3^-, CO_3^{2-}, indirectly pH
Surface-enhanced Raman Spectroscopy (SERS)	[60, 82–85]	Compatible w. objective	in x-y, sub-μm	sub-second	No	Yes	pH, adsorbed species
Scanning Electrochemical Microscopy (SECM)	[57, 86, 87]	Tip must be in electrolyte at controlled position	along electrode surface, sub-μm, depends on tip	seconds, depends on probe and field of view	No	Yes	pH, surface reactivity, topography
Scanning Ion Conductance Microscopy (SICM)	[88–90]	Nanopipette must be in electrolyte at controlled position	along electrode surface, 50 nm - 10 μm, depends on nanopipette	seconds, depends on probe and field of view	No	Yes	pH, topography
Rotating ring-disc electrode (RRDE)	[91–93]	rotating solid electrode	in z, depends on rotation speed	depends on sensor	No	Yes	pH, potential

Fluorescent microscopy with a widefield illumination setup allows mapping of the pH value in the lateral direction. In that configuration, a large signal contribution from out-of-focus light has to be accounted for. This problem can be solved by using a confocal laser scanning microscope (see section 1.4.1) where a confocal pinhole blocks out-of-focus light. This technique further allows for pH mapping in three spatial dimensions by capturing images in the x-y plane at different z-positions and stacking them together. A sub-micrometer resolution can be achieved in all three spatial dimensions and a sub-seconds to seconds time resolution, depending on the captured volume and the spatial resolution. Further, this technique allows to image whole macroscopic samples on the length scale of tens to hundreds of micrometers. This is a capability none of the described pH imaging techniques offer. The disadvantages of fluorescent confocal microscopy are that the fluorescent pH-sensitive dyes usually have a limited pH range that is determined by the dye's pK_a value (see section 1.5.1). This can be overcome by the combination of multiple dyes. Further,

the fluorescent probes can potentially interfere with the electrochemical processes that are studied. Luckily, low probe concentrations (tens to hundreds of micromolar) are usually sufficient to reliably resolve the local pH value. The resolution of fluorescent microscopy is on the order of hundreds of nanometers which makes it ideally suited to image the local pH value within the boundary layer, however, it is impossible to resolve the pH value within the electrical double layer.

1.4 Fluorescent Microscopy

pH imaging techniques should be chosen according to the application and the system studied since different techniques can be best suited for different applications. Fluorescent microscopy is ideal to investigate CO_2R electrodes with distinct micrometer-scale 3D features and to study the pH value inside microcavities since it is the only technique that can map the pH value with 3D resolution on a macroscopic scale. This provides the unique opportunity to correlate a CO_2R electrode's micromorphology to the local pH value and to the CO_2R performance.

1.4.1 Principles of Fluorescent Confocal Laser-Scanning Microscopy

Fluorescent confocal microscopy requires the use of fluorescent molecules. These are molecules that can be excited via the absorption of light and emit light nanoseconds later via relaxation to the ground state. In most cases, the emitted light has a longer wavelength than the absorbed light because the excited molecule undergoes non-radiative transitions. The difference between the excitation and emission wavelength is called Stokes shift [94]. A Jablonski diagram of the fluorescence process can be seen in Fig. 1.8 (a). The Stokes shift allows a fluorescence microscope's detector to differentiate between the scattered excitation light beam and emitted fluorescent light.

Fluorescence microscopy is very commonly used in biology. Specific parts of a biological sample can be labelled with fluorescent molecules. By specifically imaging the fluorescent signal, only the areas of interest are revealed while the background appears black. Thousands of fluorescent probes have been developed that allow labeling of many different aspects of biological samples [94].

A wide-field fluorescent microscope has the major disadvantage that the whole sample is flooded with light and background signal from out of focus reaches the detector. This problem can be solved with the use of a confocal laser scanning microscope as schematically depicted in Fig. 1.8 (b). A laser beam is focused onto the sample where it excites a fluorescent probe. On the way to the detector,

the emitted light must pass through a confocal pinhole that eliminates out-of-focus light such that only light that originates from the in-focus plane reaches the detector. The point illumination and employment of a pinhole allows the elimination of background signal. A two-dimensional image can be created by scanning the laser beam in the lateral plane and detecting the fluorescent signal at each point. Further, the use of confocal microscopy allows the 3D rendering of a structure by capturing images in different planes and stacking them together. Finally, fluorescent confocal microscopy has the advantage that is can be used for quantitative measurements. The property that can be quantified depends on the fluorescent probe used.

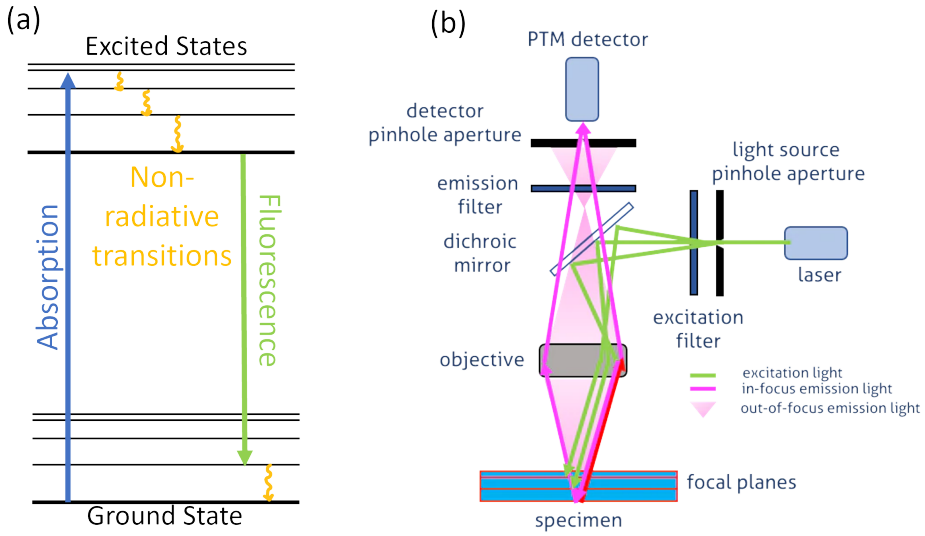

Figure 1.8: Schematics of fluorescence and confocal microscopy. (a) Jablonski diagram of fluorescence displaying how a photon is absorbed to excite an electron which relaxes via non-radiative transitions before fluorescing at a longer wavelength. (b) Schematic representation of a confocal laser-scanning microscope (CLSM), adapted from [95].

The quantity that is of particular interest for this work is the local pH value. Several fluorescent probes have been reported that can resolve the local pH value with CLSM [78, 96–100].

The drawback for CLSM compared to widefield fluorescent microscopy is that the laser scanning requirement makes it considerably slower. In addition, the confocal pinhole, while eliminating unwanted background noise, also reduces the overall signal strength which can lead to a weak signal-to-noise ratio. Slow scanning can improve the signal-to-noise ratio and resolution. The trade-off between spatial resolution and speed must be considered.

1.5 Fluorescent pH Sensors

The local pH value is an important parameter in biological and life-science research and as a result, many fluorescent pH probes compatible with fluorescent CLSM have been developed and targeted towards the biology community [96–100]. There are three different fluorescent sensing mechanisms. The first is fluorescent quenching, meaning that the fluorescence turns off upon a change in pH. The second is fluorescent enhancement where the fluorescence turns on upon a change in pH. The latter is more practicable and easier to use than the first but both methods are sensitive to parameters like the probe concentration. The third sensing mechanism is via ratiometric probes that have opposing responses to pH at two different excitation or emission wavelenghts. The pH is extracted from the ratio between the two responses which makes the signal independent of the dye concentration. Ratiometric probes are therefore preferable, especially if quantitative measurements are performed. Other desirable fluorecent pH probe properties are a large Stokes shift and brightness that can increase the signal-to-noise ratio [98].

pH probes are usually designed by choosing suitable fluorophores and engineering proton sensitive groups. To create a ratiometric probe, two fluorophores with opposing pH sensitive properties can be covalently linked together. Commonly used ratiometric fluorescent pH probes include fluorescein and rhodamine derivatives, cyanine derivatives or naphtaliminde derivatives as well as fluorescent nanoparticles [98].

A challenge that fluorescent pH probes commonly face is a poor photostability. Further, pH probes are almost exclusively developed for the use in biological research and, in most cases, span a limited pH range around a neutral pH value since that is most biologically relevant [99]. However, in the context of electrochemical CO_2R, very high pH values can be relevant. As outlined in section 1.3, the local pH value within the boundary layer increases under CO_2R operation and consequently, very basic pH values can be reached for very negative current densities. Further, a high pH value can suppress the parasitic HER [58, 60] and increase the multicarbon product selectivity [60–63] which makes the investigation of high pH values very relevant in the context of CO_2R.

A class of molecules that has potential to extend the pH range of fluorescent probes are reversible excited-state photoacids and photobases [101, 102].

1.5.1 Reversible Excited-State Photoacids and Photobases as Dynamic Fluorescence Sensors of Local pH

Photoacids and photobases are defined as molecules that can perform reversible excited-state proton transfer (ESPT) from or to another molecule. Since the molecules are reversible, they can be used for prolonged light-to-ionic power conversion. ESPT is caused by a modification of the energy of a protonic bond that causes a change in the Brønsted-Lowry acidity of the photoacid or photobase. This can be quantified by the acid dissociation equilibrium constant K_a, or K_a^* in the excited state [102]. The pK_a is defined as the base-10 logarithm of K_a,

$$pK_a = -\log_{10}(K_a). \tag{1.4}$$

Among others, ESPT can proceed to and from OH^- and H^+, respectively in aqueous environments. As a consequence, the presence of OH^- can quench the photoluminescent intensity of a photoacid and the presence of H^+ can quench the photolumenscence of a photobase. Therefore, photoacids and photobases can be used as fluorescent pH probes and have been employed to investigate the pH value in electrochemical systems [67, 75–78].

Fig. 1.9 (a) shows a Förster cycle square scheme, a thermodynaic cycle that explains the photophysics and photochemistry of a weak photoacid [102, 103]. Depicted on the left are the ground and excited states of the photoacid PAH/ PAH*. The right side depicts the ground and excited states of the conjugate base PA^- and PA^-*. The photoacid (PA / PA*) can be reversibly deprotonated to the conjugate base (PA^- / PA^-*) by a solvated water or hydroxide and the conjugate base can be reversibly protonated to the photoacid by a solvated water or proton, both in the ground and excited states. Since the energy states of the deprotonated conjugate bases are different from those of the photoacid, the photoluminescence of the molecule is quenched in the presence of OH^- and the molecule can be used as a sensor of the local OH^- activity.

Fig. 1.9 (b) displays a typical curve of a pH-sensitive photoacid's photoluminscence intensity as a function of solution pH. It displays a sigmoidal shape around the pK_a^* value when quasi-equilibrium is reached in the excited state [102].

In this work, mainly the two photoacids DHPDS and APTS are used as fluorescent pH probes.

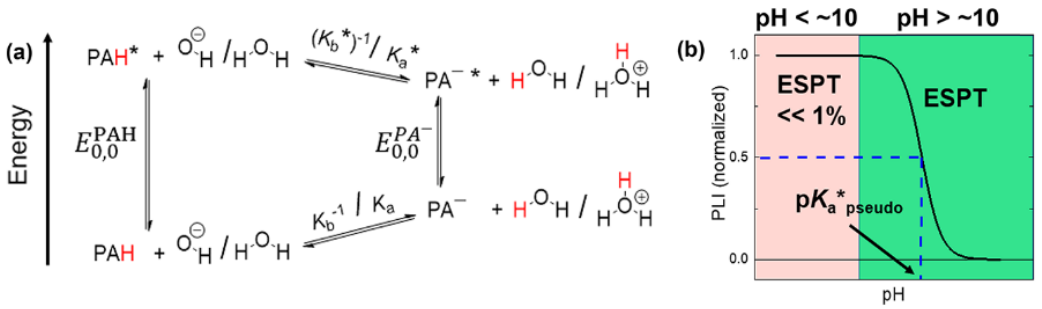

Figure 1.9: Principles governing a reversible photoacid. (a) Förster cycle square scheme for a reversible photoacid PA. It illustrates the excitation of PAH to PAH* and its reversible deprotonation to PA^- / PA^{-*} by a solvated water or hydroxide. (b) Exemplary photoluminescence curve of a pH-sensitive photoacid as a function of solution pH. Adapted from [102].

The Strong Photoacid DHPDS

One photoacid that can been used as a fluorescent pH probe is 6,8-dihydroxypyrene-1,3-disulfonic acid disodium salt (DHPDS). Its molecular structure is displayed in Fig. 1.10 (a). It has a high fluorescence quantum yield, good water solubility and, very importantly, exhibits ratiometric properties that are enabled by two hydroxyl groups with pK_a values of 7.33 and 8.53 [100]. Its absorption spectrum (see Fig. 1.10 (a)) exhibts three distinct peaks, connected to the doubly deprotonated ($R-(OH)_2$), monoprotonated ($R-(OH)(O^-)$), and doubly deprotonated ($R-(O^-)_2$) states in the ground state. DHPDS is a strong photoacid ($pK_a^* \approx 0$) which means that the excited-state proton transfer kinetics are significantly faster than the lifetime of the excited state and therefore, the excited state can reach a chemical quasi-equilibrium. As a consequence, excitation of either protonated state of DHPDS in near-neutral pH solution results in the emission from a deprotonated form of the electronic excited state [78].

These properties can be utilized to employ DHPDS as a pH probe. Since it exhibits ratiometric properties, two of the characteristic absorption peaks, at 405 nm (laser power 1.2 %, gain 100) and at 485 nm (laser power 2 %, gain 80) can be excited. The signal can be collected over the fluorescent spectrum from 495 nm and 835 nm separately for both excitations. The ratio of emission (ratio of the signal from the first excitation divided by the signal from the second excitation) is then a function of the solution pH value. It fits well to the nonideal Henderson-Hasselbach equation,

$$(\text{Ratio of Emission}) = \frac{1}{1 + 10^{n\cdot(pH - pK_{a,obs})}}, \tag{1.5}$$

with n the Hill coefficient ideality factor and $pK_{a,obs}$ an effective excited-state pK_a [78]. For the aforementioned settings, the resulting curve can be seen together with experimental values in Fig. 1.10 (c) in orange color. The resulting pH sensitivity range is 6 - 11.5.

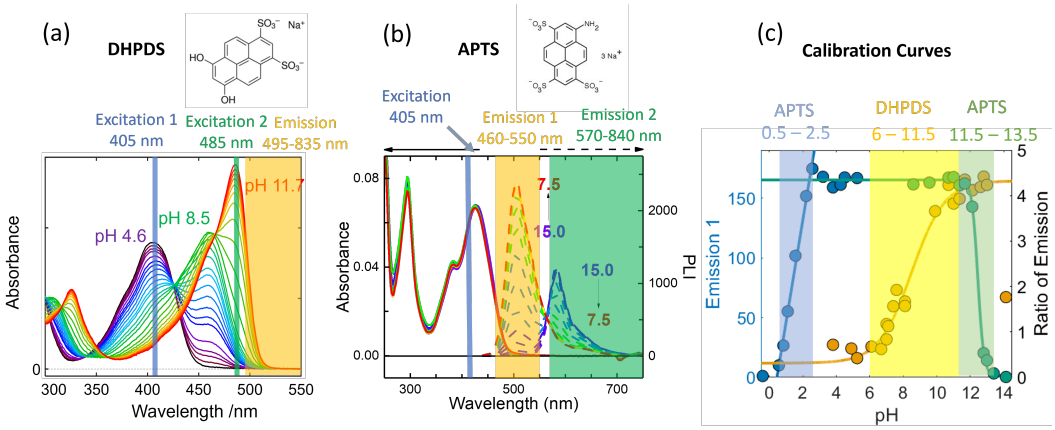

Figure 1.10: Spectra and calibration curves for the fluorescent probes DHPDS and APTS. (a) Molecular structure of DHPDS (adapted from [100]) and its absorption spectrum for different pH values between 4.6 and 11.7 (adapted from [77]). Two excitation wavelengths that match two of the absorption peaks, as well as the wavelength range within which the fluorescence is captured, are indicated. (b) Molecular structure of APTS and its absorption as well as fluorescent emission spectrum for different pH values between 7.5 and 15. The excitation at 405 nm and two separate detection windows matching the distinct fluorescence peaks are indicated (adapted from [102]). (c) Calibration curves of DHPDS (orange) and APTS in a basic regime (green) as the ratio of emission as a function of pH as well as the calibration of APTS in an acidic regime (blue) as the emission intensity as a function of pH. Together, the pH range 0.5 – 2.5 as well as 6 – 13.5 is covered.

The Weak Photoacid APTS

While the strong photoacid DHPDS is a potent optical pH probe and can cover a wide range from pH 6 to pH 11.5, it is unable to resolve very alkaline pH values higher than 11.5. The weak photoacid 8-aminopyrene-1,3,6-trisulfonic acid trisodium salt (APTS) has that capability. While DHPDS had been described previously as a ratiometric pH probe [100], this work is the first demonstration of the weak photoacid APTS as a pH probe. Its molecular structure, along with the absorption and fluorescence spectra for different pH values is displayed in Fig. 1.10 (b). The fluorescence spectrum of APTS exhibits two distinct peaks that are related to the protonated ($R-NH_2$) and deprotonated ($R-NH^-$) states in the thermally

equilibrated electronic excited states. This characteristic makes APTS a ratiomtric probe. APTS is a very weak photoacid ($pK_a > 14$) and therefore, pH > 14 is required for the deprotonation of the electronic ground state. As a consequence, only the protonated ground state can be excited. However, if the concentration of OH^- is high, the equilibrated excited state can be quenched by via a proton transfer to OH^- [78].

It is important to note that the sensing mechanism of APTS varies from that of DHPDS. While DHPDS undergoes a proton-transfer reaction in its ground state, APTS participates in a proton-transfer reaction to aqueous OH^- in its thermally equilibrated electronic excited state [78].

To use APTS as a pH probe in a basic pH regime, it can be excited at 405 nm (laser power 2 %) as well as at 448 nm (laser power 0.3 %), where APTS exhibits strong absorption (see Fig. 1.10 (b)). The fluorescence is captured separately over the two characteristic emission peaks, between 460 nm and 550 nm (gain 13) as well as between 570 nm and 840 nm (gain 25). The ratio of emission is calculated as the ratio between the signals from the two emission peaks and is a function of the pH between 11.5 and 13.5. The ratio of emission as a function of pH can be fitted to the nonideal nonlinear Stern-Volmer equation,

$$\text{(Ratio of emission)} = \frac{1}{1 + ((K_{SV,OH^-}) \cdot a_{OH^-})^n}, \tag{1.6}$$

with K_{SV,OH^-} the Stern-Volmer quenching constant, a_{OH^-} the activity of OH^- and n an ideality factor [78]. For the settings described above, APTS is sensitive to pH values between 11.5 and 13.5, see Fig. 1.10 (c), green markers and green Stern-Volmer fit curve.

Interestingly, APTS also has the capability to sense the pH value in an acidic pH regime following a mechanism analogous to the one described for DHPDS. In an acidic environment, APTS first undergoes proton-transfer reactions in the ground state. While there are two distinct absorption peaks, one of them is at a wavelength well below 405 nm and can therefore not be excited with common confocal laser-scanning microscopes. As a consequence, it is only possible to excite one channel with confocal microscopy and APTS can therefore not be used as a ratiometric probe in acidic solution. It is however possible to use it as a single-channel linear pH probe. If APTS in acidic solution is excited at 405 nm (laser power 2 %) and 448 nm (laser power 0.3 %) and the fluorescent signal is detected between 460 nm

and 550 nm, there is a linear relation between the collected signal intensity and the pH value between pH 0.5 and 2.5. This is depicted in Fig. 1.10 (c) in blue.

If the sensing capabilities of APTS in the acidic and basic regimes are combined with DHPDS, both dyes can cover the pH range 0.5 – 2.5 and 6 – 13.5.

Photoacids apart from DHPDS and APTS that have been identified as potential pH sensor candidates include e.g., HPTS or the weak photoacids 8-anilinonaphthalene-1-sulfonic acid sodium salt, 5-((2 aminoethyl)amino)naphthalene-1-sulfonic acid sodium salt and 5-aminonaphtalene-1-sulfonic acid [101]. Further, various fluorescent probes have been reported that can sense the local concentrations of important CO_2R products, including CO, methanol, formic acid and ethylene. Chapter 8 includes a detailed analysis of the potential of such probes for the use in electrochemical CO_2R applications.

1.6 Thesis Outline

The focus of this work is the interplay between the CO_2R electrode microenvironment and the CO_2R performance. This is mainly investigated with fluorescent CLSM, with an emphasis on GDEs. Chapter 2 demonstrates the imaging of the local pH value around operating CO_2R GDEs with DHPDS and provides evidence about the influence of a GDE's micromorphology on the CO_2R performance. In Chapter 3, time-dependent measurements are presented that illuminate how CO_2 diffuses through an inhomogeneous GDE. Chapter 4 includes more data about the interplay between a GDE's micromorphology and the CO_2R performance with the sensing capacity extended by APTS and a detailed look on the product distribution. Based on these results, the focus in Chapter 5 shifts towards the fabrication of CO_2R GDEs with tailored micromorphology that allow boosting the CO_2R performance as well a more systematic investigation of the influence of microcavities in a GDE's surface. In Chapters 6 and 7, the developed confocal pH imaging technique is applied to investigate the influence of a GDE's pore size on CO_2R and to gain a more mechanistic understanding of CO_2R in acidic electrolytes. Finally, Chapter 8 aims to expand the sensing capacities to image the local CO concentration around operating CO_2R electrodes. Chapter 9 summarizes the outcomes of this work and provides a perspective on future research directions. The appendix presents additional data and focuses on lessons learned over the course of this work.

Chapter 2

OPERANDO LOCAL PH MEASUREMENT WITHIN GAS DIFFUSION ELECTRODES PERFORMING ELECTROCHEMICAL CARBON DIOXIDE REDUCTION

Contents drawn from: A. J. Welch, A. Q. Fenwick, **Annette E. Böhme**, H.-Y. Chen, I. Sullivan, X. Li, J. S. DuChene, C. Xiang, and H. A. Atwater. "Operando Local pH Measurement within Gas Diffusion Electrodes Performing Electrochemical Carbon Dioxide Reduction". In: *J. Phys. Chem. C* 125 (2021), pp. 20896–20904. DOI: https://doi. org/10.1021/acs.jpcc.1c06265.

A.E.B. assisted with and performed pH imaging experiments as well as conceptualized, designed, performed and analyzed all COMSOL Multiphysics simulations.

2.1 Introduction

As outlined in section 1.3.2, the local pH value around an operating CO_2R GDE plays a vital role in determining the local CO_2R activity and selectivity. Although challenging to determine experimentally, the local pH near the electrode surface should be measured under operating conditions to provide the necessary insight required to further improve the activity, selectivity, and stability of these fuel-forming devices. In this chapter, we focus on understanding the pH in GDEs due to their superior CO_2R performance as described in section 1.2.3.

The application of high current densities to a GDE results in the creation of multiple hydroxide ions per unit time, thus rapidly increasing the pH, while any unreacted CO_2 will acidify the electrolyte via reaction with OH^- to form HCO_3 and H^+ ions. These two characteristics have opposing effects on the pH near the electrode surface. If the pH is increased locally, then the activity of the hydrogen evolution reaction (HER) decreases substantially, while the CO_2 reduction reaction becomes relatively more favorable[60, 104]. While both reactions consume water molecules, the rate of H_2 evolution has been shown to be far more dependent on the local pH than the rate of CO_2 reduction [61, 104]. In addition to suppressing the HER, the local pH also influences which CO_2 reduction pathways are most energetically favorable[60, 62, 63]. Alkaline conditions in particular promote the formation of multicarbon products (C_{2+}) such as ethanol, propanol, acetate, etc.[61–63], see section 1.3.2.

Techniques to measure the local pH value in electrochemical applications are described in section 1.3.3.

Previously, SERS has been used to measure the local pH in a CO_2 reduction GDE with a 1 M KOH electrolyte (pH 14). It was found that the local pH was near 7 in the absence of any current flow, and as the current density increased to 100 mA/ cm^2, the local pH increased to 10. It is interesting to note that even with an electrolyte with a bulk pH of 14, the electrode surface remained in the pH range of 7-10 for a wide range of current densities. However, this measurement did not provide any resolution along the plane of the electrode surface. SECM studies confirm that the local pH increases during device operation[54, 55, 57]. While SECM allows for better spatial resolution than confocal fluorescence microscopy, it is unable to probe the pH within the trenches that exist in the surface of a typical carbon paper GDE (see SEM images in Fig. 2.1 (e) and (f)).

Our study builds on previous work by mapping the pH both on the surface and within the heterogeneous reaction environments encountered in GDEs. This experimental approach therefore allows us to correlate the width of trenches in GDEs to the local pH. Here, we use confocal microscopy (see section 1.4.1) and the pH-sensitive two-color fluorescent dye DHPDS (see section 1.5) to probe the operando local pH of a copper (Cu) GDE under CO_2R conditions. This chapter focuses on the imaging of the local pH value in near-neutral conditions. A study including higher pH values that can be resolved with the fluorescent probe APTS can be found in Chapter 4. With CLSM, micron-scale resolution in all three spatial dimensions (within the plane of the electrode (x, y) and perpendicular to its surface (z)) can be achieved. This approach offers new insight into how CO_2 reduction affects the local electrolyte pH near the Cu catalyst. Interestingly, our study indicates that at low overpotentials, the pH varies widely across the electrode surface. Specifically, in narrow trenches throughout the electrode, the pH is significantly elevated compared to the surroundings. Our findings highlight the electrocatalytic heterogeneity in GDEs and strongly suggest that these regions of locally high pH are the most active parts of the electrode for CO_2 reduction.

A Cu-based GDE was investigated owing to the unique ability of Cu to produce C_{2+} products (e.g., ethanol, see Chapter 1.2.2)[47, 50]. Figure 2.1 shows a schematic of the GDE and experimental setup used, as well as scanning electron microscopy (SEM) and optical bright-field microscopy images of different layers of the device. The GDE used here and in many other devices[61, 105–107] is composed of three

layers: (1) a gas diffusion layer, (2) a microporous layer, and (3) a catalyst layer (Figure 2.1 (b), compare also section 1.2.3). The CO_2 first diffuses through the gas diffusion layer, composed of carbon fibers (Figure 2.1g,h), and then through the microporous layer, which is made of carbon black coated in hydrophobic PTFE to regulate local electrolyte availability (Figure 2.1e,f). After diffusion through the microporous layer, CO_2 comes into contact with the electrolyte at the catalyst layer (Figure 2.1c,d), where it can then undergo reduction to yield a variety of chemical products.

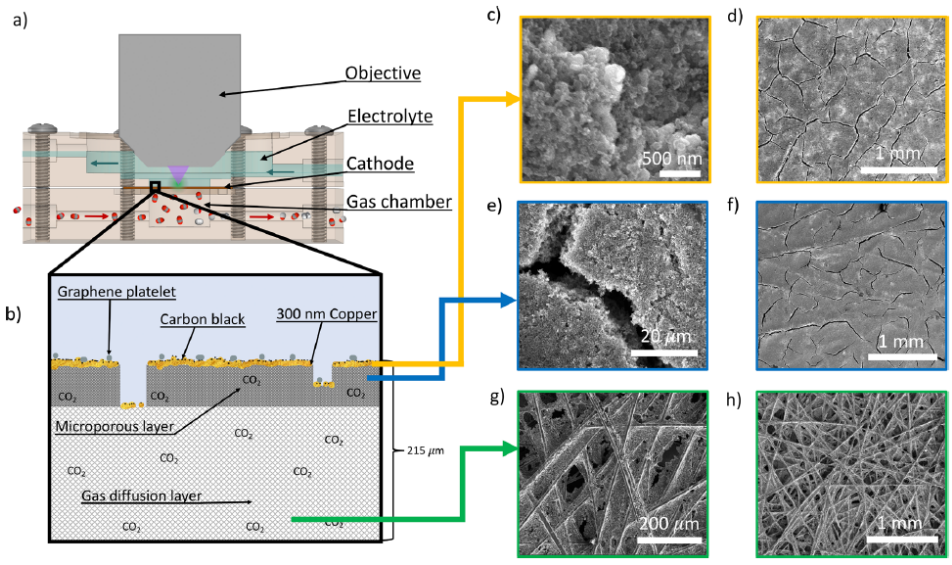

Figure 2.1: Overview of a Cu gas diffusion electrode (GDE) for CO_2 reduction studies. (a) Cross-sectional diagram of the custom electrochemical cell designed to enable in situ confocal fluorescence microscopy experiments. (b) Schematic of a typical Cu GDE, not to scale. (c, d) Scanning electron microscopy (SEM) images of the 300 nm thick Cu catalyst layer. (e, f) SEM images of an uncoated microporous layer. (g, h) SEM images of the gas diffusion layer.

Some CO_2 reacts at the catalyst surface into products such as CO, HCOOH, or CH_4. The remaining unreacted portion of the CO_2 then passes into the electrolyte and increases its acidity[108]. While several reports quantified the one pass CO_2 utilization efficiency[109], the vast majority of the CO_2 reduction experiments did not seek to optimize the utilization of CO_2. The competition between these two processes acidification and hydroxide ion generation can be investigated via measurement of the local pH at the catalyst-electrolyte interface.

2.2 Methods

Copper Gas Diffusion Electrode Fabrication and Characterization

Cu GDEs were fabricated by depositing 300 nm of Cu onto the microporous layer of a Sigracet 22BB carbon paper substrate purchased from Fuel Cell Store with an AMOD dual electron beam deposition system by Angstrom engineering. For samples that were used for confocal fluorescent microscopy, an aluminum foil shadow mask with 3 mm diameter holes was used. For electrodes used for product detection, no shadow mask was used. After deposition, the samples were first spray coated with a solution of carbon black and Nafion. The solution is one-part DI water and one-part isopropyl alcohol with 2.5 mg of carbon black per ml of solution and 50 ml of 5 weight % Nafion per ml of solution. For both coatings, the solution was sprayed from a distance of 3 inches for 1 second per square inch of electrode. After the samples were coated, they were dried under vacuum overnight.

The samples were characterized with a NOVA NanoSEM 450 scanning electron microscope and an Oxford Instrument's Xmax 80 mm^2 energy-dispersive X-ray spectroscopy system in a NOVA NanoSEM 450.

Product Distribution Measurements

An electrochemical parallel-plate compression cell made of polyether ether ketone (PEEK) was used to perform CO_2 reduction reaction experiments and measure the product distribution. A volume of 20 mL of CO_2-saturated 100 mM $KHCO_3$ was added to the catholyte bath and the anolyte bath. The electrolyte was then flowed by the cathode and anode separately at a rate of 6.3 ml/min. The Cu GDE served as the working electrode with a Ag/AgCl leakless reference electrode and a Pt mesh counter electrode. The cathode and the anode were separated by an anion exchange membrane (AGC, Selemion AMV). CO_2 was flowed through the serpentine gas chamber at the back of the cathode at a rate of 10 standard cubic centimeters per minute (SCCM). The outflowing gas was fed into a SRI-8610 gas chromatograph. All experiments were performed at room temperature with a Biologic VSP-300 potentiostat. All experiments were chronoamperometric, meaning that they were at constant voltage. All potentials were converted to the reversible hydrogen electrode (RHE) scale using the equation:

$$\text{E vs. RHE} = \text{E vs. Ag/AgCl} + 0.197\,\text{V} + 0.059\,\text{V pH}^{-1} \cdot (\text{bulk solution pH}). \quad (2.1)$$

Before each experiment, potentiostatic electrochemical impedance spectroscopy (PEIS) was performed to determine the solution resistance of the cell, which was

typically between 10 – 50 Ω. The applied electrochemical potential was then compensated by 85 % using iR compensation of the potentiostat.

pH Imaging Experiments

We used CLSM to measure the local pH due to its high spatial resolution relative to the dimensions of interest in the system. The electrochemical cell used for pH imaging experiments was different from the one used for product detection since it must be compatible with confocal microscopy. The main constraint is that the working distance of the objective is 1.7 mm. This necessitated the removal of the ion exchange membrane, so that the objective could be placed close to the cathode. Additionally, this required that the cell be rotated by 90° relative to a typical cell. Since the objective is being submerged in the electrolyte this means that the electrolyte is open to the atmosphere and not sealed. The fact that the membrane is removed and the electrolyte is open to air makes it impossible to perform gas chromatography (GC) experiments with it. First, since the cell is not sealed, not all of the products can be captured and sent to the GC. Therefore, it is not possible to obtain an accurate Faradaic efficiency. Also since there is no membrane the anode can oxidize liquid products that are formed which also will make it impossible to get an accurate Faradaic efficiency. The change in electrochemical cell between product detection and pH imaging experiments caused a significant change in current density. To make the results as relevant as possible, we used the same potentials in both systems because similar potentials should produce similar products. Everything besides the electrochemical cell was kept the same between experiment – catalyst, electrolyte, CO_2 flow rate, reference electrode, etc.

Figure 2.1 (a) shows a schematic of the electrochemical cell used for pH imaging, and Figure 2.2 shows a more detailed schematic, as well as photos of the cell.

In this study, a Zeiss LSM 710 CLSM with 458 nm, 488 nm, 514 nm, 543 nm and 633 nm diode lasers was used. The technical resolution of this system is 280 nm in x - y and 560 nm in z. However, due to noise from the electrolyte pump and diffusion, the resolution is on the order of a micron under our conditions.

The fluorescent dye DHPDS, that is ideally suited to resolve near-neutral pH values, was employed (see also section 1.5.1) [100]. The absorbance vs wavelength of DHPDS in different standard solutions of known pH is shown in Fig. 1.10 (a). At the most acidic pH of 4.6, the peak absorbance is centered at approx. 400 nm; at pH 8.5, the peak absorbance is at approx. 455 nm; and at pH 11.7, the peak absorbance

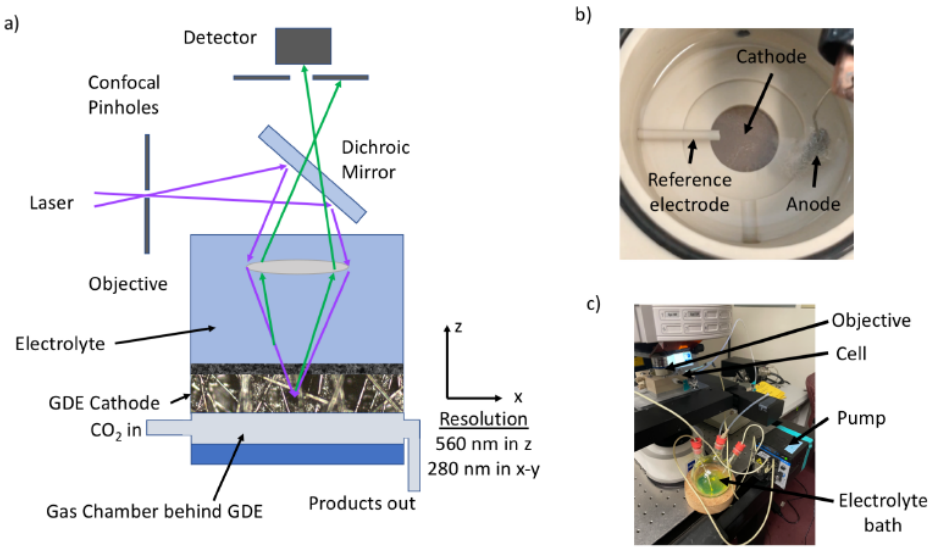

Figure 2.2: Overview of the experimental setup. (a) shows a schematic of the electrochemical cell used for imaging the pH via confocal fluorescent microscopy. The bottom plate is the gas chamber and the top plate holds the electrolyte. This setup has no membrane and the electrolyte is constantly being flowed across the active catalyst layer. (b) shows a top-down photo of the electrochemical cell without the microscope objective. (c) shows a photo of the entire experimental setup with the objective in the cell, the electrolyte bath, and the pump to circulate the electrolyte through the electrochemical cell.

shifts toward approx. 480 nm. We sequentially excited the dye line by line with a 458 nm (λ_{ex1}) and 488 nm (λ_{ex2}) laser. The fluorescence signal from both λ_{ex1} and λ_{ex2} was collected individually from 515 to 700 nm.

DHPDS was calibrated using a range of pH solutions. The solutions were made by mixing KOH, bicarbonate, water and standard buffer solutions. The pH of these solutions was measured by a Denver Instruments Ultra Basic pH meter and results were confirmed with color changing pH strips. The solution was then placed under the microscope and the water immersion objective was immersed in it. The objective was then focused on a point in the middle of the solution. The ratio of the fluorescence was then plotted vs. pH to generate the calibration curve displayed in Fig. 2.3 (a). We fit the pH data to the function

$$y = \frac{-a}{1 + \exp(-b \cdot (x - c))} + d. \tag{2.2}$$

We found the coefficients to be a = –33.72, b = 1.413, c = 8.083, and d = 5.571. The error was determined to be 0.3 pH units. These data demonstrate that the DHPDS

dye is sensitive to changes in solution pH from pH 6 to 10 under the aforementioned excitation conditions.

Note that for the calibration curve that is presented in Fig. 1.10 (c) in orange color, the dye was excited at 405 nm and at 485 nm which resulted in a pH range from 6 to 11.5. This was not possible in this study since these wavelengths were not available with the CLSM system used.

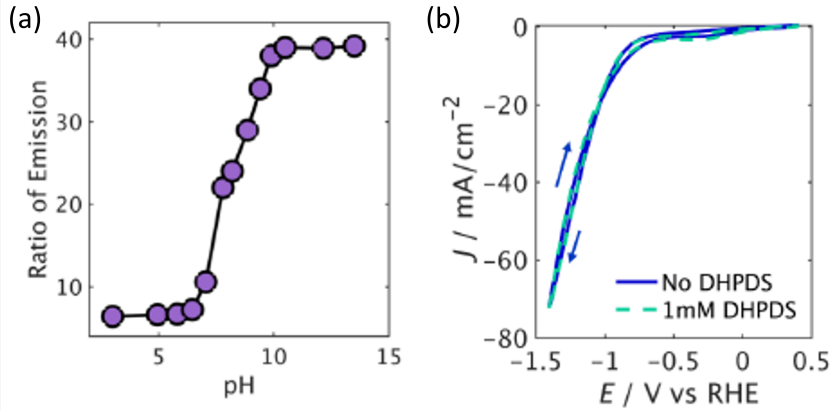

Figure 2.3: Characterization of the pH-sensitive fluorescent dye DHPDS. (a) shows the ratio of fluorescence emission from a 458 nm and 488 nm excitation wavelength as a function of solution pH. After acquiring all of the data, we fit the pH data to the function, y = –a/(1+exp(–b*(x – c)))+d. We found the coefficients to be a = –33.72, b = 1.413, c = 8.083, and d = 5.571 for 95% confidence bounds. From the fit accuracy we can estimate an error of 0.3 pH units. (c) shows the current (J) vs applied electrode potential (E) for a CO_2 reduction electrode with (dashed line) and without (solid line) DHPDS dye in the electrolyte.

A CO_2-saturated solution of 100 mM $KHCO_3$ with a bulk pH of 6.8 was used as the electrolyte in our experiments, ensuring that the bulk pH will be at the lower-sensitivity limit of the DHPDS. DHPDS is electrochemically stable under CO_2 reduction reaction conditions. In Fig. 2.3 (b), the current-voltage characteristics of the electrode are nearly identical with or without the ratiometric dye. Fig. 2.4 shows that upon addition of the dye, HER activity slightly increases but the CO_2 reduction reaction activity remains largely unchanged. Based on these control experiments, the DHPDS dye is relatively inert with regard to CO_2R GDE operating conditions.

For operando pH imaging experiments, a volume of 40 mL of 100 mM CO_2-saturated $KHCO_3$ with 100 μM DHPDS was added to the electrolyte bath. The electrolyte was then flowed through the cell at a rate of 6.3 ml/min. CO_2 flowed through the gas chamber at the back of the cathode at a rate of 10 SCCM. The Cu GDE served

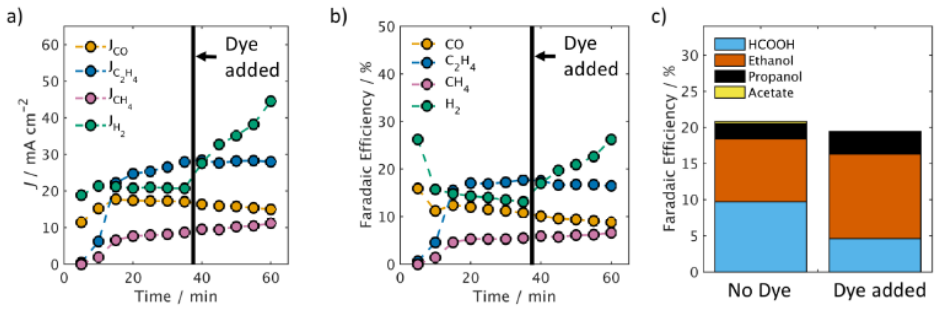

Figure 2.4: Characterization of how the pH-sensitive DHPDS fluorescent dye affects the activity and selectivity of the copper GDE. (a) shows the current density (J) vs time before the dye is added (0 to 34 minutes) and after the dye is added to the electrolyte at 35 minutes. The partial current density for HER increases but the CO_2 reduction partial current densities remain stable. (b) shows the Faradaic efficiency for gas products vs time. The dye is added to the electrolyte at 35 minutes. The Faradaic efficiency for HER increases but the CO_2 reduction Faradaic efficiency remains stable. (c) shows the Faradaic efficiency for liquid products before and after the dye was added. The Faradaic efficiency for the CO_2 reduction reactions remain similar before and after the addition of the dye, albeit with slight increase in ethanol (orange) and decrease in formic acid (blue).

as the working electrode with a Ag/AgCl leakless reference electrode and a Pt mesh counter electrode. The objective (WN Achroplan 63x water immersion objective with a numerical aperture of 0.9) of the LSM 710 microscope was lowered into the electrolyte and focused at the surface of the electrode. The power of the Argon laser was set to 100 % power for 458nm and 20 % power for 488 nm, and the gain for each channel was 800. The data was post-processed using the calibration curve to determine the pH. A 'z-stack' of images was taken to create a series of images at the same location but at different heights above the electrode.

When the electrode was passing current, the electrode was first allowed to stabilize for 1 – 5 minutes until the working electrode potential was constant before a set of images was taken. All electrolysis experiments were performed under galvanostatic conditions. The working electrode potential was measured and is depicted in Fig. 2.3. All potentials were converted to the reversible hydrogen electrode (RHE) scale using equation 2.1. Before each experiment, potentiostatic electrochemical impedance spectroscopy (PEIS) was performed to determine the solution resistance of the cell, which was typically between 5 – 30 Ω.

Multiphysics Simulations

To perform Multiphysics simulations, a two-dimensional stationary COMSOL Multiphysics 5.5 model [110] with a combination of the Laminar Flow Module and the Transport of Diluted Species Module was used.

To model the electrolyte flow through the electrochemical cell, a three-dimensional COMSOL model with the Laminar Flow Module was set up. The velocity at the inlet of the cell was experimentally determined to be 1.3 mm/s. As expected, the flow velocity underneath the objective is found to be much lower than around it. The average flow velocity 30 μm above the electrode surface was determined to be 0.14 μm/s. This value was used as an input for the two-dimensional model of pH around a trench.

The geometry of the two-dimensional model of the pH is depicted in Fig 2.15 (a). At the inlet (left), we assume a flow velocity of 0.14 μm/s, at the outlet (right), a zero pressure condition is applied. On the electrode surface as well as on the trench walls and at the bottom of the trench we apply no-slip boundary conditions. Both convection and diffusion are taken into consideration for the transport properties. The inputs here are the velocity field calculated with the laminar flow module and the diffusion coefficients of all species (see Table 2.2). We assume a boundary layer thickness of 60 μm where we apply concentration boundary conditions as expected for a CO_2-saturated 100 mM $KHCO_3$ electrolyte in equilibrium (see Table 2.2). The same concentrations are used as inflow concentrations at the inlet. On the surface of the electrode as well as at the bottom and the side wall of the trench we assume a CO_2 flux of 1 $\frac{\mu\text{mol}}{\text{cm}^2\cdot\text{s}}$. This value was determined experimentally by measuring the difference in the CO_2 flow rate with a flow meter before and after passing the GDE in the electrochemical cell. Note that this method only provides an estimate as the CO_2 flux though the GDE since it is not homogeneous.

We assumed that there is catalytic activity at the planar electrode surface, the trench walls, and trench bottom, because SEM and EDS images of our samples show that copper coats the surface, trench sidewalls, and trench bottom (compare Figures 2.11 and 2.12). The charge-transfer reactions (see also section 1.2.1) considered on these surfaces are

$$CO_{2(aq)} + H_2O + 2\,e^- \longrightarrow CO + 2\,OH^- \quad \{9\}$$

$$2\,H^+ + 2\,e^- \longrightarrow H_2 \quad \{10\}$$

$$2\,H_2O + 2\,e^- \longrightarrow H_2 + 2\,OH^- \cdot \quad \{11\}$$

The source terms are determined with

$$R_n = -\sum \frac{s_j \cdot J \cdot FE_n}{n_j \cdot F} \tag{2.3}$$

with s_j the stoichiometric coefficient of equation j, J the current density, FE_n the Faradaic efficiency of species n determined experimentally (see Fig. 2.5, the Faradaic efficiency for CO is assumed to be the sum of the Faradaic Efficiency of all carbon products), n_j the number of transferred electrons and F is the Faraday constant.

Furthermore, bulk carbonate reactions (see section 1.3.1) are assumed to take place in the whole electrolyte body (see also section 1.3.1):

$$CO_{2(aq)} + H_2O \overset{k_1, k_{-1}}{\longleftrightarrow} H^+ + HCO_3^- \quad \{12\}$$

$$HCO_3^- \overset{k_2, k_{-2}}{\longleftrightarrow} H^+ + CO_3^{2-} \quad \{13\}$$

$$CO_{2(aq)} + OH^- \overset{k_3, k_{-3}}{\longleftrightarrow} HCO_3^- \quad \{14\}$$

$$HCO_3^- + OH^- \overset{k_4, k_{-4}}{\longleftrightarrow} H_2O + CO_3^{2-} \quad \{15\}$$

$$H_2O \overset{k_w, k_{-w}}{\longleftrightarrow} H^+ + OH^- \cdot \quad \{16\}$$

The source terms are calculated with

$$R_n = \sum_j s_j \cdot (k_j \prod_{s_j<0} c_n - k_{-j} \prod_{s_j>0} c_n) \tag{2.4}$$

where s_j is the stoichiometric coefficient of reaction j, k_j the forward rate constant, k_{-j} the reverse reaction rate constant, $k_{-j} = \frac{k_j}{K_j}$ with the equilibrium constant K_j (see Table 2.2). c_n is the concentration of species n.

2.3 Results and Discussion

2.3.1 Experimental Results

We first characterized the electrochemical performance of our Cu-based GDEs prior to imaging the local solution pH. Chronoamperometry experiments were performed across a range of applied potentials, and the products were measured via gas chromatography and high-performance liquid chromatography, see Fig. 2.5. All applied

Table 2.1: Diffusion coefficient, concentration, and rate constant parameters used for the COMSOL model.

Diffusion Coefficients [35]	
K^+	$1.957 \cdot 10^{-5} \frac{cm^2}{s}$
H^+	$9.311 \cdot 10^{-5} \frac{cm^2}{s}$
OH^-	$5.293 \cdot 10^{-5} \frac{cm^2}{s}$
CO_2	$1.91 \cdot 10^{-5} \frac{cm^2}{s}$
HCO_3^-	$1.185 \cdot 10^{-5} \frac{cm^2}{s}$
CO_3^{2-}	$0.91 \cdot 10^{-5} \frac{cm^2}{s}$
Equilibrium Concentrations [35]	
K^+	$100 \frac{mol}{m^3}$
H^+	$1.58 \cdot 10^{-4} \frac{mol}{m^3}$
OH^-	$6.31 \cdot 10^{-5} \frac{mol}{m^3}$
CO_2	$37.13 \frac{mol}{m^3}$
HCO_3^-	$99.94 \frac{mol}{m^3}$
CO_3^{2-}	$3.02 \cdot 10^{-2} \frac{mol}{m^3}$
Forward Rate Constants [110]	
k_1	$3.71 \cdot 10^{-2} \frac{1}{s}$
k_2	$59.44 \frac{1}{s}$
k_3	$2.23 \cdot 10^{-3} \frac{L}{mol \cdot s}$
k_4	$6 \cdot 10^{9} \frac{L}{mol \cdot s}$
k_w	$1.4 \cdot 10^{-3} \frac{mol}{L \cdot s}$
Equilibrium Constants [110]	
K_1	$10^{-6.37} \frac{mol}{L}$
K_2	$10^{-10.32} \frac{mol}{L}$
K_3	$\frac{K_1}{K_W}$
K_4	$\frac{K_2}{K_W}$
K_W	$10^{-14} \frac{mol^2}{L^2}$

potentials (E) are reported vs the reversible hydrogen electrode (E vs RHE). As shown in Fig. 2.5a, at potentials more positive than -1.0 V vs RHE, the Cu GDE produced primarily H_2 with some C_1 and C_2 products.

Consistent with prior observations from Cu GDEs, H_2 is the dominant product at low overpotentials, while higher overpotentials favor CO_2 reduction[36, 49]. Cu requires higher overpotentials to perform the C-C coupling reactions necessary to synthesize C_2 products[111]. At -1.0 V vs RHE, we begin to observe many CO_2 reduction products, with the largest fraction consisting of the C_2 products ethylene and ethanol. Higher overpotentials were not evaluated because the limited pH sensitivity range of

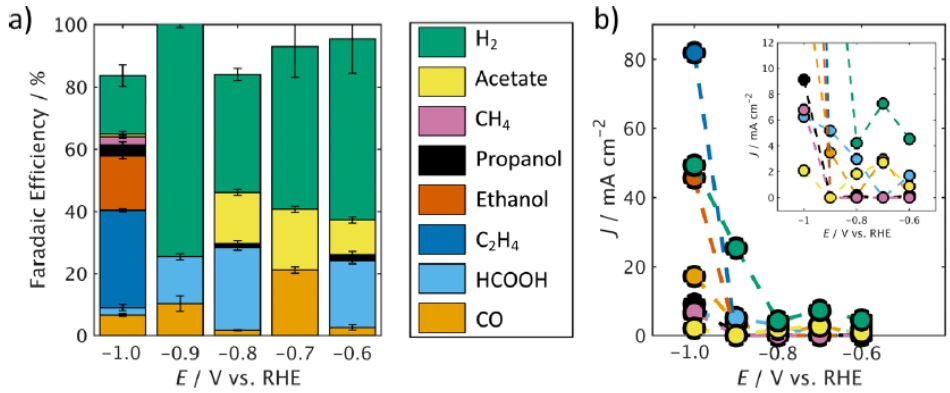

Figure 2.5: Electrocatalytic characterization of a GDE composed of carbon paper coated with 300 nm of Cu on top of the microporous layer. (a) Faradaic efficiency and (b) partial current density, J, for each product as a function of electrode potential, E. The figure legend applies to both panels (a) and (b).

the DHPDS dye is not suited for higher current densities. We therefore restricted our electrocatalytic characterization to those conditions that could be directly examined with confocal microscopy and DHPDS.

The DHPDS dye (100 μM) was dissolved in the electrolyte, and the electrolyte was replaced between every experiment to ensure that the initial conditions were standardized to keep the flux of hydroxide ions constant between experiments. The electrode was stable between experiments with minimal changes in the potential of the working electrode after 5 min as displayed in Fig. 2.6.

For each current density that was tested, a series of images were taken 3 μm apart in the z-direction (perpendicular to the electrode surface). Figure 2.7 shows two-dimensional (x, y) maps of solution pH obtained from a single lateral location on the cathode surface at varying distances from the electrode surface (within a column) and at different current densities (along a row). The color scale in each map from blue to yellow denotes the local solution pH from pH = 7-10. Each set of images took approximately 30 min to collect.

In the first column of Figure 2.7, at 0 mA/cm^2, the solution pH is uniform throughout the z-direction. The second row of pH maps at 0 μm defines the surface of the electrode; as the electrode is not flat, the highest point of the electrode in the image area was chosen as the 0 μm height. Black regions in the pH map indicate areas where no fluorescence was observed and therefore no electrolyte was present. The bottom row of pH maps in Figure 2.7 shows the solution pH within a trench in the microporous layer. As the current density increases from left to right along a row,

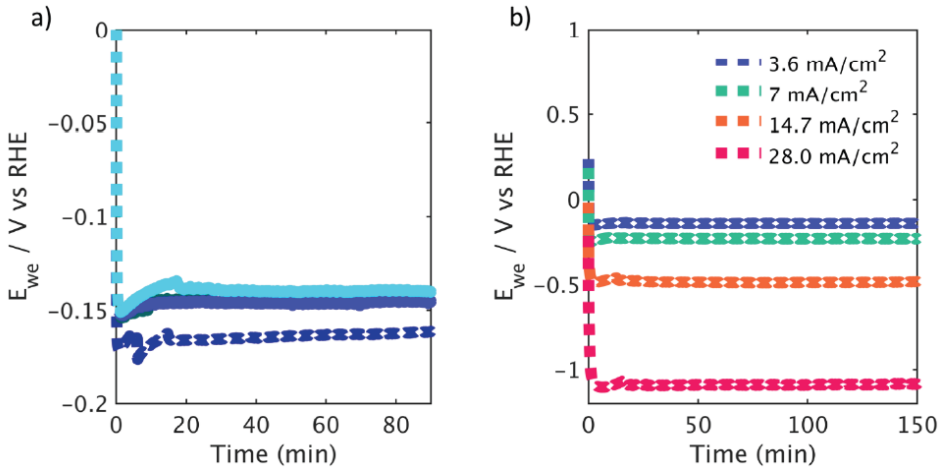

Figure 2.6: Stability of the Cu GDE working electrode potential (E_{we}) over time. (a) shows four different electrochemical tests where the current density is set to 3.4 mA/cm^2. From this we can see that there are only very small changes in potential of the working electrode between tests. (b) shows electrochemical tests with varying current density. We note that the potential of the working electrode is very stable after the first 5 minutes indicating that the electrode is stable throughout the run.

the local solution pH increases both within the trench of the microporous layer and above the electrode surface. It is particularly interesting to note that the pH is not completely uniform over the electrode surface, which can be most easily seen in the 0 and -15 μm height maps at a current density of -3.4 mA/cm^2. We are only able to observe this inhomogeneity at low current density where the pH gradient built up is not large. As the current density is further increased and all catalyst particles become electrochemically active, we are no longer able to disentangle the pH gradient creation from individual locations along the catalyst. This effect was repeatedly observed at multiple locations across the electrode surface, as shown in Figure 2.8. We observe much smaller local variations at -1.6 mA/cm^2 because the applied bias is smaller.

We can use pH as a proxy for the total current density, as each electron catalyzing either the HER or the CO_2 reduction reaction corresponds to the creation of one hydroxide ion in the electrolyte. Hence, higher pH regions are indicative of higher activity. As the current density was further increased, the fluorescent signal from the dye eventually saturates. To confirm that only electrochemically active areas of the electrode were responsible for locally increasing the solution pH, a map was obtained 9 μm above the electrode surface over a region that was only partially covered with Cu (Fig. 2.9). The electrolyte flowed left to right across the electrode,

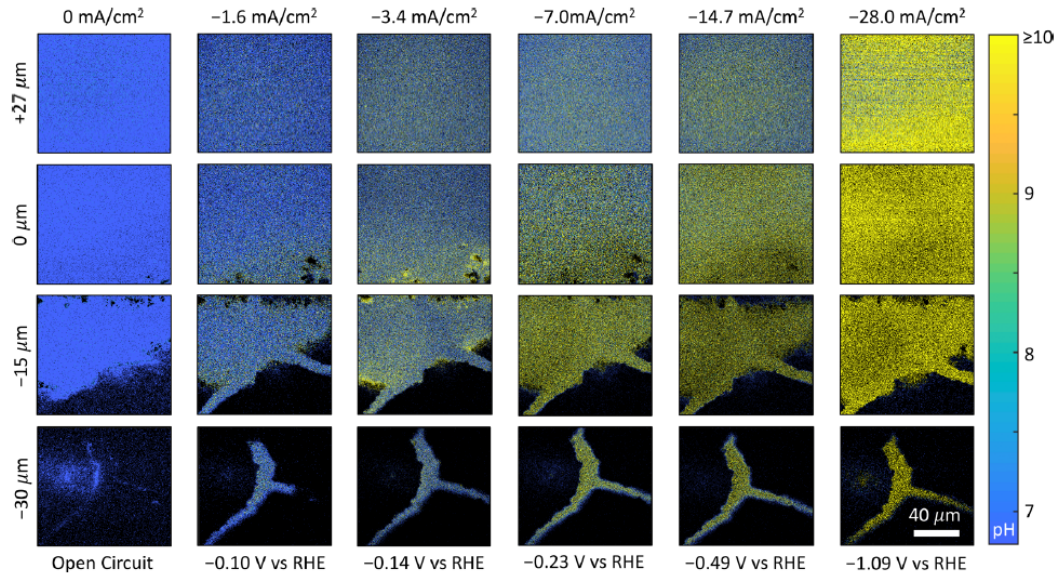

Figure 2.7: Operando mapping of solution pH in three dimensions over a Cu GDE. Maps are obtained at the same location on the electrode at different heights above the electrode surface and at different current densities. From top to bottom, each row of maps corresponds to 27 μm above, 0 μm (at the surface), 15 μm below, and 30 4μm below the electrocatalyst surface. From left to right, each column of maps were obtained at 0 mA/cm^2 (no reaction under open-circuit conditions), -1.6,-3.4, -14.7, and -28.0 mA/cm^2. The pH color scale and the scale bar in the bottom right corner apply to all images.

and the current density was set at -14.7 mA/cm^2. As shown in Figure 2.9 (a), the left-hand side of the map has a pH approx. 7, which was obtained above a region of the catalyst without Cu, while the right-hand side of the map has a pH approx. 9, which was taken from above a region coated in Cu. It is clear from this map that regions of locally high pH only occur near regions of the electrode where hydroxide ions are being created via electrocatalysis. In addition, we measured the pH under the same conditions at the back edge of the electrolyte (Figure 2.9 (b)).

When the average pH at the surface of the electrode is below pH 9.5 (J > -14.7 mA/cm^2, or applied potentials less negative than -0.7 V vs RHE), the electrode mostly produces C_1 products and H_2. In contrast, many C_2 products were observed when the solution pH at the surface of the electrode was above pH 10 (J < -28.0 mA/cm^2, or at -1.0 V vs RHE). Potentials more negative than -0.9 V vs RHE are required to produce these higher current densities and C_2 products, but the local pH also plays a role in suppressing the HER and promoting CO_2 reduction[58, 104]. The activity of CO_2 reduction is independent, whereas the HER activity is greatly

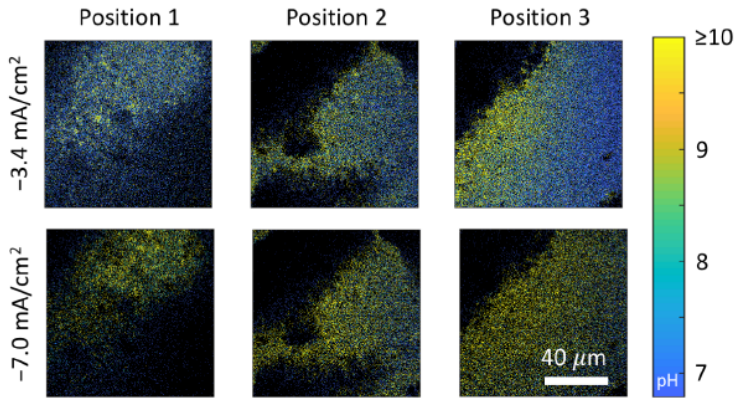

Figure 2.8: pH maps at three different locations along the electrode surface. Position 1 is off to the side of the electrolyte inlet, position 2 is near the electrolyte inlet, and position 3 is near the electrolyte outlet. The first row shows pH maps all taken at -3.4 mA/cm^2 and the second row shows pH maps all taken at -7.0 mA/cm^2. We observe the hot spots for all 3 positions at -3.4 mA/cm^2 and we do not observe the hot spots at -7.0 mA/cm^2.

dependent on the hydroxide ion concentration[104]. For CO reduction on Cu, locally high pH conditions reduce the free energy required for important steps along the reaction pathway to yield C_2 products such as ethanol[62]. Areas of locally high pH may also reduce the free energy for CO_2 reduction pathways. Thus, our results indicate that a highly alkaline local pH increases the selectivity toward C_2 products while decreasing the selectivity toward the HER.

Finally, we explore the local pH within trenches in the microporous layer, as shown in Fig. 2.10. The trenches are randomly distributed throughout the electrode and have an average width of 18.8 ± 8 μm (Fig. 2.10 (a)). Fig. 2.10 (b) shows a higher-magnification SEM image of a crack, with an overlay of an energy-dispersive spectroscopy (EDS) map indicating regions that contain Cu (red shading).

Fig. 2.11 and Fig. 2.12 show more EDS maps of Cu, fluorine (F), and carbon (C) from different trenches. From these data, we found that Cu is coated not only on top of the microporous layer but also at the bottom and on the sides of the trenches, suggesting that CO_2 reduction can be performed within these confined regions of the electrode.

These trenches within the microporous layer offer an interesting opportunity for studying the influence of physical confinement on the CO_2 reduction process in a GDE device. Accordingly, we employed our pH mapping techniques to these regions

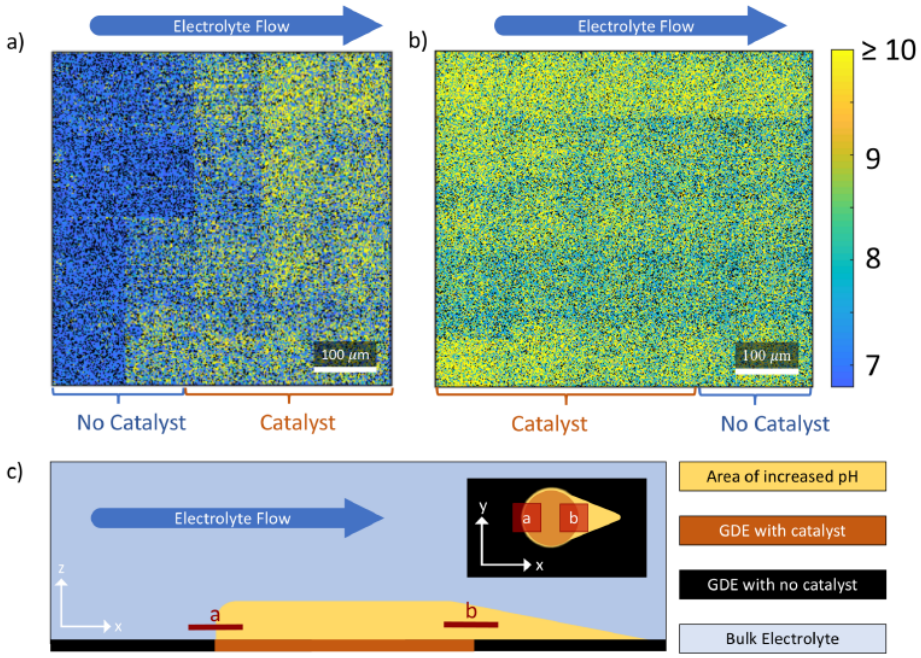

Figure 2.9: Influence of the presence of catalyst and the electrolyte flow on the pH. (a) and (b) are pH maps stitched together, taken at 9 μm above the surface of the electrode and at a current density of -14.7 mA/cm^2. In (a), the left half of the image has no Cu while the right half has Cu catalyst. The electrolyte is flowing from left to right across the surface of the electrode. In (b), the left half of the image is coated with Cu while the right half has no Cu catalyst. The electrolyte is flowing from left to right across the surface. (c) shows a schematic that is not to scale of what the pH gradient looks like in both x-y and x-z planes. The area within the orange circle in the x-y plane indicates where the Cu catalyst is located on the GDE. The position where images (a) and (b) were taken are indicated in panel (c) by the red squares and the red lines labeled 'a' and 'b'.

of the electrode to see how the reduced dimensions of the device influence the local solution pH near the active Cu electrocatalyst (Fig. 2.10 (c) - (e)). At a current density of -3.4 mA/ cm^2, we found that the solution pH within a narrow trench (approx. 3.2 μm wide) was pH 9.5. We emphasize that this local pH was much higher than the pH of 7.3 within a comparatively wider trench (approx. 16.2 μm wide). Interestingly, even at this relatively low current density (-3.4 mA/cm^2), the more confined electrochemically active region produces a higher local pH than more open regions, which serves to suppress the HER without substantially impeding CO_2 reduction[112, 113].

We also note that the pH within a narrow trench is higher than the surrounding surface of the electrode as can be seen in Fig. 2.13.

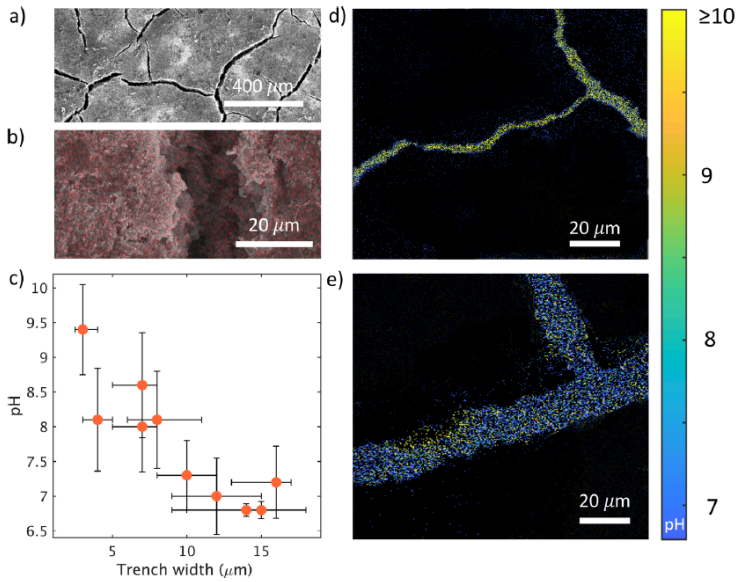

Figure 2.10: Influence of physical confinement on CO_2 reduction performance. (a) Low-magnification SEM image of a Cu gas diffusion electrode. (b) High-magnification SEM image of a Cu gas diffusion electrode with an overlay of the Cu signal obtained from an EDS map; red shading indicates Cu covered regions. (c) Measured pH as a function of trench width. The orange data points denote the average trench width. The error bars in the abscissa axis indicate the variation in trench width with the smallest and largest end points denoting the thinnest and widest points along the trench, respectively. The error bars in the ordinate axis represent the standard deviation of pH values within the trench. (d, e) pH maps obtained from two representative trenches with different widths located at different regions on the electrode at a distance of 8 μm below the electrode surface while operating at a current density of -3.4 mA/cm^2.

We proceeded to elucidate the trend of local pH vs. trench width, as shown in Fig. 2.10 (c). While we find that the electrolyte flow is very small between the objective and the catalyst in our COMSOL flow model (see section 2.3.2 and Fig. 2.14), we only measured the pH within trenches that were perpendicular to the electrolyte flow to ensure that the flow dynamics are as comparable as possible. We observed that as the trench width decreased, the local solution pH within the trench increased. This observation is consistent with prior electrochemical studies[104, 112] and has important implications for the design of more active GDEs capable of performing selective CO_2 reduction at lower overpotentials with improved energy efficiency. More detailed studies about the influence of trenches on the CO_2R selectivity as well as an improved GDE design are presented in chapters 4 and 5.

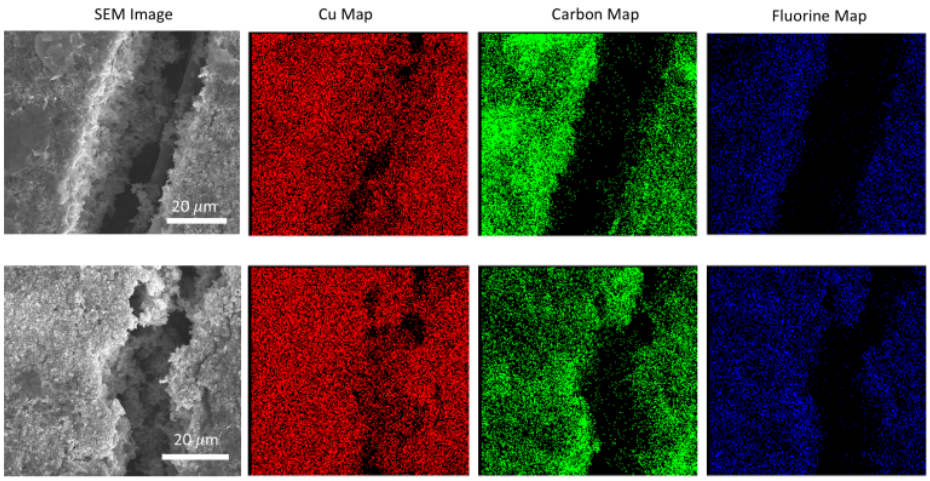

Figure 2.11: SEM and EDS maps of two locations on a GDE with 300 nm Cu. The SEM images at the left show the location for all EDS maps in the corresponding row. From the EDS maps we can see that at the bottom of the cracks, there is Cu while less carbon and PTFE (Fluorine signal) is present.

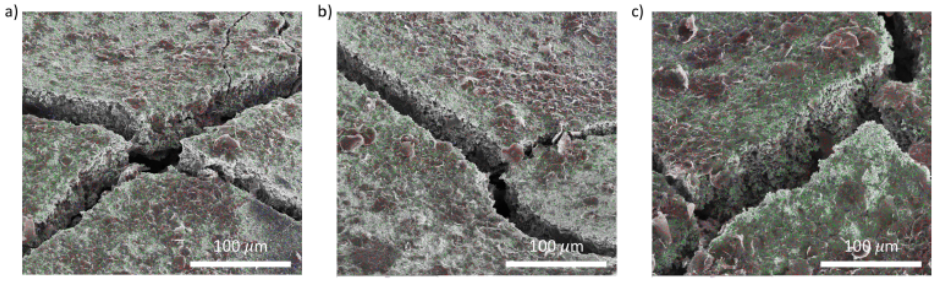

Figure 2.12: Angled SEM and EDS maps of three locations on a GDE with 300 nm Cu as an overlay. Red shading denotes C, green shading denotes Cu, and blue indicates F. From the EDS maps we can see that there is Cu deposited on the side walls of the trenches.

2.3.2 Multiphysics Simulations

We additionally confirm the experimentally measured pH within the trenches for various widths and current densities by simulating the solution pH using the charge transfer and bulk reactions in a two-dimensional stationary COMSOL Multiphysics 5.5 model [110] with a combination of the Laminar Flow Module and the Transport of Diluted Species Module. To estimate the appropriate flow velocity close to the electrode surface, a three-dimensional COMSOL model with the Laminar Flow Module simulating the electrolyte flow in the electrochemical cell and around the immersion objective used for experiments was set up, see Fig. 2.14. The geometry of the two-dimensional model of the pH is depicted in Fig 2.15 (a).

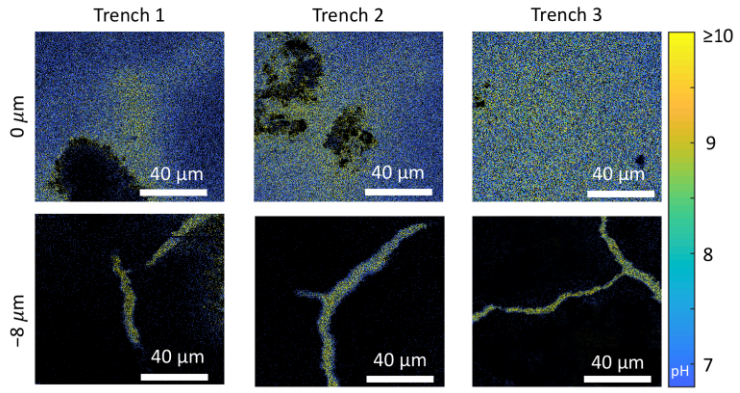

Figure 2.13: pH maps at three different locations along the electrode surface. All measurements were taken at -3.4 mA/cm^2. The image in the first row is taken at the surface of the electrode (0 μm) and the second row is at 8 μm below the surface. We observe that for all cases the pH within the narrow trench is higher than it is at the surface of the GDE.

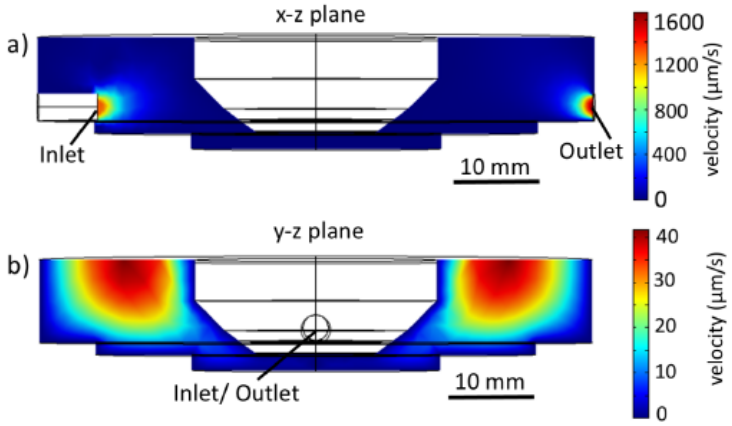

Figure 2.14: COMSOL simulation of the velocity of the electrolyte in the electrochemical cell with the objective submerged in the electrolyte. (a) shows the velocity in the x-z plane with the inlet on the left and outlet on the right. (b) shows the velocity in the y-z plane with the electrolyte flowing into the page. From these simulations it is clear that the velocity underneath the objective is small.

The simulation results are presented in Fig. 2.15 (b) - (d). As we expected, the pH was increased close to the electrode surface and inside the trench due to charge transfer reactions locally creating hydroxide ions. The pH decreased further away from the electrode surface due to convection and diffusion within the bulk electrolyte. There was a dip in the pH profile above the trench because more CO_2 comes through the electrode at this point and acidifies the electrolyte close to the trench. Additionally, there is increased CO_2 flux here because CO_2 is able to diffuse

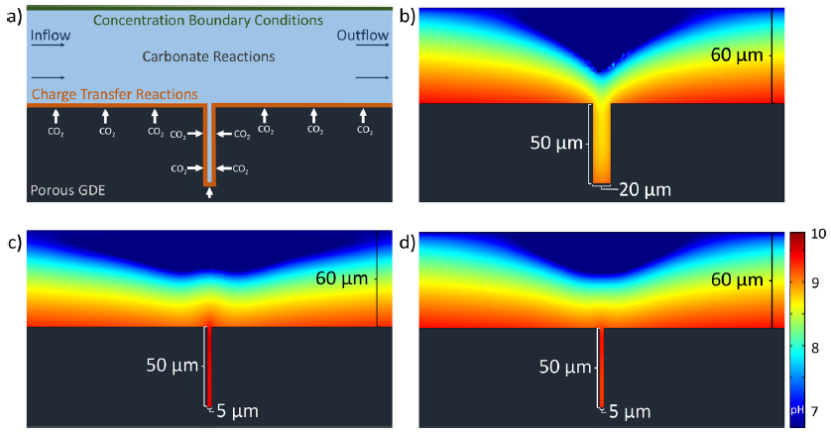

Figure 2.15: Simulations of local pH within and around trenches of various dimensions in the GDE. (a) Schematic of the model used for simulations indicating regions of CO_2 flux (white), current density (orange), concentration boundary conditions (green), and electrolyte flow (blue). pH map in the x - z plane at a uniform current density of -3.4 mA/cm^2 for a trench with a depth of 50 μm and widths of (b) 20 μm and (d) 5 μm. (c) pH map in the x - z plane for a trench [50 μm deep × 5 μmm wide] with an average current density of -3.4 mA/cm^2, where the current density in the trench is twice as high as the current density on the surface. The CO_2 flux is constant through all surfaces, and boundary conditions are kept the same for all simulations. The pH scale bar applies to all pH profiles (b)-(d).

not only through the bottom of the trench but also through the sidewalls. This feature was also observed experimentally, as shown in the pH map in Fig. 2.7 for -3.4 mA/cm^2 at -15 μm. We note that the pH gradient is nearly symmetric above the crack because the electrolyte velocity is low. At higher current densities, we observed that pH increases in the trench and on the surface of the electrode as expected (Fig. 2.16).

Comparing Figure 2.15 (b) and (d), it is clear that the pH is considerably lower in the wider trenches than the narrower trenches, which is in agreement with experimental results (Figure 2.10 (c)). In Figure 2.15 (c), we simulated a trench with the same dimensions as the trench shown in Figure 2.15 (d). However, we modeled a nonuniform catalyst activity where the activity in the trench is twice as high as it is on the electrode surface, while maintaining the same average current density over the whole electrode. We observed that in this case, the pH within the trench is higher than the pH above the surface of the electrode, which is in agreement with our observations in the experiment (see Fig. 2.13). This leads to the conclusion that the experimentally observed higher pH in narrow trenches cannot only be explained

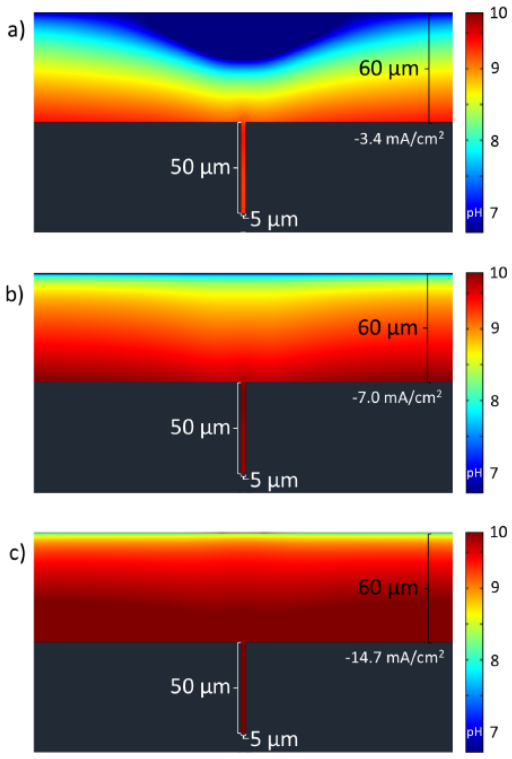

Figure 2.16: COMSOL simulations of the pH profile in a trench that is 5μm wide and 50 μm deep at different current densities. The current density is constant over all surfaces. (a) shows the pH profile at -3.4 mA/cm^2, (b) shows the pH profile at -7.0 mA/cm^2, and (c) shows the pH profile at -14.7 mA/cm^2. From these simulations we observe that the pH near the catalyst layer increases as the current density increases.

by the confinement of the trench, but must also be due to increased catalytic activity within the trench.

2.4 Conclusion

In conclusion, we have employed CLSM to elucidate how the operando local pH changes with current density as a function of distance above and below the surface of a Cu-based GDE. It is clear from the experimentally obtained pH maps that there are nonuniform hotspots of locally high pH across the catalyst even at relatively low overpotentials. Through experimental results confirmed by simulations, we show that the catalyst within narrow trenches is more active than catalyst at the surface of the electrode. We also observed that the pH was higher in narrow trenches as opposed to wider trenches, and we confirmed this result with COMSOL simulations. Further work towards understanding why catalyst in narrow trenches performs better than catalyst in wider trenches is presented in Chapters 3, 4 and 5. The ability to

locally image the solution pH in three dimensions (x, y, and z) with micrometer spatial resolution is an important tool for understanding and identifying which part of the catalyst is most productive under real operating conditions. Our results have therefore demonstrated that the overpotential required to perform selective CO_2 reduction can be reduced within narrow trenches. We anticipate that this knowledge will help inform the design and construction of more efficient CO_2 reduction devices as outlined in Chapter 5.

Chapter 3

OBSERVATION OF TIME-DEPENDENT CO_2 FLOW PATTERNS THROUGH GAS DIFFUSION ELECTRODES

Contents drawn from: A. E. Böhme, J. C. Bui, A. Q. Fenwick, R. Bhide, C. N. Feltenberger, A. J. Welch, A. J. King, A. T. Bell, A. Z. Weber, S. Ardo, and H. A. Atwater. "Direct observation of the local microenvironment in inhomogeneous CO_2 reduction gas diffusion electrodes via versatile pOH imaging". In: *Energy Environ. Sci.* 16 (2023), pp. 1783– 1795. DOI: https://doi.org/10.1039/D2EE02607D.

A.E.B. contributed to the conceptualization of the study and performed dye calibration and all pOH imaging experiments as well as data analysis.

3.1 Introduction

As described in section 1.4.1 and chapter 2, confocal microscopy in combination with pH-sensitive fluorescent dyes allows measurement of the local equilibrium pH values around operating CO_2R electrodes.

Additionally, CLSM has the capacity to perform time-dependent measurements to map the local pH value as a function of time. This capability can be used to observe time-dependent CO_2 flow patterns through GDEs.

Note that in this and the next chapter (Chapter 4), we refer to the pOH value instead of the pH value since local measurements in these chapters are performed with the fluorescent dye APTS which is a direct sensor of the local OH^- activity. At equilibrium, pH + pOH = pK_w, with pK_w = 14 under ambient conditions, so if the system is in equilibrium, the pH can be directly inferred from the pOH (see also sections 1.3 and 1.5.1).

For a GDE at open circuit, CO_2 diffuses through the macroporous and microporous layers into the electrolyte where it rapidly reacts with OH^- to form bicarbonate and carbonate anions, according to the chemical equilibrium reactions 17 - 21 (see also section 1.3.1).

$$CO_{2(aq)} + H_2O \rightleftharpoons H^+ + HCO_3^- \quad \{17\}$$

$$HCO_3^- \rightleftharpoons H^+ + CO_3^{2-} \quad \{18\}$$

$$CO_{2(aq)} + OH^- \rightleftharpoons HCO_3^- \quad \{19\}$$

$$HCO_3^- + OH^- \rightleftharpoons H_2O + CO_3^{2-} \quad \{20\}$$

$$H_2O \rightleftharpoons H^+ + OH^- \cdot \quad \{21\}$$

This decreases the local OH^- concentration and thereby increases the pOH in the electrolyte. This process is schematically depicted in Fig. 3.1 (a) (compare also Fig. 1.7 (a)). Due to the participation of CO_2 in these buffer reactions, the ability to map the spatially and time-resolved pOH around a GDE enables us to assess the local concentration of CO_2 in the electrolyte around a GDE. This can illuminate the time scales of the CO_2 transport through a GDE as well as the influence inhomogeneities in the GDE have on the CO_2 transport.

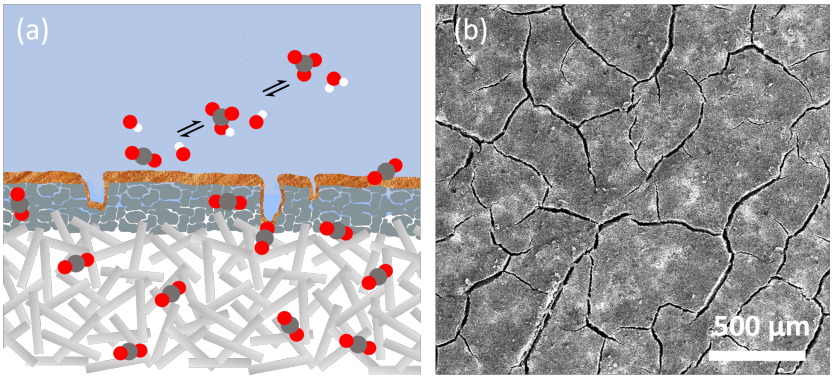

Figure 3.1: Structure of a carbon paper CO_2R GDE. (a) Schematic cross section of a carbon paper GDE (not to scale), including bicarbonate reactions in the electrolyte, (b) Top–down SEM image of the GDE surface (Sigracet 22BB carbon paper with 300 nm Cu).

3.2 Methods

The GDE is made of a Sigracet 22 BB carbon paper substrate covered with 300 nm Cu as well as a carbon black, graphite and Nafion coating and is fabricated and characterized as described in section 2.2. The substrate's surface is covered by an irregular pattern of trenches 5–30 μm wide which is shown schematically as a cross section in Fig. 3.1 (a) as well as in a top-down scanning electron microscopy (SEM) image in Fig. 3.1 (b) More SEM as well as EDS maps can be found in Chapter 4, Fig. 4.5. The trenches cover approximately 6 % of the sample surface.

An electrochemical cell similar to the one described in Chapter 2 was used in conbination with CLSM. The main difference is that the electrochemical cell was

3D-printed and exhibits two perpendicular inlet tubes to create a turbulent flow pattern at the GDE surface to mitigate the buildup of bubbles. The cell was 3D-printed, the surfaces were sanded. A rubber gasket is placed in between the bottom gas chamber part and the top electrolyte chamber part for sealing. A hole where the GDE is placed connects the gas- and electrolyte chambers, which is circular and has a surface area of 0.2 cm^2. The electrolyte chamber, including the tubes used for pumping, holds approximately 10 mL of electrolyte when the objective is immersed into it. The cell is depicted schematically in Fig. 3.2 (a) as a cross section and (b) as a top view. Fig. 3.3 displays photographs of the imaging setup.

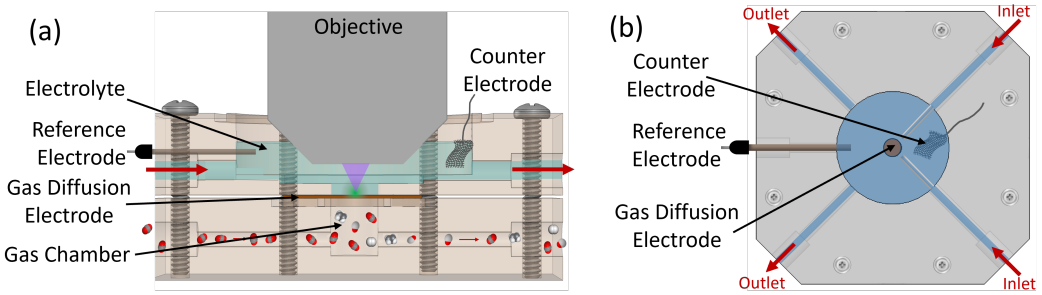

Figure 3.2: Setup of the electrochemical cell. (a) Cross section of the electrochemical cell with water-immersion objective. The reference electrode is a leakless Ag/AgCl electrode, the counter electrode is a Pt mesh. (b) Top view of the electrochemical cell showing two perpendicular electrolyte inlets and outlets.

The maximum spatial resolution of the confocal microscope is 250 nm in the x–y plane and 500 nm in the z-direction, however, electrolyte flow introduces noise, so the resolution is estimated to be on the order of one micron. We investigate features that are no smaller than 5 μm, so this resolution is satisfactory.

The pOH was resolved with the dye APTS (see section 1.5.1) that is sensitive to pOH 0 – 2.8. Its spectrum is displayed in Fig. 1.10 (a). In this chapter, we use a Zeiss LSM 710 confocal microscope with a WN Achroplan 63x water immersion objective dipped into the solution. We excite APTS using 458 nm laser light (100power) with the pinhole set to 57.1 μm and the gain set to 800. Emitted light is detected separately in the wavelength intervals of 480 – 550 nm and 551 – 754 nm, and thus the emission ratio is the ratio between the signals collected in the two emission wavelength ranges. To determine the APTS calibration curve of the ratio of emission as a function of pOH, aqueous solutions of known pOH were prepared. For this, aqueous stock solutions of KOH and HCl were diluted with nanopure water. The pOH of the solutions was confirmed by measuring the pH separately with two

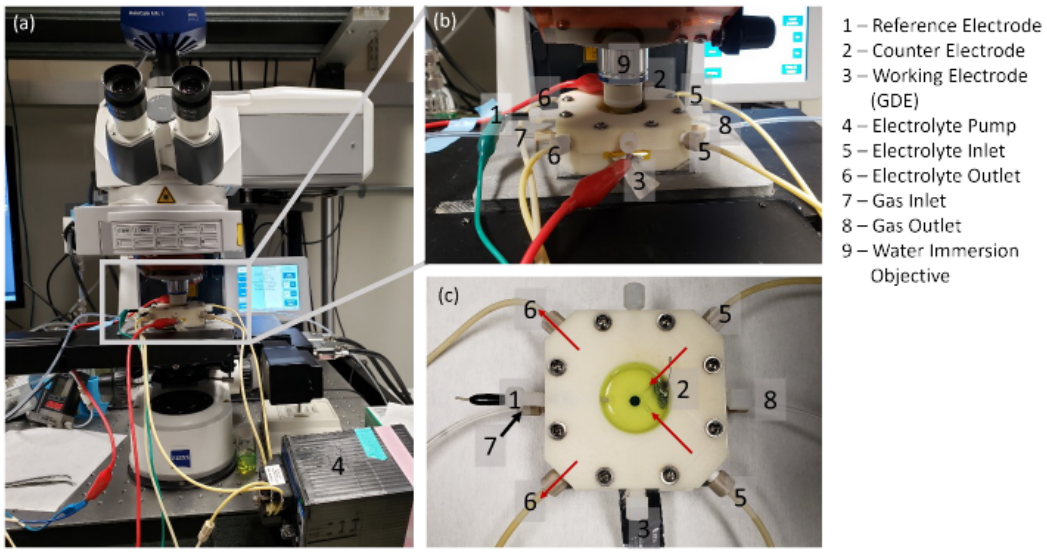

Figure 3.3: Photographs of the imaging setup with labels. (a) Electrochemical flow cell placed under a Zeiss LSM 710 confocal microscope with water-immersion objective. (b) Close-up image of the cell. (c) Top view of the cell filled with electrolyte, showing two perpendicular electrolyte inlets and outlets (marked with arrows).

different pH meters and calculating the pOH using pOH = 14 – pH. In the prepared solutions with known pOH, 100 μM APTS was diluted from a stock solution. A laser beam scans the sample solutions line by line over the center of a liquid droplet, which was repeated three times and the average ratio of emission was calculated and correlated with the known pOH. The ratio of emission was plotted as a function of pOH (see Fig. 4.1, green curve) and best fit to a sigmoidal function:

$$\begin{aligned}(\text{Ratio of Emission})_{\text{APTS}} &= \frac{5.005}{(1+\exp(1.413\cdot(\text{pOH}_{\text{DHPDS}}-5.971)))}+5.571 \longrightarrow \\ \text{pOH}_{\text{APTS}} &= 2.05-\frac{1}{2.743}\cdot\ln(-1+\frac{5.005}{(\text{Ratio of Emission})_{\text{APTS}}-0.1041}).\end{aligned} \tag{3.1}$$

1 M KOH (pOH 0) was chosen as the electrolyte, so an expected increase in pOH upon exposure to CO_2 can be detected with APTS. Experiments were performed with carbon paper GDEs prepared as described in section 2.2, both at locations with a trench present and at locations without a trench present. In addition, laminated PTFE substrates with different pore sizes, coated with 300 nm Cu in the same way as carbon paper, were investigated. Experiments were carried out both with and without electrolyte flow through two perpendicular inlet tubes at a rate of 6

mL/min. Measurements were performed in the plane perpendicular to the GDE surface by scanning the laser line by line and moving the stage in the z-direction. The measuring speed was adjusted such that capturing one frame takes four to five seconds. The experiment was conducted as a time-series. A CO_2 gas stream of 10 SCCM through the gas chamber along the back of the GDE was turned on after 1 minute of continuous measurements. This time point was later defined as t = 0 s.

3.3 Results and Discussion

We investigated how the local pOH in the electrolyte surrounding a GDE changed upon exposure to CO_2 at open circuit. This allowed us to draw conclusions about the diffusion of CO_2 molecules through a GDE. Our developed measuring technique is ideal for this study as it combines time resolution with the capability to spatially resolve the local pOH inside inhomogeneities in the surface of a GDE. Fig. 3.4(a) shows color-coded maps of the local pOH in the plane perpendicular to the electrode surface as a cross-section through a trench as well as the above electrolyte for different times without electrolyte flow. We define t = 0 s as the time when the CO_2 flow through the gas chamber of the electrochemical cell was turned on. A distinct change in pOH is immediately visible in the first frame after starting the CO_2 flow but it is restricted to the trench. The pOH changes at the electrode surface and in the bulk electrolyte as time proceeds. In Fig. 3.4(c), the average pOH at three different positions is tracked as a function of time. To this end, we draw a line 20 μm above the electrode surface (+20 μm), at the electrode surface (0 μm), and 20 μm below the electrode surface inside the trench (20 μm) as indicated in the first panel of Fig. 3.4(a). The pOH is averaged along these lines as a function of time. The vertical gray line in Fig. 3.4(c) indicates the time when the CO_2 gas supply was turned on. This data confirms that the pOH first changes inside the trench, then at the GDE surface and approximately five seconds later at 20 μm above the surface, which is consistent with the gaseous CO_2 feed coming from the backside of the GDE. After 20 s, the pOH values converge at all positions monitored and remain constant for the duration of the experiment.

An analogous measurement was performed in a region of the electrode void of trenches (Fig. 3.5) and we observed that the pOH increases at a slower rate in comparison to measurements at a location with a trench. This demonstrates that microstructures such as trenches promote faster CO_2 transport through a GDE substrate.

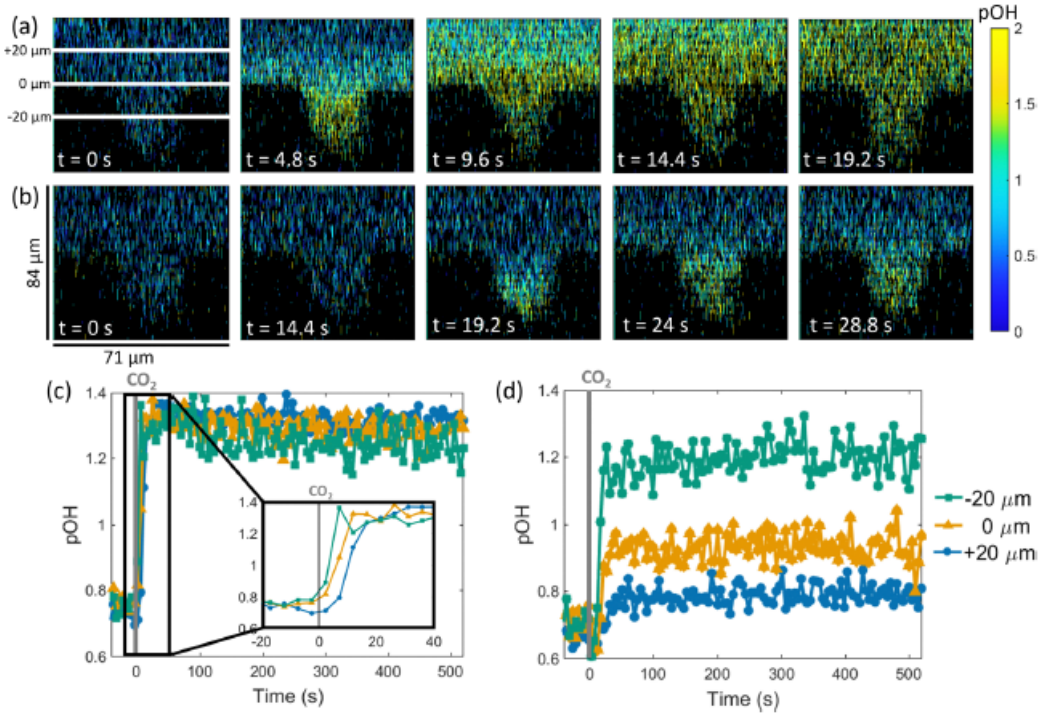

Figure 3.4: Changing pOH in the electrolyte due to CO_2 diffusion around a trench in a carbon paper GDE at open circuit, without electrolyte flow (a), (c) and with electrolyte flow (b), (d). Measurements performed with 1 M KOH electrolyte with 100 mM APTS, 10 SCCM CO_2 turned on at the backside of the electrode at t = 0 s. Frames in (a) and (b) show pOH maps as a cross section through a trench in the plane perpendicular to the electrode surface for different times. The scale bars apply to both (a) and (b). Panels (c) and (d) track the average pOH at locations 20 μm above the surface (+20 μm), at the surface (0 μm) and 20 μm below the surface in the trench (-20 μm), as specified in the first frame of (a), as a function of time. The vertical gray lines indicate the start of the CO_2 flow.

The experiment displayed in Fig. 3.4 (a) was repeated under an electrolyte flowrate of 6 mL/min (Fig. 3.4 (b)). This has a dramatic effect on the pOH around the GDE: the first change in pOH is only visible after 19 s, compared to less than 5 s without electrolyte flow. A significant increase in pOH caused by the diffusion of CO_2 is solely observed inside the trench. Fig. 3.4 (d) tracks the pOH over time in a similar manner as Fig. 3.4 (c). This confirms that the pOH increases little at the GDE surface as well as 20 μm above the surface, and even within the trench, the pOH remains below the value obtained without electrolyte flow. A steady state, with constant pOH up to 20 μm above the electrode surface, is reached after 40 s. However, the pOH at the three locations never converges to a single value, in contrast to the measurements performed with stationary electrolyte. Electrolyte flow results

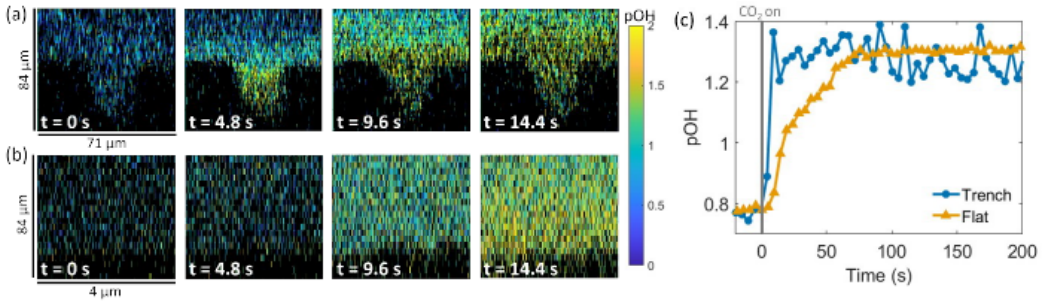

Figure 3.5: pOH change in the electrolyte due to CO_2 diffusion through a carbon paper GDE (a) with a trench, (b) without a trench, both without electrolyte flow. Measurements performed with 1M KOH electrolyte with 100 μM APTS, 10 SCCM CO_2 turned on at t = 0 s. Panels in (a) and (b) show pOH maps in the plane perpendicular to the electrode surface for different times. (c) Average pOH at a location 20 μm above the surface, showing how it changes as a function of time both with and without a trench. The vertical gray line indicates when the CO_2 flow was turned on.

in a well-defined boundary layer around the GDE surface which leads to a CO_2 concentration gradient. In the absence of electrolyte recirculation, diffusion is the dominant transport mechanism for CO_2 and subsequent CO_2R products. When the electrolyte is circulated however, convection dominates the mass transfer and causes OH^- to be more quickly removed from the GDE surface. This prevents the pOH from rising as much as it would without electrolyte flow. As the electrolyte is more stationary inside trenches, a larger pOH increase can be observed in these confined spaces.

An additional study was conducted to compare the CO_2 diffusion through homogeneous GDE substrates made of laminated polytetrafluoroethylene (PTFE) with pore sizes that are specified by the manufacturer as 0.1 to 0.2 mm and 0.45 μm, respectively. Fig. 3.6 shows a schematic representation of the structure of both a carbon paper GDE and a PTFE GDE together with SEM images.

Fig. 3.7 compares the flow patterns through PTFE GDEs with different pore sizes. We observe that, as expected, the pOH in the electrolyte above the surface increases faster for PTFE with a larger pore size. After 45 seconds it converges to the same value for both substrates. This result gives evidence that, not only microcavities in a GDE's surface, but also larger pore size can promote faster CO_2 transport.

However, there is a critical pore size that should not be exceeded, otherwise the pores will be flooded with liquid electrolyte during an experiment. We observed this for

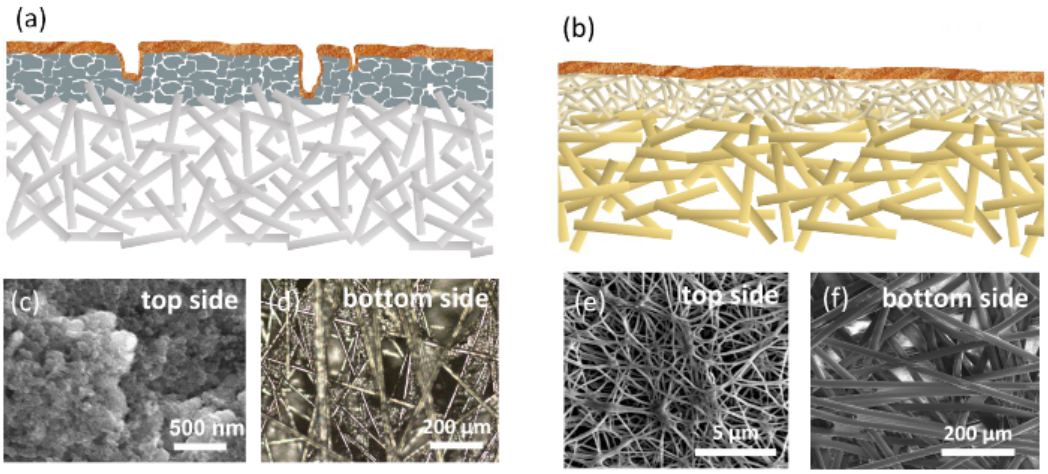

Figure 3.6: Schematic representations of the structure of a Sigracet 22 BB carbon paper GDE (a) and a PTFE membrane GDE (not to scale) (b), both coated with 300 nm Cu, together with SEM images of the top side (c) and the bottom side (d) of the carbon paper GDE as well as of the top side (e) and the bottom side (f) of the PTFE GDE.

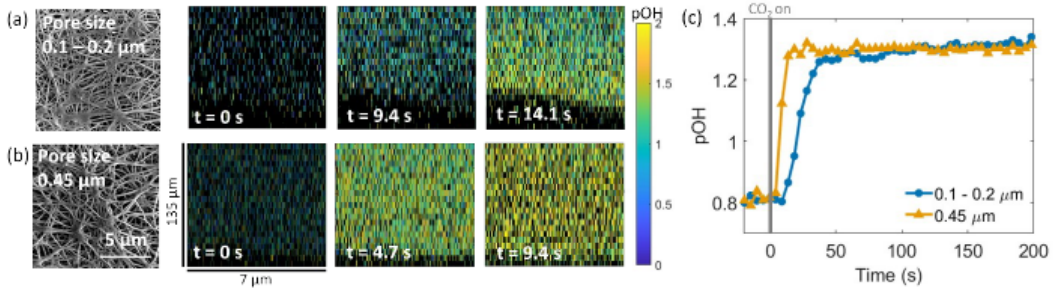

Figure 3.7: pOH change in the electrolyte due to CO_2 diffusion through a PTFE GDE with pore size 0.1-0.2 μm (a) and 0.45 μm (b), both without electrolyte flow. Measurements performed in 1 M KOH electrolyte with 100 μM APTS, 10 SCCM CO_2 turned on at t = 0 s. Panels in (a) and (b) show SEM images of the GDE (scale bar applies to both (a) and (b)) as well as pOH maps as a cross section in the plane perpendicular to the electrode surface for different times. (c) Change in average pOH at a location 20 μm above the surface as a function of time for both GDE substrates with different pore sizes. The vertical gray line indicates when the CO_2 flow was turned on.

a laminated PTFE substrate with pore sizes of 5 μm or greater. Flooding prevents effective CO_2 transport through a GDE and inhibits CO_2 diffusion to catalytic sites [35, 52]. A more detailed analysis of the influence of the pore size on the CO_2R performance of PTFE GDEs can be found in chapter 6.

These results suggest that consideration of the influence of microstructures, even in commercially available GDE substrates, is a critical parameter to understand device performance.

3.4 Conclusion

We investigated the diffusion patterns of CO_2 through CO_2R GDEs. This study revealed that CO_2 diffuses through microcavities first before it reaches the bulk electrolyte. Electrolyte flow leads to a lower pOH due to the convective transport of OH^- and a CO_2 concentration gradient with the highest concentration confined to trenches. We further observed the CO_2 transport through PTFE GDEs with different pore sizes and found that larger pore sizes promote faster CO_2 transport as long as the pore size does not exceed a threshold value above which the GDE floods.

The microcavities in a GDE surface as well as large pore sizes promote faster CO_2 transport, highlighting the importance to understand the influence of the micron-scale morphology of a CO_2R GDE.

Chapter 4

DIRECT OBSERVATION OF THE LOCAL MICROENVIRONMENT IN INHOMOGENEOUS CO_2 REDUCTION GAS DIFFUSION ELECTRODES VIA VERSATILE POH IMAGING

Contents drawn from: A. E. Böhme, J. C. Bui, A. Q. Fenwick, R. Bhide, C. N. Feltenberger, A. J. Welch, A. J. King, A. T. Bell, A. Z. Weber, S. Ardo, and H. A. Atwater. "Direct observation of the local microenvironment in inhomogeneous CO_2 reduction gas diffusion electrodes via versatile pOH imaging". In: *Energy Environ. Sci.* 16 (2023), pp. 1783– 1795. doi: https://doi.org/10.1039/D2EE02607D.

A.E.B. contributed to the conceptualization of the study and performed dye calibration and all pOH imaging experiments as well as data analysis.

4.1 Introduction

We know based on the results presented in Chapters 2 and 3 that trenches in the surface of a CO_2R GDE can play an important role in determining the CO_2R activity and CO_2 transport properties. This chapter presents a more systematic study of the influence of the micron-scale morphology of a GDE on the CO_2R performance, with extended sensing capabilities and including the effect on the selectivity.

As detailed in section 1.2, if a non-zero current is applied to a CO_2R GDE, a portion of the CO_2 molecules is reduced to form products such as carbon monoxide, formic acid, methane or ethylene, among others [36–41]. This is outlined in Tables 1.1 and 1.2. During this non-equilibrium process, one OH^- is created, or one buffer species is deprotonated for each electron involved [114]. The same holds true for the competing hydrogen evolution reaction (HER) that must be suppressed to maximize the CO_2R yield. As a result, at sufficiently high current density magnitudes, we expect that the pOH will decrease, as is depicted schematically in Fig. 1.7 (b). This effect is in competition with an increase in pOH caused by unreduced CO_2 molecules that undergo reactions to form bicarbonate and carbonate anions (see Fig. 1.7 (a) and Fig. 3.1 (a)). As a result, a low observed pOH indicates the presence of CO_2R activity. In addition, it has been shown that the pH and pOH themselves have a substantial impact on the reactivity and selectivity of CO_2R. It has been

demonstrated that high pH (corresponding to low pOH) suppresses the parasitic HER [58, 60] and shifts the CO_2R selectivity towards C_{2+} products [60–63], see also chapter 1.3.2. The reason for the latter is that OH^- actively suppresses the creation of single carbon products (C_1) and hydrogen molecules (H_2), while it does not affect the C_{2+} current density. This leads to an increased faradaic efficiency (FE) towards C_{2+} products at a given current density [63, 115]. As a result, knowledge of the pOH in the vicinity of an operating GDE is critical and can aid researchers in better optimizing the performance of a GDE.

As in Chapters 2 and 3, CLSM is the technique of choice to measure the local pOH due to its sub-micrometer spatial resolution in three spatial dimensions that makes it ideally suited to resolve the local pH inside the microcavities in a GDE. No other technique allows one to probe the operando pOH within cavities in the surface of a GDE. This capability presents the unique opportunity to correlate the microstructure geometry of a GDE with its CO_2R performance. Understanding the local chemical microenvironment near a CO_2R catalyst is key for understanding selectivity and performance of these devices, as well as to validate continuum level theories of CO_2R in porous electrodes [116]. Furthermore, this novel technique might also prove to be useful for the investigation of other electrochemical applications beyond CO_2R.

In this chapter, we combine the fluorescent dye DHPDS, also used in Chapter 2 that is sensitive to pOH 4 – 8 with the fluorescent dye APTS used in Chapter 3 that is sensitive to pOH 0 – 2.8. A more detailed analysis of the working mechanisms of both probes can be found in section 1.5.1.

We showed in Chapter 2 that the pH increased locally inside trenches 5-20 μm wide in the GDE surface. Furthermore, the pH increased as the trench width diminished, which indicated that narrow trenches exhibit a higher CO_2R activity than wider trenches and planar surfaces [77]. While these results were insightful, they were limited by the pH range in which DHPDS is sensitive. We observed that the DHPDS signal saturated at current density magnitudes larger than 20 mA/cm^2 in aqueous 100 mM $KHCO_3$. However, there is an interest in operating GDEs at high current density magnitudes to increase the CO_2R rate up to industrially relevant-levels ($|J| > 100$ mA/cm^2) [117, 118].

The inclusion of an excited state proton-transfer mechanism for weak photoacids, such as APTS allows to significantly extend the pOH sensing range and hence, the accessible current density scale, from 0 to at least 200 mA/cm^2 in magnitude. It

must be emphasized that this is the first demonstration of APTS as a sensor for the local pOH. APTS exhibits a novel sensing mechanism and greatly enhances the capabilities of our technique to map the local pOH value with CLSM. By combining DHPDS with APTS, we are now able to cover a pOH range from 0 to 8 (with a gap between 2.8 and 4) and investigate operating GDEs under current densities as large in magnitude as 200 mA/cm^2. Note that if DHPDS is excited at 405 nm, the gap between pOH 2.8 and 4 can be closed (see Chapter 1.5.1). However, the confocal microscope that was used in this study (Zeiss LSM 710) did not offer a 405 nm laser line.

Additionally, we explore the influence of different bicarbonate concentrations in the electrolyte and of different microstructure geometries. All told, this chapter crucially enables a correlation between the bulk electrolyte properties and electrode structure with the pOH present at the electrochemical active site across a broad range of operating current densities. We also evaluate the CO_2R performance of our GDEs with gas chromatography measurements and supplement our experimental analysis with continuum modeling to enable a better understanding of the correlation between local pOH and CO_2R performance.

4.2 Methods

Product Distribution Measurements

An electrochemical cell optimized for use with gas chromatography was used for product detection during the performance of CO_2R experiments with copper on carbon paper GDEs. A leakless Ag/AgCl electrode served as reference electrode and a platinum mesh as counter electrode. An anion exchange membrane (AGC, Selemion AMV) was used to separate cathode and anode. The gas chamber takes the form of a serpentine channel at the back of the GDE. The cell was sonicated before each experiment for at least 40 minutes and rinsed thoroughly after each experiment. 100 mM $KHCO_3$ saturated with CO_2 was pumped through the catholyte and anolyte chambers at a rate of 6.3 mL/min. CO_2 was fed into the gas chamber at a rate of 10 SCCM. A flow meter placed before and after the cell was used to ensure that there were no gas leaks. The gas coming from the cell was returned to a electrolyte bath as a precaution in case of electrolyte breakthrough through the GDE. From there, the gas was sent through a vapor trap to an SRI-8610 gas chromatograph. Chronopotentiometry experiments (constant current) were carried out at -10, -50, -100 and -200 mA/cm^2 with a potentiostat. Before each experiment, potetiostatic electrochemical impedance spectroscopy (PEIS) was carried out to measure the

resistance of the cell. This allowed us to compensate the electrochemical potential by 85 % with iR compensation.

pOH Imaging Experiments

CLSM with the two fluorescent dyes DHPDS and APTS was used to map the pOH around an operating GDE performing CO_2R over a wide pOH range. The same electrochemical call as used in chapter 3, see Fig. 3.2 and Fig. 3.3, was used. For experiments at constant current densities, a leakless Ag/AgCl reference electrode and a Pt mesh counter electrode are submerged into the electrolyte. The GDE is made of a Sigracet 22 BB carbon paper substrate covered with 300 nm Cu as well as a carbon black, graphite and Nafion coating and is fabricated as described in section 2.2. The substrate's surface is covered by an irregular pattern of trenches 5–30 μm wide as is schematically shown in Fig. 3.1. The trenches cover approximately 6 % of the sample surface. Energy dispersive X-ray spectroscopy (EDS) measurements performed with a NOVA NanoSEM 450 scanning electron microscope confocal with an Oxford Instrument's Xmax 80 mm2 reveal that copper covers not only the planar carbon paper surface but also the trench walls and bottoms, see Fig. 4.5.

A Zeiss LSM 710 confocal microscope is used in this chapter. The maximum spatial resolution of the confocal microscope is 250 nm in the x–y plane and 500 nm in the z-direction, however, electrolyte flow introduces noise, so the resolution is estimated to be on the order of one micron. We investigate features that are no smaller than 5 μm, so this resolution is satisfactory.

We used both dyes DHPDS and APTS to map the pOH around an operating GDE performing CO_2R at current density magnitudes between 0 mA/cm^2 and 200 mA/cm^2. DHPDS was calibrated as described in section 2.2 and APTS as lined out in section 3.2. Both calibration curves are displayed in Fig. 4.1 where the red shaded area indicates the pOH gap that can be resolved by neither dye.

Before each experiment, the electrolyte was bubbled with 30 SCCM CO_2 gas for at least 30 minutes. The pH was monitored with an Oakton 5+ pH meter and bubbling was continued until the pH stabilized. This ensured that the electrolyte was saturated with CO_2. The dye was dissolved in the CO_2-saturated electrolyte: DHPDS at a concentration of 100 μM to investigate current densities smaller in magnitude than -20 mA/cm^2, APTS at a concentration of 200 μM for 100 mM $KHCO_3$ electrolyte/ 300 μM for 200mM and 400 mM $KHCO_3$ electrolyte, to investigate current densities larger in magnitude than -20 mA/cm^2. All experiments were conducted with

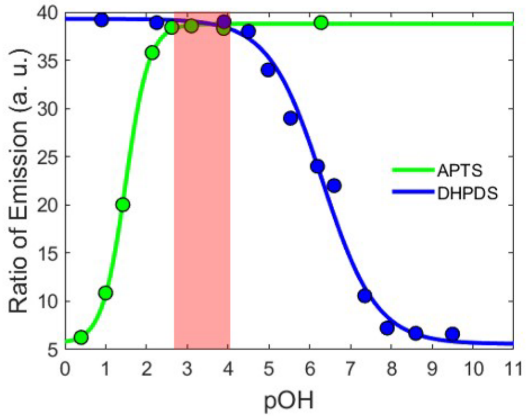

Figure 4.1: Calibration curves of both DHPDS (blue) and APTS (green) with the measured ratio of emission as a function of pOH together with best fit curves (Equations S1 and S2). In this plot, the signal for APTS was scaled by (Ratio of Emission) · 3 + 5 for better visibility. The shaded red area indicates the pOH range that cannot be resolved by use of either dye.

electrolyte flow (6 mL/min through two perpendicular inlets) and with a gas stream of 10 SCCM CO_2 through the gas chamber of the electrochemical cell. To determine the series resistance of the cell filled with electrolyte, potentiostatic electrochemical impedance spectroscopy (PEIS) was performed before each experiment with a Biologic SP-200 potentiostat. This allowed us to perform an 85 % IR electronic compensation of the electrochemical potential. A trench that is approximately 20 μm wide was identified on the GDE surface. A constant current was applied with a Biologic SP-200 potentiostat. Measuring under galvanostatic conditions enables a constant flux of ions between electrodes. The system was allowed to reach steady state for at least 15 seconds.

Measurements were performed in the plane parallel to the electrode surface, at 20 μm above the surface, at the surface, and at 20 μm below the surface inside a trench. The speed was set to three such that taking one image takes approximately 45 seconds. The electrolyte with dilute dye was removed from the cell and replaced after each measurement. Every measurement was performed at least three times.

COMSOL Model Outline

The model domain is presented in Fig. 4.2, which considers a single, periodic trench in a gas diffusion electrode (GDE).

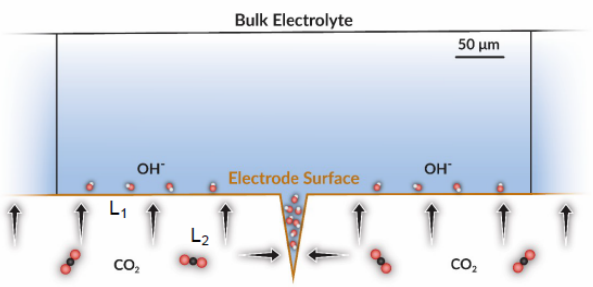

Figure 4.2: Schematic of the GDE model domain.

Steady-state species conservation governs the species transport for dissolved CO_2, OH^-, H^+, HCO_3^-, CO_3^{2-}, and K^+ within the entire model domain,

$$\nabla \cdot N_i = R_{B,i'}, \tag{4.1}$$

where N_i is the flux of species i, and $R_{B,i'}$ is a volumetric source term describing generation of species i due to homogeneous buffer reactions. The Nernst-Planck equation is used to calculate the molar flux of species i [119],

$$N_i = -D_i \nabla c_i - \frac{z_i F}{RT} D_i c_i \nabla \Phi_L, \tag{4.2}$$

where D_i, c_i, z_i are the diffusivity, concentration, and charge of species i, respectively, Φ_L is the liquid-phase electric potential, F is the Faraday constant, R the ideal gas constant, and T is the temperature. The first term captures the transport of species by diffusion, and the second term describes charged species migration, which does not affect uncharged CO_2 [120]. The diffusivities are provided in Table 4.1. To solve for the liquid-phase potential, electroneutrality is enforced,

$$\sum_i z_i c_i = 0. \tag{4.3}$$

The homogeneous bulk reactions captured by the source term, $R_{B,i}$, are (see also section 1.3.1)

$$CO_{2(aq)} + H_2O \overset{k_1, k_{-1}}{\rightleftharpoons} H^+ + HCO_3^- \qquad K_1 \qquad \{22\}$$

$$HCO_3^- \overset{k_2, k_{-2}}{\rightleftharpoons} H^+ + CO_3^{2-} \qquad K_2 \qquad \{23\}$$

$$CO_{2(aq)} + OH^- \overset{k_3, k_{-3}}{\rightleftharpoons} HCO_3^- \qquad K_3 \qquad \{24\}$$

Table 4.1: List of model diffusivities and their source.

Species	Diffusivity (m^2/s)	Reference
$D_{K^+,w}$	$1.957 \cdot 10^{-9}$	[121]
$D_{H^+,w}$	$9.311 \cdot 10^{-9}$	[121]
$D_{OH^-,w}$	$5.293 \cdot 10^{-9}$	[121]
$D_{HCO_3^-,w}$	$1.185 \cdot 10^{-9}$	[121]
$D_{CO_3^{2-},w}$	$9.10 \cdot 10^{-10}$	[121]
$D_{CO_2,w}$	$1.91 \cdot 10^{-9}$	[121]

$$HCO_3^- + OH^- \overset{k_4,\, k_{-4}}{\rightleftharpoons} H_2O + CO_3^{2-} \qquad K_4 \qquad \{25\}$$

$$H_2O \overset{k_w,\, k_{-w}}{\rightleftharpoons} H^+ + OH^- \qquad K_5 \qquad \{26\}$$

where k_n/ k_{-n} are the rate constants and equilibrium constant for reaction n, respectively. These constants are provided in Table 4.2. k_{-n} is calculated by [35, 115]

$$k_{-n} = \frac{k_n}{K_n}, \tag{4.4}$$

and $R_{B,i}$ is given by

$$R_{B,i} = \sum_n s_{i,n} c_{ref} (k_n \prod_{s_{i,n}<0} a_i^{-s_{i,n}} - \frac{k_n}{K_n} \prod_{s_{i,n}>0} a_i^{s_{i,n}}), \tag{4.5}$$

where $s_{i,n}$ is the stoichiometric coefficient for species i in reaction n, and a_i is the activity of species i. c_{ref} is a reference concentration defined as 1 M. Although it is well-established that Reaction 22 involves two elementary reaction steps with an H_2CO_3 intermediate, we omit them from the model, as is commonly done, because intermediate concentrations are very small and inconsequential to simulation results. In this regard, K_3 and k_3 are overall observed equilibrium and rate constants, respectively.

The forward rate constants were scaled by a factor of 0.2 to achieve electrolyte buffering more reflective of the experimental results. This minor scaling is reasonable given the large degree of reported rate constants.

The boundary conditions at the edge of the mass-transport boundary layer are Dirichlet boundary conditions, defined by the equilibrium concentrations of a $KHCO_3$ electrolyte saturated with CO_2. The boundary layer thickness employed is 200 μm thick, consistent with prior research in similar flow cells [122], and recent work in this area that have done full CFD simulations of electrochemical CO_2 reduction cells have shown that within the boundary layer, electrolyte convection is not important

Table 4.2: List of buffer reaction constants and their source.

Reaction	Constant	Unit	Reference
K_1	$4.27 \cdot 10^{-7}$	-	[122]
k_1	0.0371	1/s	[122]
K_2	$4.58 \cdot 10^{-11}$	mol/L	[122]
k_2	59.44	1/s	[122]
K_3	$4.27 \cdot 10^{-7}$	L/mol	[122]
k_3	$2.23 \cdot 10^{3}$	L/(mol·s)	[122]
K_4	$4.86 \cdot 10^{3}$	-	[122]
k_4	$6.9 \cdot 10^{9}$	L/(mol·s)	[122]
K_w	$1 \cdot 10^{-14}$	mol/L	[122]
k_w	$1.4 \cdot 10^{-3}$	mol/(L·s)	[122]

due to the no-slip boundary condition at the electrode surface [62]. The key mode of transport in the boundary layer is ionic diffusion, which dictates the local pH at the surface and in the trench and is captured adequately by the present model. Moreover, the liquid-phase potential is set to zero. At the left and right boundaries, n is the normal vector.

$$\Phi_L^{right} = \Phi_L^{left} \tag{4.6}$$

$$c_i^{right} = c_i^{left} \tag{4.7}$$

$$-n \cdot N_i^{right} = n \cdot N_i^{left} \tag{4.8}$$

$$-n \cdot \nabla\Phi_L^{right} = n \cdot \nabla\Phi_L^{left} \tag{4.9}$$

This boundary condition simulates the periodicity of the trenches in the GDE. At the Cu surface, we specify the CO_2 concentration to be 34 mM, since CO_2 gas is being fed from the backside and dissolving into the electrolyte next to the Cu surface. This boundary condition is of course a simplification, and assumes no gaseous CO_2 transport losses within the gas diffusion layer, which will not hold at higher current densities. However, modeling gaseous phase CO_2 transport in the gas diffusion layer is beyond the scope of the present study, wich is primarily focused on the transport OH^- anions and dissolved CO_2 reacting at the electrode surface.

In addition, the following electrochemical reactions are assumed to occur:

$$2\,H_2O + 2\,e^- \longrightarrow H_2 + 2\,OH^-, \qquad {U_1}^0 = 0\,\text{V vs. SHE} \qquad \{27\}$$

$$CO_2 + H_2O + 2\,e^- \longrightarrow CO + 2\,OH^-, \qquad {U_2}^0 = -0.11\,\text{V vs. SHE} \qquad \{28\}$$

$$CO_2 + H_2O + 2\,e^- \longrightarrow HCOO^- + OH^-, \qquad U_3{}^0 = -0.02\ \text{V vs. SHE} \quad \{29\}$$

$$CO_2 + 6\,H_2O + 8\,e^- \longrightarrow CH_4 + 8\,OH^-, \qquad U_4{}^0 = 0.17\ \text{V vs. SHE} \quad \{30\}$$

$$2\,CO_2 + 8\,H_2O + 12\,e^- \longrightarrow C_2H_4 + 12\,OH^-, \qquad U_5{}^0 = 0.07\ \text{V vs. SHE} \quad \{31\}$$

$$2\,CO_2 + 9\,H_2O + 12\,e^- \longrightarrow C_2H_5OH + 12\,OH^-, \qquad U_6{}^0 = 0.08\ \text{V vs. SHE} \quad \{32\}$$

$$3\,CO_2 + 13\,H_2O + 18\,e^- \longrightarrow C_3H_7OH + 18\,OH^-, \qquad U_7{}^0 = 0.09\ \text{V vs. SHE} \quad \{33\}$$

$$3\,CO_2 + 11\,H_2O + 16\,e^- \longrightarrow C_3H_6O + 16\,OH^-, \qquad U_8{}^0 = 0.05\ \text{V vs. SHE}\cdot \quad \{34\}$$

To capture the formation of H_2, C_1 (CO, $HCOO^-$, and CH_4), and C_{2+} (C_2H_4, C_2H_5OH, C_3H_7OH, and C_3H_6O) products on Cu in the model, Neumann boundary conditions are specified by a concentration-dependent Tafel expression, equation 4.10, and Faraday's law, equation 4.11,

$$i_k = -i_{0,k}\left(\frac{c_{CO_2}}{c_{ref}}\right)^{\gamma_{CO_2,k}} \exp(-\gamma_{pH,k,SHE}\,pH) \exp\left(-\frac{a_{c,k}F}{RT}(\Phi_s - \Phi_l - U_{0,k})\right) \quad (4.10)$$

$$N_k = -\frac{\nu_k i_k}{nF} \quad (4.11)$$

where $\gamma_{CO_2,k}$ is the CO_2 reaction order, $\gamma_{pH,k}$ is the sensitivity of the current density to pH, Φ_s is the solid phase electrode potential, Φ_l is the liquid phase electrolyte potential, and $i_{0,k}$, $a_{c,k}$, $U_{0,k}$, and ν_k are the exchange current density, transfer coefficient, equilibrium potential, and reaction stoichiometric coefficient for product k, respectively. Moreover, n is the number of electrons transferred in the electrochemical reaction. $\gamma_{CO_2,k}$ are taken from fits of experimental data from CO_2 and CO reduction at varied partial pressure as discussed in a prior study by Weng et al. [63, 116, 123]. $\gamma_{pH,k,SHE}$ are taken from fits of experimental data for partial current vs. pH at a constant potential on an SHE scale [120, 123], wherein HCOOH, H_2 and CH_4 have been observed to have pH dependent kinetics [62, 115, 124–126]. $i_{0,k}$ and a_c are fit to the experimental data collected in this study for dark electrolysis on a Cu GDE in 1 M $KHCO_3$ and take into account the fit rate orders for CO_2 and pH. The fitted rate parameters are provided in Table 4.3, and the agreement with our experimental GDE data is shown in Figure 4.7.

The governing equations (electrolyte species material balances and electroneutrality) were used within the Tertiary Current Distribution Module and were solved with

Table 4.3: Final kinetic parameters for modeling CO_2 reduction on a Cu GDE in 1 M $KHCO_3$.

Product	$i_{0,k}$ (mA/cm^2)	$a_{c,k}$	$\gamma_{CO_2,k}$	$\gamma_{pH,k,SHE}$
H_2	$3.84 \cdot 10^{-3}$	0.23	0	0.40
CO	$1.10 \cdot 10^{-3}$	0.3	1.50	0
$HCOO^-$	$2.13 \cdot 10^{2}$	0.4	2.00	1.56
C_2H_4	$9.91 \cdot 10^{-8}$	0.40	1.36	0
C_2H_5OH	$8.14 \cdot 10^{-10}$	0.43	0.96	0
CH_4	$6.80 \cdot 10^{-4}$	0.5	0.84	1.56

the MUMPS general solver in COMSOL Multiphysics 6.0 with a relative tolerance of 0.001. The modeling domain was discretized with a uniform square mesh and was comprised of 20284 elements. A sensitivity analysis on the mesh size was performed, and the results were found to be independent for meshes greater than the 1000 elements required to achieve convergence at low current densities, but higher current densities required 20000 elements or more.

To compare simulation to experiment, the simulation current densities, which are averaged to the electrochemically active surface area, must be rescaled to the geometric area. To do so, the following expression is used to approximate the geometric current density:

$$i_{Geo} = i_{ECSA} \cdot \frac{L_1 + L_2}{200\,\mu\text{m}} \tag{4.12}$$

where L_1 and L_2 are labelled in Fig. 4.2. Using this expression assumes that the geometry of a single, periodic trench domain is characteristic of the geometry of the entire cracked GDE, where in actuality the geometry will consist of a distribution of trenches of varying width and height. Nonetheless, accounting for the true geometry would require employing a high-fidelity pore-network model or a direct numerical simulation of the entire 3D porous electrode, both of which are beyond the scope of the present work.

4.3 Results and Discussion

4.3.1 Experimental Results and Supporting Simulations

In a first step, we verified the CO_2R performance of our GDE samples (300 nm Cu on carbon paper) with gas chromotography. We performed chronopotentiometry experiments for different current densities. The results are displayed in Fig. 4.3. Our results are consistent with copper GDEs previously reported in literature [29, 49, 127]. H_2 production dominates for low current density magnitudes. As the

magnitude of the current density increases, we observe more CO_2R products, and the selectivity shifts towards C_{2+} products. We observe ethylene for current densities of 50 mA/cm^2 or higher in magnitude and ethanol for 200 mA/cm^2. We can therefore assume that the analogous electrodes we use for our pOH imaging experiments behave as one would expect from literature.

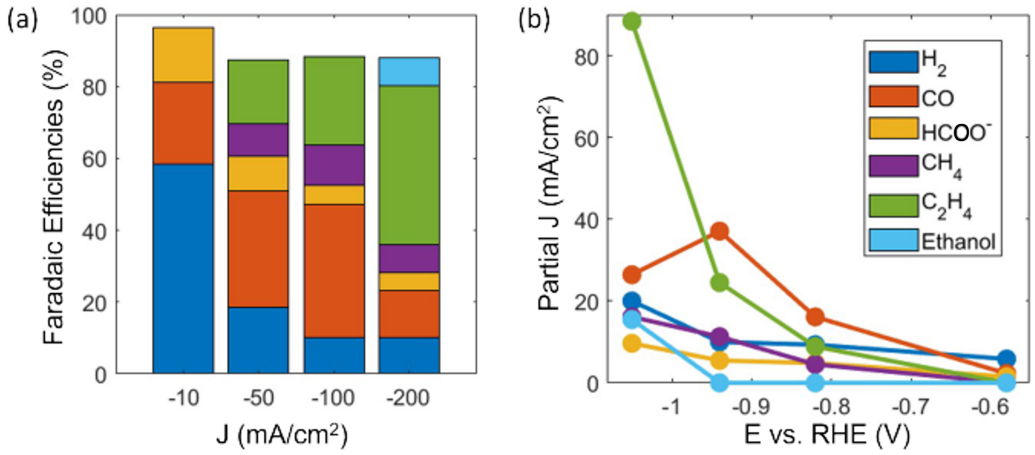

Figure 4.3: CO_2R performance characterization of 300 nm Cu on carbon paper GDEs with gas chromatography. (a) Faradaic efficiencies at different current densities. (b) Partial current densities for different products as a function of electrode potential vs. the reversible hydrogen electrode. The legend applies to both panels (a) and (b).

By combining the two pOH-dependent fluorescent ratiometric dyes, DHPDS and APTS, we are able to cover the pOH range from 0 to 8. In the context of CO_2R, a low local pOH under operation indicates high CO_2R activity and is desirable because it has been shown that high pH can help suppress the parasitic HER and favor the formation of C_{2+} products [60–63, 115]. Fig. 4.4 displays pOH maps in the plane parallel to the electrode surface in 100 mM $KHCO_3$ electrolyte for different current density magnitudes between 0 mA/cm^2 and 100 mA/cm^2 and at three different z-positions: 20 μm above the electrode surface, at the electrode surface, and 20 μm below the electrode surface inside a trench. The panels on the left-hand side were captured using DHPDS, and the ones on the right-hand side were captured using APTS.

We observed that APTS degrades and slowly loses its fluorescence for high current density magnitudes. We hypothesize that this is connected to the reduction of APTS at the electrode surface. A more detailed analysis of this effect can be found in the

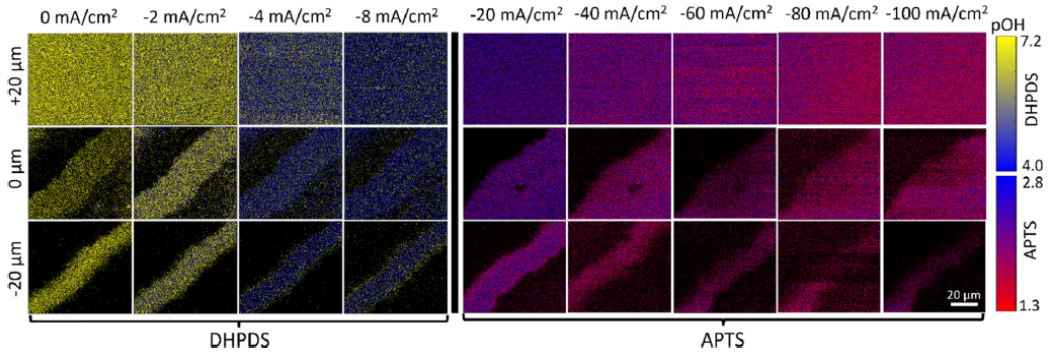

Figure 4.4: pOH maps in the plane parallel to the electrode surface 20 μm above the surface, at the surface and 20 μm below the surface inside a trench in 100 mM $KHCO_3$ electrolyte for different current densities between 0 mA/cm^2 and -100 mA/cm^2, obtained with 100 μM DHPDS (left) and 200 μM APTS (right). Note the different color legends for the panels obtained with DHPDS and APTS.

appendix, section A.2. Despite the slow degradation of APTS, the pOH measurements obtained with APTS are reliable because APTS is a ratiometric dye. The pOH value is calculated from the ratio between two signals that are captured independently in two different wavelength intervals. As some dye molecules degrade, both signals become weaker. This leads to a decreased signal-to-noise ratio, however, the ratio between both signals remains unchanged (see Fig. A.4). The dye degradation effect could be mitigated by using an APTS concentration of 200 μM (compared to DHPDS, where 100 μM is sufficient), removal and replacement of the electrolyte after each measurement, and the introduction of two perpendicular electrolyte inlets to ensure the transportation of fresh APTS to the GDE surface. Some of the panels under high current density magnitudes still appear relatively dark and noisy. This is especially evident inside the trench as the electrolyte is more stationary in confined spaces and this encumbers the transport of fresh, undegraded dye. However, since APTS is a ratiometric dye, the pOH it predicts does not depend on concentration. At magnitudes of the current density as high as 200 mA/cm^2, we were still able to collect enough fluorescence signal to determine the pOH.

For a current density of J = 0 mA/cm^2, the pOH equals 7.2 everywhere (pOH of CO_2-saturated 100 mM $KHCO_3$). When the current is non-zero, the local pOH decreases because OH^- is created as a byproduct of CO_2R. The pOH is lower at the electrode surface than 20 μm above the surface because CO_2 is reduced at the electrode surface and for the pOH to decrease at +20 μm, OH^- has to diffuse away from the surface. Due to electrolyte flow, a concentration gradient is created.

Furthermore, the pOH inside the trench is lower than at the surface. This can be seen especially well in the panels for current densities of -2 mA/cm^2 and -20 mA/cm^2.

The surface morphology of copper does not change during CO_2R experiments. We performed SEM as well as EDS measurements for samples before and after CO_2R. We observed potassium deposits on the sample after CO_2R that originate from $KHCO_3$ molecules in the electrolyte, but the copper catalyst does not change in appearance, neither in the trenches nor on the planar electrode surface, see Fig. 4.5.

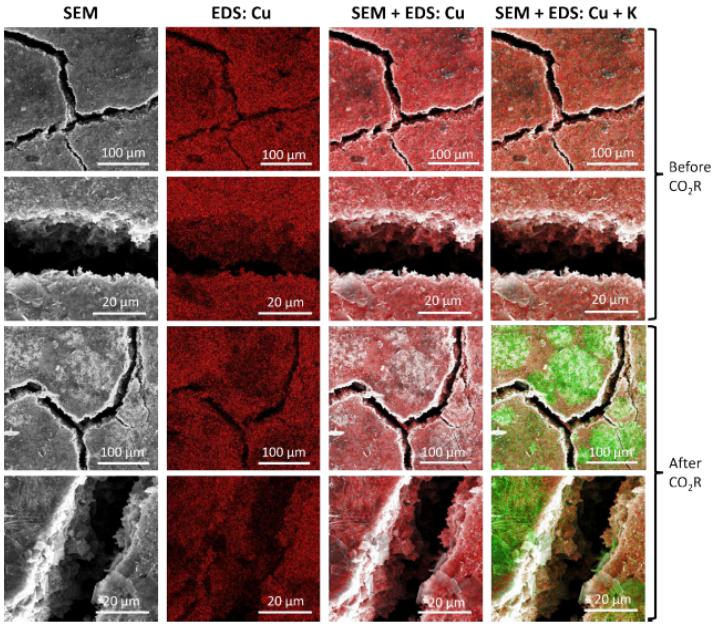

Figure 4.5: SEM and EDS maps of trenches in a copper GDE surface, before and after CO_2R experiments. First column: SEM images. Second column: EDS maps of the same area with red color signaling the presence of copper. Third column: Overlay of SEM and EDS maps of copper. This shows that copper is present on trench walls and at the bottom of trenches with a similar morphology and appearance before and after CO_2R. Forth column: Overlay of SEM and EDS maps of copper (red) and potassium (green). No potassium is present before CO_2R experiments, but there are potassium deposits on samples after CO_2R experiments that originate from the $KHCO_3$ electrolyte.

Fig. 4.6 shows the average pOH as a function of current density, both from experiments and from multiphysics simulations. For the experimental values, the pOH is averaged over at least three independent measurements. The data for low current density magnitudes was obtained with DHPDS, while the data for higher current density magnitudes was obtained with APTS. The red shaded areas indicate the pOH

range that is inaccessible by either dye. The insets are a zoom-in on the experimental data for low current density magnitudes.

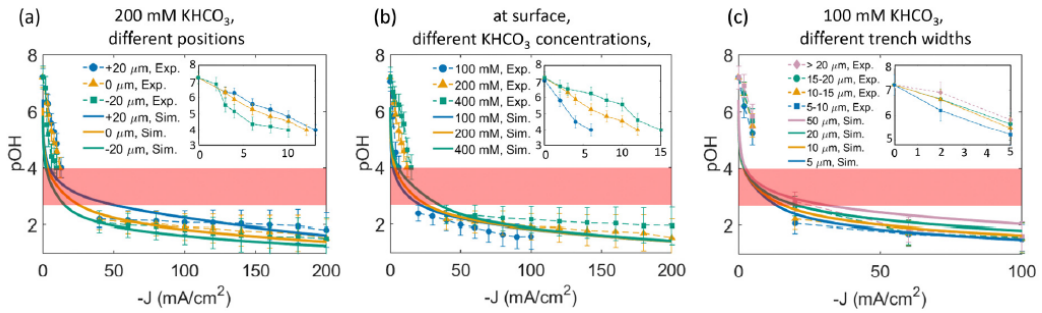

Figure 4.6: The pOH as a function of current density at different positions (a), for different $KHCO_3$ concentrations (b) and for different trench widths (c), in experiments and simulations. (a) Averaged pOH as a function of current density for 200 mM $KHCO_3$, obtained with 100 μM DHPDS ($|J| \leq 13$ mA/cm^2)/ 300 μM APTS ($|J| \geq 20$ mA/cm^2) at three different positions around the electrode surface together with simulation results. (b) Averaged pOH as a function of current density at the electrode surface for three different $KHCO_3$ concentrations between 100 and 400 mM, obtained with 100 μM DHPDS ($|J| \leq 15$ mA/cm^2)/200–300 μM APTS ($|J| \geq 20$ mA/cm^2) together with simulation results. (c) pOH inside a trench 20 μm below the surface as a function of current density for different trench widths between 5 μm and 30 μm. In all panels, the pOH range shaded in red is not accessible by either dye, the inset is a zoom on the data for low current density magnitudes.

Simulations were performed to better understand the variations of pOH with respect to position, electrolyte concentration and trench geometry. A 2-dimensional continuum model of a periodic trench in a GDE was developed. The multiphysics simulations solve for the concentration profiles of all species involved, along with the liquid electrolyte potential in a single, periodic trench of a given width and depth. Concentration-dependent Tafel kinetics are employed to simulate the electrochemical reduction of CO_2 to various products on the Cu electrode surface [63, 115]. Greater detail regarding the physics, parameters, and assumptions employed in the continuum model (shown schematically in Fig. 4.2) can be found in the next section 4.3.2. The model replicates the experimental results with outstanding accuracy. This is true both for the pOH values observed in all panels in Fig. 4.6 as well as for the product distribution that was measured with gas chromatography, see Fig. 4.7. The agreement between model and experiment gives us confidence that the model is a good representation of the real world and predictions beyond what can be observed in experiments can be trusted.

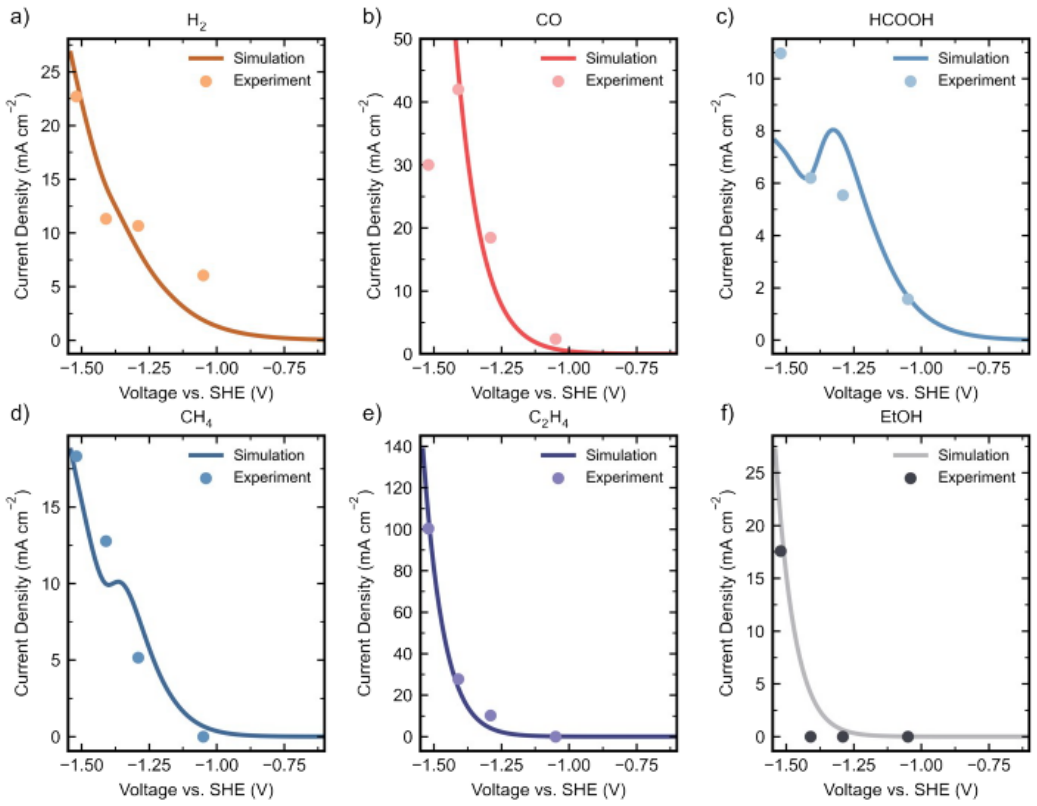

Figure 4.7: Agreement between experimental (markers) and simulated (solid lines) partial current densities to (a) hydrogen, (b) carbon monoxide, (c) formic acid, (d) methane, (e) ethylene and (f) ethanol formed via electrochemical CO_2R on a Cu GDE.

Fig. 4.6 (a) compares the pOH in 200 mM $KHCO_3$ electrolyte at positions around a GDE analogous to that shown in Fig. 4.4. As the magnitude of the current density increases, the pOH decreases accordingly, due to the generation of OH^- from the CO_2R reactions. At first, the slope of the pOH decrease is steep, then gradually tapers as the current density magnitude increases. This can be explained by the logarithmic nature of the pOH scale. A decrease in pOH from 4 to 3 requires the OH^- concentration to increase from 0.1 mM to 1 mM, while a decrease in the pOH from 2 to 1 requires the OH^- concentration to rise from 10 mM to 100 mM, a much larger absolute change in concentration. The pOH in trenches is lower than at the surface, which again is lower than 20 μm above the surface for all current densities; this confirms our previously described results. The simulations agree well with the CLSM experiments, particularly for data at the electrode surface (z = 0 μm) and in the trench (z = 20 μm). Agreement between experiments and simulations is similarly strong for bulk electrolyte concentrations of 100 mM and 400 mM (Fig.

4.8 (a) – (c)).

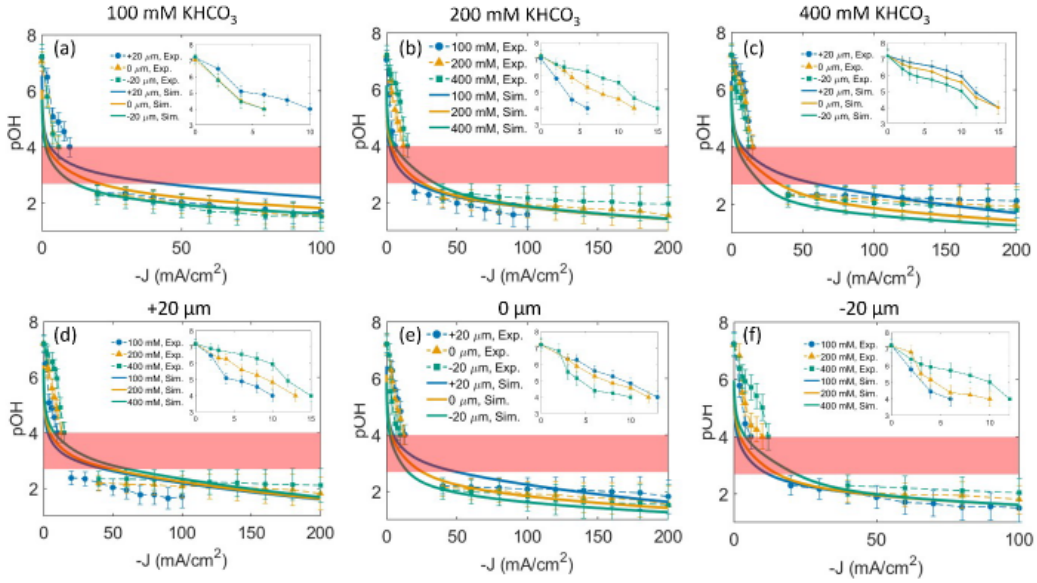

Figure 4.8: Average pOH as a function of current density, obtained with 100 μM DHPDS ($J \geq$ -10 mA/cm^2) and 200/ 300 μM APTS ($J \leq$ -20 mA/cm^2). The top row compares the pOH at different positions around a GDE for $KHCO_3$ concentrations of 100 mM (a), 200 mM (b) and 400 mM (c). The bottom row compares the pOH for different $KHCO_3$ concentrations at positions around a GDE (d) 20 μm above the surface, (e) at the surface and (f) 20 μm below the surface inside a trench. All panels show both experimental and simulation results.

The greatest discrepancy between experiments and simulations is apparent in the z = +20 μm data, which more closely represents the pOH of the bulk electrolyte. The discrepancy is likely due to the static nature of the boundary layer in the simulations, which is set to a constant value of 150 μm, regardless of the applied current density. Previous experimental studies have shown that the bulk electrolyte pH, and thus, the boundary layer thickness is a function of current density at higher current density magnitudes [58, 60]. However, implementing an adaptive, 2–D mesh that grows with current would be very computationally intensive, and for the present study, the pOH in the trench, where CO_2R occurs, is more critical to simulate accurately.

Fig. 4.6 (b) displays a study of the influence of $KHCO_3$ concentration in the electrolyte on the pOH at the GDE surface. The trend observed at the electrode surface is the same as it is 20 μm above the electrode surface and 20 μm below in the trenches (Fig. 4.8 (d) – (f)). Measurements for higher concentrations could be carried out at higher current density magnitudes due to the enhanced electrical conductivity

of the electrolyte. Again, the model generally agrees with observed experimental trends that show that the pOH decreases more slowly as electrolyte concentration is increased. This is because $KHCO_3$ acts as a buffer and, as the $KHCO_3$ concentration increases, the buffering capacity is enhanced, which restrains the decrease in pOH. However, at higher current density magnitudes, the simulated pOH becomes more independent of current density whereas the experimental pOH remains impacted by buffer capacity. This discrepancy at higher current density magnitudes can be attributed to a multitude of factors, such as the large uncertainty in the rate constants for the homogeneous-phase buffer reactions used in the simulations [110, 116, 128], and the fact that dilute-solution theory was employed in the simulations whereas concentrated solution theory may be necessary to simulate adequately the behavior at higher current density magnitudes [129]. Additionally, the simulations assume that there are no mass transport losses of gas phase CO_2 throughout the GDE itself, and thus the CO_2 concentration is at a constant value of 34 mM at the electrode surface. This assumption is unrealistic at high current density magnitudes and could potentially impact the simulated pOH due to the participation of CO_2 in homogeneous buffer reactions. Nonetheless, the simulations are capable of generally capturing the impact of buffer composition, and the incorporation of these second-order phenomena is beyond the scope of the present study.

Lastly, the influence of the trench geometry on the local pOH was investigated (Fig. 4.6 (c)). Eighteen trenches with different widths in 100 mM $KHCO_3$ were taken into consideration. The average pOH inside the trenches, i.e., 20 μm below the surface, was evaluated at different current densities. The trenches were divided into widths of 5–10 μm, 10–15 μm, 15–20 μm, and $\geq$ 20 μm and the average pOH was calculated for each. Both measurements and simulations agree that the pOH decreases as trench width diminishes for all current densities investigated. This behavior is due to the increased surface-area-to-volume ratio of the thinner trenches (Fig. 4.9).

The increased surface-area-to-volume ratio means that more OH^- is generated via CO_2R on the trench walls relative the electrolyte volume contained within a trench. In addition, the mass transfer out of trenches is poor compared to a planar surface, which leads to trapping of OH^-. Thus, the OH^- concentration is increased for thinner trenches as a result of both the increased surface-area-to-volume-ratio as well as mass transport effects. This result is in line with previously reported electrochemical studies that have demonstrated that smaller pore radii in meso- or microstructured

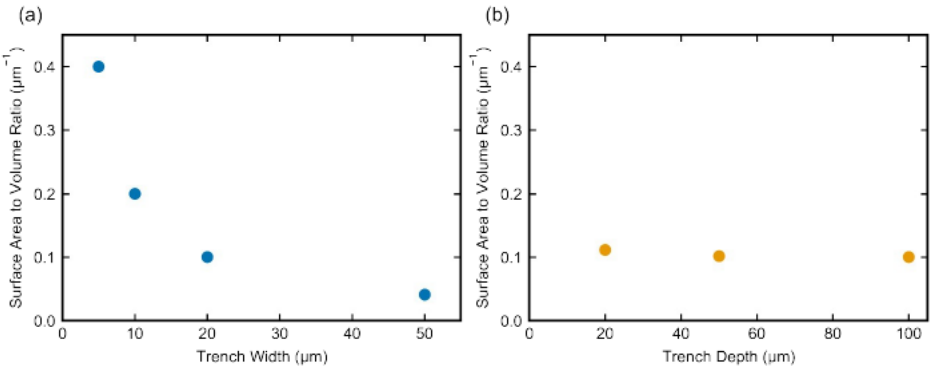

Figure 4.9: Simulated surface area to volume ratio of trenches as a function of (a) trench width at a constant trench depth of 100 μm and (b) trench depth at a constant trench width of 20 μm.

electrodes enhance local OH^- trapping [104, 112, 117, 130]. Interestingly, the measured pOH is less sensitive to trench width at higher current density magnitudes than the simulated pOH. A possible explanation for this discrepancy could be the lack of bubble-induced convection in the present simulations. At high current density magnitudes, the latter could ameliorate OH^- trapping within GDE trenches and reduce sensitivity to trench geometry. The influence of trench width on the pOH further emphasizes the importance to understand how a GDE's micrometer-scale geometry affects CO_2R.

When we combine the results from Fig. 4.6 (a) and (c), we find that the pOH is decreased inside trenches compared to the planar electrode surface and furthermore, this effect is stronger for more narrow trenches. This observation is caused by the altered mass transport inside narrow trenches. Our experiments therefore suggest that the micrometer-scale morphology of a GDE plays an important role in determining the mass transport properties of a GDE, and with it the CO_2R performance.

4.3.2 Multiphysics Simulations and Local Product Distribution

Beyond elucidating trends observed in the CLSM experiments, continuum simulations can be used to identify pOH variations at resolutions that are not achievable experimentally.

Fig. 4.10 (a) depicts OH^- transport within a simulated periodic GDE trench operating at a current density of -50 mA/cm^2 (OH^- transport for -1, -10, and -100 mA/cm^2 is depicted in Fig. 4.11). As shown in the contour plot, the pOH is lowest, and thus the concentration of OH^- is greatest deep within the trench. Examination

of the OH^- flux rationalizes the diminished pOH within the trench: OH^- generated via CO_2R in the trench exits to the bulk electrolyte, but the presence of the trench increases the surface area available for the electrochemical reduction of CO_2 and, accordingly, the generation of OH^-. The trench also provides a volume where the generated OH^- can accumulate due to the altered mass transport. OH^- generated by CO_2R in the trench is thus effectively trapped within the trench, decreasing the local pOH. Similar OH^- trapping behavior has been observed in prior multi-dimensional continuum studies of mesostructured electrodes [65, 116] and has been shown to be beneficial for CO_2R selectivity [65].

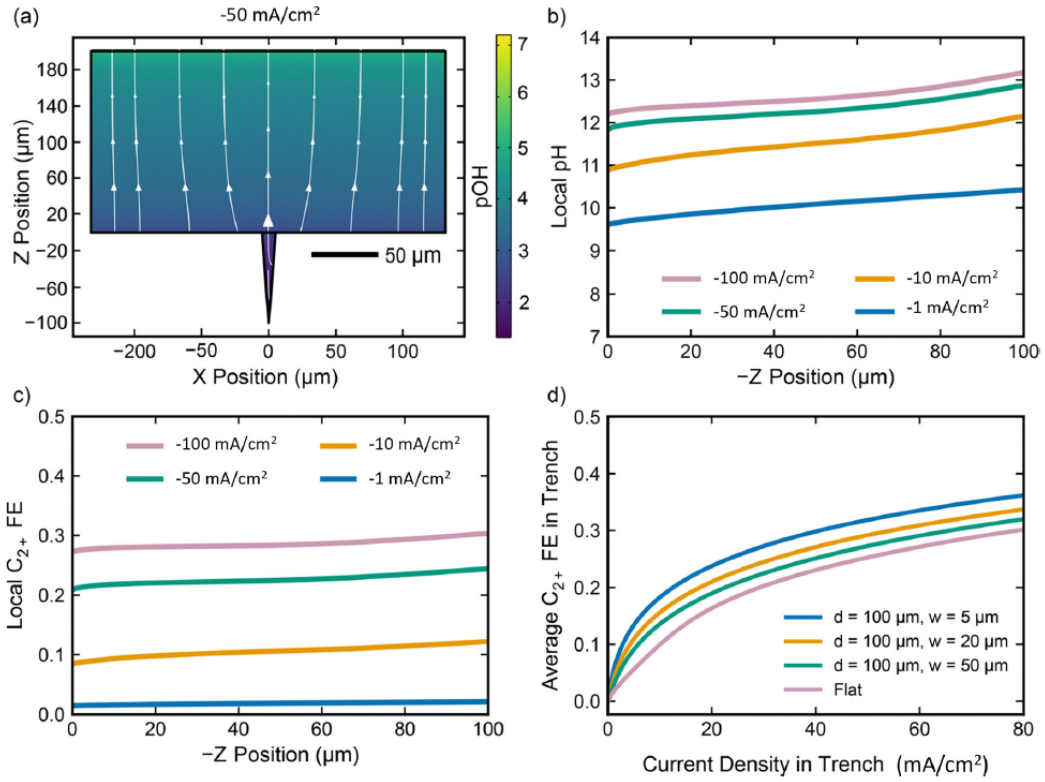

Figure 4.10: Multiphysics simulation results. (a) pOH contour plot and OH^- flux (white arrows) throughout the simulated domain for a periodic GDE trench (width of 20 μm and depth of -100 μm) operating a -50 mA/cm^2 of geometric current density. (b) Simulated electrode surface pH (14 - pOH) as a fuction of depth into the trench for different current densities. (c) Simulated C_{2+} FE as a function of depth into the trench for different current densities. (d) Average C_{2+} FE on trench walls as a function of the current density passed solely through the trench. Z = 0 μm represents the top of the trench, and Z = -100 μm represents the bottom of the trench. d and w are the trench depth and width, respectively.

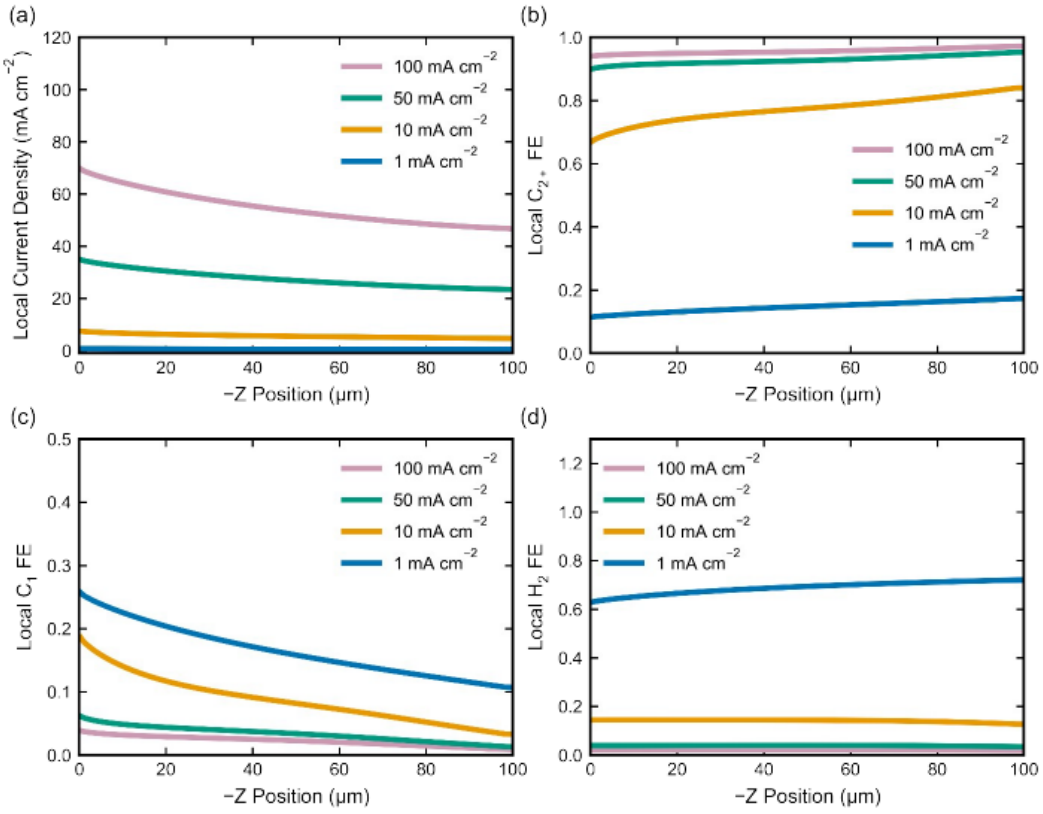

Figure 4.11: Simulated variation of various performance metrics along the walls of the trench as a function of depth into the trench. Z = 0 μm represents the electrode surface or top of the trench, Z = -100 μm represents the bottom of the trench. (a) Local total current density to all electrochemical reactions on Cu. (b) C_{2+} FE along the trench walls. (c) C_1 FE along the trench walls. (d) H_2 FE along the trench walls. Metrics shown in panels (a)-(d) are measured at the surface of the trench walls as opposed to averaged within a cross section of the electrolyte, because these metrics are based on current densities to various electrochemical reactions which only occur at the trench walls, and not within the bulk electrolyte.

To evaluate the influence of the pOH gradient within the trench on local selectivity variations, concentration-dependent Tafel kinetics were employed in the multiphysics model. These concentration dependent Tafel kinetics were fit to experimental data collected on Cu GDEs used in the present study, and are capable of replicating observed partial current densities quite well (Fig. 4.7). The study relates local changes in OH^- activity to changes in current densities for product formation. Fig. 4.10 (b) depicts the change in pH as a function of depth into the trench. Note that Fig. 4.10 (b) shows the pH value while for the most part, this study focuses on the dynamics of OH^- and hence, the pOH. Here, we chose to display the pH instead

to emphasize the correlation between Fig. 4.10 (b) and (c). In the model, the relation pH + pOH = 14 holds true everywhere because we only consider the diffuse transport layer while the electrical double layer is not taken into consideration in the model because its length scale is much smaller than the length scales we study. Therefore, within the frame of this model, pH and pOH are directly connected. Consistent with Fig. 4.10 (a), pH increases (pOH decreases) deeper inside the trench (more negative z) due to trapping of CO_2R-generated OH^-.

The simulations exhibit a direct, albeit modest, relationship between pH and C_{2+} FE (Fig. 4.10 (c)). As the pH increases or the pOH decreases within the trench, the C_{2+} FE correspondingly increases (variations of C_1, H_2, and local current density within the trench are shown in Fig. 4.11). This relationship between C_{2+} FE and pH has been widely reported, and is connected to the suppression of HER and C_1 products [50, 63, 115, 130, 131]. The disproportionate suppression of H_2, CH_4, and HCOOH partial current density within the trench can be observed in Fig. 4.12.

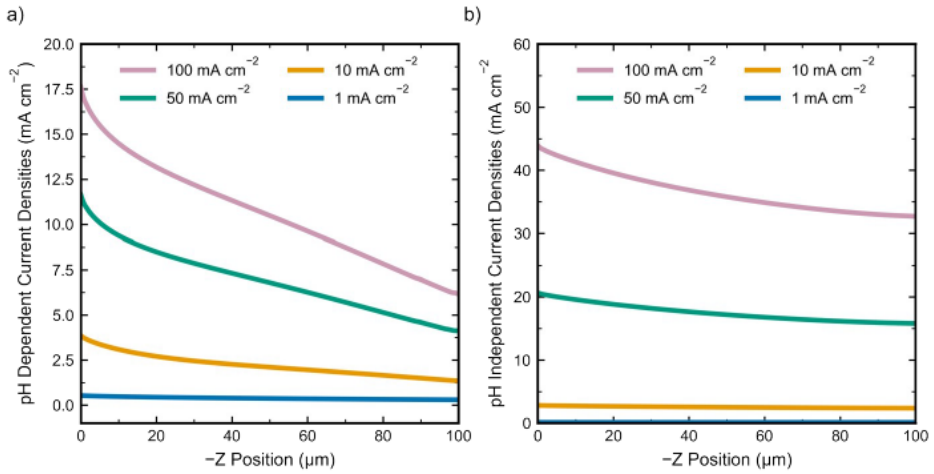

Figure 4.12: Simulated variation in local partial current density for (a) species with pH dependent partial current densities (H_2, HCOOH, and CH_4), and (b) species with pH independent partial current densities (EtOH, C_2H_4, and CO).

This suppression of C_1 and H_2 in the trench results in an approximately 5 % increase in C_{2+} FE across the depth of the trench, regardless of current density (Fig. 4.10 (c)). The enhancement of the performance in the trench is modest, as the change in pH is only about 1 pH unit across the trench depth. Nonetheless, the simulations serve to understand local selectivity trends and provide better understanding of variations in performance within the GDE heterogeneities.

Lastly, performance of CO_2R within trenches was compared to the performance on a flat surface without trenches (Fig. 4.10 (d)). The simulations demonstrate that the C_{2+} FE at a given current density is higher within a trench compared to that on a flat surface due to the improved OH^- trapping. In addition, as the width of the trench decreases, and with it the pOH (Fig. 4.6 (c) and Fig. 4.13), the C_{2+} FE increases.

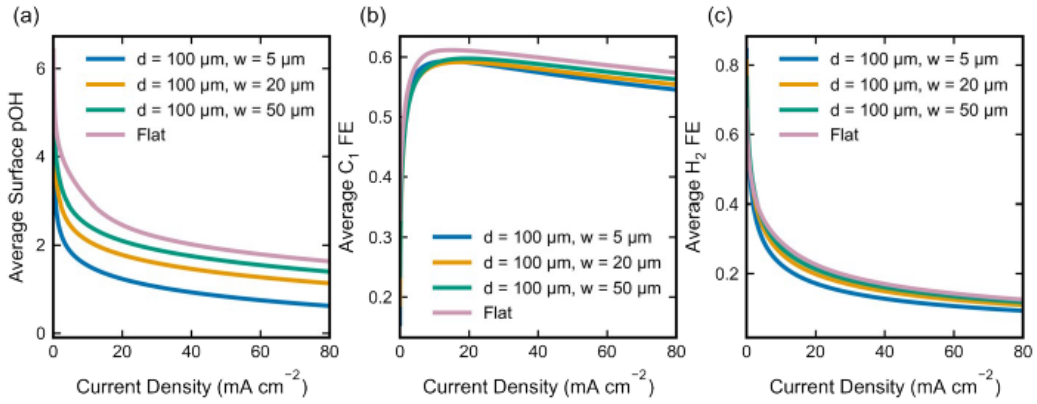

Figure 4.13: Simulated variation in average (a) pOH, (b) C_1 FE, and (c) H_2 FE as a function of trench width. Current density, pOH, and FEs are averaged across the trench walls.

This is a result of the changed mass transport properties in the confined space as well as the enhanced trench surface-area-to-volume ratio (Fig. 4.9), leading to a lower pOH value. The simulations indicate that the micrometer-scale morphology on a GDE surface has an impact on the product distribution with narrow trenches on the order of 5 μm favoring the creation of C_{2+} products across the entire current density range (Fig. 4.10 (d)) by approximately 5 % compared to the flat Cu case. Within the scope of this work, the connection between surface morphology and CO_2R selectivity can only be demonstrated via multiphysics simulations because we have no means to locally resolve the product distribution. However, the accuracy of our model has been demonstrated as there is an excellent agreement with the experimentally measured CO_2R performance as well as the local pOH. The simulations demonstrate the potential for improved C_{2+} FE within these microcavities and experimental demonstration of enhanced C_{2+} FE inside microcavities in the surface of an operating GDE should be the subject of a future study.

The effect of the trench depth on CO_2R was also evaluated (Fig. 4.14), which demonstrates that the ability of a trench to enhance C_{2+} FE increases as the trench deepens.

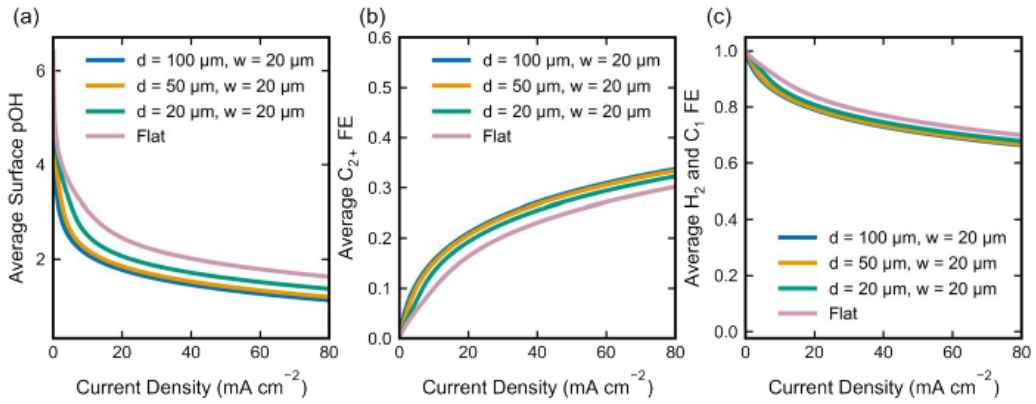

Figure 4.14: Simulated variation in average (a) pOH, (b) C_1 FE, and (c) H_2 FE as a function of trench depth. Current density, pOH, and FEs are averaged across the trench walls.

This is due to the increased surface area available for electrochemical OH^- generation for deeper trenches. The surface-area-to-volume ratio is far less sensitive to trench depth than to trench width (Fig. 4.13) which indicates that compared to the surface area, the volume plays a minor role in determining the C_{2+} FE. However, enhancements in C_{2+} FE become marginal beyond trench depths of 50 μm. Finally, the fraction of the surface covered by the trenches was varied in the simulations, to further evaluate the efficacy of trenches. Fig. 4.15 depicts the pOH and C_{2+} FE as a function of trench coverage, evaluated at current densities of -20 mA/cm^2 and -50 mA/cm^2 (normalized now to the electrochemical active surface area (ECSA)).

This figure aims to deconvolute the effects of roughness from the effects of changes in the microenvironment. As the trench surface coverage increases, the pOH decreases, and the C_{2+} FE increases, due to the OH^- trapping ability of the trenches. While the increase in C_{2+} FE is minor (still approximately 5 % from a flat surface to a completely trenched surface), the enhancement with morphology is similarly observed at both current densities and the results reveal that heterogeneities in commercially available GDEs can serve as local hotspots for enhanced C_{2+} FE and benefit CO_2R due to their OH^- trapping capacity. The simulation results serve as a great support to our novel measurements that allow to probe the microenvironment in a GDE under operando conditions. Both experiment and simulations highlight the importance of the micromorphology of a GDE that influences the mass transport properties. Future work should aim to leverage this insight to develop geometries for which transport is tailored to better trap OH^-. Techniques like laser ablation can be utilized to realize these tailored electrodes as is outlined in chapter 5.

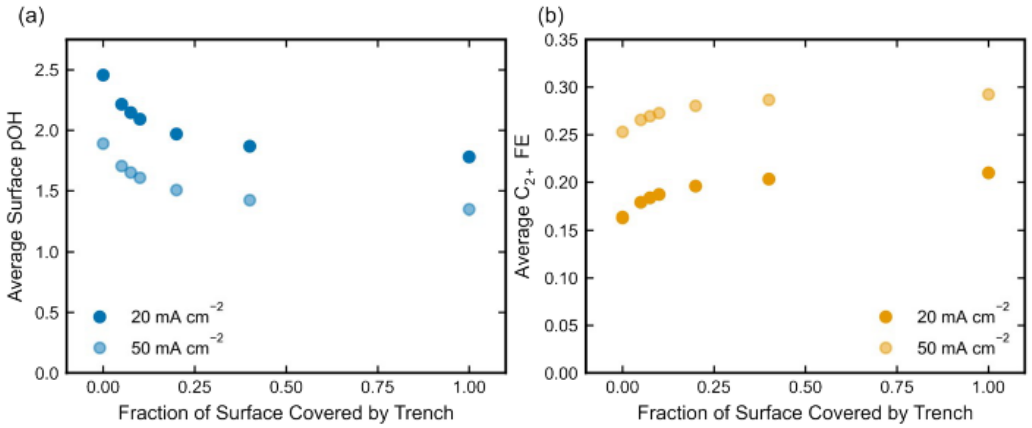

Figure 4.15: Simulated variation in (a) pOH, and (b) C_{2+} FE at an applied current density of -20 mA/cm^2 (normalized to ECSA) as a function of the fraction of GDE surface covered by trenches. A current of -20 mA/cm^2 was chosen due to the increased sensitivity of C_{2+} to pOH at lower current densities. At higher current densities, the C_{2+} FE approaches 1 and is less sensitive to changes in microenvironment. Variation of the surface coverage was achieved by changing the width of the domain (shown schematically in Fig. 4.2) from 400 μm to 20 μm, while keeping trench width and depth constant at 20 μm and 100 μm, respectively. For the zero-coverage case, a rectangular domain with no trench was simulated.

Notably, apart from the influence of pOH, the effect of cations has been highly studied in recent CO_2 reduction literature on Cu electrodes. While important, because the same cation is used throughout all experiments (K^+), these effects will be implicitly captured in the fit exchange current densities [132], as recent work has shown that beyond the type of cation employed, the concentration of the cation is not as important in dictating the electrochemical performance due to the saturation of cations in the outer Helmholtz plane of the Cu double layer [133]. Nonetheless, future experimental and simulation work should be employed to more thoroughly probe and understand the impact of cations in the double layer on CO_2R performance to further advance understanding of the kinetics of this reaction on Cu.

Lastly, while it is known that *CO coverage is a major defining factor in the performance of CO_2R at high overpotentials, fully accounting for *CO coverage effects would require the implementation of a microkinetics model, which requires far deeper understanding of the mechanism of CO_2R on Cu, beyond the scope of the present work. We note that the lack of consideration of *CO coverage effects could also potentially explain the discrepancy between the modeled and observed product distributions at -200 mA/cm^2, wherein the model overpredicts the formation of CO

and underpredicts the formation of HCOOH. Nonetheless, the model still replicates the trends very well at all other current densities, and future work should seek to address the effects of coverage and expand the understanding of microenvironment on CO_2R activity at higher current densities.

4.4 Conclusion

We demonstrate a novel technique to probe the microenvironment in a CO_2R GDE under operating conditions. We map the local pOH value around a GDE resolved in time and three spatial dimensions with fluorescent confocal laser scanning microscopy (CLSM) with a combination of two ratiometric dyes, DHPDS and APTS, that operate by different sensing mechanisms. Critically, this work could hold potential applications beyond the investigation of CO_2R. We were able to capture pOH maps in the pOH range between 0 and 8 and at current densities as large in magnitude as 200 mA/cm^2.

We mapped the local pOH around an operating GDE under applied current. This revealed that the pOH in the vicinity of a GDE decreases as the magnitude of the current density is increased. For all current densities covered, the pOH inside trenches is lower than on the planar surface with the lowest pOH observed inside narrow trenches that are approximately 5 μm wide. This decrease in pOH can be connected to the trapping of OH^- in narrow trenches caused by altered mass transport properties.

Multiphysics simulations confirmed all experimental trends, providing pOH maps consistent with measured pOH and also reproduced product distributions with high accuracy. These simulations indicate that there is a correlation between the pOH and the Faradaic efficiency towards C_{2+} products. Narrow trenches exhibit a decreased pOH and simulations suggest that this results in a locally increased Faradaic efficiency towards C_{2+} products.

We conclude that we successfully developed a superior technique to probe the microenvironment around a CO_2R GDE. The micrometer-scale morphology of a GDE has a strong effect on the mass transport properties and with it, on the CO_2R performance. Microcavities on the order of 5 μm on the surface of a copper GDE serve as local hotspots with decreased pOH. This can inform the design of future CO_2R devices as described in Chapter 5.

Chapter 5

PROBING THE EFFECT OF INTENTIONALLY TAILORED GAS DIFFUSION ELECTRODE MICROMORPHOLOGY GEOMETRIES ON ENHANCING THE SELECTIVITY OF CO_2 REDUCTION

Contents drawn from: A. E. Böhme, A. Q. Fenwick and H. A. Atwater. "Probing the Effect of Intentionally Tailored Gas Diffusion Electrode Micromorphology Geometries on Enhancing the Selectivity of CO_2 Reduction". *In preparation.*

A.E.B. conceptualized the study, fabricated all samples, performed dye calibration, pH imaging experiments and data analysis as well as performed and analyzed multiphysics simulations.

5.1 Introduction

We know from Chapters 2 – 4 that narrow microcavities in the surface of a Cu CO_2R GDE can serve as local hotspots with enhanced pH as well C_{2+} FE. We learned that the pH is locally increased inside trenches compared to the surface of a CO_2R GDE and that this effect is particularly pronounced for narrow trenches that are roughly 5 μm wide [77]. We attribute this to a combination of electrolyte confinement and altered mass transport properties as well as an enhanced surface area and surface-to-volume ratio inside narrow trenches. Multiphysics simulations revealed that the elevated pH inside trenches comes hand in hand with an increased C_{2+} FE and that narrow trenches in the surface of a copper GDE serve as local CO_2R hotspots [78].

The aim of this study is to exploit the effects that we found for random trench patterns (Fig. 5.1 (a)) and to fabricate copper CO_2R GDEs that exhibit a controlled pattern of microcavities (see SEM images in Fig. 5.1 (c), (d) and cross-section schematic in Fig. 5.1 (a)). This was realized by patterning carbon paper substrates including a filler (Fig. 5.1 (b)) using laser ablation. We fabricated samples with regular patterns of both trenches and holes of varying geometries. The novel GDEs serve two purposes:

(1) To systematically study the influence of different microcavity geometry parameters like shape, width, depth and surface coverage on the CO_2R performance. This is done by measuring the local pH inside these features using CLSM and additionally

via the measurement of the bulk product distribution using gas chromatography (GC). Since the GDEs exhibit controlled, regular patterns, bulk product detection can provide direct information about how microcavities influence the CO_2R selectivity. This is impossible for samples covered with random trenches of altering geometries. (2) To develop GDEs with improved C_{2+} selectivity.

In this chapter, we perform spatially resolved measurements via a combination of CLSM with the ratiometric fluorescent probe DHPDS [134] that, due to an additional excitation capability compared to Chapters 2 and 4 allows to sense pH values between 6 and 11.5 with three-dimensional spatial resolution. Under ideal conditions, the resolution of this technique can reach 250 nm in the plane parallel to the GDE surface and 500 nm in the plane perpendicular to the GDE surface.

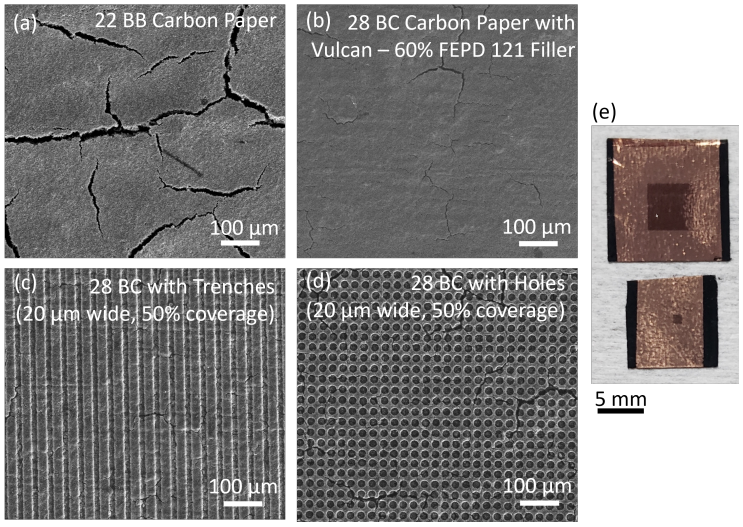

Figure 5.1: Scanning electron microscopy (SEM) images of (a) a Sigracet 22 BB carbon paper GDE that exhibits a pattern of random trenches and was studied in Chapters 2, 3 and 4. (b) Sigracet 28 BC carbon paper post-treated with a 60% Vulcan FEPD filler to fill trenches, (c) a GDE with a regular pattern of trenches (20 μm wide, 20 μm deep, 50% surface coverage) created with laser ablation and (d) a GDE with a regular pattern of holes (20 μm wide, 20 μm deep, 50% surface coverage) created with laser ablation. (e) Photograph of two Cu GDEs with tailored microcavity patterns of size 5 mm x 5 mm (top) used for product detection and of size 1 mm x 1 mm used for pH imaging. More SEM images can be found in Fig. 5.2 and 5.3.

Experimental results are supported by Multiphysics simulations to provide a better understanding of the underlying processes that govern the CO_2R performance in and around tailored microstructures.

5.2 Methods

Fabrication and Characterization of Cu GDEs with Tailored Micropatterns

Patterns of tailored microstructures were carved into Sigracet 28 BC carbon paper with 60% vulcan FEPD filler as the gas diffusion substrate. Carbon paper was chosen because of its good electrical conductivity. However, untreated Sigracet carbon paper exhibits a random pattern of trenches (see Fig. 5.1 (a)) that would interfere with the patterning process. Consequentially, carbon paper that had been post-treated with a Vulcan carbon filling and consequentially exhibits only very minor trenches (Fig. 5.1 (b)) was used. A regular pattern of trenches (Fig. 5.1 (c)) and holes (Fig. 5.1 (d)) with different geometry parameters was carved into this substrate using a UP-193 laser ablation system. The sample fabrication with laser ablation has the advantage that the structure geometry can very easily be tuned and it is faster than most lithography processes. The pattern is created by moving a 193 nm pulsed laser over the substrate surface with 90% laser power and a 10 Hz repetition rate. Patterns of both trenches and holes were created. For the trenches, the laser was moved across the substrate in a continuous motion at a defined speed. To make holes, the laser was kept at a fixed position for a period of time before moving to the next position. The width or diameter of the feature can be determined with the laser spot size, the depth with the scan speed for trenches or the dwell time for holes and the surface coverage by defining the distance between the trenches or holes that are carved into the surface.

We created patterns of trenches and holes with similar size parameters with widths/ diameters in the range 5 μm – 50 μm (constant depth 20 μm, constant surface coverage 50%), with depths in the range 10 μm – 40 μm (constant width/ diameter 20 μm, constant surface coverage 50%) and with surface coverages in the range 10% – 75% (constant width/ diameter 20 μm, constant depth 20 μm). The geometry parameters as well as the laser ablation settings can be found in Table 5.2 for the creation of trench patterns and in Table 5.2 for the creation of hole patterns. The total size of the patterns is 1 mm x 1 mm for samples that are studied with pH imaging via CLSM and 5 mm x 5 mm for samples that are used to determine the product distribution via gas chromatography, see Fig. 5.1 (e).

Following the laser ablation patterning procedure, 300 nm Cu was deposited on the samples with an AMODS dual electron beam deposition system at a rate of 2 angstrom/s while rotating the substrate holder.

Table 5.1: Geometry and laser ablation parameters for trench patterns. The width refers to the trench width at the very top of the trench, the surface coverage to the percentage of the planar sample surface that is covered with trenches, where the trench size at the top is used as a reference. The scan speed refers to a single pass, unless noted otherwise. The line distance is the distance between the center of a trench to the center of an adjacent trench.

Width (μm)	**Depth (μm)**	**Surface Coverage (%)**	**Spot Size (μm)**	**Scan Speed (μm/s)**	**Line Distance (μm)**
5	20	50	5	1, 3 passes	10
10	20	50	10	1	20
20	20	50	20	10	40
50	20	50	50	20	100
20	10	50	20	20	40
20	30	50	20	1	40
20	40	50	20	1, 3 passes	40
20	20	10	20	10	200
20	20	25	20	10	80
20	20	75	20	10	26.7

The samples were characterized with SEM and EDS using a NOVA NanoSEM 450 SEM with an Oxford Instrument Xmas 800 mm2 EDS system using an acceleration voltage of 15 kV. This reveals that copper covers not only the flat surfaces, but also the walls and bottoms of trenches and holes, see Fig. 5.2.

The cross-section of the resulting trenches and holes resembles a parabola, as can be seen from cross-sectional SEM images (Fig. 5.3), see also schematic in Fig. 5.8 (a).

Operando pH Imaging with Confocal Laser-Scanning Microscopy

We utilized a custom-made electrochemical cell (Fig. 5.8 (b)) with a Leica Stellaris 5 confocal microscope and the fluorescent pH probe DHPDS [77, 78, 134] (compare Chapters 2 and 4) to image the local pH value inside the GDE structures under operando CO_2R conditions. The dye calibration was performed analogous to the procedure described in Chapter 2. The calibration curve corresponds to the one shown in Fig. 1.10 (c), orange curve and takes the form

$$(\text{Ratio of Emission}) = \frac{1.147}{1 + \exp(-1.014 \cdot (\text{pH} - 8.504))} + 0.08953. \tag{5.1}$$

The custom-made electrochemical cell was 3D-printed with a Bambu Lab X1-Carbon filament 3D printer. Its setup is analogous to the one described in Chapter

Table 5.2: Geometry and laser ablation parameters for hole patterns. The diameter refers to the hole diameter at the very top of the hole, the surface coverage to the percentage of the planar sample surface that is covered with holes, where the hole size at the top is used as a reference. The spot distance is the distance between the center of a hole to the center of an adjacent hole.

Diameter (μm)	**Depth (μm)**	**Surface Coverage (%)**	**Spot Size (μm)**	**Dwell Time (s)**	**Spot Distance (μm)**
5	20	50	5	60s	6.3
10	20	50	10	5	12.5
20	20	50	20	2	25
50	20	50	50	1	62.6
20	10	50	20	1	25
20	30	50	20	5	25
20	40	50	20	20	25
20	20	10	20	2	56
20	20	25	20	2	35.4
20	20	75	20	2	20.5

4. The active surface area of the GDE that is exposed to electrolyte is 0.2 cm^2. A Cu GDE prepared as described above with a pattern covering an area of 1 mm x 1 mm serves as the working electrode, a Ag/AgCl electrode as the reference electrode and a platinum mesh as the counter electrode.

An aqueous 100 mM $KHCO_3$ electrolyte spiked with 100 μM DHPDS is purged with 30 SCCM CO_2 gas for at least 30 minutes prior to experiments to ensure saturation. The cell is placed under a Leica Stellaris 5 confocal microscope with a HC Fluotar L 25x/0.95 W VISIR water immersion objective that is dipped into the electrolyte. Electrolyte is pumped into the electrolyte chamber through two perpendicular inlet tubes at a rate of 6 mL/min. A 10 SCCM CO_2 gas stream is fed into the gas chamber. Potentiostatic electrochemical impedance spectroscopy (PEIS) is performed in the beginning of each experiment using a Biologic SP-200 potentiostat to determine the impedance and to perform IR electronic compensation. Images are captured by scanning the electrolyte sequentially with a laser beam at 405 nm (1.2% laser power, gain 100) and at 485 nm (laser power 2%, gain 50). The fluorescent signal is collected separately in the range between 495 nm and 835 nm with a pinhole size of 1 Airy unit. Images are captured around a hole or trench in the GDE surface in the plane parallel to the electrode surface. A z-stack is performed such that images are taken for a range of z-positions, starting below the bottom of a feature and ending at least 20 μm above the GDE surface. The distance between each image

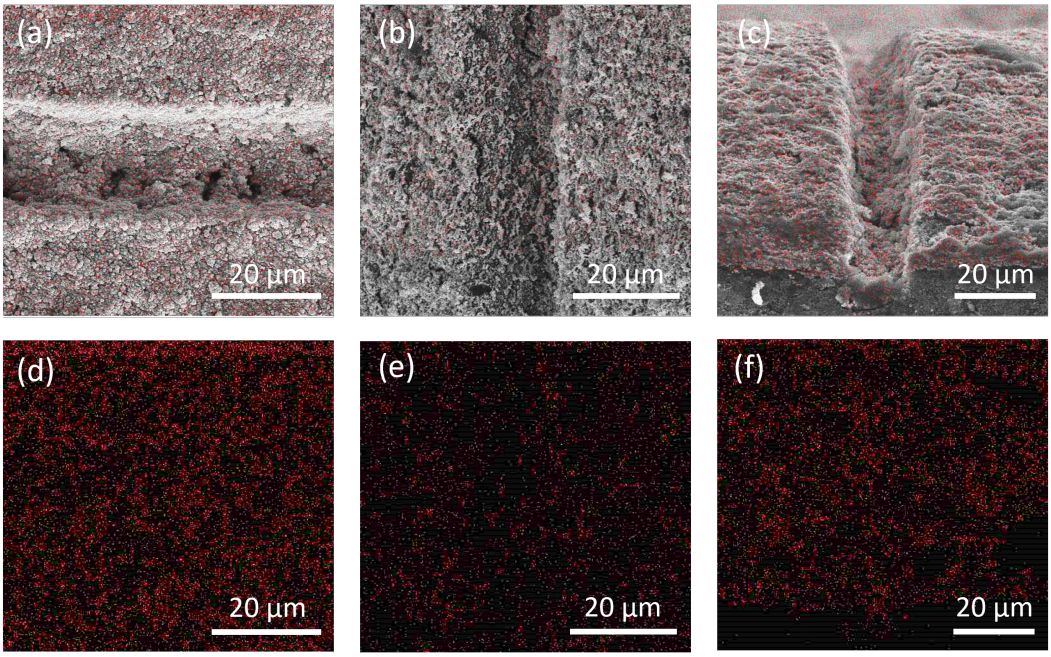

Figure 5.2: SEM and EDS maps of a trench (20 μm wide and 20 μm deep) in a carbon paper GDE under different angles. (a) – (c): Overlay of an SEM image with a EDS map where red color indicates the presence of Cu, (d) – (f): EDS maps, red color again is an indicator for Cu. (a), (d) in the plane parallel to the sample surface, (b), (e) under an angle of 45° and (c), (f) under an angle of 90°. The EDS measurements reveal that copper is not only present on the planar electrode surfaces, but also on the bottom and walls of trenches.

plane is 565 nm. A series of such measurements is performed under galvanostatic CO_2R conditions, at current densities of 0 mA/cm^2, -2.5 mA/cm^2, -5 mA/cm^2, and -10 mA/cm^2. For current densities more negative than -10 mA/cm^2, pH values higher than the detection limit of DHPDS (pH 11.5), are reached. The electrolyte with DHPDS is replaced between measurements at different current densities. Each measurement is repeated at least three times.

Quantitative pH Analysis

pH maps (Fig. 5.8 (c), (d)) can be calculated from the raw fluorescence data pixel by pixel with the calibration curve (equation 5.1). To obtain quantitative pH-z profiles, a rectangle within a trench or hole is defined (see Fig. 5.8 (c), (d), panel at z = 0 µm). The average pH value within that rectangle is calculated as a function of z-position where z = 0 μm is defined as the GDE surface. It is taken into consideration that the focus point of the two laser excitations is shifted by ≈4 μm, hence the ratio of emission is calculated from two different frames that resemble the same z-position.

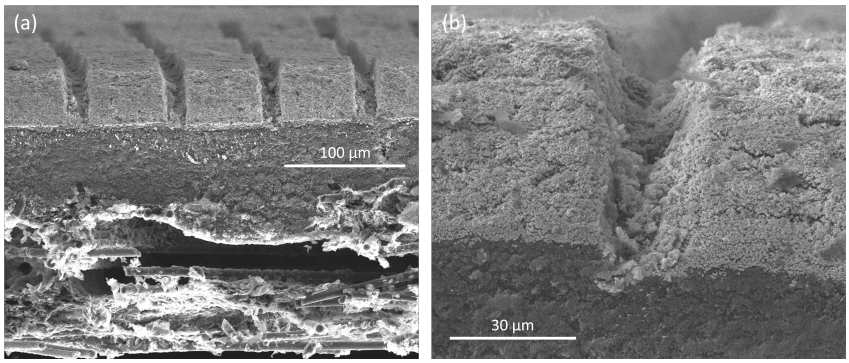

Figure 5.3: Cross-sectional SEM images of a carbon paper GDE structured with a regular pattern of trenches via laser ablation (width 20 μm, depth 20 μm, surface coverage 25 %). (a) Cross section of the whole GDE, displaying the macroporous layer at the bottom and the microporous layer that is laced with trenches, (b) Cross section of a single trench, highlighting the parabola-like cross-sectional shape.

Further, pixels with less than half of the absolute intensity of the maximum pixel intensity within a frame are not taken into consideration when calculating the average pH value from the ratio of emission since their signal-to-noise ratio is weak.

Fig. 5.4 (a) illustrates the different steps of the quantitative pH analysis. The dark orange curve is the pH as calculated from the raw fluorescent signal (equation 5.1). Once the shift between the focus positions of the two lasers is considered and pixels with low absolute intensity are discarded, the pH-z profile takes the shape of the pink curve. Finally, we take the confinement and mass-transport limitations of the pH probe DHPDS inside microcavities into consideration. The yellow curve in Fig. 5.4 (a) displays the pH profile in and above a trench at a current density of 0 mA/cm^2. Since no charge transfer reactions proceed at open bias and the electrolyte is saturated with CO_2, it is expected that the pH remains constant as a function of z-position. This is indeed the case in the bulk electrolyte, see Fig. 5.4 (b), pink curve. However, as the pH profile is recorded around a microcavity in the GDE surface (Fig. 5.4 (a), yellow curve and Fig. 5.4 (b), orange curve), the pH value decreases as a function of decreasing z-position. It is not expected that this is caused by CO_2 diffusing through the GDE since the electrolyte is saturated with CO_2. To confirm this, we performed a control experiment in argon-saturated electrolyte and with argon fed to the backside of the GDE, see Fig. 5.4 (b). While the pH value is more than one pH unit higher than in the experiment with the acidifying CO_2 gas, the trends are the same. The pH vs. z curve is flat in the bulk argon-saturated electrolyte (green curve), but the pH decreases as a function of decreasing z-position around a microcavity in

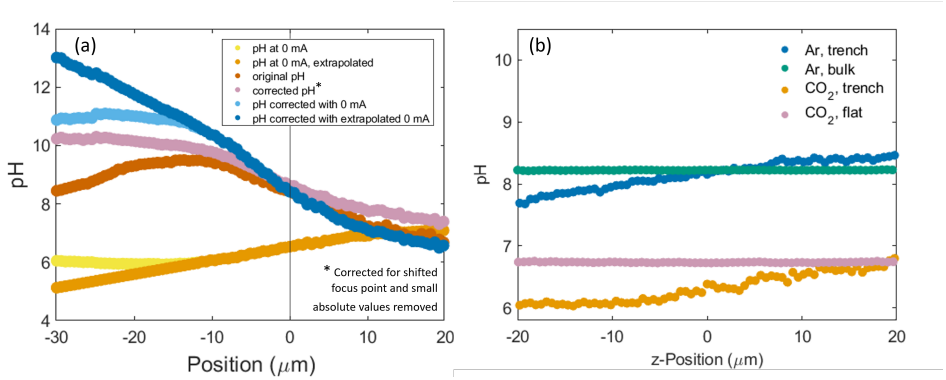

Figure 5.4: Illustration of quantitative pH data analysis. (a) Exemplary pH profiles for a sample with trenches (width 20 μm, depth 30 μm, surface coverage 50%, current density -2.5 mA/cm^2). The original pH curve (dark orange) is corrected by a shift of the focus point of the two excitation wavelengths, the removal of dark pixels and by a factor determined from the extrapolated pH curve at 0 mA/cm^2 (bight orange), resulting in the dark blue curve. (b) Measured pH-z profiles at open circuit both in Ar- and CO_2-saturated electrolyte, inside a trench (where the 0 μm z-position marks the GDE surface) and in the bulk electrolyte (random z-position). The measured pH in the bulk electrolyte is constant for both Ar- and CO_2-saturated electrolyte as expected, indicating that the non-constant pH profile observed at 0 mA/cm^2 in a trench or hole is not an intrinsic artifact. The pH profile in and above a trench in both Ar- and CO_2-saturated electrolyte decreases as a function of decreasing z-position. This allows the conclusion that the pH profile at open bias is not connected to electrolyte acidification caused by additional CO_2 diffusion through the GDE but by mass transfer limitations of the pH probe DHPDS. This result justifies the pH correction with the curve at 0 mA/cm^2. The baseline pH in the argon-saturated electrolyte is higher than that in CO_2-saturated electrolyte due to the equilibrium reactions of CO_2 to bicarbonate and carbonate that acidify the electrolyte.

the GDE surface that is fed with argon (blue curve). We conclude that the reason for the observed non-constant pH at open circuit around a trench is an artifact caused by mass transfer limitations of the probe DHPDS. The measurement at open circuit provides us with the opportunity to correct measurement under bias for the mass-transfer limitation effect. For this purpose, we measure the pH profile at open circuit for each trench or hole investigated. Note that the lower detection limit of DHPDS is pH 6. The pH vs. z profile at open bias therefore plateaus inside microcavities once it reaches pH 6 (see Fig. 5.4 (a), yellow curve and (b), orange curve). We therefore extrapolate the pH profile by performing a linear fit to extrapolate the curve beyond pH 6, see Fig. 5.4 (a), bright orange curve. Using this extrapolated open-bias pH curve, we determine for each z-position separately by which factor the observed pH

value varies from the expected pH which corresponds to the bulk pH (green and pink curves in Fig. 5.4 (b)). To account for the probe's mass-transfer limitation effect for the measurements under applied bias, the measured pH at each z-position is divided by the factor calculated from the curve at open bias. The light blue curve in Fig. 5.4 (a) corresponds to the pH profile that is corrected with the open-bias curve without extrapolation, the dark blue curve is the pH profile that is corrected with the extrapolated open-bias curve. We believe that a pH calculation that takes into consideration the shifted laser focus point, the weak signal-to-noise ratio of pixels with low signal intensity as well as the mass transport limitations of DHPDS is the most realistic representation of the pH.

Product Detection

A different electrochemical cell optimized for use with gas chromatography was 3D-printed with a Elegoo Mars 3 Pro 4K resin 3D printer and used for product detection during the performance of CO_2R experiments with copper on carbon paper GDEs. The active cathode surface area is 0.25 cm^2 and the anode surface area is 4 cm^2 to ensure no current limitation. For intentionally patterned GDEs, the full 0.25 cm^2 cathode surface area is covered with uniform microstructures. A leakless Ag/AgCl electrode serves as reference electrode and a platinum mesh as the counter electrode. An anion exchange membrane (AGC, Selemion AMV) is used to separate cathode and anode. The gas chamber takes the form of a serpentine channel at the back of the GDE. The cell is sonicated before each experiment for at least 40 minutes and rinsed thoroughly after each experiment. An aqueous 1M $KHCO_3$ solution saturated with CO_2 serves as the electrolyte and is pumped through the catholyte and anolyte chambers at a rate of 10 mL/min. CO_2 is fed into the gas chamber at a rate of 10 SCCM. A flow meter placed before and after the cell is used to ensure that there are no gas leaks. The gas coming from the cell is circulated through the cathode electrolyte reservoir to catch any product gas that seeps into the electrolyte. The product passes through a vapor trap en route to the SRI-8610 gas chromatograph which separates gaseous species. Chronopotentiometry experiments (constant current) are carried out at -100 mA/cm^2 and are preceded by potentiostatic electrochemical impedance spectroscopy (PEIS) to ascertain the cell's uncompensated resistance.

COMSOL Model

The COMSOL simulations consist of two separate models. The first simulates the flow of CO_2 through the gas chamber at the backside of a GDE and the diffusion of

CO_2 through the porous GDE. It separately quantifies the average amount of CO_2 that diffuses through trench or hole walls as well as the flat surfaces between cavities in a GDE (Fig. 5.5 (a)). The CO_2 flux quantification is used in the second model that simulates the electrochemical processes in the electrolyte around the surface of a CO_2R GDE with a pattern of trenches or holes (Fig. 5.5 (b)).

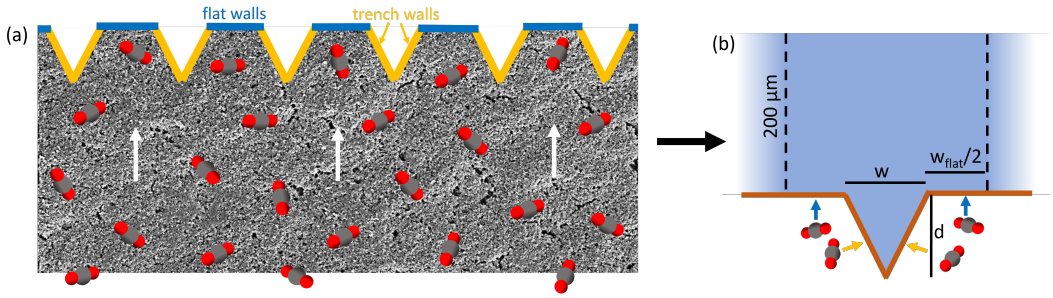

Figure 5.5: Schematic overview of (a) the CO_2 diffusion as well as (b) electrochemistry simulations. (a) The CO_2 diffusion model simulates the transport of CO_2 through a porous domain with a regular pattern of microcavities. The average CO_2 outflow is calculated separately through trench walls (orange) and for flat walls (blue). The results are used as input in the electrochemistry model (b) that simulates a single trench with width w, depth d and surface coverage $\frac{w}{w+w_{flat}}$.

CO_2 Diffusion Model

A stationary three-dimensional COMSOL Multiphysics model with the Free and Porous Media Flow, Brinkman equations module is used to simulate the CO_2 diffusion through a porous GDE with tailored microcavities. The model includes the CO_2 flow through the gas chamber as well as the diffusion through the porous GDE. The model setup is systematically depicted from different perspectives in Fig. 5.6. CO_2 is assumed to enter through Inlet 1 (left) with a velocity of 0.021 m/s which corresponds to a flow rate of 10 SCCM. The specific density and viscosity of gaseous CO_2 at room temperature and atmospheric pressure are used as fluid property input. A pressure difference of 3 Pa is assumed between the gas outlet (Outlet 2) and the GDE (Outlet 1). No slip wall boundary conditions are applied at walls except for inlets and outlets. Gravity is included along the axis indicated in Fig. 5.6.

Fig. 5.7 shows the simulated CO_2 velocity profile through the gas chamber. The GDE is treated as a continuous porous matrix that is 225 μm thick which corresponds to the thickness of Sigracet 28 BC carbon paper [135]. A 1 mm x 1 mm pattern in the center of the GDE of either trenches or holes (see Fig. 5.6, inset) is included

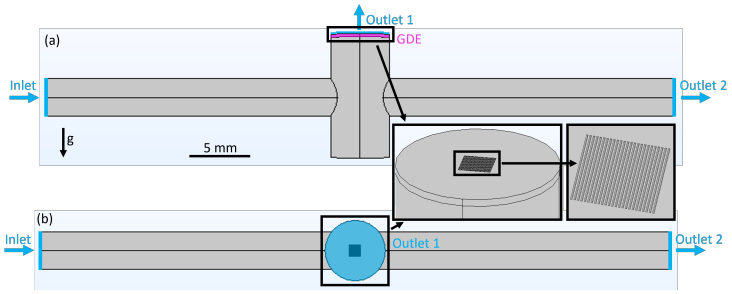

Figure 5.6: Schematic of the geometry of the COMSOL model that simulates the diffusion of CO_2 through a GDE, in the front view (a), in the top view (b) and close-up of the GDE and the pattern in the GDE (insets). The model entails the free flow of CO_2 through a gas chamber with a gas inlet on the left and an outlet on the right. The GDE (marked in pink in panel (a)) sits at the top of the gas chamber and is treated as a second gas outlet. A 1 mm x 1 mm trench or hole pattern is included in the center of the GDE (see insets).

with the same geometry parameters used in experimental studies (see Table 5.2 and Table 5.2). Non-Darcian flow is implemented in the porous medium. The porosity is assumed to be 0.6 and the permeability is set to $1 \cdot 10^{-13}$ m^2 which corresponds to the permeability reported for Sigracet 28 BC carbon paper [135]. The average outflow of CO_2 through the GDE surfaces is calculated separately for trench or hole walls and for planar surfaces surrounding the microcavities (Fig. 5.5 (a)). To this end, the gas velocity in the outward direction through these walls is integrated and then divided by the surface area over which it was integrated. The resulting outward CO_2 volume flux is multiplied with the density of CO_2 at room temperature and atmospheric pressure and divided by the molar weight to obtain the CO_2 outflow in mol/(s·m^2). These results are used as an input for the electrochemistry COMSOL model described below.

Electrochemistry Model

The model developed in Chapter 4 has been adapted for this study. Unless otherwise noted, all model parameters remain unchanged. The model domain is schematically depicted in Fig. 5.5 (b). Since the model is two-dimensional and it would be significantly more computationally expensive to extend the model to three dimensions, only trenches but no holes are considered. The model domain consists of a single trench with varying geometries resembling the parameters used in experiments and in the CO_2 diffusion model outlined above (see Table 5.2). Periodic boundary conditions are applied to simulate a regular pattern of trenches. The surface coverage of

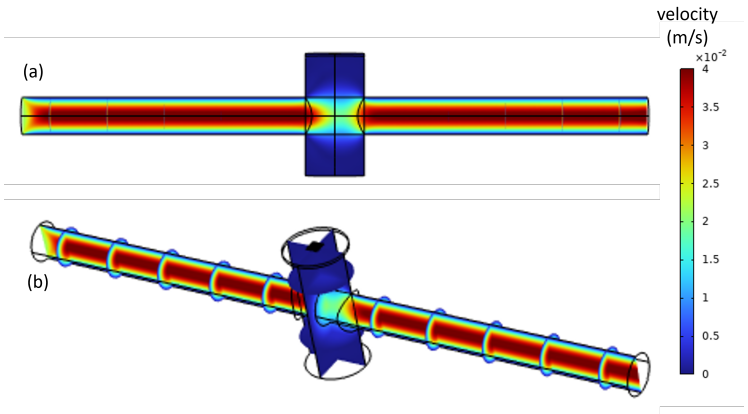

Figure 5.7: Simulated CO_2 flow velocity through the gas chamber at the backside of a GDE in two different perspectives, obtained with the model geometry outlined in Fig. 5.6.

trenches can be controlled by the distance of the model boundaries from the trench ($w_{flat}/2$ in Fig. 5.2 (b)).

In the original model reported in Chapter 4, a simplified boundary condition had been applied at the electrode surface assuming the CO_2 concentration of saturated electrolyte. This assumption most likely breaks down at high current densities. Further, deep trenches or holes with a high surface coverage can impede CO_2 transport through a GDE because larger GDE surfaces must be delivered through a smaller volume, see Figs. 5.9 and 5.14. For this study, the CO_2 concentration boundary condition is therefore replaced by an inward CO_2 flux through trench walls as well as flat surfaces as calculated from the diffusion model outlined above. While more complicated, this is a more realistic representation of the experimental system and allows to study the influence of the CO_2 transport through a patterned GDE.

5.3 Results and Discussion

As a first step, we imaged the local pH value inside tailored microstructures within our custom-made GDEs using CLSM and the fluorescent pH probe DHPDS. This allows to correlate the geometry parameters of the microcavities with the local pH value. We investigated patterns of different shapes (trenches and holes), widths/ diameters (5 μm - 50 μm), depths (10 μm - 40 μm) and surface coverages (10% - 75%) while keeping the other geometry parameters constant. The various geometries are listed in Table 5.2 and Table 5.2. For each sample, the local pH value was mapped with sub-micrometer spatial resolution in three dimensions, covering a microcavity

and the area around it as well as the bulk electrolyte up to 20 μm above the GDE surface which is well within the boundary layer. Since protons are consumed and hydroxides are created during electrochemical CO_2R, it is expected that the pH increases as function of the proximity to the GDE surface and as a function of current density. In Chapters 2 and 4, we could further show that the pH increases inside microcavities compared to the surface of a GDE due to electrolyte confinement and altered mass transfer properties. In this study, we combine local pH imaging with measurements of the bulk product selectivity of patterned GDEs as well as with simulations of the CO_2 transport through structured GDEs and electrochemical CO_2R processes.

Fig. 5.8 (c) and (d) show exemplary operando pH maps for a current density of -2.5 mA/cm^2 in the x-y plane at various z positions for a trench and a hole (both with a width/ diameter of 20 μm, depth 20 μm and surface coverage 50%). Directly from the maps, we can observe that the local pH value increases inside the trench and hole compared to the surface and hence confirms our previous observation with random trench patterns (Chapters 2 and 4).

The interplay between several different effects influences the operando local pH value inside and around microcavities in the surface of a CO_2R GDE:

1. Electrolyte confinement and altered mass transport properties inside microcavities, including CO_2, CO_2R products, H^+ and OH^-. Confinement and impeded mass transport lead to the accumulation of OH^- and hence, an increase in pH.

2. The catalyst surface area, specifically the surface-to-volume ratio (ratio between the catalyst surface and the electrolyte volume inside a microcavity). A higher surface-to-volume ratio means that more catalyst surface is available to facilitate CO_2R (as well as HER) which leads to a higher pH value.

3. The transport and availability of CO_2 at the catalyst-electrolyte interface. Microcavities can promote CO_2 transport [78] (see Chapter 3) if the surface coverage is low, however, if microstructures are deep and very close together (high surface coverage), they can have the opposite effect and lead to less CO_2 availability per surface area because less space is available for CO_2 to travel through and a larger surface area must be delivered. This is schematically illustrated in Fig. 5.9. We further performed simulations to calculate how

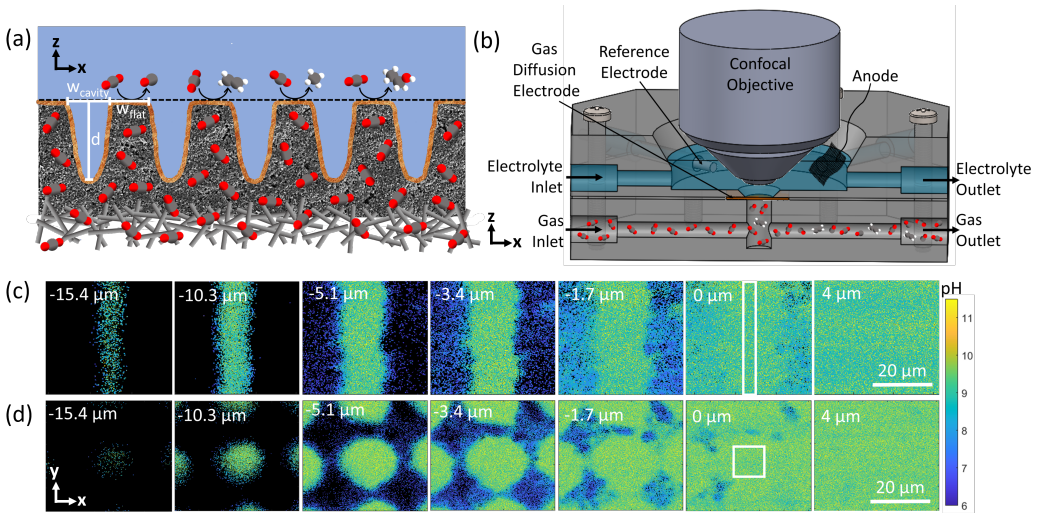

Figure 5.8: Schematic cross-section of a custom-made GDE and electrochemical cell and exemplary pH maps. (a) Schematic cross-section illustration of a custom-made carbon paper GDE with a regular pattern of trenches or holes. CO_2 diffuses through the macropourous and laser-ablated microporous layers of the GDE to the catalyst-electrolyte interface where CO_2 is reduced to C_1 and C_{2+} products. The black dashed line indicates the definition of the GDE surface (z = 0 μm). The white markers illustrate the geometry parameters with d the depth, w_{cavity} the trench width or hole diameter and w_{cavity}/w_{flat} the surface coverage. Illustration not to scale. (b) Schematic of the custom-made electrochemical cell for operando pH imaging with CLSM. The electrolyte used is 100 mM aqueous $KHCO_3$ spiked with 100 μM DHPDS, the reference electrode a leakless Ag/AgCl electrode and the anode a platinum mesh. (c) and (d) Exemplary maps of the local pH value in and around (c) a trench and (d) a hole in a Cu GDE with width/ diameter 20 μm, depth 20 μm and surface coverage 50%. Maps are captured in the plane parallel to the electrode surface at different positions in the direction perpendicular to the surface. The scale bars and color bar apply to all panels in (c) and (d).

microcavities influence the CO_2 transport, see Fig. 5.5 - 5.7. If not enough CO_2 is present at the electrode surface, the CO_2R efficiency is limited by the availability of CO_2, leading to a decreased selectivity towards CO_2R products. This effect is expected to be especially prominent at high current densities. On the other hand, any unreduced CO_2 leads to an acidification of the electrolyte due to equilibrium reactions with OH^- to bicarbonate and carbonate [110, 136, 137]. Excess CO_2 is therefore expected to lower the local pH value.

4. The proximity to catalyst surfaces. Since charge transfer reactions that increase the pH value proceed at the catalyst surface, the local pH is expected to increase as a function of proximity to any catalytic surfaces.

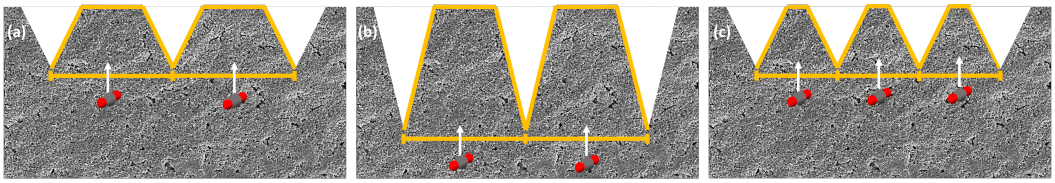

Figure 5.9: Schematic representation of the CO_2 delivery through a GDE with regular surface patterns with a simplified triangular cross-sectional shape with different geometry parameters. (a) GDE with features with the same width and depth (e.g., 20 μm) and a surface coverage of 50%. (b) GDE with features with a depth (e.g., 40 μm) twice as high as the width (e.g., 20 μm) and a surface coverage of 50%. (c) GDE with features with the same width and depth (e.g., 20 μm) and a surface coverage of 75%. Marked in orange is the surface through which CO_2 can diffuse into the volume between structures as well as the GDE's surface area that must be delivered with CO_2. The ratio between the two decreases with increasing structure depth and with increasing surface coverage which can lead to limited CO_2 transport and a shortage of CO_2 molecules at the GDE surface.

The advantage of our novel structured GDEs is that they allow to systematically study the interplay between pH effects and various geometry parameters which is impossible for random trenches. One important geometry parameter is the microcavity shape. We created structures that have the shape of circular holes or rectangular trenches in the plane parallel to the electrode surface and a parabola-like cross-sectional shape (see Fig 5.1, Fig. 5.8 (a), (c), (d) and Fig. 5.3). It is directly visible from the exemplary pH maps in Fig. 5.8 (c) and (d) that the local pH value increases deeper inside the trench and hole and is higher in the hole compared to a trench with same dimensions (width/ diameter, depth and surface coverage). Fig. 5.10 shows a more quantitative analysis of the pH value averaged in the x-y plane as a function of z-position in and above a microcavity for a current density of -2.5 mA/cm^2. Analogous measurements were performed for -5 mA/cm^2 and -10 mA/cm^2 that exhibit similar trends at an overall higher pH. To obtain these graphs, an area within the microstructures is defined (signified by white rectangles in Fig. 5.8 (c) and (d) in the panels at 0 μm) and the pH is averaged over that entire area as a function of the z-position. Factors like a focus point shift, noise and pH probe mass-transfer limitations inside the features are taken into account as described in section 5.2. Fig. 5.10 (a) – (c) shows the average pH as a function of z-position in trenches and (d) – (f) in holes, for various geometric variations. In addition, the pH profile as a function of distance from a flat Cu GDE without any microcavities (compare Fig. 5.1 (b)) is displayed.

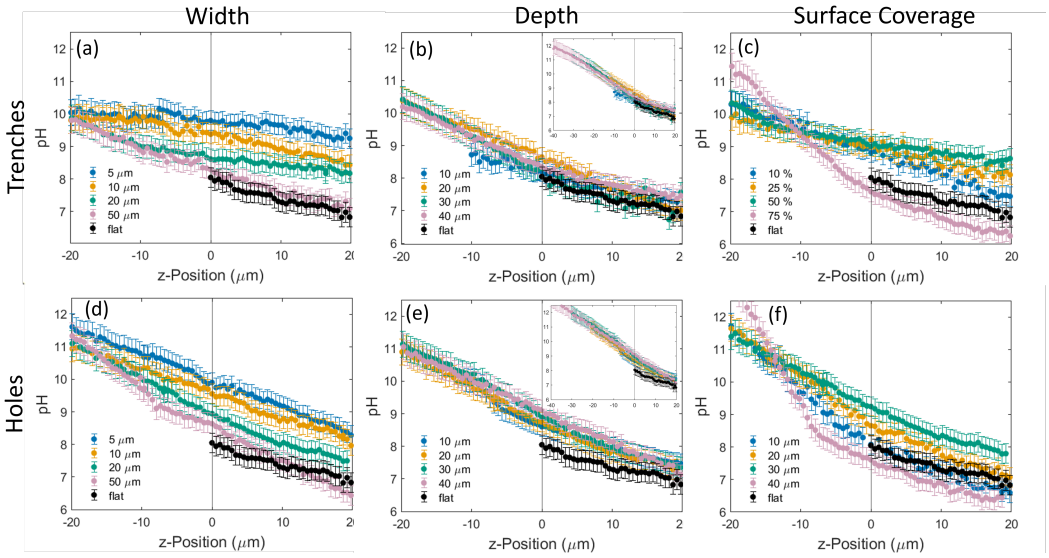

Figure 5.10: Local pH averaged over an area encompassing a trench or hole (see white rectangles in Fig. 5.8 (c) and (d)) vs. z-position (z = 0 μm signifies the GDE surface, negative z values are inside trenches or holes and positive z values above the GDE surface) for various geometry parameters at a current density of -2.5 mA/cm^2. (a) – (c) shows the average pH in and around trenches, (d) – (f) in and around holes. (a), (d) pH as a function or trench width/ hole diameter for constant depth (20 μm) and constant surface coverage (50%). (b), (e) pH as a function of depth for constant trench width/ hole diameter (20 μm) and surface coverage (50%). For better comparison with other panels, the z-position axis is extended to -20 µm while the insets show data up to -40 μm. (c), (f) pH as a function of surface coverage for constant trench width/ hole diameter (20 μm) and depth (20 μm). All panels include the pH profile for a flat GDE without patterns (black color).

We observe that the pH value increases as a function of the negative z-position for all geometry parameters considered. This can easily be explained by considering that the mass transport of OH^- is more limited deeper inside microstructures. Further, owing to the parabola-like cross-sectional shape of the structures, the average proximity of any point in the plane parallel to the electrode surface is closer to the catalyst deeper inside a structure (see Fig. 5.8 (a), (c) and (d)) and this proximity further increases the local pH value.

Comparing the pH value in holes to that in trenches, the local pH inside holes is significantly higher by up to one pH unit at the bottom of the features (compare top and bottom row in Fig. 5.10). We hypothesize that this can be connected to the four pH effects described above: electrolyte confinement, surface-to-volume ratio, CO_2 transport and proximity to the catalyst. OH^- gets more effectively trapped inside

holes compared to trenches due to the confinement in two dimensions rather than one. Further, the surface-to-volume ratio is higher for holes than for trenches. Fig. 5.11 displays the surface-to-volume ratio for both trenches and holes as a function of width/diameter and depth under the simplified assumption that the cross-section of trenches has a triangular shape and holes take the form of a cone. Under this assumption, the surface-to-volume ratio for holes is larger than that of trenches with same geometry parameters by a factor of 1.5. The increased surface area in holes can facilitate the CO_2 transport into the electrolyte in a hole where unreduced CO_2 can acidify the electrolyte. This is confirmed with simulations, see Fig. 5.14. However, the increased catalyst surface overpowers this phenomenon, leading to an overall higher pH in holes. Further, due to the different geometries of holes and trenches, a larger catalytic surface area is in the proximity of a certain point in a hole compared to a trench which is one main contributing factor for a high pH. Note that the effect of enhanced pH in holes is pronounced inside the features but less so on or above the GDE surface. This is again related to the stronger confinement of OH^- in holes. While this effect contributes to a higher pH inside holes compared to trenches, it also results in less OH^- diffusing out of holes to the GDE surface and hence explains the faster pH decline above holes compared to trenches.

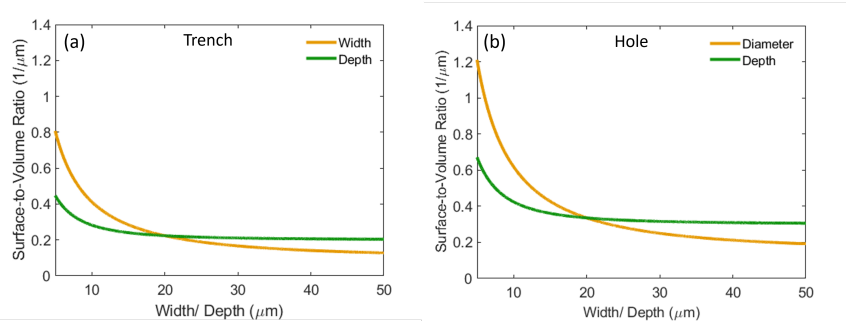

Figure 5.11: Surface-to-volume ratio as a function of (a) trench width (depth constant at 20 μm) and depth (width constant at 20 μm) and (b) hole diameter (depth constant at 20 μm) and depth (diameter constant at 20 μm). A trench is assumed to have a simplified triangular cross-sectional shape which allows to calculate the surface-to-volume ratio for a trench as $\frac{S}{V} = 4 \cdot \frac{\sqrt{d^2+\frac{w^2}{2}}}{d \cdot w}$ where d is the feature depth and w the width. A hole was simplified to a cone, which gives a surface-to-volume ratio of $\frac{S}{V} = 6 \cdot \frac{\sqrt{d^2+\frac{w^2}{2}}}{d \cdot w}$ with w the diameter. The surface-to-volume ratio inside a hole is higher than that in a trench by a factor of 1.5. Further, the surface-to-volume ratio is much more dependent on the trench width/ hole diameter than on the depth, particularly for depths between 10 μm and 40 μm that are considered in this study.

Fig. 5.10 (a) and (d) show the pH vs. z profile as a function of trench width and hole diameter. There is a clear trend towards higher pH for narrower trenches and holes. This is mainly caused by the confinement and trapping of OH^- in narrower features as well as the increasing surface-to-volume ratio with decreasing trench width and hole diameter, see Fig. 5.11. This result is in alignment with previous reports that studied the effect on trenches on CO_2R [77, 78] as well as reports that showed that smaller pores in structured electrochemical electrodes can enhance OH^- trapping and hence lead to an increased pH value [104, 112, 117, 130]. Interestingly, all curves seem to converge to the same pH value at the bottom of the feature. We think that this is caused by the cross-sectional shape of the features that resembles a parabola. No matter the width at the top of the feature, all geometries converge to a similar shape and catalyst proximity at the very bottom of the cavity. Note that for z > 0 μm, the pH profile of trenches or holes with a width/ diameter of 50 μm overlap with that of a flat, unpatterned GDE. This is a first indication that once a microcavity reaches or exceeds a size of 50 μm, its effect becomes minimal.

Fig. 5.10 (b) and (e) display the pH profiles for trenches and holes as a function of feature depth. For easier comparison with the other panels, the z-axis is only extended to -20 μm while the inserts show the pH curve up to -40 μm. Interestingly, when comparing the pH at the same z-position, the feature depth seems to have very little influence, both inside the cavity and above the surface. However, it must be noted that the pH value continues to grow as a function of depth of a microcavity, so even if the pH value at the same z-position is not influenced by how far the cavity continues below that position, a higher pH value is reached at the bottom of deeper structures. Again, this behavior can be explained with the pH effects described above. Considering the OH^- mass transport, the depth has little influence. While it becomes more and more limited the more negative the z-position is, at a certain depth within a cavity of the same shape, OH^- confinement is similar, no matter how far the structure continues below that z-position. Further, compared to the width or diameter of a cavity, the depth only marginally changes the surface-to-volume ratio especially in the range within which the depth is modulated in this study (10 μm – 40 μm), see Fig. 5.11. This explains why the width has a significant but the depth very little influence on the local pH within microstructures. Finally, the CO_2 availability must be considered. Deeper microcavities can limit the diffusion of CO_2 into the electrolyte per surface area unit. This is schematically depicted in Fig. 5.9 and confirmed by simulations (Fig. 5.14). Since excess CO_2 that is not reduced has the capability to acidify the electrolyte, the restricted CO_2 delivery in deep trenches

has the potential to lead to a higher observed pH value. On the other hand, due to the cross-sectional shape of trenches and holes, at a fixed depth, the average proximity to catalytic surfaces is higher in shallower trenches as schematically displayed in Fig. 5.12. This can potentially lead to a higher pH value in shallower trenches. The two opposing effects of CO_2 availability and catalyst proximity cancel each other out, leading to a local pH value that is independent of the trench depth.

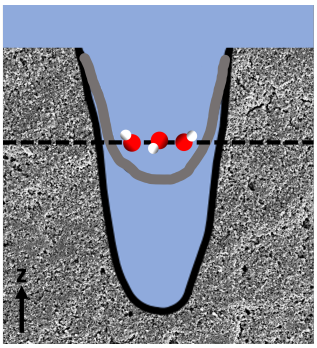

Figure 5.12: Schematic representation of the cross section through two trenches or holes with different depths. When considering the pH value at a certain z-position (indicated by the dashed line), more catalytic surfaces of the narrower trench (grey) are in the proximity than the catalytic surfaces of the deeper trench (black).

Finally, the influence of the surface coverage of microstructures is displayed in Fig. 5.10 (c) and (f). Considering surface coverages between 10% and 50%, there is a clear trend towards higher pH above the surface of the GDE with increasing surface coverage while inside the trenches, the pH value is only marginally influenced. This can easily be explained by the fact that the geometry of the trenches and holes themselves remains constant, so inside a cavity it is irrelevant how close the next feature is. Above the GDE surface, the pH decrease as a function of distance from the electrode surface is slower for higher surface coverages because the density of microcavities that serve as hotspots with enhanced pH is higher. However, the pH profile for a surface coverage of 75% does not follow this trend, neither in trenches nor in holes. Unexpectedly, the local pH for the 75% surface coverage curve is lower than for a coverage of 50% or less for z > -10 μm, below which the pH suddenly increases dramatically and surpasses the pH of the other curves. Note that similar trends can also be observed at current densities of -5 mA/cm^2 and -10 mA/cm^2. We attribute this unexpected behavior to two effects: Limited CO_2 transport as well as species crossover between features. As the surface coverage increases, the thickness of the walls between microcavities decreases, specifically close to the surface. This can allow the crossover of dissolved species. Fig. 5.13 shows SEM images of a

GDE sample with a trench coverage of 75%. Small cracks and faults through the thin trench walls are clearly visible. We believe that this causes severe flooding and crossover through the walls in the upper sections (z > -10 μm) of trenches and holes. The consequence is that for less negative z-positions, the microcavities lose their effect and the GDE behaves as though it were flat with severe surface roughness. This explains the very low pH for z > -10 μm. The thin separator walls not only allow crossover of dissolved species, they also limit the transportation of CO_2 through the GDE, schematically depicted in Fig. 5.9 (c) and confirmed by simulations, Fig. 5.14 (c) and (f). The diminished CO_2 availability is likely the reason for the enhanced pH at z < -10 μm deep within features with 75% surface coverage. It can also be an indicator that the CO_2 availability is so low that CO_2R becomes mass-transfer limited. We conclude that while a surface coverage as high as 50% is beneficial to sustain a high pH value above the GDE surface, microcavities loose its effect as soon as the surface coverage reaches 75% due to a combination of species crossover and limited CO_2 transport.

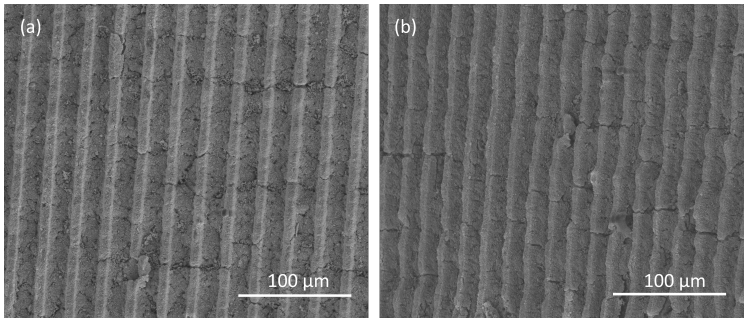

Figure 5.13: SEM images of a GDE with trenches with width 20 μm, depth 20 μm and surface coverage 75%, created with laser ablation, (a) in the plane parallel to the sample surface and (b) at an angle of 45°. Small cracks in the walls between the trenches are clearly visible.

We performed Multiphysics simulations to connect the measured pH value with the selectivity and to deconvolute the influence of different pH effects. In a first step, we aimed to gain an understanding of the influence the microcavity geometry has on the CO_2 transport through a GDE. To this end, we modelled the free CO_2 flow through a gas chamber at the backside of a GDE as well as the diffusion of CO_2 through a porous GDE domain with a regular pattern of microtrenches or microholes with a simplified triangular cross-section (Figs. 5.5 (a) - 5.7). We averaged the outward CO_2 flux through the GDE separately for the walls of trenches or holes as well as for the flat surfaces in between microcavities (see Fig. 5.5(a)). We found that

microcavities have a strong influence on the CO_2 transport through the GDE (Fig. 5.14). For both holes and trenches there is a trend towards higher CO_2 flux for increasing width/ diameter, decreasing depth and decreasing surface coverage. This can easily be explained with geometry considerations. If a larger GDE surface area is delivered through the same GDE volume, the CO_2 flux per surface area unit decreases, see Fig. 5.9. When comparing the CO_2 flux through the walls of microcavities to that through flat walls, there are opposing trends for trenches and holes with the flux being higher through hole walls. This can be explained considering that the surface-to-volume ratio is higher for holes than for trenches (Fig. 5.11) and holes therefore provide a larger surface area through which CO_2 can diffuse into the electrolyte. As a consequence, more CO_2 diffuses through hole walls compared to trench walls before it can reach the flat surface. Hence, there is a large CO_2 availability inside holes but limited availability at the flat catalytic surfaces between holes. For trenches on the other hand, the CO_2 availability at flat surfaces is even higher than on trench walls for most geometries.

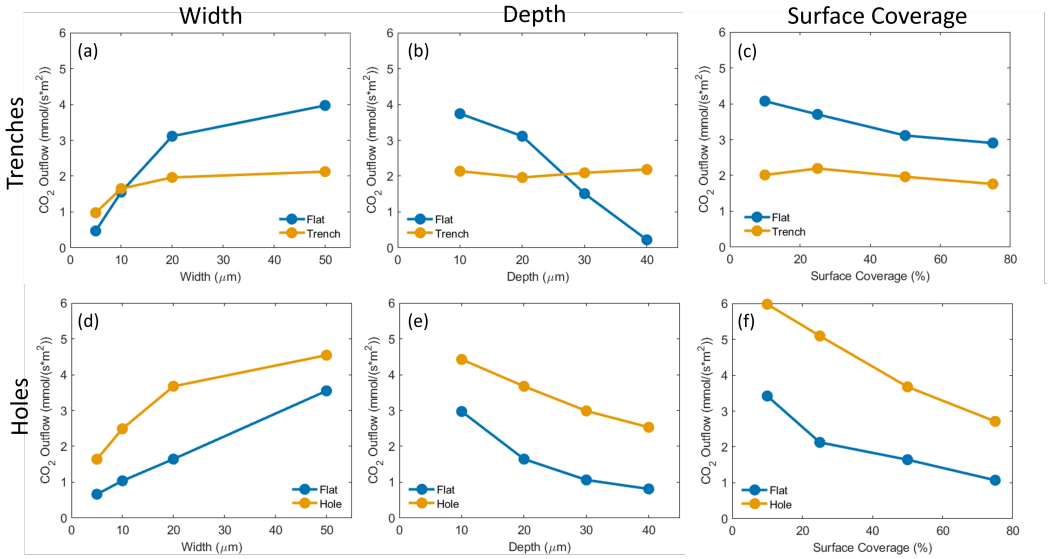

Figure 5.14: Simulated CO_2 outflow in mol/(s·m^2) through trench walls ((a) – (c)) or hole walls ((d) – (f)) as well as flat walls in between trenches or holes in a GDE for different microcavity geometries, see also Fig. 5.5 (a).

We used the CO_2 flow results (Fig. 5.14) as an input for a second Multiphysics model that simulates electrochemical CO_2R processes around a periodic trench in a GDE (see schematic in Fig. 5.5 (b)). Concentration-dependent Tafel kinetics were used to model the CO_2R performance for different potentials and microcavity geometries. We simulated a regular pattern of trenches with a simplified triangular cross-section

with varying width, depth and surface coverage, with the same geometry parameters as used in experiments (Table 5.2). Note that the aim of this model is not to exactly replicate the experimental data which is very challenging without precise knowledge of all input parameters; it is rather to confirm trends and gain an understanding of the mechanistic processes that govern the pH and the CO_2R performance for different microcavity geometries. Exemplary simulated pH maps for different potentials can be found in Fig. 5.15, confirming our prior observation that the pH is higher inside trenches and increases as a function of decreasing z-position. Fig. 5.16 shows exemplary simulated maps of the local CO_2 concentration for varying potential. At low overpotential, the CO_2 concentration close to the GDE surface is considerably higher than the equilibrium concentration of CO_2 in water due to the constant CO_2 flux from the GDE. Note that in reality, CO_2 would not reach such high concentrations but form gas bubbles, an effect that the model does not capture. At high overpotentials however, CO_2 is reduced at such rates that it is depleted at the cathode.

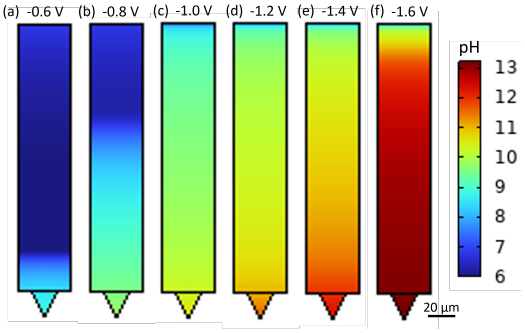

Figure 5.15: Simulated maps of the pH value over a periodic trench (20 μm wide, 20 μm deep and 50% surface coverage) in a CO_2R GDE at various potentials reported vs. SHE. The pH is higher inside trenches and increases with increasing potential.

Fig. 5.17 shows the simulated pH value as well as C_{2+} FE as a function of z-position inside a trench for various geometry parameters at a potential of -1 V vs. SHE. There is a very clear resemblance between the pH and the C_{2+} FE profiles, providing evidence that there is a distinctive relationship between high pH and high C_{2+} FE as has been reported previously [60–63, 78]. Most experimentally observed trends could be replicated in the simulations. We find that the pH, and with it the C_{2+} FE, increase as a function of decreasing z-position. The pH increases with decreasing trench width while inside a trench, the depth and surface coverage play a minor role. One discrepancy between the model and the experimental results is that for different trench widths, the pH value does not converge to a similar value

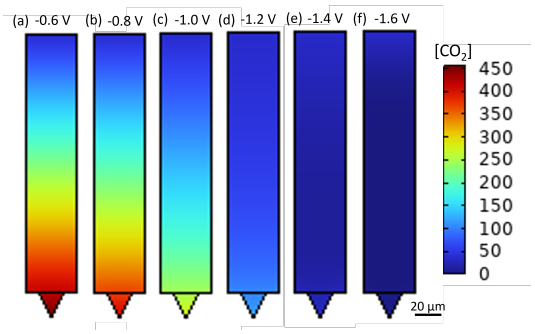

Figure 5.16: Simulated maps of the CO_2 concentration over a periodic trench (20 μm wide, 20 μm deep and 50% surface coverage) in a CO_2R GDE at at various potentials reported vs. SHE. The CO_2 concentration is set to 34 mM at the top boundary and a CO_2 inflow calculated with simulations (see Fig. 5.14) is assumed through the trench and flat GDE walls. This leads to excess CO_2 at low potentials but at high potentials, the CO_2 consumption is so high that it gets depleted despite the constant inflow.

at the bottom of trenches. We believe that the reason for this is that the model assumes a simplified triangular cross-section for a trench while the created trenches in GDEs exhibit a parabola-like shape. Parabolas converge to a similar outline at the bottom irrespective of the width which is not the case for triangles. A further simplification applied to the model is the assumption that the CO_2 flux through trench walls is a constant average irrespective of the z-position while it is expected that it is higher towards the bottom of trenches. This could be another contributing factor for the diverging curves in Fig. 5.17 (a). Further, the pH profile resembling a surface coverage of 75% deviates from the experimental observation since species-crossover is not captured by the model. We conclude that with the exception of the effect of simplifications applied to the model, it captures experimentally observed trends well. This confirms that the pH and with it, the C_{2+} FE, inside the trenches in a CO_2R GDE are governed by the effects of electrolyte confinement, surface-to-volume ratio, CO_2 transport and proximity to catalytic surfaces since these are captured by the model.

In a final step, we measured the product distribution of structured GDE samples with different geometries as displayed in Fig. 5.18. Results for width, depth or surface coverage set to zero correspond to a control experiment performed with a standard Cu on Sigracet 28 BC carbon paper GDE. Note that this is preliminary data. While gas chromatography only allows to measure bulk FEs, we can still draw conclusions about the local selectivity in microcavities since entire samples

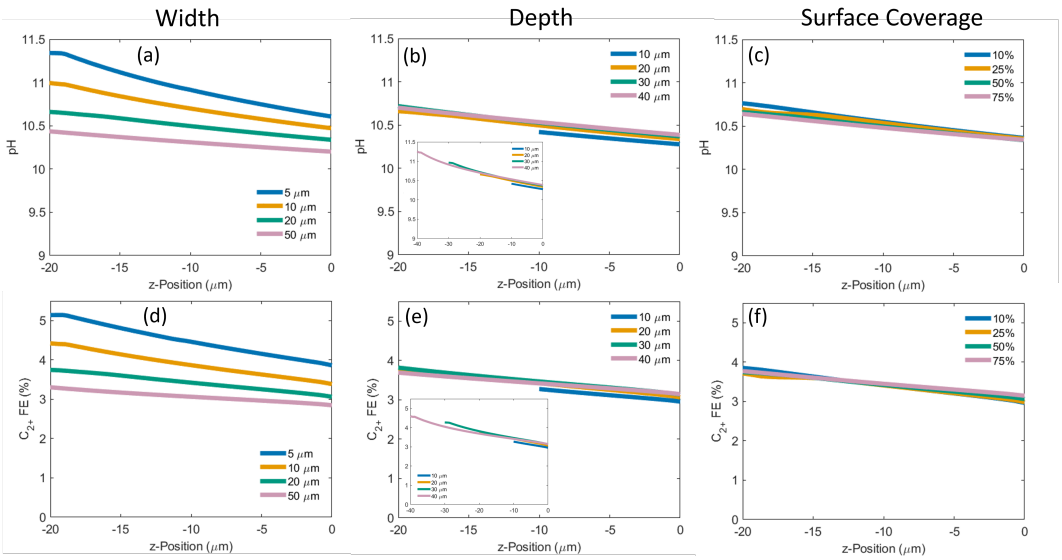

Figure 5.17: Simulation results of (a) – (c) the local pH value and (d) – (f) the local C_{2+} FE along trench walls inside trenches with varying geometry parameters at -1 V vs. SHE. (a), (d) pH and C_{2+} FE as a function of trench width for constant depth (20 μm) and constant surface coverage (50%). (b), (e) pH and C_{2+} FE as a function of depth for constant trench width (20 μm) and surface coverage (50%). (c), (f) pH and C_{2+} FE as a function of surface coverage for constant trench width (20 μm) and depth (20 μm). A clear correlation between pH and C_{2+} FE is immediately recognizable.

are covered with a regular, periodic pattern. The measurements were performed at a current density of -100 mA/cm^2 which is sufficient to observe significant amounts of the C_{2+} product ethylene. In analogy to pH measurements, we evaluated the CO_2R selectivity as a function of microcavity width/ diameter, depth and surface coverage for both trenches and holes while keeping all other geometry parameters constant. We expect that the C_{2+} FE is influenced by the microgeometry due to its strong correlation to pH. This is confirmed by our measurements; while the hydrogen, carbon monoxide, formate and methane FEs change only insignificantly as a function of geometry, the ethylene FE for a structured sample increases by up to 7% compared to a flat control GDE.

Fig. 5.19 separately shows the C_{2+} FE as a function of different geometry parameters for GDEs with holes and with trenches.

Comparing the FE towards ethylene in trenches (Fig. 5.18, top row) to that in holes (5.18, bottom row), the difference between the two is within the expected error (see also Fig. (5.19). This is unexpected since a higher pH was observed in holes

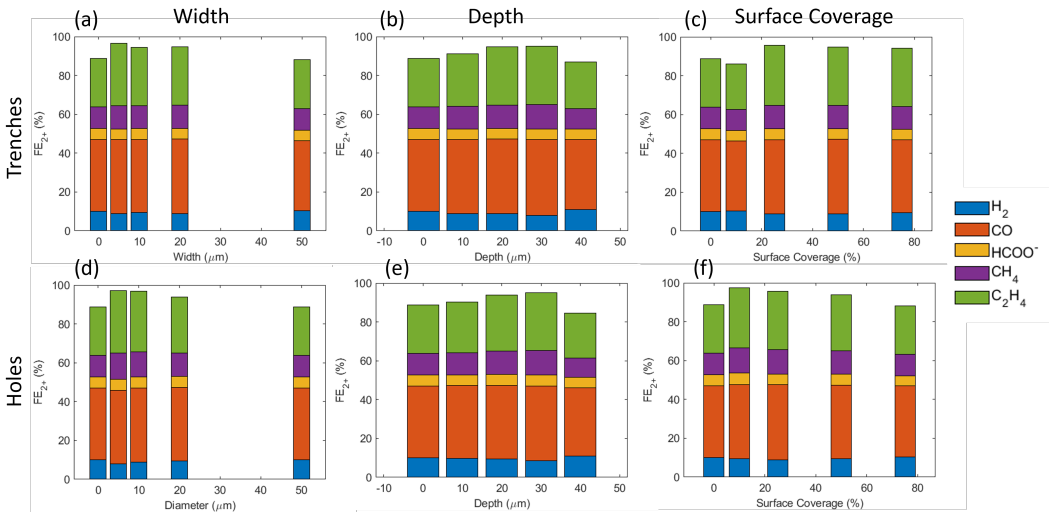

Figure 5.18: FEs at a current density of -100 mA/cm^2 determined with gas choromotography for GDE samples with regular patterns of (a) – (c) trenches and (d) – (f) holes. (a), (d) FEs as a function or trench width/ hole diameter for constant depth (20 μm) and constant surface coverage (50%). (b), (e) FEs as a function of depth for constant trench width/ hole diameter (20 μm) and surface coverage (50%). (c), (f) FEs as a function of surface coverage for constant trench width/ hole diameter (20 μm) and depth (20 μm). The data where the width, depth or surface coverage is 0 corresponds to a GDE without tailored microstructures. While the selectivity towards H_2, CO, $HCOO^-$ and CH_4 is only insignificantly influenced by a change of the microcavity geometry, the selectivity towards C_2H_4 changes with changing feature width, depth and surface coverage.

compared to trenches (Fig. 5.10) and due to the strong correlation between pH and C_{2+} FE (Fig. 5.17), a higher C_{2+} FE could be expected for samples with a regular hole pattern compared to a trench pattern. The deviation from this expectation can be explained by the limited transport of CO_2 through holes. Since holes have a higher surface area than trenches (Fig. 5.11), the majority of CO_2 molecules diffuse into the electrolyte through hole walls before reaching the planar surfaces between the holes (Fig. 5.14). Further, as explained above, OH^- is very strongly confined inside holes which leads to a steep pH decline above a GDE surface that is patterned with holes (Fig. 5.10 (d) – (f)). As a consequence, the CO_2 availability as well as the pH is very high deep inside holes which are ideal conditions for the reduction of CO_2 to ethylene. On the other hand, close to and on the surface of a GDE, the CO_2 availability is low (Fig. 5.14) which can lead to mass-transfer limitations and in addition, the pH is on the same order or even lower than at the surface of samples patterned with trenches. Hence, the C_{2+} FE is limited. We therefore hypothesize

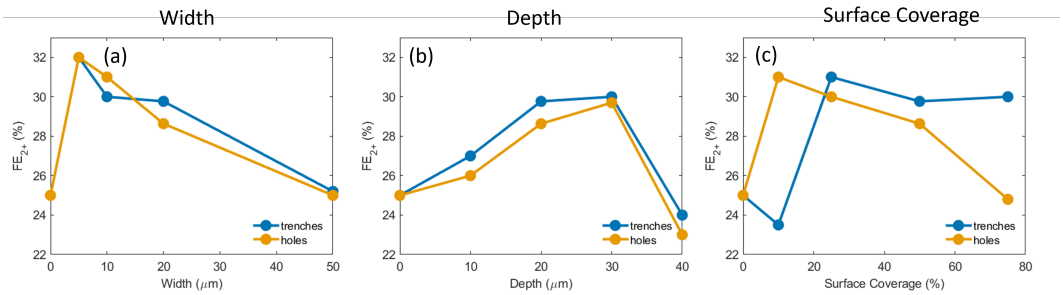

Figure 5.19: Measured bulk C_{2+} FE for samples with trenches (blue) and holes (orange) as a function of (a) trench width/ hole diameter, (b) trench depth/ hole depth and (c) surface coverage.

that there is a steep selectivity gradient in holes. The C_{2+} FE is higher deep within holes than in trenches. Close to the GDE surface however, it is lower which leads to an overall comparable C_{2+} FE for samples patterned with holes and with trenches.

We do find a clear trend of increasing C_{2+} FE as a function of decreasing trench width or hole diameter which goes hand in hand with an increasing pH (5.10). This is experimental proof that there are local variations in the product selectivity across the GDE surface with the highest C_{2+} selectivity inside narrow trenches or holes. Interestingly, the C_{2+} FE for a trench or hole with width/ diameter 50 μm is similar to that of a control GDE without intentional patterns. Together with the fact that the pH profile above the GDE surface for these samples overlaps with that of a flat control GDE (Fig. 5.10 (a), (d)), we can conclude that microcavities lose their ability to boost pH and selectivity once the size reaches or exceeds 50 μm.

Considering the depth, an increase in bulk C_{2+} FE can be observed as the cavity depth increases up to 30 μm. The behavior up to a depth of 30 μm can be connected to the pH profiles. While the pH at a certain z-position is not influenced by the feature depth (Fig. 5.10 (b), (e) and Fig. 5.17 (b)), the pH at the bottom of a cavity increases with increasing depth due to confinement. The increasing C_{2+} FE is therefore likely a local effect at the catalyst deep within cavities. However, once the depth reaches 40 μm, the C_{2+} FE suddenly drops for both trenches and holes. A plausible explanation is that the availability of CO_2 per surface area decreases with both trench and hole depth, especially at the flat surfaces in between microcavities (Fig. 5.14) and at a depth of 40 μm, a threshold is reached at which CO_2R becomes mass-transfer limited. Another explanation could be partial flooding of the GDE caused by the thinning of the microporous layer due to deep cavities. This effect is not captured by the simulations (Fig. 5.17 (e)), likely because a simplified constant

CO_2 inflow was assumed across the trench walls and because GDE flooding is not considered in the model.

Finally, there does not seem to be a clear trend for the C_{2+} FE as a function of surface coverage. Two opposing effects must be considered: The density of CO_2R hotspots with enhanced pH increases with increasing surface coverage but at the same time, high coverage can impede the effective CO_2 transport to catalytic surfaces (Fig. 5.14) and cause mass-transfer limitations. Further, for a surface coverage as high as 75%, we hypothesize that there is species crossover through the thin, cracked walls between trenches and holes (compare Fig. 5.10 (c), (f) and Fig. 5.13). As a consequence, a medium surface coverage between 25% and 50% seems to be most beneficial to boost the C_{2+} FE.

These results highlight the interplay between GDE micromorphology geometry, local pH and CO_2R selectivity and shed light on the underlying mechanisms that govern the CO_2R performance in geometric microcavities.

5.4 Conclusion

We investigated the mechanistic influence of tailored micromorphology patterns in a gas diffusion electrode on the CO_2R performance. We studied the influence of different microcavity geometries, including shape, width, depth and surface coverage with spatially resolved pH imaging, multiphysics simulations as well as product analysis. We found that, compared to a control GDE void of intentional patterns, the local pH as well as the ethylene FE in and around GDEs with tailored microstructures is enhanced. A clear correlation between high pH and high C_{2+} FE was found. We observed geometrical pH and selectivity effects that are caused by electrolyte confinement inside microcavities, the catalyst-surface-to-electrolyte-volume ratio, the CO_2 transport through a structured GDE and the proximity to catalytic surfaces. The CO_2R selectivity varies locally across a GDE surface with microcavities.

We found that while the pH is higher deep inside holes compared to trenches, it declines faster close to and above the GDE surface. Together with the low CO_2 availability at flat surfaces in between holes, this leads to a steep C_{2+} selectivity gradient and a similar bulk C_{2+} FE for samples with hole patterns and trench patterns. There is a clear trend of both increasing pH and increasing C_{2+} FE for decreasing trench width and hole diameter with the best results observed for widths/ diameters of 5-10 μm. Once the size reaches 50 μm, the microcavities loose their

capability to boost CO_2R. The pH at a certain z-position is independent of the feature depth, but the pH at the bottom of a microcavity decreases as a function of depth, leading to an enhancement in C_{2+} FE for a depth up to 30 μm. Once the depth exceeds 30 μm however, the CO_2 transport is impeded to an extend that CO_2R becomes mass-transfer limited and causes a decrease in C_{2+} FE. Considering the surface-coverage, there is a trade-off between the density of CO_2R hotspots inside cavities and CO_2 transport limitation as well as species crossover. As a result, a medium surface coverage of 25% - 50% is ideal.

Overall, we found that both trenches and holes can modestly boost the CO_2R selectivity towards ethylene with the strongest effect observed for features that are 5-10 μm wide, 30 μm deep and exhibit a surface coverage of 25% - 50%. Overall, we observe a strong correlation between a GDE's micromorphology geometry, the local pH value and the CO_2R selectivity.

Chapter 6

LOCAL MICROENVIRONMENT TUNING INDUCES SWITCHING BETWEEN ELECTROCHEMICAL CO_2 REDUCTION PATHWAYS

Contents drawn from: A. E. Böhme*, S. B. Dolmanan*, Z. Fan*, A. J. King, A. Q. Fenwick, A. D. Handoko, W. R. Leow, A. Z. Weber, X. Ma, E. Khoo, H. A. Atwater, and Y. Lum. "Local Microenvironment Tuning Induces Switching between Electrochemical CO_2 Reduction Pathways". In: *J. Mater. Chem.* A 11 (2023), pp. 13493–13501. doi: https://doi.org/10.1039/D3TA02558F. *These authors contributed equally to this work.

A.E.B. designed, performed and analyzed all pH imaging and confocal microscopy experiments.

6.1 Introduction

Chapters 2 – 5 focused on the influence of a GDE's micrometer-scale micromorphology, specifically trenches and holes, on the CO_2R performance. Here, we turn our attention to a different GDE parameter that influences the microenvironment: the gas diffusion layers's (GDL) pore size. In the previous chapters, carbon paper was predominantly used as the GDL because it is commercially available, cheap and exhibits good electrical conductivity [135]. Further, it exhibits a random pattern of trenches that allow to study the influence of microcavities on the CO_2R performance, see Chapters 2 and 4. Another common GDL substrate is woven polytetrafluoroethylene (PTFE) or Teflon, a synthetic fluoropolymer. It lacks electrical conductivity and therefore requires the application of a conductive coating. However, it is considerably more stable under operando CO_2R conditions than carbon paper [61, 107]. Further, it is also commercially available. Important for this work is that PTFE GDL membranes are available with various different pore sizes [138]. This allows to tune the microenvironment around GDEs via the GDL pore size. Both silver and copper are used as catalyst materials. A more detailed explanation of GDEs and the influence of different catalyst materials can be found in sections 1.2.3 and 1.2.2. The confocal laser-scanning microscopy imaging technique that

has been developed in this work is ideally suited to investigate the interplay between GDL pore size, local pH value and CO_2R performance.

Although the mass transport of CO_2 through the GDL should in principle be rapid, it is known that its effective diffusion coefficient is related to the porosity and average pore radius of the porous medium through the Bruggeman relationship [35]. We therefore reasoned that tuning these parameters could be used to influence the mass transport of CO_2, which directly impacts the catalyst microenvironment (local pH and CO_2 reactant supply). This is because CO_2 molecules can directly react with and hence neutralize electrochemically generated OH^- to form bicarbonate and carbonate anions [36, 136], see also Chapter 1.3.1. The altered microenvironment could in turn result in a significant change in catalytic outcomes: an additional experimental knob to control CO_2R selectivity beyond catalyst design and choice of electrolyte. In this work, we demonstrate this concept using sputtered Ag films onto hydrophobic PTFE substrates with 6 different pore sizes as the GDL [53, 61] (Fig. 6.1).

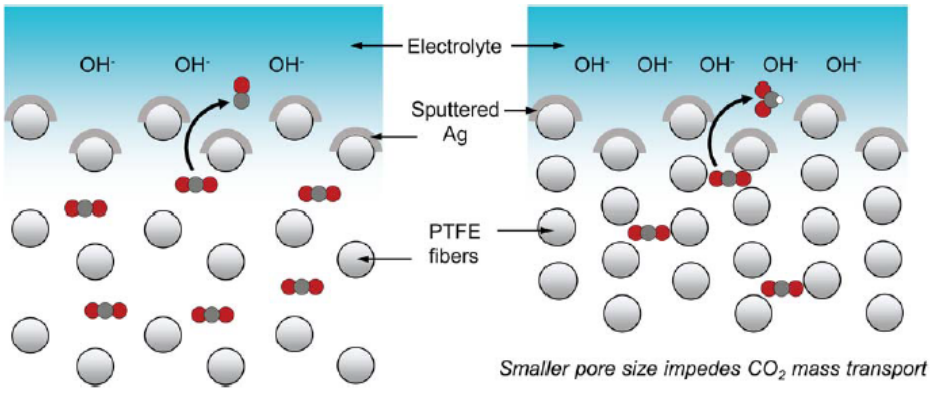

Figure 6.1: Schematic of GDLs with different pore sizes. CO_2 mass transport through the gas diffusion layer is slower with a smaller GDL pore size. This results in a higher local pH, which then induces a higher selectivity towards formate. Note: items in the schematic are not drawn to scale.

Even though Ag is well known to predominantly produce CO [48, 139–142], we find that smaller PTFE pore sizes favor formate production up to a FE of 43 %. Combined experimental and simulation results show that a decrease in GDL pore size slows down CO_2 mass transport, leading to a higher local pH and hence reaction pathway switching from CO to formate. This is in agreement with the results presented in Chapter 3. The pH trend was confirmed using a confocal microscopy setup [77, 78] equipped with a custom-built electrochemical cell and the pH sensitive fluorescent

dye APTS in the electrolyte. Our results highlight the importance of the properties of the GDL, which can significantly impact the catalyst local microenvironment and should be an important consideration for the design of CO_2R systems.

6.2 Methods

Sample Fabrication and Characterization

Hydrophobic PTFE substrates of various pore sizes were obtained from Beijing Zhongxingweiye Instrument Co. Ltd. Samples were fabricated by sputter deposition of 325 nm Ag or Cu onto PTFE substrates of various pore sizes, using a DC sputtering system (Denton Discovery D18).

XRD analysis of Ag/PTFE samples was carried out with a Bruker D8 Discover diffractometer. Catalyst morphology was studied using scanning electron microscopy (SEM) using a JEOL 7600F. For cross-section SEM images, focus ion beam (FIB) scanning electron microscopy (FEI Helios NanoLab 450) was used. The sample is milled down slowly, moving deeper into the depth of the sample until the desired SEM cross-section is achieved.

Electrocatalytic Characterization

The Ag/PTFE samples were tested in a custom designed electrochemical flow cell system (Fig. 6.2), with an active area of 1 cm^2 (cathode).

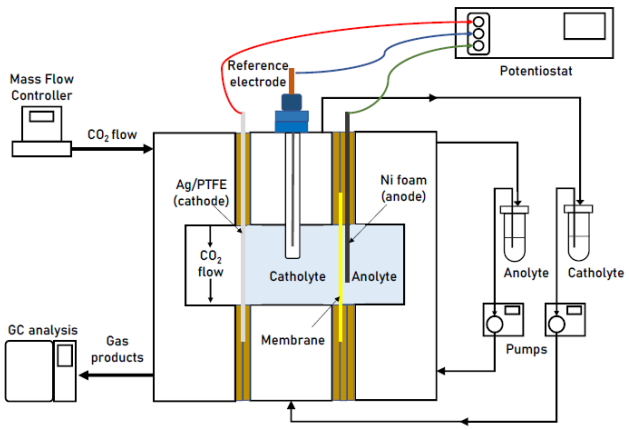

Figure 6.2: Schematic of the experimental setup used to perform electrochemical CO_2 reduction. A flow type system is employed, with the catholyte and anolyte continuously recirculated through the cell from an external reservoir using peristaltic pumps. Gas products are analyzed using a gas chromatograph and formate is analyzed using liquid chromatography. Note: items in the schematic are not drawn to scale.

In the flow cell, Ni foam was used as the counter electrode (anode) and an anion exchange membrane was used to separate the cathode and anode chambers. Ag/AgCl (3M KCl) was used as the reference electrode. Aqueous $KHCO_3$ solution of varying concentrations was employed as the electrolyte used for both the catholyte and anolyte. The electrolyte was stored in external centrifuge tube reservoirs and continuously recirculated through the electrochemical cell using peristaltic pumps. CO_2 was supplied at a flow rate of 20 sccm using a mass flow controller (Alicat Scientific) to the backside of the Ag/PTFE gas diffusion electrode. The effluent CO_2 exiting the cell was directly connected to an online gas chromatography (GC) system (Shimadzu Nexis GC-2030), for analysis of gas products. At the end of the experiment, the formate in both the catholyte and anolyte were analyzed using high-performance liquid chromatography (Shimadzu LC-2030C NT).

Double layer capacitance measurements were performed in the same electrochemical cell. Aqueous 1 M $KHCO_3$ was employed as the electrolyte and cyclic voltammetry was carried out in a potential window where faradaic processes do not take place. This was carried out under various scan rates of 80, 60, 40 and 20 mV/s. The capacitance current density was plotted vs scan rate and the slope of this graph gives the double layer capacitance. This value is directly proportional to the electrochemically active surface area (ECSA) [143].

pH Imaging Experiments

Confocal microscopy experiments similar to the ones described in the previous Chapters 2 – 5 were performed with a Zeiss LSM 880 confocal microscope (Fig. 6.3).

A WN Achroplan 63x water immersion objective with a working distance of 1.7 mm was used. A customized electrochemical cell was designed and 3D-printed to be compatible with confocal microscopy and a water immersion objective (Fig. 6.11 (a), analogous to the cell described in Chapter 3). The cell is oriented horizontally and operates without an ion exchange membrane. A rubber gasket between the gas chamber and electrolyte chamber seals the cell. The flow rate of the CO_2 gas stream through the gas chamber was adjusted to 10 sccm. The electrolyte chamber exhibits two perpendicular inlet and outlet tubes. Electrolyte is recirculated through the electrochemical cell at a flow rate of 6 mL/min. The active surface area of the working electrode is 0.2 cm^2. A leakless Ag/AgCl reference electrode and a Pt mesh counter electrode are both immersed into the electrolyte. 200 μM APTS was

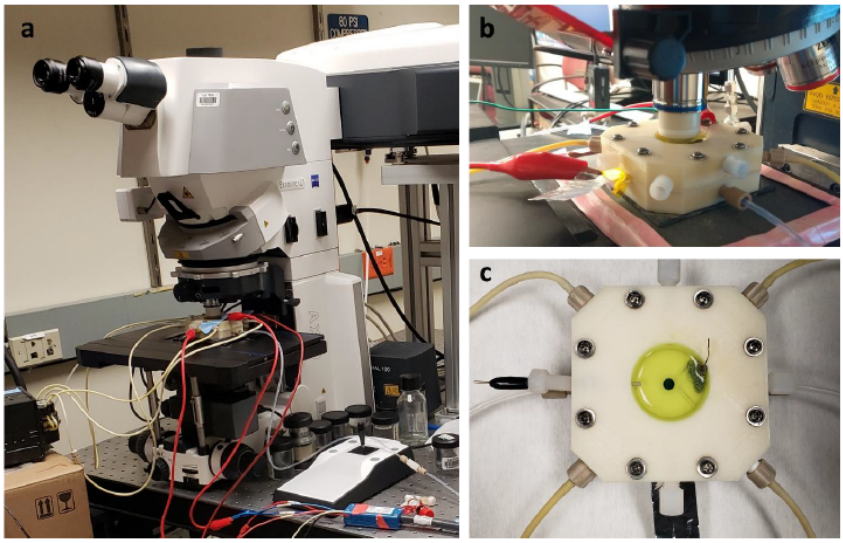

Figure 6.3: Photographs of the confocal microscopy setup used to map the local pH value. (a) Zeiss LSM 880 confocal microscope with a 63x water immersion objective and an electrochemical flow cell. (b) Close-up image of the electrochemical cell. (c) Top view of the electrochemical cell, filled with APTS-spiked electrolyte.

dissolved in aqueous 1 M $KHCO_3$ electrolyte and filled into the electrolyte chamber. A 458 nm laser scans the sample and excites the fluorescent APTS dye molecules. The laser power is set to 100 %, the pinhole to 57.1 μm and the gain to 800. The emission is collected separately in the wavelength intervals 480 – 550 nm and 551 – 754 nm. The ratio between the two signals collected is a measure of the local pH value. The pH value can be calculated with a previously determined sigmoidal calibration curve:

$$\mathrm{pH} = \frac{1}{2.743} \ln\left(-1 + \frac{5.005}{(\text{Ratio of Emission})_{\mathrm{APTS}} - 0.1041}\right) - 11.95. \tag{6.1}$$

More details about the calibration of APTS can be found in Chapter 3.2. Before each experiment, a potentiostatic electrochemical impedance spectroscopy (PEIS) was performed with a Biologic SP-200 potentiostat to determine the solution resistance of the cell. A constant current was then applied with the potentiostat while performing an automatic 85 % IR electronic compensation of the electrochemical potential. The system was allowed to equilibrate for 15 seconds before taking fluorescence measurements. The laser beam scanned the electrolyte in the vicinity of the electrode in the plane perpendicular to the electrode surface by scanning the laser line by line and moving the stage in the z-direction in 0.5 μm increments. The

first line was placed a few micrometers below the electrode surface. The dimensions of the resulting map are 120 μm in x and 50 μm in z. The measuring speed was adjusted so that capturing one frame takes approximately 30 seconds. In between measurements, the electrolyte was removed from the electrochemical cell and replaced with electrolyte containing fresh APTS. Each measurement was performed at least six times.

Multiphysics Simulations

The model employed was previously reported by Weng et al. and full details can be found in the corresponding publication [35]. The simulations were implemented using the COMSOL Multiphysics software. The model is a stationary, isothermal and 1D axisymmetric model for the cathodic compartment of the cell, which contains the nanoparticle Ag catalyst layer and diffusion medium. CO formation and the hydrogen evolution reaction are the two electrochemical reactions focused on. Triangular meshes were applied. The governing equation is the mass balance, the conservation of mass is implemented with the Nernst-Planck equation. The reaction rate is composed of the electrochemical reaction, CO_2 dissolution and homogeneous bulk reactions. The current density of each reaction is calculated with Butler-Volmer type kinetics. For electrochemical reactions, the process is governed by charge conservation and Ohm's law. The Bruggeman relationship is applied to obtain the effective electrical conductivity as the diffusion medium is porous. The dissolution rate of CO_2 is obtained by Fick's law. The homogeneous buffering reactions are mainly carbonate and water dissociation reactions. For the purposes of this work, the porosity values of the diffusion media and catalyst layer were set to be identical to each other and varied across the values of 0.4, 0.5, 0.6, 0.7 and 0.8. The CO_2 concentration and pH profile were determined for each porosity value, at cathodic current densities of -100, -200, -300, -400 and -500 mA/cm^2.

6.3 Results and Discussion

6.3.1 Simulation Results

To lend support to our hypothesis, we fist turned to multiphysics simulations [35] to understand the impact of the GDL porosity on the local pH of the electrode during CO_2R. In our simulations, we varied the porosity values from 0.4 to 0.8 and obtained the steady-state results through a series of applied current densities. Fig. 6.4 shows the simulation results, and we observed a qualitative trend of lower pH and higher CO_2 concentration as the porosity of the diffusion medium increases.

This is consistent with the notion that a lower porosity can indeed impede CO_2 mass transport, hence resulting in changes in the reaction microenvironment of the catalyst.

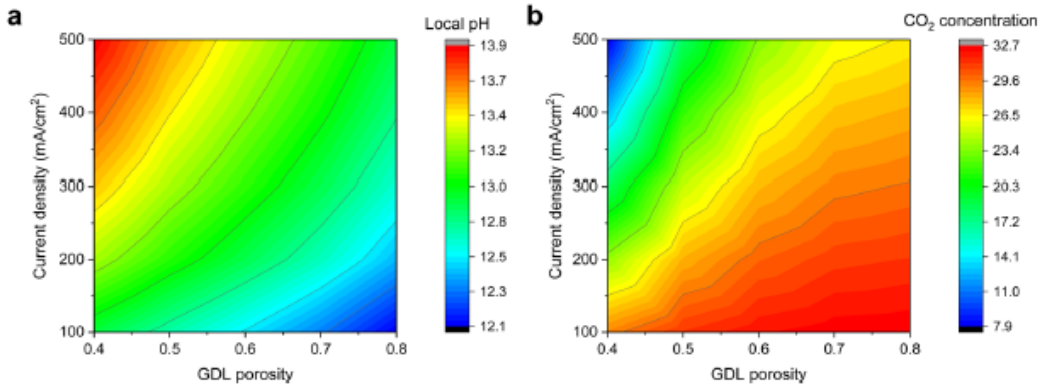

Figure 6.4: Multiphysics simulation results of varying GDL porosity on the (a) local pH and (b) CO_2 concentration at various cathodic current densities of -100, -200, -300, -400 and -500 mA/cm^2. A lower porosity is observed to result in a higher local pH and lower CO_2 concentration.

6.3.2 Electrocatalytic Analysis

Encouraged by these results, we began by sputtering 325 nm thick Ag films onto hydrophobic PTFE [53, 61] substrates with different pore sizes of 0.02, 0.1, 0.22, 0.45, 1.0 and 3.0 μm for use as gas diffusion electrodes. Each electrode will hence be termed as Ag/PTFE(X), where X is the pore size. Top-down scanning electron microscopy (SEM) images show the structure of these electrodes, with a web-like morphology of interconnected PTFE fibers coated conformally with Ag (Fig. 6.5).

These SEM images reveal the 3D network of macro-scale pores that are inherently formed between the fibers, serving as pathways for reactant and product transport. Cross-sectional SEM images can be found in Fig. 6.6. As would be expected, the PTFE substrates with larger pore sizes appear visibly more open and less dense.

X-ray diffraction (XRD) characterization of the electrodes was performed (Fig. 6.7 (a)), with Ag (111) observed as the dominant crystal facet and with no obvious differences between each of the Ag/PTFE with various GDL pore sizes.

We also carried out cyclic voltammetry in a potential range where only non-faradaic processes occur to determine the double layer capacitance of each Ag/PTFE electrode. This gives an indication of the electrochemically active surface area (ECSA) since this value is directly proportional to the double layer capacitance [143]. The

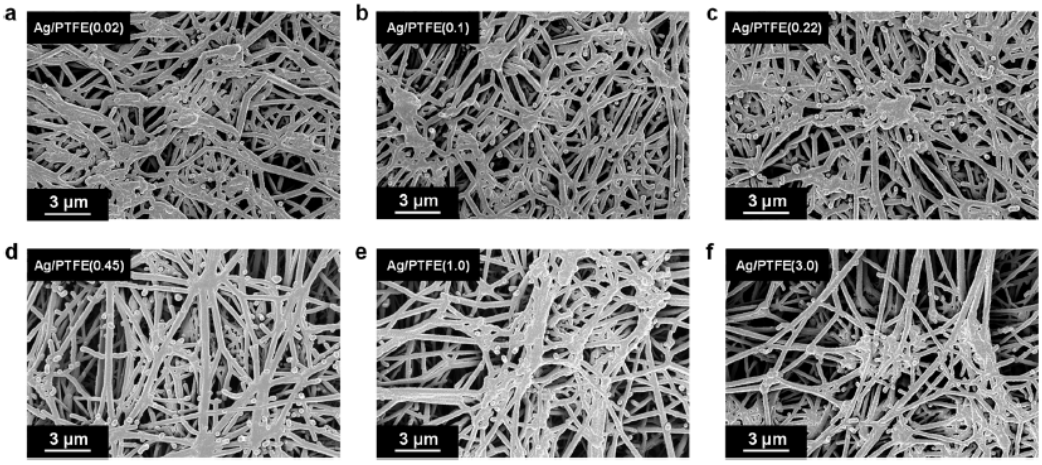

Figure 6.5: SEM images of hydrophobic PTFE substrates of various pore sizes coated with 325 nm of Ag using sputter deposition. The pore sizes are: (a) 0.02 μm, (b) 0.1 μm, (c) 0.22 μm, (d) 0.45 μm, (e) 1.0 μm and (f) 3.0 μm. Cross-section SEM images of the samples can be found in Fig. 6.6.

results show that despite pore size differences, the double layer capacitance and hence ECSA remains approximately within the same order of magnitude.

We then designed experiments to obtain a qualitative measure of the CO_2 mass transport for the different pore size Ag/PTFE electrodes. Each electrode was assembled into a gas diffusion flow cell system (Fig. 6.2), with a similar design to what was previously reported in the literature [61, 144]. 15 ml of aqueous 1 M KOH was used as the electrolyte, which was continuously recirculated between the cathode chamber and an external centrifuge tube reservoir using a peristaltic pump. CO_2 was flowed at a rate of 20 sccm, through a gas chamber in contact with the backside of Ag/PTFE. Without applying any current, we monitored the bulk pH of the electrolyte over a 120 min period by placing a pH probe into the external centrifuge tube reservoir. The results in Fig. 6.7 (b) show that the bulk pH decreases significantly with time, as a result of the CO_2 gas continuously diffusing from the backside of the Ag/PTFE and reacting with hydroxide in the electrolyte to form carbonate [136]. We also observe that the bulk pH decreases more rapidly with increasing PTFE pore size. Importantly, this allows us to experimentally confirm that larger pore sizes do indeed facilitate faster CO_2 mass transport. These results are in agreement with local pH imaging experiments to monitor the CO_2 diffusion through GDEs that are presented in chapter 3.

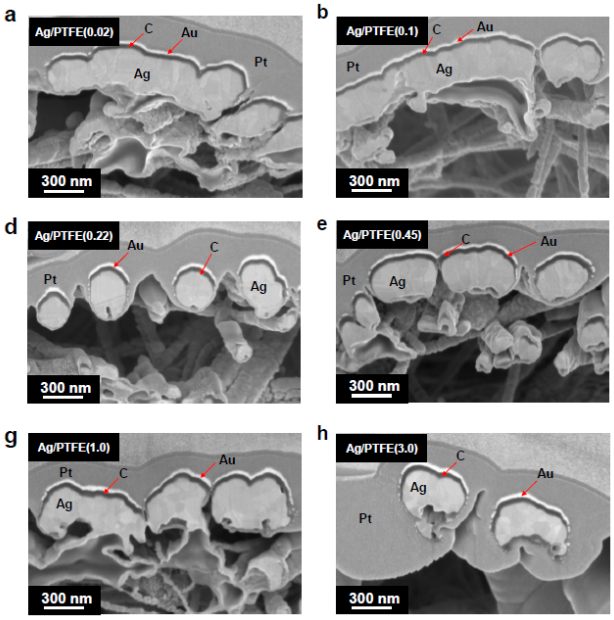

Figure 6.6: Cross-section SEM images of (a) Ag/PTFE(0.02), (b) Ag/PTFE(0.1), (c) Ag/PTFE(0.22), (d) Ag/PTFE(0.45), (e) Ag/PTFE(1.0) and (f) Ag/PTFE(3.0).

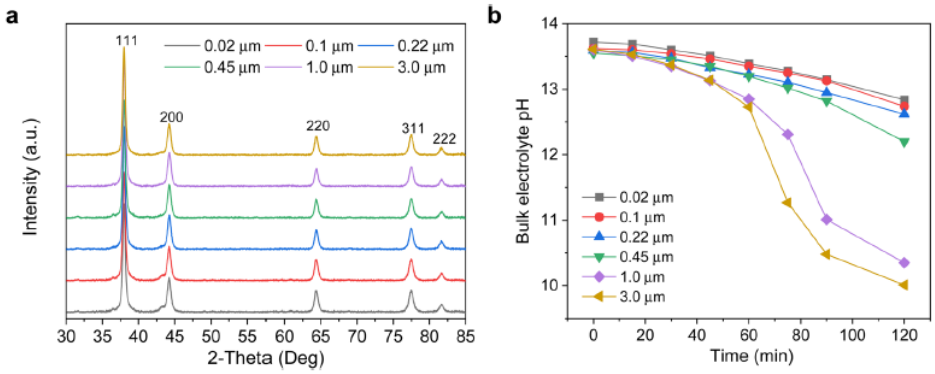

Figure 6.7: XRD spectra and evolution of the bulk pH. (a) XRD spectra of Ag sputtered onto PTFE substrates with various pore sizes. (b) Evolution of the bulk electrolyte pH over a 120 min period, with no current applied to the system. 15 ml of aqueous 1 M KOH was used as the electrolyte and was continuously recirculated through the electrochemical cell using a peristaltic pump.

Next, we sought to assess the influence of the PTFE pore size on the product selectivity of the Ag/PTFE catalysts. Using the same flow cell system, we evaluated each Ag/PTFE under cathodic current densities of 100, 200 and 300 mA/cm^2 in 1 M $KHCO_3$ electrolyte. The FE data are shown in Fig. 6.8 (a) – (c). Based on the results, we observe that the formate FE appears to increase with decreasing pore size, from 24 % for Ag/PTFE(3.0) up to a value of 43 % for Ag/PTFE(0.02) at 200

mA/cm^2. For better visualization, the formate FE is also presented as a contour plot (Fig. 6.8 (d)), where the general trend of higher formate FE with smaller pore sizes is observed to hold true for all tested current densities. Also, the H_2 FE tends to increase with larger pore size. These combined effects result in the CO FE initially increasing with pore size and then decreasing again, with a peak value of around 80 % at 100 mA/cm^2 for Ag/PTFE(1.0).

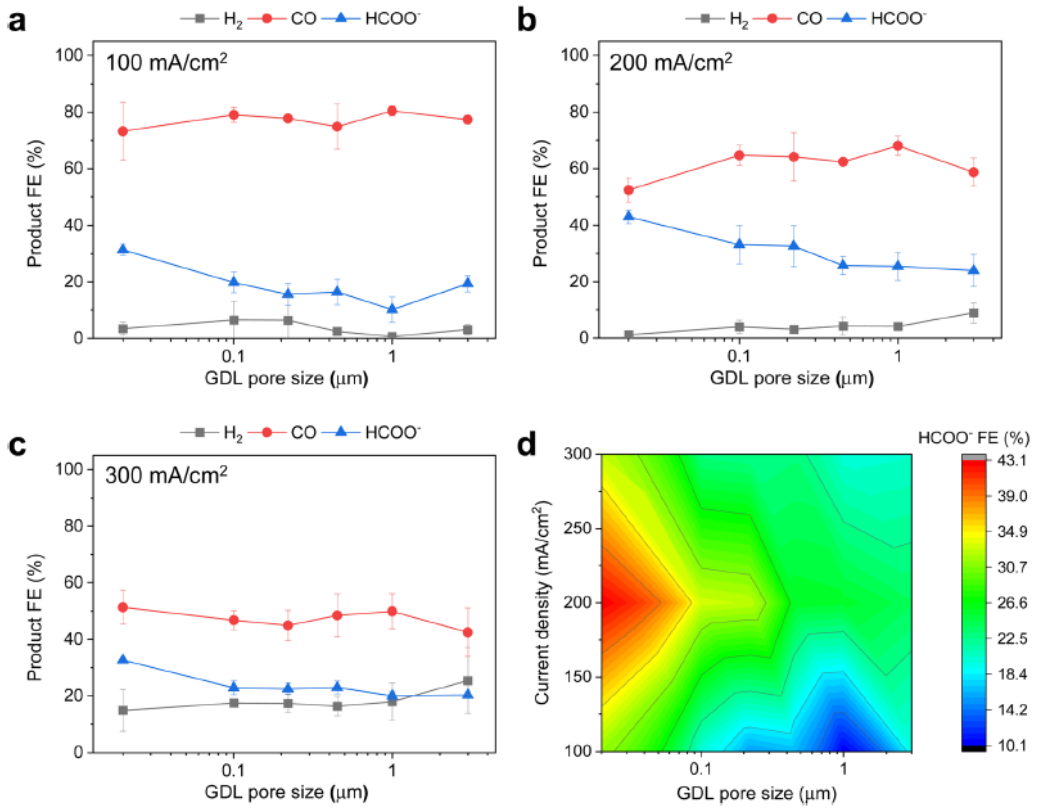

Figure 6.8: Electrochemical CO_2R FE results with 1 M $KHCO_3$ as the electrolyte. (a), (b) and (c) show the product FE data for Ag/PTFE as a function of GDL pore size under cathodic current densities of 100, 200 and 300 mA/cm^2, respectively. (d) is the corresponding color contour map of the $HCOO^-$ FE data for Ag/PTFE as a function of current density and GDL pore size.

Based on the bulk pH monitoring and simulation results, we hypothesized that this could be due to reduced CO_2 mass transport at the smaller pore sizes, resulting in a higher local pH and, thus, switching selectivity towards formate. This selectivity switching was previously observed by Seifitokaldani et al., where CO_2R was performed with Ag catalysts in KOH electrolyte [145] with concentrations ranging from 0.1 M to 11 M. It was found that formate was produced with almost 60 % FE in 11 M KOH, compared to only about 4 % in 0.1 M KOH. Using DFT simulations, they

concluded that this was due to the activation energy barrier for formate becoming lower than that compared to CO, in the absence of hydronium ions.

Hence, we employed a suite of experiments to further understand these initial observations and verify our working hypothesis. First, we tested the Ag/PTFE catalysts in 2 M aqueous $KHCO_3$, which has a stronger pH buffering ability as compared to 1 M $KHCO_3$ [146]. In this case, we did not observe any significant differences in the formate FE as a function of GDL pore size (Fig. 6.9 (a) and (b)) at cathodic current densities of 100 and 200 mA/cm^2. This suggests that the stronger buffer results in a similar local pH value for each of these cases, leading to a similar formate FE of around 14 %. However, at the higher current density of 300 mA/cm^2, the trend of higher formate FE with smaller pore size appears again (Fig. 6.9 (c)), with a FE of 19 % for Ag/PTFE(3.0) as compared to a FE of 29 % for Ag/PTFE(0.02). This results from the expected higher local pH rise with a larger current density and is therefore consistent with the notion that pH effects are indeed influencing the observed FE to formate.

To further investigate the effect of buffering, similar CO_2R experiments were carried out with additional buffer conditions of 0.5 M and 1.5 M $KHCO_3$ at 300 mA/cm^2 for each pore size condition. The results for Ag/PTFE(0.22) are represented in Fig. 6.10 (a), where a trend of higher formate FE with lower buffer concentration is observed. This is because lower buffer concentrations result in a higher local pH [146], which then promotes the conversion of CO_2 to formate. Formate FE for all Ag/PTFE samples under the different buffer conditions are shown as a colour contour map (Fig. 6.10 (b)), where the trend of higher formate FE with a lower buffer concentration is observed to hold true for all GDL pore sizes.

We also carried out CO_2R electrolysis experiments where the CO_2 feed was diluted with N_2. For a lower CO_2 partial pressure, we expect the local pH to be higher due to fewer available CO_2 to react with electrochemically formed OH^-. For these experiments, Ag/PTFE(0.45) was used as the electrode and a constant current density of 300 mA/cm^2 was applied. From the results (Fig. 6.10 (b) and (c)), we observe that lower CO_2 partial pressures do indeed result in a higher formate to CO ratio, consistent with our working hypothesis.

Furthermore, we also conducted in situ measurements using confocal microscopy with a pH sensitive fluorescent dye to provide experimental verification of the local pH trends as a function of GDL pore size and applied current density. Fluorescent confocal laser scanning microscopy enables imaging of the local pH in three spatial

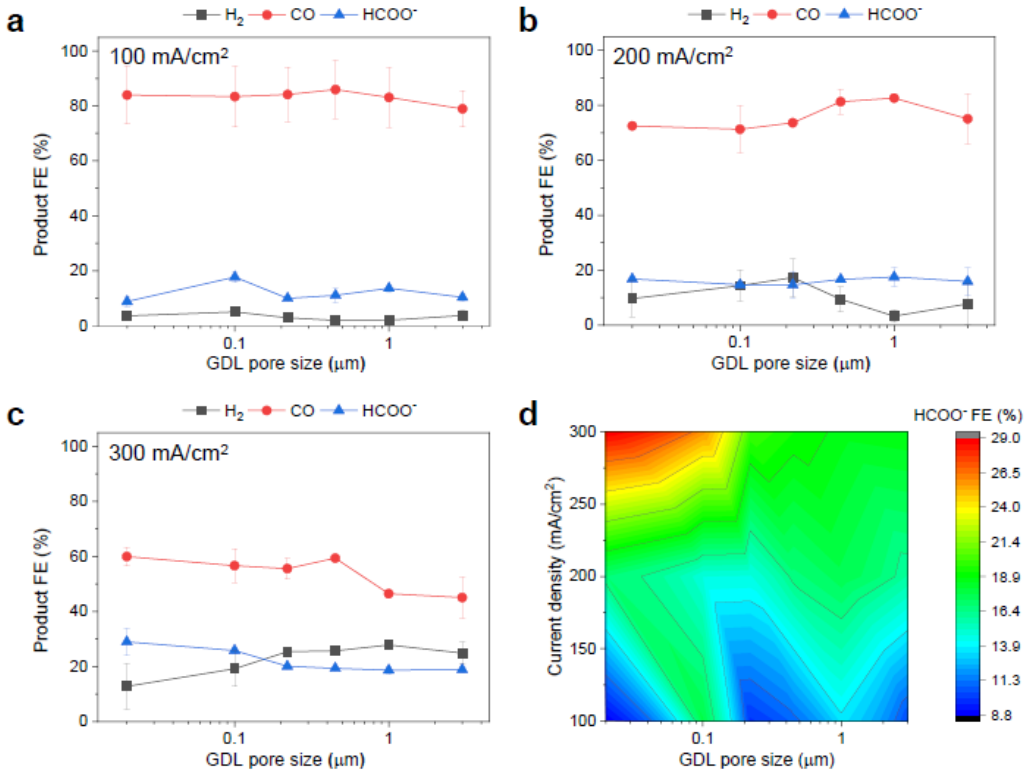

Figure 6.9: Electrochemical CO_2 reduction FE results with 2 M $KHCO_3$ as the electrolyte. (a), (b) and (c) show the product FE data for Ag/PTFE as a function of GDL pore size under cathodic current densities of 100, 200 and 300 mA/cm^2, respectively. (d) is the corresponding color contour map of the $HCOO^-$ FE data for Ag/PTFE as a function of current density and GDL pore size.

dimensions with a resolution of one micrometer under operating conditions [77, 78]. Such experiments were carried out using a custom-built electrochemical cell (Fig. 6.3 and Fig. 6.11 (a)), consisting of a gas chamber for CO_2 flow and an electrolyte chamber that is stacked above it. The electrolyte chamber is open at the top, which allows for a water immersion objective to be dipped into the electrolyte, in close proximity to the electrode surface.

We studied the local pH in the vicinity of the Ag/PTFE electrodes with the ratiometric fluorescent dye APTS, which is descibed in more detail in chapter 1.5.1. Measurements for all cases were performed using aqueous 1 M $KHCO_3$ electrolyte with 200 mM APTS, which was constantly circulated through the electrochemical cell. The pH was mapped for a series of current densities between -20 mA/cm^2 and -200 mA/cm^2, in the plane perpendicular to the electrode surface, starting from a few micrometers below the electrode surface. The dimensions of each pH map are

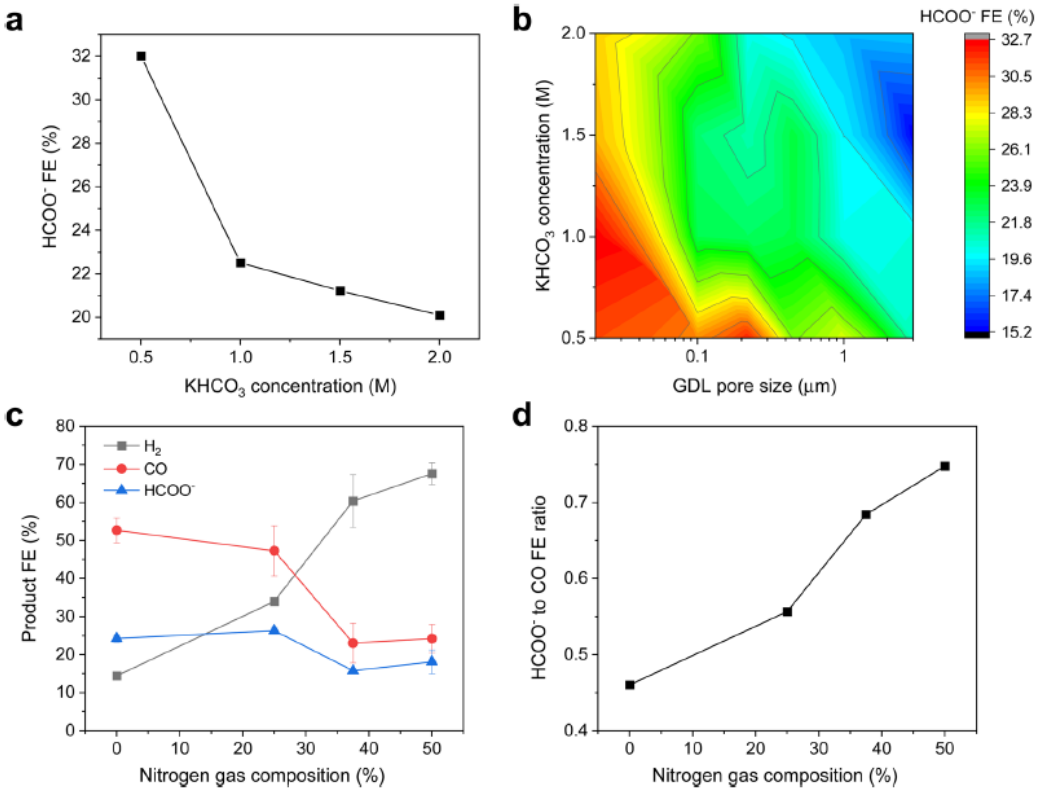

Figure 6.10: $HCOO^-$ FE as a function of $KHCO_3$ concentration, GDL pore size and gas composition. (a) $HCOO^-$ FE data for Ag/PTFE(0.22) as a function of $KHCO_3$ concentration. (b) Color contour map of the $HCOO^-$ FE data for Ag/PTFE as a function of $KHCO_3$ concentration and GDL pore size. (c) Product FE data for the case where the CO_2 feed stream was diluted with various amounts of N_2. Ag/PTFE(0.45) was used as the cathode and 1 M $KHCO_3$ was used as the electrolyte at an applied cathodic current density of 300 mA/cm^2. (d) Graph showing the formate to CO ratio as a function of N_2 gas dilution, based on the data shown in (c).

120 μm in the x direction and 50 μm in the z direction (Fig. 6.11 (c) and Fig. 6.12). From the maps, a pH gradient can be clearly observed for all cases, with the pH being higher at points closer to the electrode surface. We averaged the pH in the area between the electrode surface and 40 micrometers above the electrode surface and plotted this as a function of current density (Fig. 6.11 (b)). As expected, the pH increases as the current density increases since OH^- is created as a by-product of CO_2 reduction and hydrogen evolution.

Most importantly, for all current densities investigated, there is the clear trend that the local pH decreases with increasing pore size of the GDL. This is consistent with our preceding experimental and simulation results, that a larger GDL pore size

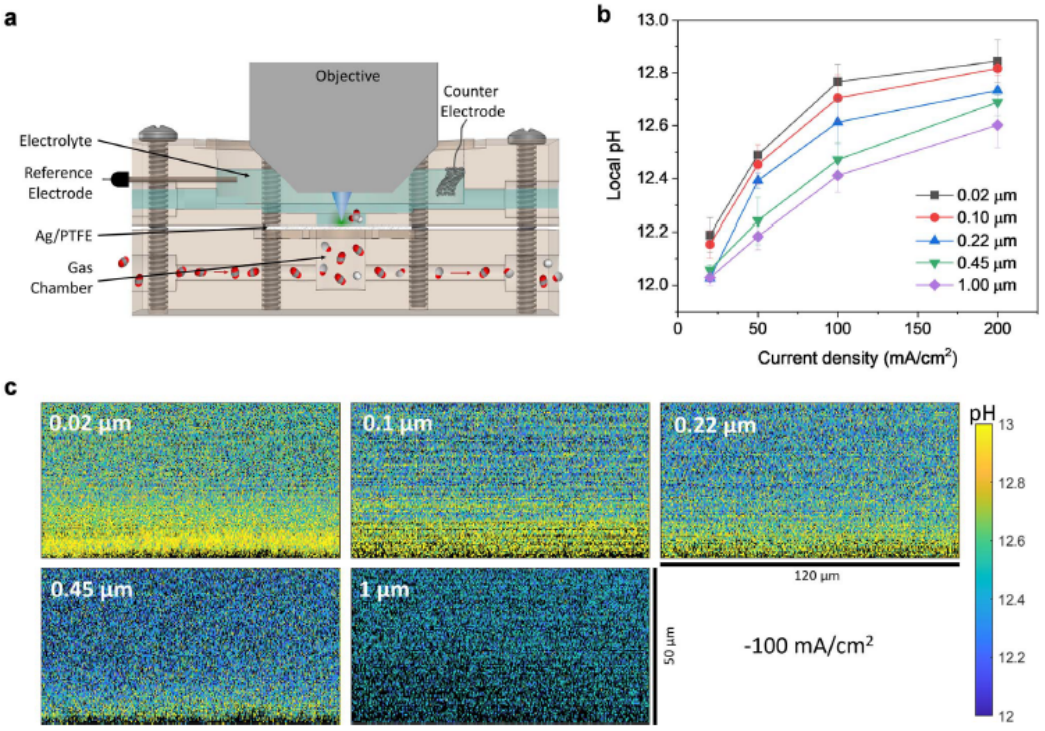

Figure 6.11: pH imaging experiments and results. (a) Cross section of the custom-built electrochemical cell with water immersion objective for local pH measurements with APTS. (b) Local pH value averaged from zero to forty micrometers above the electrode surface as a function of current density for different Ag/PTFE GDLs. (c) Representative pH maps as a cross section through the plane perpendicular to the electrode surface for different Ag/PTFE samples at 100 mA/cm^2. pH maps for other current densities can be found in Fig. 6.12.

can indeed better facilitate CO_2 mass transport. This leads to more excess CO_2 molecules that are available at the electrode surface to react with electrochemically generated OH^-, leading to a lower pH value. These results are therefore strong experimental evidence for our hypothesis that tuning the GDL pore size can indeed directly impact the local pH. This then results in selectivity switching, leading to the observed increased selectivity towards conversion of CO_2 to formate.

Finally, we sought to understand if this local microenvironment effect could also affect other catalysts for electrochemical CO_2 reduction. Previous literature reports have indicated that an increased local pH can induce a higher selectivity towards multicarbon (C_{2+}) products with Cu based catalysts. Hence to explore this effect, we prepared a series of samples by sputtering 325 nm of Cu onto PTFE substrates of different pore sizes. These catalysts were then tested at a constant cathodic current density of 200 mA/cm^2 in aqueous 1 M $KHCO_3$ electrolyte. The results (Fig. 6.13)

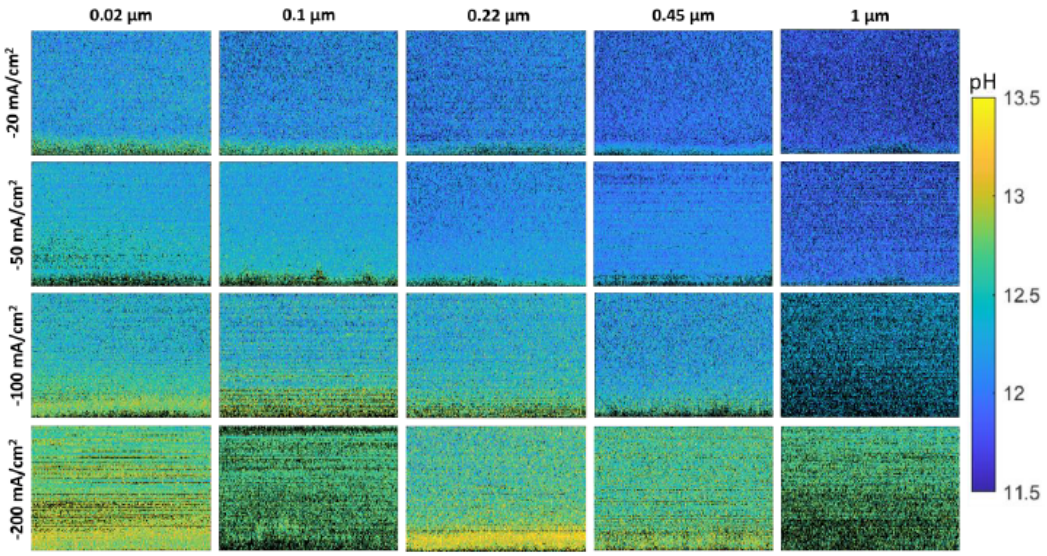

Figure 6.12: Representative pH maps as a cross section through the plane perpendicular to the electrode surface for different Ag/PTFE samples at four different cathodic current densities between -20 mA/cm^2 and -200 mA/cm^2. The dimension of each of the maps is 120 μm in x and 50 μm in z.

show that a smaller pore size does indeed lead to an increase in the FE towards C_{2+} products, as a consequence of the induced higher local pH.

However, the C_{2+} FE was observed to drop once the pore size becomes too small. This is because the local CO_2 availability is expected to diminish at the smallest pore sizes, and these conditions are less favorable towards the formation of C_{2+} products. Our findings are consistent with the work by Strasser and co-workers, where they observed different "selectivity zones" within their Cu nanoparticle catalyst coatings on a gas diffusion layer [147]. Zones closer to the gas diffusion layer experience higher local pH and increased CO_2 availability, which enhances the C_{2+} selectivity. On the other hand, zones further away from the gas diffusion layer experience CO_2 depletion, which reduces C_{2+} product formation. These observations are supported by another report in the literature [148], which showed that a lowered CO_2 partial pressure suppresses the C_{2+} FE.

6.4 Conclusion

In this work, we investigated how the pore size of the gas diffusion layer can be tuned to impact the catalyst local microenvironment and hence, the selectivity for electrochemical CO_2 reduction. We first performed multiphysics modelling of the reaction system, which showed that smaller GDL porosity can slow down CO_2 mass

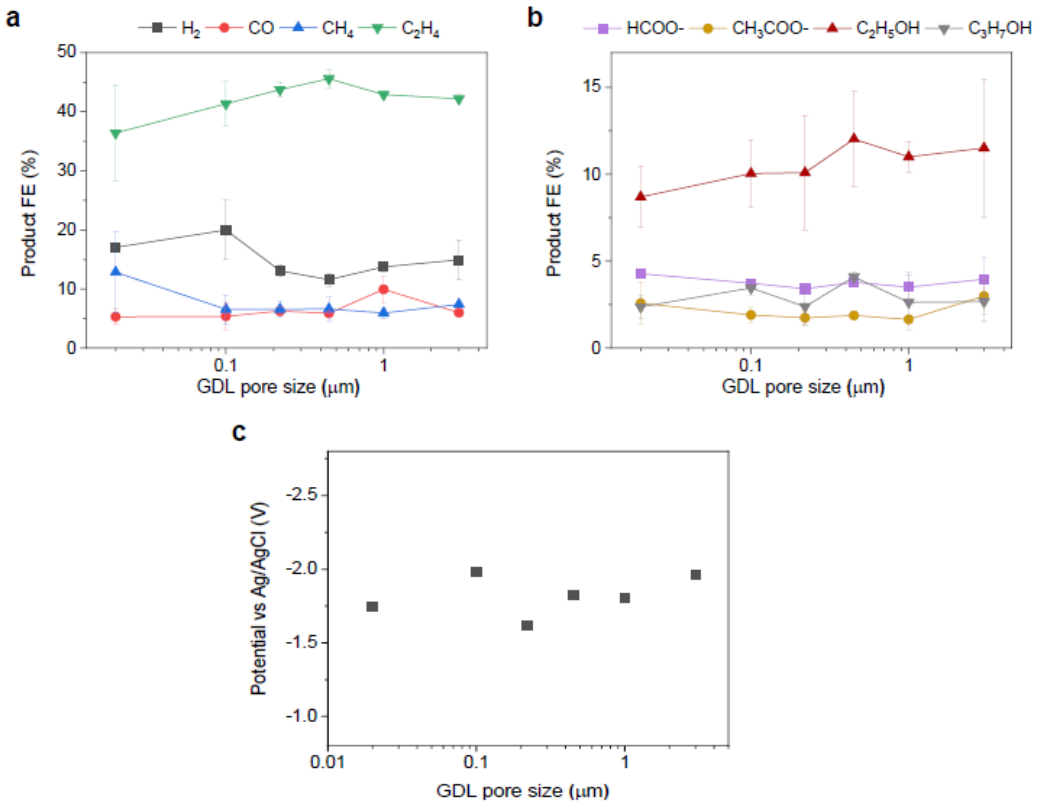

Figure 6.13: Electrochemical CO_2 reduction results with Cu sputtered on PTFE substrates of various pore sizes. A constant cathodic current density of -200 mA/cm^2 was applied and aqueous 1 M $KHCO_3$ was used as the electrolyte. Multicarbon (C_{2+}) products are ethylene (C_2H_4), acetate (CH_3COO^-), ethanol (C_2H_5OH) and 1-propanol (C_3H_7OH). (a) Gas product FE as a function of pore size. (b) Liquid product FE as a function of pore size. (c) Applied potential as a function of pore size.

transport, resulting in a higher local pH at the electrode. Encouraged by these results, we studied this experimentally using sputtered Ag films on hydrophobic PTFE substrates with 6 different pore sizes. Although Ag is known to be a predominantly CO generating catalyst, we find that smaller pore sizes favor the generation of formate up to a faradaic efficiency of 43 %. This is due to the higher local pH, which induces reaction pathway switching towards formate at the expense of CO. These observations are also supported by further investigations with different buffer concentrations and partial pressure experiments. A confocal laser-scanning microscopy setup was further used together with the fluorescent pH probe APTS to map out the electrode local pH. Through this, we experimentally verified that a smaller (larger) pore size does indeed result in a higher (lower) local pH. Overall, our results show

how the GDL pore size can be used to impact the catalyst microenvironment and hence serve as an experimental knob that can be rationally controlled to influence the product selectivity. These findings will inform and aid the future design of more selective and efficient CO_2R systems.

Chapter 7

ELECTROCHEMICAL CO_2 REDUCTION IN ACIDIC ELECTROLYTES IS ENABLED BY AN INCREASE IN THE MICROENVIRONMENT PH

Contents drawn from: A. E. Böhme*, W. Nie*, M. H. Hicks, H.A. Atwater, T. Agapie, J. C. Peters. "Electrochemical CO_2 Reduction in Acidic Electrolytes is Enabled by an Increase in the Microenvironment pH". *in preparation.* *These authors contributed equally to this work.

A.E.B. designed and conducted confocal laser-scanning microscopy measurements, related pH imaging and data analysis.

7.1 Introduction

The majority of CO_2R studies are conducted in neutral and basic electrolytes that help favor the selectivity for CO_2R over the hydrogen evolution reaction (HER) [50, 149]. This is also the case for the studies presented in Chapters 2 – 6. Unfortunately, these electrolytes suffer from low CO_2 utilization due to parasitic (bi)carbonates formation and their subsequent migration to the anolyte [136, 150], see also section 1.3.1. Strategies to mitigate this problem include the use of artificial membrane-electrode assemblies (MEA) with bipolar membranes or solid electrolytes [151–154], and performing CO_2R in acidic electrolytes [155–157].

CO_2R at low pH poses the challenge of significant competition from HER. Recent studies have shown that using electrolytes with high alkali cation concentrations ($[M^+]$) can suppress HER and promote CO_2R, although consensus has yet to be reached concerning the mechanistic basis of the cation effects [155–163]. A limitation of high $[M^+]$ is the potential formation of carbonate deposits that block active sites and reduce the hydrophobicity of the catalyst surface. These factors can result in decreased stability of catalytic systems [164–167], especially at high current densities <j> when applied to CO_2R under acidic conditions [156]. Moreover, preparing highly pure electrolytes at high $[M^+]$, or pre-treating concentrated electrolytes to avoid catalyst poisoning [168, 169], may also pose significant technoeconomic constraints. Therefore, it is desirable to explore the feasibility of alternative strategies to promote CO_2R under acidic conditions that do not rely on high $[M^+]$. A better

understanding of the roles cations play in enabling CO_2R, especially under acidic conditions, will benefit the development of alternate strategies.

While there exist a variety of studies pertaining to alkali cation effects in neutral-to-basic electrolytes and/or at high [M^+] [133, 159, 170–173] there exist relatively few investigations in acidic conditions at low [M^+] or nominally in M^+ free conditions [44, 164, 174]. This is probably due to the inherent difficulty in suppressing HER and/or detection limitations for CO_2R products in low yields. Very recently, a number of studies have focused on the mechanistic roles of M^+ with respect to CO_2R under acidic conditions [44, 155, 156, 162, 164, 173–176]. The primary mechanistic hypotheses that have been advanced include (Figure 7.1 (a)): (i) Partially dehydrated M^+ ions play key roles in the CO_2 adsorption/activation steps, via a short-range electrostatic or direct bonding interactions with adsorbed CO_2R intermediates [44, 171, 174]. (ii) Physisorbed M^+ ions on the electrode surface enhance the local electric field to stabilize adsorbed polar intermediates to promote CO_2R; these accumulated M^+ cations also screen the electric field generated from the cathode to suppress migration of H^+ and hence competing HER [155, 159, 164, 172, 176]. (iii) Solvated M^+ ions buffer microenvironment pH to a non-acidic regime based on the pK_a of the coordinated H_2O; the buffered microenvironment mitigates carbonate formation and maintains appropriate microenvironment [CO_2] to facilitate CO_2R [173]. Notably, some recent studies have also reported effective CO_2R in the absence of M^+ [164, 176, 177], or in the presence of weakly coordinating organic cations instead of M^+ [175], underscoring that M^+ is not strictly required for CO_2R.

In the present study, we investigate CO_2R under acidic conditions via controlled-current electrolysis on Cu electrodes (Figure 7.1 (b)). We further perform time-resolved in-situ electrode surface pH measurements via fluorescent confocal laser scanning microscopy (CLSM) using the pH-dependent ratiometric florescent dye DHPDS, in analogy to Chapters 2, 4, 5 (Figure 7.2 and section 1.5.1) [77, 78, 134]. Together, the electrolysis and pH imaging results highlight the importance of microenvironment pH near the electrode as the dominant factor controlling CO_2R versus HER. The correlation shows that depletion of surface [H^+] at a high <j> and control of H^+ mass transport in combination lead to CO_2R at the electrode by attenuating HER from H^+ reduction in the resulting non-acidic microenvironment (Figure 7.1 (b)).

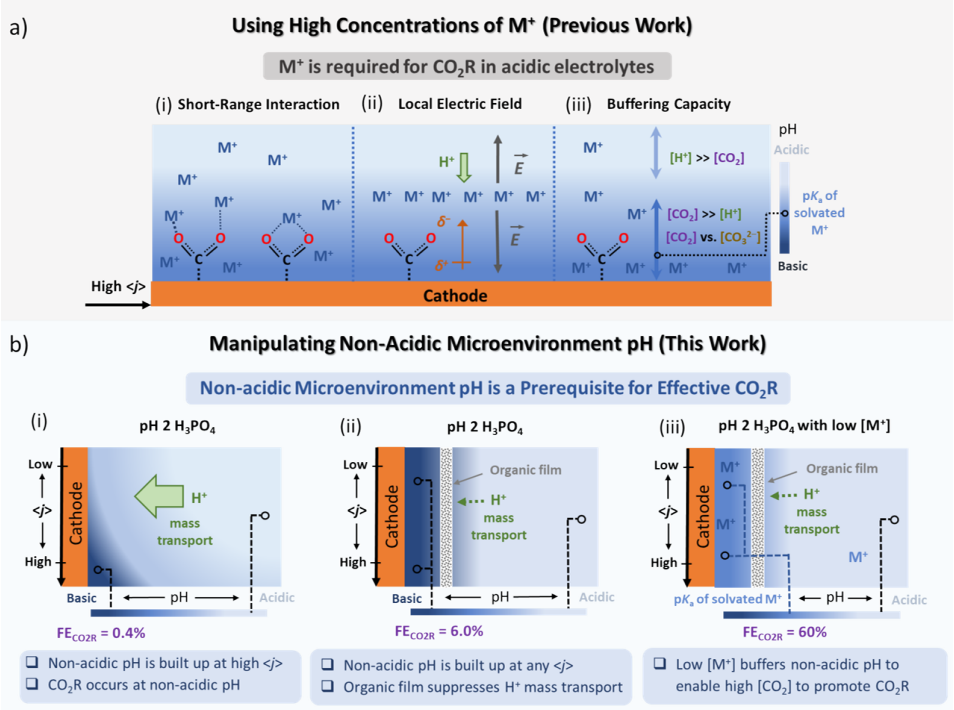

Figure 7.1: Proposed hypotheses for CO_2R with high M^+ concentrations and an alternative strategy via manipulation of the microenvironment pH. (a) The strategy of using electrolytes with high $[M^+]$ has been reported to promote CO_2R in acidic electrolytes. It has been hypothesized that M^+ is required for effective CO_2R based on the following proposals: (i) short-range interactions between partially dehydrated M^+ and the reaction intermediate; (ii) local electric field enhanced by physisorbed M^+; (iii) buffering capacity of M^+ to maintain the microenvironment pH. (b) An alternative strategy of accessing and manipulating non-acidic microenvironment pH is developed in this study to promote CO_2R in acidic electrolytes. We suggest that a non-acidic microenvironment pH is a prerequisite for effective CO_2R, which has been validated by the results of controlled-current electrolysis in pH 2 H_3PO_4 (i) on bare Cu electrodes; (ii) on organic film modified Cu electrodes; and (iii) in aqueous pH 2 H_3PO_4 with low $[M^+]$ on organic film modified Cu electrodes.

The data presented collectively suggests that a non-acidic microenvironment is the essential requirement for achieving CO_2R in aqueous pH 2 H_3PO_4, and not a high $[M^+]$; cations play an important role in suppressing H^+ mass transport and buffering the pH near the electrode [155, 164, 173].

7.2 Methods

Sample Preparation

Before each electrochemical experiment, Cu foil was mechanically polished to a mirror-like finish using nanodiamond suspension, then rinsed with water and dried.

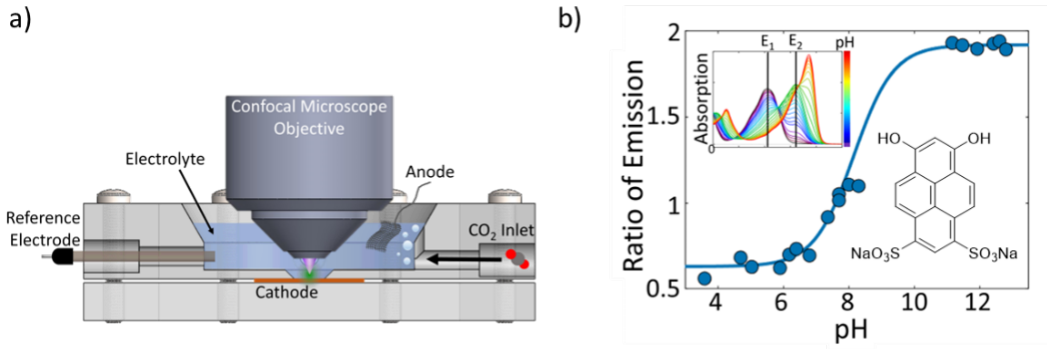

Figure 7.2: Schematic of the CLSM setup and calibration curve. (a) Schematic of the CLSM setup (cathode: Cu foil; anode: Pt mesh; reference electrode: leakless Ag/AgCl; CO_2 continuously purges the electrolyte from the right inlet, the fluorescent dye is dissolved in the cycled electrolyte); (b) the calibration curve for the local pH based on the ratio of emission of the dye (inset: absorption spectrum of the dye as a function of pH showing the two excitation wavelengths and chemical structure of the pH-sensitive ratiometric florescent dye DHPDS).

The Cu foil was then electropolished at +2.3 V vs. a carbon rod electrode in a phosphoric acid bath for 5 minutes before being rinsed and dried again. Nearly-M^+-free pH = 2 electrolyte (H_3PO_4) was prepared by making 0.01 M H_3PO_4 aqueous solution first, with pH then adjusted to ≈2.0 using concentrated H_3PO_4. Inductively coupled plasma mass spectrometry (ICP-MS) was applied to test the nearly-M^+-free pH 2 electrolyte (H_3PO_4), showing ≈1 ppm M^+ in the solution. pH 2 electrolytes with 0.2 - 500 mM K^+ were prepared by adding KCl into nearly-K^+-free pH = 2 electrolyte (H_3PO_4). Prior to each electrolysis for CO_2 reduction, the electrolyte solutions were sparged with CO_2 gas for at least 30 min. The pH of electrolytes were measured by a SB90M5 Benchtop sympHony Meter.

Electrocatalysis Experiments

Controlled-current electrolysis experiments were carried out in a custom-made PEEK cell setup with a copper foil as the working electrode and a platinum foil as the counter electrode. The cathode and anode compartments were separated with a Selemion AMV anion-exchange membrane. Chronopotentiometry (CP) measurements were conducted using a Biologic VMP3 multichannel potentiostat, the working current was kept constant and the electrode potential vs. a leakless Ag/AgCl reference electrode was measured. Potentiostatic electrochemical impedance spectroscopy (PEIS) measurements were conducted before each electrolysis experiment to determine the Ohmic resistance of the cell setup. The potentiostat was not set

for any iR drop compensation but the reported electrode E was compensated after measurements based on applied current and measured Ohmic resistance of the cell setup.

All experiments were performed at room temperature for 35 min in corresponding electrolytes under CO_2 or Ar atmosphere. The effluent gas stream through the cell (5 mL/min) was flowed into the sample loops of a gas chromatograph (GC-FID/TCD, SRI 8610C, in Multi Gas 5 configuration) equipped with a HayeSep D column. Every 10 min, 1 mL of gas was sampled to determine the concentration of gaseous products. After electrolysis, the main liquid products (formate, ethanol and 1-propanol) in catholytes were quantified by high performance liquid chromatography (HPLC) (Thermo Scientific Ultimate 3000).

Fluorescence confocal laser scanning microscopy (CLSM) measurements

CLSM measurements were performed with a Leica Stellaris 5 upright confocal microscope with a HC FLUOTAR L 25x/0,95 W VISIR water immersion objective. A custom-made electrochemical cell was 3D-printed. It exhibits a horizontal orientation to be compatible with confocal microscopy. It consists of a flat base plate, topped with a rubber gasket to prevent leakage as well as an electrolyte chamber. A polished copper foil cathode is placed between the gasket and the electrolyte chamber which exhibits a circular hole in the center with an area of 0.2 cm^2 that exposes the copper cathode. The electrolyte chamber is open at the top to allow the water immersion objective to be dipped into the electrolyte. It further has an inlet with a straw that leads to the cathode surface as well as an outlet at the opposite side of the chamber that allows for electrolyte recirculation. A third inlet port enables constantly bubbling the electrolyte with 5 sccm CO_2. A leakless Ag/AgCl reference electrode and a Pt mesh counter electrode are immersed into the electrolyte (Fig. 7.2). pH imaging is possible by the addition of the pH-sensitive dye DHPDS that is sensitive to pH values between 6 and 11.5. Hence, only local pH values exceeding 6 can be resolved. 50 μM DHPDS were dissolved in the electrolyte. Compared to pH imaging in alkaline electrolytes (compare Chapters 2, 4 and 5), different settings must be chosen for the acidic environment. For acidic pH values, the absorption of DHPDS is close to zero at one of the main absorption peaks around 485 nm (see Fig. 7.2 (b), inset). The excitation of that peak had been utilized in the previous chapters. We therefore decided to use the absorption peaks around 405 nm as well as around 448 nm instead. Consequentially, DHPDS can still be used as a ratiometric probe while both channels exhibit a signal >0 even if the solution pH is <6. The dye

molecules were excited separately with a laser beam at 405 nm (laser power 1.2%) and a second laser beam at 448 nm (laser power 0.5%). The emission was collected separately for both excitations between 495 and 835 nm with a gain of 100. The pinhole was set to 1 Airy unit. The ratio between the emission from both excitations is a measure for the local pH value. A calibration curve was determined previously by measuring the ratio of emission for various solutions of known pH value and determining a sigmoidal fit curve (Fig. 7.2 (b)). It was determined as

$$\mathrm{pH} = 8.153 - \frac{1}{1.651} \ln\left(\frac{10}{(\text{Ratio of Emission}) - 0.01305} - 1\right). \tag{7.1}$$

Before each pH imaging experiment, potentiometric electrochemical impedance spectroscopy (PEIS) was performed using a Biologic SP-200 potentiostat. Three-dimensional confocal microscopy images were captured as a time series approximately every 5 s. The image format was chosen to be 512 x 16 pixels in the x-y plane with a pixel size of ≈500 nm × 500 nm. A stack of images in the z-direction (perpendicular to the cathode surface) was captured with a distance of 565 nm between each frame, starting below the surface of the cathode to ≈20 μm above the surface. The local pH value was averaged over all pixels between what was determined to be the cathode surface and ≈1 μm above the surface as a function of time.

The exemplary pH maps in Fig. 7.3 and 7.4 (c) are pH maps in the x-z plane, averaged over the 16 pixels in the y direction. A constant current of <j> = -1.25 mA/cm^2, -5.00 mA/cm^2 or -10.0 mA/cm^2 was applied 30 seconds after starting a confocal time series.

Fresh electrolyte with unused DHPDS dye was used for each time series measurement and the cell and objective were rinsed extensively with nanopure water between each experiment. The electrolyte was circulated through the cell at a rate of 1 mL/min during measurements to mitigate the buildup of bubbles that impede pH imaging. Large bubbles still formed at high current densities. In that case, the measurement was interrupted, the bubbles were removed with a glass pipette and the measurement was resumed. This caused gaps and noise in the data obtained at higher current densities, however, the pH trend is still clearly distinguishable. During the course of a measurement, the buildup of bubbles intensified which is why the duration of CLSM confocal measurements was limited to 10 min.

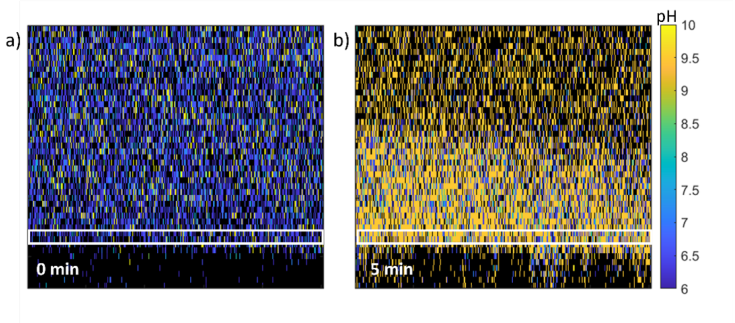

Figure 7.3: Exemplary pH maps in the plane perpendicular to the cathode surface captured with confocal microscopy and the fluorescent dye DHPDS in aqueous pH 2 H_3PO_4 with 20 mM K^+ at -10 mA/cm^2 and 5 SCCM CO_2 flow at (a) 0 minutes and (b) 5 minutes after starting the current. The white frames indicate the area approximately between the electrode surface and 1 μm above the surface in which the pH value that is displayed in other figures was averaged.

7.3 Results and Discussion

CO_2R in pH 2 H_3PO_4 electrolytes

To explore the possibility of CO_2R in the absence of M^+, controlled-current electrolysis experiments were conducted on Cu foil electrodes in CO_2 saturated aqueous pH 2 H_3PO_4 electrolyte. At low <j> (-1.25 mA/cm^2), the electrode potential E remained at ≈-0.50 V_{RHE} (versus the reversible hydrogen electrode, RHE) with a negligible shift during 35 min electrolysis, while higher <j> (-5.00 mA/cm^2) caused a slow cathodic E shift from -0.50 to -1.40 V_{RHE} (Figure 7.4 (a)). At both <j>, neither gas nor liquid CO_2R products could be detected, which is consistent with previous studies showing a lack of CO_2R in the absence of M^+ in electrolytes [174]. However, as -10.0 mA/cm^2 was applied, a rapid E drop was observed from -0.50 to ≈-4.00 V_{RHE} (Figure 7.4 (a)). Once E dropped below -1.40 V_{RHE}, gaseous products (CO, CH_4) were observed by on-line gas chromatography (GC) and formic acid was detected in the liquid phase after electrolysis (Figure 7.4(b)), albeit at very low FEC_{CO_2R} = 0.4 ± 0.2%.

To further validate the 0.4% FEC_{CO_2R}, we conducted the same controlled-current electrolysis using Cu gas diffusion electrodes (Cu-GDE) and obtained FEC_{CO_2R} = 19.8 ± 5.4% in pH 2 H_3PO_4 at -10.0 mA/cm^2, probably due to improved CO_2 mass transport in the GDE configuration.

As the electrolyte bulk pH remains unchanged after electrolysis, the E shift is assigned to a dynamic change within the catalytic microenvironment, with local pH at the electrode being a plausible cause. CLSM measurements were performed using

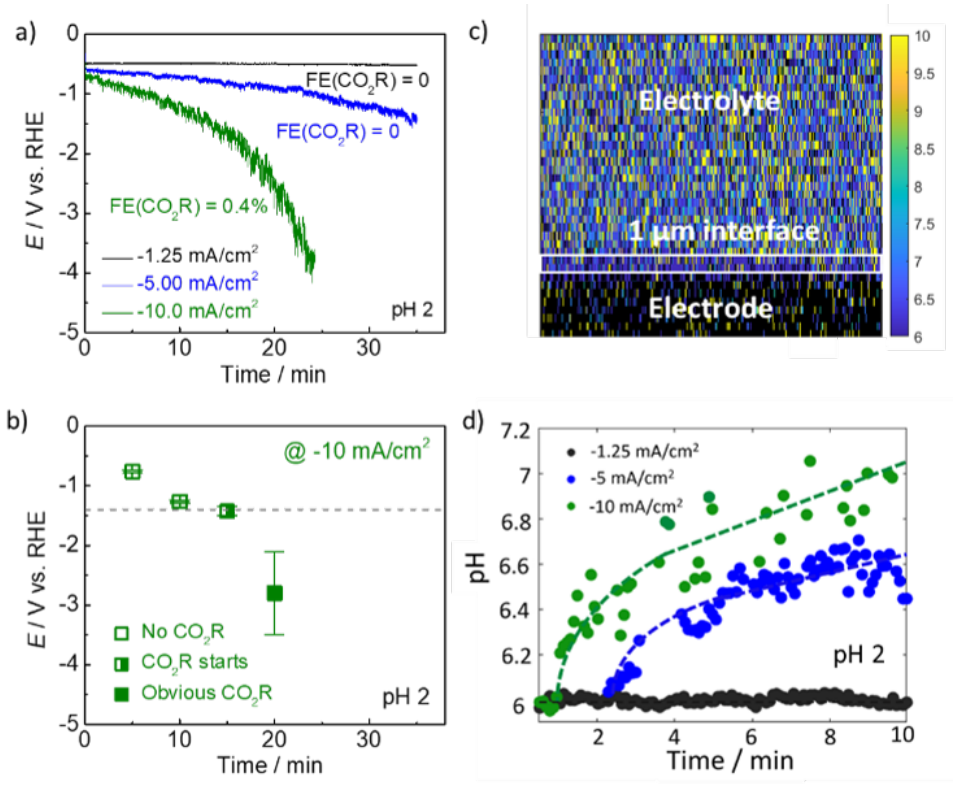

Figure 7.4: [E and pH profiles in pH 2 H_3PO_4. (a) The E profiles with FEC_{CO_2R} on Cu foil electrodes at different <j> in aqueous pH 2 H_3PO_4; (b) the time-dependent E and detection of CO_2R on Cu foil electrodes at -10.0 mA/cm^2 in pH 2 H_3PO_4; (c) the pH map in the plane perpendicular to the cathode in pH 2 H_3PO_4 with DHPDS; (d) the microenvironment pH at the electrode surface as a function of time and <j> in pH 2 H_3PO_4 with the electrolyte circulated at 1 mL/min. The dashed lines are guides to the eye.

the ratiometric florescent dye DHPDS to monitor the in-situ microenvironment pH at the electrode surface at different <j>. The DHPDS dissolved in the electrolyte is sensitive to pH values between 6 and 11.5. Although DHPDS contains Na^+ in the structure, its low concentration in the test solution ([Na^+]=0.05 mM, close to 1 ppm (≈0.03 mM) M^+ in aqueous pH 2 H_3PO_4) is assumed to have a negligible effect on the CO_2R results, in accord with results presented in the following section.

An electrolyte flow of 1 mL/min was applied to mitigate the buildup of bubbles that cause noise due to blocking the fluorescent signal of the dye. Figure 7.4 (c) shows a representative color-coded pH map in the plane perpendicular to the cathode surface captured with confocal microscopy in aqueous pH 2 H_3PO_4 containing 50 μM DHPDS after 5 minutes at a current density of -10 mA/cm^2. Although the spatial resolution of these CLSM measurements (≈ 500 nm) is not sufficient to

resolve the reactive double layer (≈ 10 nm), they do provide a resentative trend of the microenvironment pH.

CLSM measurements of the μm-scale pH gradient as a function of distance from the electrode surface for different K^+ concentrations and at different <j> (Fig. 7.5) reveal a clear trend of increasing pH as a function of proximity to the electrode surface consistent which is consistent with other literature reports [56, 58, 60, 77, 78, 178]. Based on this trend, the pH value within the double layer (≈10 nm) is expected to be even more alkaline than the pH value that was measured and averaged within 1 μm from the electrode surface (the white frame in Figure 7.4 (c)). Still, we caution that some computational models based on a local electric field argument have suggested an interesting pH drop within a 2 nm layer near the electrode surface [164, 179]. However, it remains a significant challenge to experimentally resolve pH on the nm-scale.

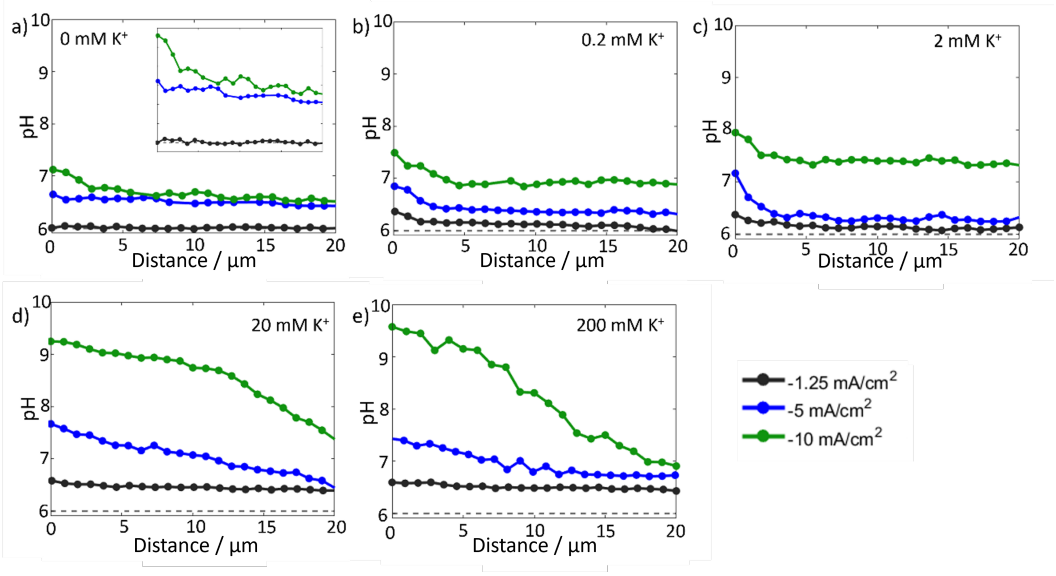

Figure 7.5: Averaged observed pH after 10 minutes as a function of current density and the distance from the electrode surface for (a) 0 mM (inset is a zoomed-in version of the same data); (b) 0.2 mM; (c) 2 mM; (d) 20 mM and (e) 200 mM [K^+] in pH 2 H_3PO_4 with 5 SCCM CO_2 flow.

At -1.25 mA/cm^2, the observed pH was maintained at ≤6 (since the detection range of the dye is between pH 6 and 11.5, pH values <6 will appear as pH 6) during the measurement (Fig. 7.4 (d)). Higher <j> (-5.00 mA/cm^2) caused a gradual pH change starting at ≈2 min; the observed pH remained weakly acidic (<6.6) overall up to 10 min. In contrast, an obvious pH increase to >6.2 was observed within one minute

of applying -10.0 mA/cm^2, with the pH continuing to increase to more neutral pH values over 10 min. Longer-time-resolved CLSM tests were unsuccessful due to gas bubbles accumulating at the cathode interface. Nonetheless, the first 10 min of pH measurements at different <j> in Figure 7.4 (d) provide consistent trends in pH change as predicted from the E profiles of the electrolysis results (Figure 7.4(a)). Based on a study by Koper and coworkers, as E becomes more cathodic than -1.40 V_{RHE}, H_2O reduction replaces H^+ reduction for HER, indicating a neutral or higher microenvironment pH [180], which is consistent with the microenvironment pH increase towards a neutral value at -10.0 mA/cm^2 in our CLMS measurements.

The observation of CO_2R exclusively at E < -1.40 V_{RHE} in our data (Figure 7.4 (b)) together with the pH imaging results suggest that a non-acidic microenvironment pH is an important prerequisite for CO_2R. This is further supported by control experiments in H_3PO_4 electrolytes at different bulk pH values, where a distinct cathodic E shift and 0.8 ± 0.2% FE_{CO_2R} was observed at low <j> = -1.25 mA/cm^2 in pH 3 H_3PO_4, but a negligible E shift and therefore 0% FE_{CO_2R} even at high <j> (-10.0 mA/cm^2) in pH 1 H_3PO_4.

CO_2R in acidic electrolytes with varying [M^+]

To investigate the role of M^+ in catalytic CO_2R, controlled-current electrolysis experiments were studied in CO_2 saturated pH 2 H_3PO_4 with varying [KCl]. At -1.25 mA/cm^2, addition of K^+ (0.2 mM and 2.0 mM) does not distinctly influence E profiles (Fig. 7.6 (a)), which is consistent with only a slight change in the acidic pH as measured by CLSM (Fig. 7.6 (d)). As a result, CO_2R does not occur at acidic microenvironment pH values regardless of [K^+]. In contrast, the microenvironment [H^+] can be effectively depleted at -10.0 mA/cm^2, leading to a rapid pH increase. Higher [K^+] (2.0 mM) facilitates the E drop and promotes CO_2R (FE_{CO_2R} = 12.4 ± 5.4%), while 0.2 mM K^+ gives only a slightly changed E profile with FE_{CO_2R} = 0.6 ± 0.2%, comparable to values in pure H_3PO_4 electrolyte (Fig. 7.6 (b)).

The CLSM measurements show a similar trend of microenvironment pH change at -10.0 mA/cm^2 as predicted by the E profiles. The presence of relatively high [K^+] (2 mM) increases the observed pH to ≈8 within 10 minutes, while at [K^+] = 0.2 mM, pH ≈7 comparable to the pH profile of pure H_3PO_4 is achieved (Fig. 7.6 (e)). Importantly, at a constant <j>, the rate of H^+ depletion (or OH^- generation) from combined HER and CO_2R can be assumed to be constant. Therefore, the facilitated microenvironment pH increase at -10.0 mA/cm^2 in the presence of K^+, in particular

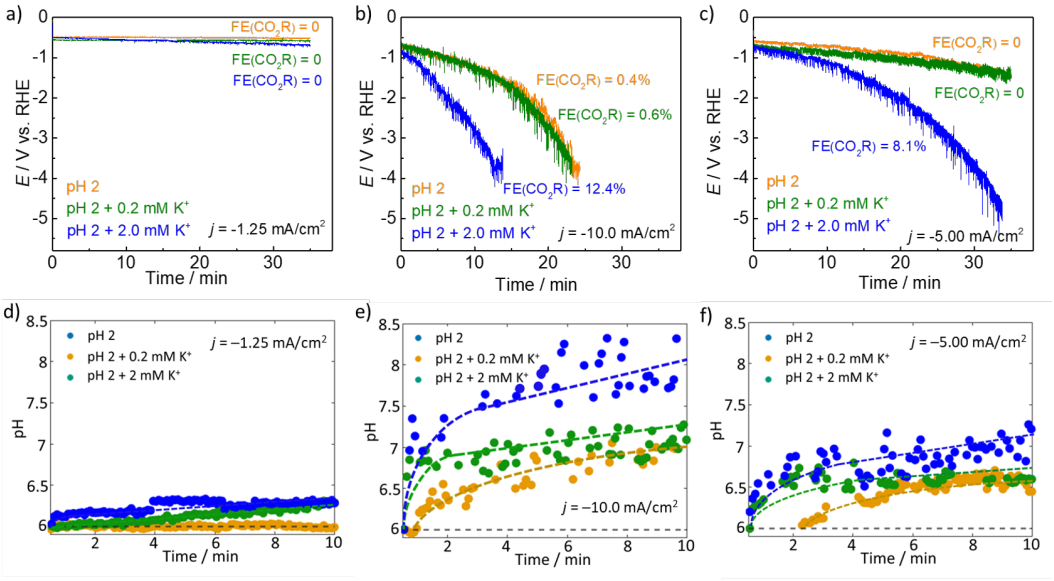

Figure 7.6: The E profiles on Cu foil electrodes at (a) -1.25 mA/cm^2, (b) -10.0 mA/cm^2, and (c) -5.00 mA/cm^2 in pure H_3PO_4, 0.2 mM K^+ and 2.0 mM K^+ pH 2 H_3PO_4; the observed pH vs. time profiles on Cu foil electrodes at (d) -1.25 mA/cm^2, (e) -10.0 mA/cm^2, and (f) -5.00 mA/cm^2 in pure H_3PO_4, 0.2 mM K^+ and 2.0 mM K^+ pH 2 H_3PO_4. The dashed lines are guides to the eye.

for [K^+] = 2 mM, is attributed to attenuated H^+ mass transport to the electrode surface due to K^+, which has been proposed previously to arise from an electric field shielding effect of M^+ on H^+ diffusion and migration [155, 164]. This effect was also observed in electrolysis at the more moderate <j> of -5.00 mA/cm^2. A faster E shift (Fig. 7.6 (c)) and observed pH increase towards ≈7 (Fig. 7.6 (f)) was observed at 2 mM K^+, and FE_{CO_2R} was promoted to 8.1 ± 3.4% once E was cathodic at -1.4 V_{RHE}. 0.2 mM or trace amounts of K^+ showed neglectable M^+ effects on H^+ mass transport and hence microenvironment pH enhancement due to low [M^+]. These data suggest that the presence of M^+ helps facilitate a microenvironment pH increase, which in turn favors CO_2R.

Similar electrolysis studies were also conducted at higher [K^+] (20 mM - 500 mM). As shown in Fig. 7.7 (a), <j> of -1.25 mA/cm^2 was too low to effectively deplete the local [H^+] to create a sufficiently non-acidic microenvironment. Therefore, no CO_2R was observed, even at high [K^+]. However, the E profiles at -5.00 and -10.0 mA/cm^2 in the presence of 20 - 500 mM K^+ display very distinct features compared to those at low [K^+] (≤2mM). With 20 mM K^+ at both <j> values (Figure 7.8 (a) and (b)), E drops faster than when using 2 mM K^+ in the first

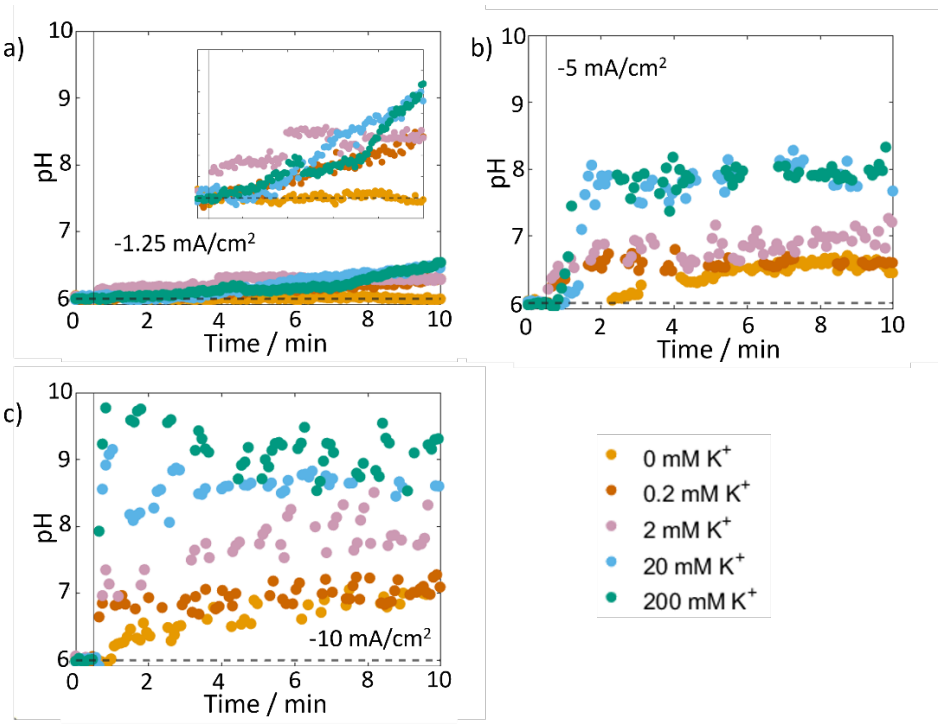

Figure 7.7: Local pH value at the electrode surface as a function of time and [K^+] for (a) -1.25 mA/cm^2 (inset is a zoomed-in version of the same data); (b) -5 mA/cm^2 and (c) -10 mA/cm^2 in pH 2 H_3PO_4 with 5 SCCM CO_2 flow.

10 min, which we presume is due to enhanced suppression of H^+ mass transport when more K^+ is present in the microenvironment. Interestingly, E then reached a plateau which is maintained during the remaining time of electrolysis (Figure 7.8 (a) and (b)). This observation suggests that a steady state microenvironment pH is dynamically established. Increasing [K^+] helps reach such a steady state more efficiently, manifested in a less negative $E_{plateau}$ that is almost independent of [K^+] at concentrations higher than 100 mM (Figure 7.8 (a) and (b)). This trend of $E_{plateau}$ with increased [K^+] is consistent with the effect of [K^+] on CO_2R: FE_{CO_2R} is enhanced as [K^+] increases from 2 mM to 100 mM, then plateaus, showing similar C_1/C_{2+} selectivity at [K^+] >100 mM (Figure 7.8 (c) and (d)).

Accordingly, CLSM measurements in pH 2 H_3PO_4 at -5.00 and -10.0 mA/cm^2 confirm a stable microenvironment pH at high [K^+] (Fig. 7.9). Notably, controlled electrolysis in pH 5.2 (200 mM KCl, CO_2 saturated) and pH 8.2 (20 mM KOH + 180 mM KCl, CO_2 saturated) electrolytes displayed almost the same $E_{plateau}$ and identical CO_2R product selectivity at -10.0 mA/cm^2 with the same [K^+] = 200 mM. These data collectively suggest that the dynamically stable microenvironment pH established in

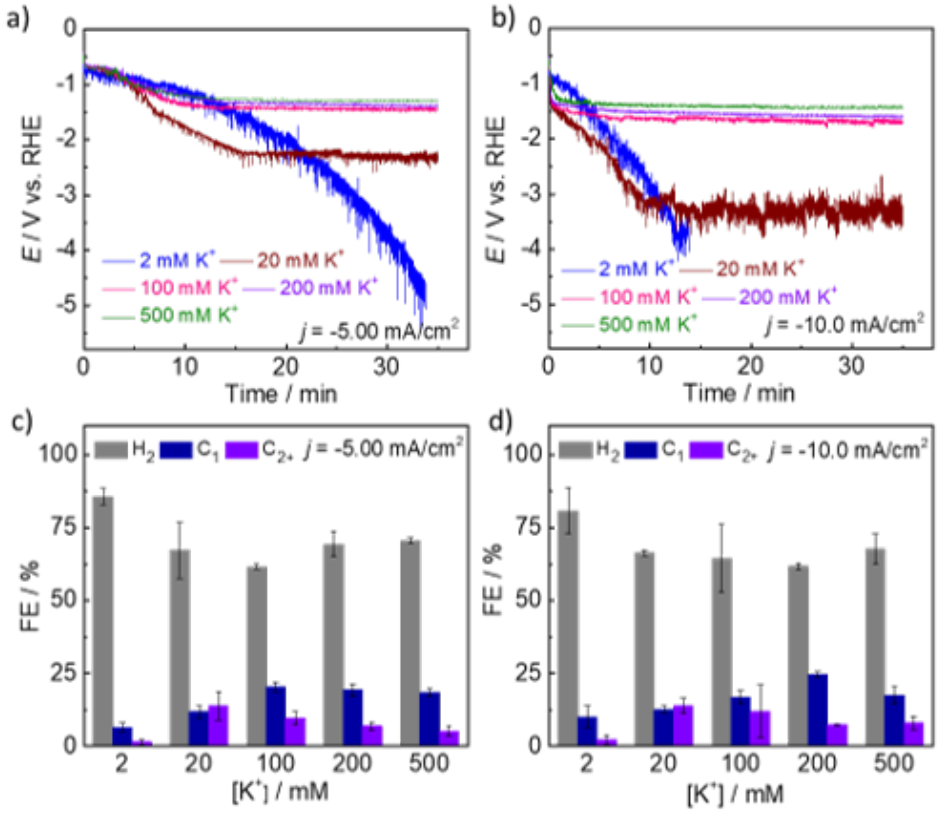

Figure 7.8: The E profiles of Cu foil electrodes at (a) -5.00 mA/cm^2 and (b) -10.0 mA/cm^2 with 2 mM ≈ 500 mM K^+ in pH 2 H_3PO_4; the electrolysis product distribution on Cu foil electrodes in pH 2 H_3PO_4 with different [K^+] at (c) -5.00 mA/cm^2 and (d) -10.0 mA/cm^2.

the presence of M^+ becomes independent of [M^+] for [M^+] >100 mM, and the bulk pH of the electrolyte. Therefore, the mechanistic role for M^+ in the catalytic CO_2R process is related to achieving and maintaining a higher microenvironment pH.

Our observation of CO_2R in nearly M^+-free pH 2 H_3PO_4 as discussed above, suggest that a coordinative interaction between an alkali M^+ and a surface-bound CO_2 intermediate, which has been implicated as essential to CO_2 activation and catalysis [171, 178], is unlikely a requirement of CO_2R. Instead, a comparatively non-acidic microenvironment at the electrode surface is, in our view, likely the governing factor for CO_2R. Adding M^+ facilitates an increase in the microenvironment pH via suppressing H^+ mass transport as M^+ is physisorbed in the double layer [155]. This phenomenon serves to maintain a stable, non-acidic microenvironment pH at a suitable [M^+]. Such a stabilized microenvironment pH is independent of higher [M^+] and the bulk pH of the electrolyte, but correlates with the buffering capacity

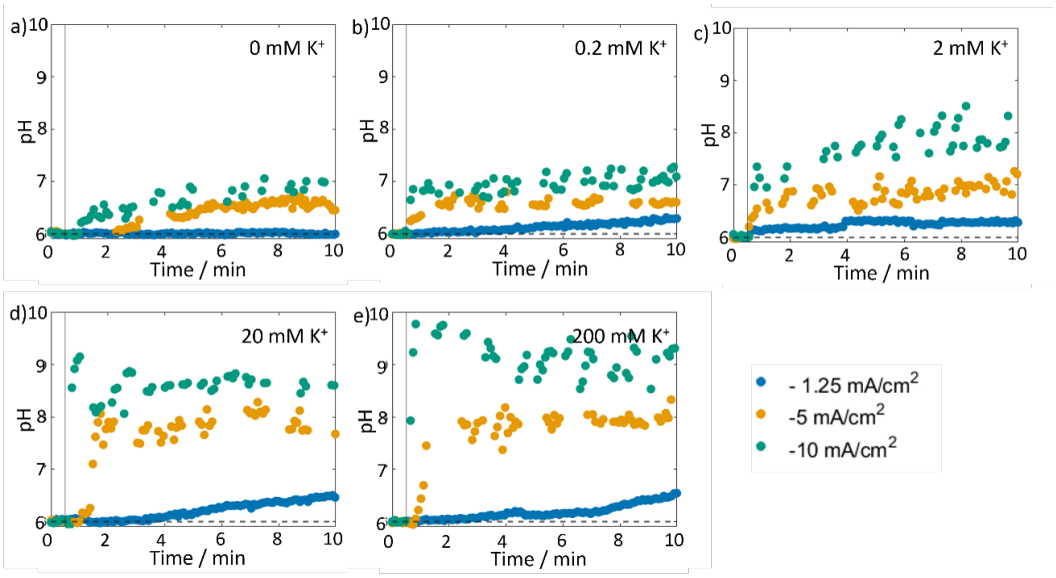

Figure 7.9: Local pH value at the electrode surface as a function of time and current density for (a) 0 mM; (b) 0.2 mM; (c) 2 mM; (d) 20 mM and (e) 200 mM [K^+] in pH 2 H_3PO_4 with 5 SCCM CO_2 flow.

of different solvated M^+ cations based on the pK_a values of their respective solvated H_2O molecules [173].

To promote CO_2R at low [M^+], one possibility is the application of additive films that mitigate H^+ mass transport and thus suppresses HER under strongly acidic conditions. This was tested with a film derived from the electrodeposition of N-tolypyridinium [181]. We found that a non-acidic microenvironment pH can be quickly established via efficient suppression of H^+ mass transport. CO_2R (FE_{CO_2R} ≈6%) on Cu/film electrodes is observed in nearly M^+-free pH 2 H_3PO_4, and is dramatically boosted to FE_{CO_2R} ≈60% in pH 2 H_3PO_4 at low [K^+] (20 mM). The added K^+ is believed to buffer the microenvironment pH in favor of CO_2R. Finally, in strongly acidic pH 1 H_3PO_4, FE_{CO_2R} ≈55% can be achieved on a film-modified Cu GDE at 0.1 M K^+ and <j> = -50 mA/cm^2. This result is distinct from the conditions needed previously to achieve such high FE_{C2+} ([M^+] > 1M and <j> > -500 mA/cm^2). This study hence establishes a promising strategy to promote CO_2R under acidic conditions using film-decorated electrodes, where a favorable microenvironment displaying a non-acidic pH, as required for CO_2R, is accessible.

7.4 Conclusion

In conclusion, we studied CO_2R in aqueous pH 2 H_3PO_4 with varying $[M^+]$ with a combination of electrocatalytic techniques and operando electrode surface pH measurements via CLSM. This reveals a mechanistic correlation between non-acidic microenvironment pH and the onset of CO_2R. At an appropriate current density <j>, CO_2R can occur in aqueous pH 2 H_3PO_4 via rapid depletion of local H^+. This process builds up a non-acidic microenvironment to attenuate the H^+ reduction process and thus facilitate CO_2R.

The presence of M^+ is not strictly required for CO_2R under acidic conditions, but can effectively increase and then buffer the microenvironment pH due to the mitigation of H^+ mass transport. This attenuates HER and thereby promotes CO_2R. Elevated $[M^+]$ leads to the build-up of a steady state non-acidic microenvironment pH at a constant <j>, which is independent of the pH and $[M^+]$ in the bulk electrolyte, and correlates with the buffering capacity of the solvated M^+.

Overall, our results suggest that a non-acidic microenvironment is the essential requirement for CO_2R in acidic bulk electrolytes.

Chapter 8

FLUORESCENT CARBON MONOXIDE PROBES IN ELECTROCHEMICAL CO_2 REDUCTION APPLICATIONS ON THE EXAMPLE OF NCCA: CHALLENGES AND PERSPECTIVES

A. E. B. conceptualized the study, performed literature research to identify a suitable probe, conducted ICP-MS experiments and performed and supervised confocal laser-scanning imaging experiments as well as data analysis.

8.1 Introduction

In the last Chapters (2, 3, 4, 5, 6 and 7), a technique to measure the spatially resolved pH value in CO_2R applications was presented and applied in various contexts. This is very useful since it offers the opportunity to gain spatially resolved information about the CO_2R process. Unfortunately, it can only indirectly (e.g., in combination with simulations, see chapter 4) provide information about the product selectivity. Specifically, it is unable to distinguish if a measured increased local pH value is the result of CO_2R or of HER.

On the other hand, the most common experimental technique to separate gaseous products and hence, evaluate the selectivity of CO_2R devices is gas chromatography (GC) that provides insight into the amount of different gaseous products formed, including CO, methane, ethane, ethylene and hydrogen. While this method is invaluable to determine the average product selectivity of bulk electrodes, it fails to provide spatial information about where different products are formed.

It would be highly desirable to measure the local concentrations of different CO_2R products around CO_2R electrodes with micrometer-scale three-dimensional spatial resolution as this would enable the identification of areas with a particularly high activity towards certain products. This possibility could provide more direct information about the CO_2R performance than local pH measurements. It would be particularly useful for samples with micrometer-scale inhomogeneities like trenches as presented in Chapters 2, 4 and 5 or tandem catalysis samples[182–184]. Locally resolved CO_2R product concentration data around operating CO_2R electrodes would enable the targeted optimization of electrodes with the goal of enhanced selectivity.

Since CO is the most common and simplest CO_2R product, it is the molecule that we focus on in this study.

Several studies that attempt to address the question of the CO distribution on a CO_2R electrode surface have been published. This includes surface-enhanced infrared absorption spectroscopy (SEIRAS) [185, 186], surface-enhanced Raman spectroscopy (SERS) [85, 187], and electrochemical real-time mass spectrometry (EC-RTMS) [188, 189]. However, none of these techniques offers the possibility to map the local CO concentration with three-dimensional micrometer-scale spatial resolution. This capability is crucial as it allows to identify sites with enhanced CO activity. Three-dimensional resolution is important to resolve electrodes that are not completely planar but exhibit features like surface facets, trenches, edges or micrometer-scale pores.

The three-dimensional imaging of the micrometer-scale CO concentration is a field of research that is actively pursued for the use in life-science and biological applications. Despite being toxic at high concentrations, CO is a molecule that is of high importance in biological research and for example plays a role as a cell-signaling molecule in living cells [190, 191]. To realize the three-dimensional imaging of the local CO concentration in biological applications, fluorescent laser-scanning confocal microscopy is used together with a CO-sensitive fluorescent probe. The general working mechanism is very similar to that of pH imaging with confocal microscopy as presented in the previous chapters. Over the past decade, a variety of fluorescent CO probes has been published, see Table 8.1. They operate primarily on the principles of Tsuji-Trost reactions, a palladium-mediated carbonylation or protonation reaction which requires the addition of heavy metal ions, in most cases Pd^{2+}. A smaller number of probes works without heavy metal ions and relies on the reduction of nitro groups to amino groups. All probes have in common that the reaction with CO leads to changes in the fluorescence intensity that signal the presence of CO and can be detected with CLSM.

Despite the tremendous potential, CLSM in combination with fluorescent CO probes has not been used to map the local CO concentration in electrochemical systems yet. As a consequence, CO fluorescent probes optimized for the application in electrochemical applications are yet to be developed. The requirements for a dye to be used in the context of electrochemistry differ from those that are developed for the use in life sciences. Some important characteristics are listed in Table 8.1 while others are not commonly reported in publications that are targeted towards

Table 8.1: Comparison of a selection of fluorescent CO probes that have been reported in literature. λ_{ex} is the excitation wavelength, λ_{em} the emission wavelength. Note that this table does not list all reported fluorescent CO probes but only those that were considered to exhibit superior performance (e.g., wide detection range, short response time, ratiometric properties or metal-free).

Probe	Reference	λ_{ex} (nm)	λ_{em} (nm)	Metal-mediated	Detection Range	Response Time	Ratiometric	Solvent
HPQ-BI-CO	[192]	400	450	Pd^{2+}	30 nM - 100 μM	2 min	No	PBS, DMSO
Rh-NIR-CO	[193]	541	676	Pd^{2+}	37 nM - 100 μM	5 min	No	PBS, 1% DMSO
Nap-Pd	[194]	440	527	Pd^{2+}	1 μM - 1000 μM	5 min	No	Dichloro-methane
CDCI-CO	[195]	510	710	Pd^{2+}	33 nM - 100 μM	10 min	No	PBS
FL-CO-1	[196]	490	520	Pd^{2+}	37 nM - 300 μM	15 min	No	PBS, 0.05% DMSO
Probe 1	[197]	420	472, 545	Pd^{2+}	58 nM - 35 μM	20 min	Yes	NaH_2PO_4/ K_2HPO_4, 30% DMSO
BTCV-CO	[198]	465	546, 710	Pd^{2+}	30.8 nM - 50 μM	20 min	Yes	PBS, 5% DMSO
Ratio-CO	[199]	430	455, 545	Pd^{2+}	17.9 nM - 50 μM	20 min	Yes	DMSO
Probe 2	[200]	490	527	Pd^{2+}	29 nM - 400 μM	20 min	No	PBS, 0.5% DMSO
Pd-BNP-OH	[201]	405	510	Pd^{2+}	1.9 μM - 825 μM	150 min	No	PBS, 5% DMSO
COSer	[202]	516	520-600	No	1 μM - 10 μM	10 min	No	25 mM MOPS
NIR-CO	[203]	580	665	No	6.1 nM - 160 μM	10 min	No	HEPES, 30% DMSO
LysoFP-NO2	[204]	440	525	No	600 nM - 100 μM	20 min	No	HEPES, 1% DMSO
HCP	[205]	420	450-700	No	21 nM - 80 μM	30 min	No	PBS
NAP-CO	[206]	441	531	No	19 nM - 200 μM	30 min	No	PBS, 10% DMSO
NCCA	[207]	405	450	No	12 nM - 800 μM	30 min	No	PBS, 1% DMSO
NucFP-NO_2	[208]	440	520	No	180 nM - 100 μM	45 min	No	HEPES, 2% DMSO

the biology community. The following criteria are strictly required for a CO probe that is to be used in electrochemical applications:

1. The excitation and emission wavelengths of the probe should be compatible with common confocal microscopes. Most CO dyes that have been reported fulfill this criterion since it's also required for the application in life-science experiments.

2. The probe must be metal-free and not require the addition of metal ions that could plate out and poison the cathode and hence significantly alter the electrochemical process. As noted in Table 8.1, top half, a majority of

fluorescent CO probes requires the addition of heavy metal ions like palladium (Pd^{2+}). This is detrimental for electrochemical CO_2R systems since Pd^{2+} can plate out on the cathode when a bias is applied. Palladium, even as a monolayer, is known to be a very potent catalyst for the parasitic hydrogen evolution reaction (HER) [209–211] that is to be suppressed to perform CO_2R efficiently and selectively.

3. The probe should be selective towards CO without interacting with other molecular species that are typically present in CO_2R experiments, including CO_2, water, formic acid, methanol, methane, ethanol, ethylene, carbonate and bicarbonate, among others. Importantly, it should not interact with H^+ or OH^- molecules that determine the local pH value. Many reports test a CO probe's selectivity compared to other biologically relevant molecules like cysteine, glutathione, and homocysteine [195, 197, 198, 200, 201] but do not focus on molecular species that are important in the context of CO_2R. Some reports present observations of a probe's stability for varying pH values, with different results.

4. The probe should be stable under electrochemical operation; it should not alter the system or interact with the cathode or anode. Since this is a requirement that is not relevant in biological studies, this criterion is generally not considered in existing publications about fluorescent CO dyes.

5. The probe should exhibit a wide detection range with a lower detection limit < 1 μM and up to 1000 μM which corresponds to the maximum solubility of CO in water [212]. It is expected that in CO_2R systems, high CO concentrations up to the solubility limit will be observed. However, in a biological context, much lower CO concentrations are relevant. Hence, most reported probes have a lower detection limit well below 1 μM which is sufficient for CO_2R applications. However, on the other end of the detection range, the maximum limit is often below or on the order of 100 μM, see Table 8.1.

Further criteria that are not strictly required but that an ideal fluorescent CO probe to be used in electrochemical applications would exhibit are:

6. The probe should have a quick response time, ideally on the order of seconds. Unfortunately, most reported probes have a response time well above one minute, with most having a response time >20 minutes, see Table 8.1.

7. Ideally, the probe should be ratiometric. The advantage of this method is that the observed signal does not depend on the local dye concentration which makes the measurement easier and more reliable. So far, only few ratiometric fluorescent CO probes have been reported and unfortunately, they all require the addition of metal ions and are therefore not suitable [197–199].

8. The probe should be reversible since this makes CO concentration measurements easier and more accurate. Reported CO probes are almost exclusively irreversible.

9. Typically, CO_2R experiments are carried out in aqueous electrolytes. Ideally, the probe should be water-soluble. Most CO dyes that have been reported require the addition of a small amount of organic solvent, see Table 8.1.

10. Ideally, the probe should be commercially available or easy and cheap to synthesize. With very few exceptions, reported CO probes are not commercially available.

Note that the fluorescent pH probes DHPDS and APTS described in previous chapters fulfill all requirements listed above as applicable to pH probes. This explains the success we had with these two probes, compare chapters 2 - 7.

On the other hand, to the best of our knowledge, no fluorescent CO dye has been reported that fulfills all listed requirements. After carefully reviewing the existing literature, we identified the probe NCCA (7-nitro-2-oxo-2H-chromene-3-carboxylic acid) [207] as one of the most promising for the use with electrochemical CO_2R systems. It exhibits a coumarin fluorophore with a reactive aromatic nitro group that, upon exposure to CO, is reduced to an amino group which turns the fluorescence of the molecule on, see schematic in Fig. 8.1 (b). NCCA has been demonstrated to image local CO concentrations in living cells. The fluorescent emission signal is a function of the local CO concentration. It can be excited at 405 nm and emits a photon with a maximum intensity at a wavelength of 450 nm which makes it compatible with standard confocal microscopy systems. Importantly, it is a metal-free probe and does not require the addition of heavy metal ions. It has been shown to exhibit a stable signal for pH values 6 - 12. The selectivity has been demonstrated for biologically relevant molecular species but not for molecules that are important for the process of CO_2R. The stability under electrochemical operation has not been tested. The lower detection limit is reported as 12 nM CO, and the linear detection

range reaches a concentration of 20 μM. However, the fluorescent signal continues to increase, despite not linearly, up to a concentration of 800 – 1000 μM. The response time is listed as 30 min. The probe in neither ratiometric nor reversible. Low concentrations of the organic solvent DMSO are required to dissolve NCCA in water. It is not commercially available.

In this study, we investigate the suitability of reported fluorescent CO probes for the application in electrochemical CO_2R devices. In particular, we closely examine the probe NCCA. In a first step, we show that for the application in electrochemical systems, a probe must be metal-free. We then demonstrate that the metal-free NCCA indeed acts as a sensor for CO molecules. We highlight challenges, including the calibration of a fluorescent CO probe and the reduction of NCAA at the cathode surface which leads to an uncontrolled fluorescence turn-on. We point out how the challenges can potentially be addressed, e.g., by the operation within a narrow potential window or via the application of additive coatings. We further report on fluorescent probes that have the potential to detect CO_2R products beyond CO. We point out where the opportunities are and propose future directions.

8.2 Methods

Identification of Pd^{2+} Deposits on the Cathode

We performed experiments to verify if CO probes that require the addition of Pd^{2+} lead to Pd deposits on CO_2R electrodes. Following the procedure described in [200] to sense CO with "Probe 2," we used 5 μM $PdCl_2$ dissolved in the common CO_2R electrolyte aqueous 100 mM $KHCO_3$. An electrochemical cell like the one used for CLSM characterization (see below, analogous to the cells used in previous chapters) with the addition of a gas chamber to accommodate the use of a gas diffusion electrode (GDE) was utilized. As the cathode, a gas diffusion electrode (GDE) made of Sigracet 39 BC carbon paper with a 300 nm copper catalyst layer was used. The anode was a Pt mesh and the reference electrode a leakless Ag/AgCl electrode. The electrolyte was pumped through two perpendicular inlet tubes at a flow rate of 6 mL/min and a CO_2 gas stream of 10 SCCM was guided through the gas chamber. A series of CO_2R experiments was performed both with Pd spiked electrolyte and Pd-free electrolyte for separate samples. To emulate a typical CO_2R experimental set, ten different current densities between 0 mA/cm^2 and -100 mA/cm^2 in steps of 10 mA/cm^2 were applied for 12 minutes each. Subsequently, the used GDE samples were investigated with inductively coupled mass spectrometry (ICP-MS) to determine if Pd is present on the sample surfaces.

NCCA Synthesis

The fluorescent CO probe NCCA was synthesized in-house following the procedure described in [207] using the raw materials 2-hydroxy-4-nitro-benzaldehyde, malonic acid diethyl ester and hexahydropyridine. The resulting product NCCA is a light yellow solid.

NCCA Calibration Attempts

A 1 mM NCCA stock solution was prepared by dissolving 2.4 mg of NCCA in 1.0 mL of DMSO followed by the addition of 9.0 mL of nano-pure water. Our initial fluorescent dye calibration attempt aimed to replicate the results previously reported [207] by utilizing the CO-releasing molecule CORM-3 as the CO source. To achieve this, 10 μM NCCA was dissolved in aqueous 1 M $KHCO_3$. After adding different CORM-3 concentrations (100 μM, 200 μM, 400 μM, 600 μM, 1000 μM and 3000 μM), the fluorescent signal in the solution was collected with CLSM as a function of time over a period of 60 minutes.

To test NCCA's response to gaseous CO, 5 mL of a 1 M $KHCO_3$ electrolyte solution spiked with 10 μM NCCA were purged with CO gas for >1 hour at a rate of 50 SCCM before detecting the fluorescent signal as a function of time with confocal microscopy. To determine an appropriate NCCA concentration for detection purposes, this procedure was repeated with NCCA concentrations of 20 μM, 50 μM, 100 μM, 200 μM, 300 μM, and 500 μM.

All fluorescent calibration measurements were performed with a Leica Stellaris 5 confocal microscope with a 25x water immersion objective. The dye was excited at 405 nm with a laser power of 50 mW, and the emitted fluorescence was collected between 430 and 470 nm with a gain of 20. Images were captured over a 442 μm by 442 μm frame with a resolution of 128 x 128 pixels.

Application of Additive Coatings

Additive Nafion coatings were applied on gold foil electrodes using a Laurell WS-400 6NPP Lite Series spin coater. A Nafion D-520 dispersion at a concentration of 5 w/w% in water and 1-propanol (BeanTown Chemical) was sonicated for at least 30 minutes and then spin-coated on gold foil at 3000 RPM for 45 seconds. Varying layer thicknesses were achieved by applying single layers of a diluted Nafion solution or several layers of undiluted solution. Each layer was allowed to dry for at least two hours in a vacuum-sealed desiccator before the next layer was applied.

Operando Confocal Microscopy Characterization

An electrochemical cell (see Fig. 8.1) compatible with CLSM, similar to the one used in chapter 7 was used to perform fluorescence measurements around operating CO_2R electrodes. It consists of a solid base plate and an open electrolyte chamber with a gas inlet to maintain saturation in the electrolyte. Gold, copper and silver foils as well as gold foils with an additive Nafion coating served as working electrodes, a Ag/AgCl electrode as the reference electrode, and a platinum mesh as the counter electrode. A 1 M $KHCO_3$ electrolyte solution was saturated with CO_2 or, for control experiments, with Argon gas and then spiked with 200 μM NCCA prior to experiments. During operando measurements, a constant gas flow of 10 SCCM CO_2 or Ar was supplied to the electrolyte chamber.

Potentioelectrochemical impedance spectroscopy (PEIS) and chronoamperometry measurements (CA) were performed with a Biologic SP-200 potentiostat. A potential between -0.1 V vs. Ag/AgCl and -1 V vs. Ag/AgCl was applied and the fluorescent signal was measured as a function of time. To measure the fluorescent response, the probe was excited with a laser at 405 nm (50 mW laser power) and the fluorescent emission was collected between 420 nm and 600 nm with a gain of 1. The line average was set to 5, the image size to 512 x 32 pixels, covering 442 μm x 28 μm. The measurements were performed as a z-stack, covering a range in the direction perpendicular to the electrode surface of 100 μm with a step size of 565 nm, starting below the electrode surface and ending in the bulk electrolyte. For data analysis, the frame located 20 μm above the electrode surface was identified and the mean fluorescent intensity, excluding zero-value pixels, was calculated as a function of time.

8.3 Results and Discussion

Heavy Metal Deposits on the Cathode

We investigated the suitability of reported CO probes for the application in CO_2R systems. The main challenge is the lack of fluorescent CO probes that are targeted for the use in electrochemical systems. For instance, many probes require the addition of Pd^{2+} ions to the probe solution that can be deposited on the cathode surface and compromise the CO_2R performance. In a first step, we performed measurements to quantify the amount of Pd^{2+} deposited during a typical CO_2R experiment. To this end, we used two GDE samples with a 300 nm Cu catalyst layer and performed a series of CO_2R experiments, for one sample in a Pd-free electrolyte and for one sample in an electrolyte spiked with 5 μM Pd^{2+}. Using ICP-MS, we compared how

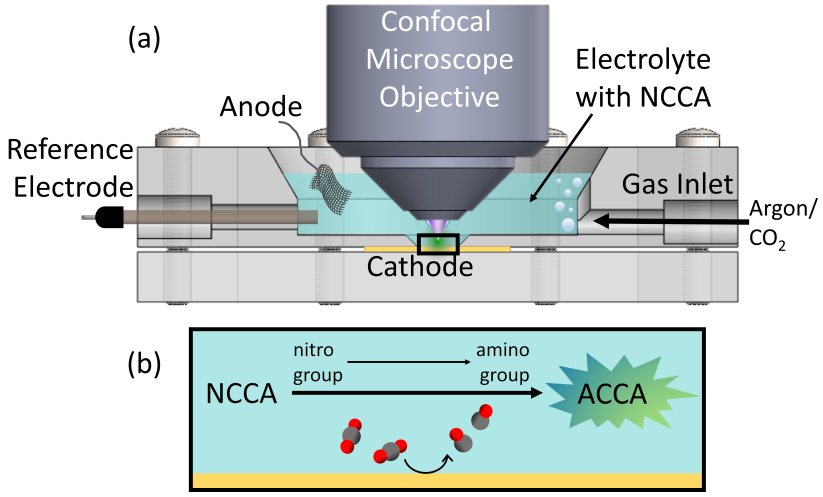

Figure 8.1: [Schematic of the experimental setup and working mechanism of the fluorescent CO probe NCCA. (a) Schematic of the experimental setup, displaying a cross-section of the electrochemical cell together with the water-immersion objective that belongs to the confocal microscope. (b) Schematic of the detection mechanism of NCCA. CO_2 is reduced to CO at the cathode surface. The nitro group of NCCA is reduced by CO to an amino group which leads to a fluorescence turn-on.

much Pd was deposited on the two samples after the experiments, see Fig. 8.2. We found a more than hundred-fold increase in Pd counts for the sample in the electrolyte spiked with Pd^{2+} (Fig. 8.2 C) compared to the sample in the Pd-free electrolyte (Fig. 8.2 A). By comparing the observed Pd counts to the Cu counts, we determined the Pd layer to be $\approx$0.2 nm thick, which corresponds to $\approx$1% of Pd molecules dissolved in the 5 μM Pd^{2+} electrolyte solution. Considering that a monolayer of Pd is sufficient to boost HER over CO_2R [209–211], this is expected to significantly alter the GDE's CO_2R performance. As a result, probes that require the use of Pd^{2+}, even at trace concentrations like 5 μM, are not suitable to probe the local CO concentration in CO_2R systems. The same is expected to hold true for other heavy metal ions that are used in the context of CO probes. Consequently, we decided that the use of metal-free probes like NCCA [207] is essential to image the CO concentration in CO_2R systems.

CO Concentration Calibration and The Unreliability of CORMs

The testing and calibration of fluorescent CO probes requires the preparation of solutions with known CO concentration. Most fluorescent CO probe reports, including the ones listed in table 8.1 and NCCA [207], use one of the CO-releasing molecules CORM-2 or CORM-3 for this purpose. The CORM concentration is usually treated

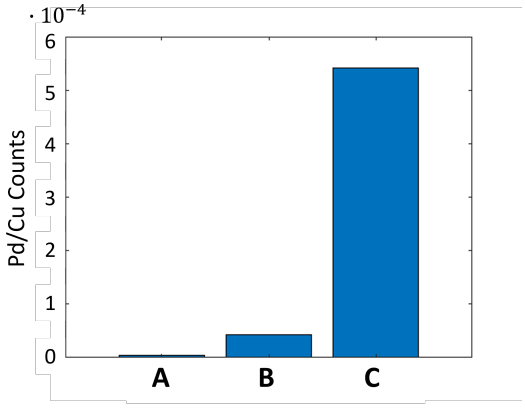

Figure 8.2: ICP-MS measurement results of the ratio of detected Pd to Cu. A is a CO_2R GDE with 300 nm Cu with which experiments had been performed in a Pd-free electrolyte, B and C are results from a sample with 300 nm Cu with which CO_2R experiments had been performed in an electrolyte spiked with 5 μM $PdCl_2$. B is at a location outside of the active surface area, C is within the active surface area that had directly been exposed to the electrolyte.

as being analogous to the CO concentration. Unfortunately, despite the wide use of CORMs, there are recent reports that suggest that CORMs do not perform as anticipated [213–216]. The widely applied CORM-3 for example does not release CO unless a strong nucleophile is present. It further has a pronounced chemical reactivity on its own [214–216]. This raises the question if many CO probes that have been reported in literature and that were only tested with CORMs can indeed sense CO or if they undergo a different kind of chemistry with CORM. When choosing a CO probe for the use in electrochemistry it is therefore of the utmost importance to verify that a probe that had previously only been demonstrated with a CORM also reacts with a more reliable CO source like CO gas.

The probe of our choice, NCCA, had been tested and calibrated with CORM-3. Additionally, it had been demonstrated to fluoresce in living cells [207] where the presence of CO rather than that of CORM-3 is expected which is a first indicator that NCCA can detect CO. In a first step, we tried to replicate the calibration results of NCCA with the use of CORM-3. The addition of CORM-3 to a solution spiked with 10 μM NCCA lead to a strong fluorescent signal turn-on which is in accordance with previous literature reports [207]. However, we were unable to observe a clear trend of an increasing fluorescent signal with increasing CORM-3 concentration. We attribute this observation to the unreliable CO releasing mechanism of CORM-3 [214–216].

As a consequence, we attempted to test NCCA with gaseous CO which, despite being more difficult to handle than CORMs, is a very reliable CO source. When we purged an aqueous 1 M $KHCO_3$ solution that was spiked with 10 μM NCCA with gaseous CO for >1 hour, we detected a small increase of the fluorescent signal (Fig. 8.3 (c)). Once we increased the NCCA concentration to $\geq$ 100 μM, a strong ($\approx$ two-fold) increase of the fluorescent response could be observed once the probe solution had been exposed to CO gas. This is can be observed by a visible color change of the solution (Fig. 8.3 (a)) and by a measurable fluorescent signal increase (Fig. 8.3 (c)). We tested the response for various NCCA concentrations in solution (Fig. 8.3 (b)) and determined that a NCCA concentration of 200 μM is sufficient for the observation of a strong fluorescent response to CO.

This promising result confirms that NCCA does not only react with CORM-3 but also turns its fluorescence on when exposed to CO gas and therefore acts as a CO sensor.

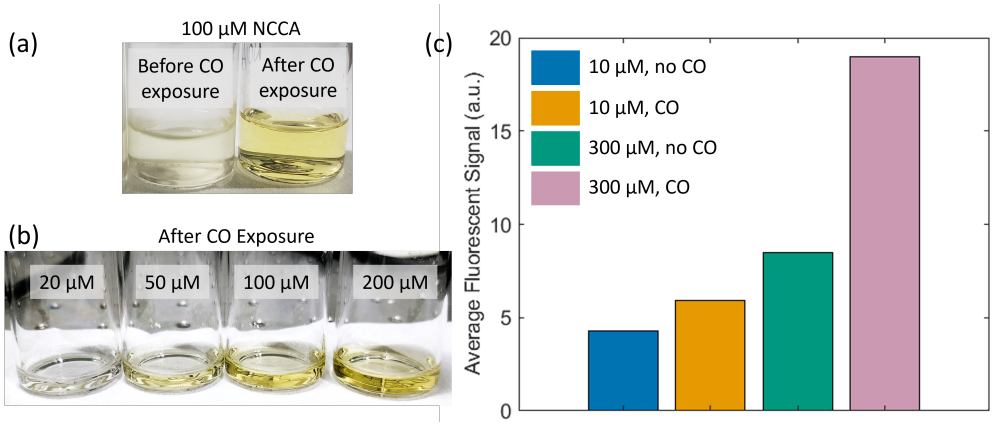

Figure 8.3: Response of NCCA to gaseous CO as photographs and fluorescent signal measurements. (a) Photograph of a solution spiked with 100 µM NCCA before and after exposure to gaseous CO. (b) Photograph of solutions spiked with different concentrations of NCCA after exposure to gaseous CO. (c) Comparison of the fluorescent signal of solutions spiked with 10 µM and 300 µM NCCA, before and after 60 min exposure to gaseous CO.

Unfortunately, it is very challenging to control the CO concentration in a solution using gaseous CO. It is expected that the saturation concentration of 1000 μM CO [212] is reached if a small amount of solution ($\leq$ 6 mL) is purged with gaseous CO for >1 hour. However, as soon as the purged solution is brought into contact with the atmosphere, CO will start to outgas on the time scale of minutes. It is therefore challenging to reliably control a CO concentration between 0 μM and

1000 μM and hold that concentration for at least 30 minutes which is the time required for the fluorescent signal of NCCA to saturate. It is vital to control the CO concentration in solution to connect an observed fluorescent signal with a certain local CO concentration to calibrate the probe.

Possible solutions for this challenge could be the the very careful use of CORMs. It has been shown for example that CORM-3 does release CO in the presence of a strong nucleophile like thiol or sulfite species [216, 217]. It must be kept in mind however that CORM-3 is known to be a reducing agent [218–220] and could have the potential to directly reduce NCCA. A different pathway to make solutions with a known CO content could be to exploit a chemical reaction that produces a known amount of CO like the dehydration of formic acid or oxalic acid [221, 222]. The development of such a procedure is however outside of the scope of this work.

Probe Reduction at the Cathode Surface

The main goal of this study is to enable the imaging of the local micrometer-scale CO concentration around operating CO_2R electrodes. This could help answer questions about their performance and improve the selectivity.

While we were unable to calibrate NCCA and connect the fluorescent signal strength with a known CO concentration, we showed that NCCA can sense gaseous CO. We therefore attempted to employ it to detect CO around operating CO_2R electrodes with different catalyst materials. In contrast to the setups described in Chapters 2, 3, 4, 5 and 6, we decided to use metal foils as the cathode instead of GDEs to ensure that produced CO remains in the electrolyte and can be detected.

Gold, silver and copper are known as good CO_2R catalysts with gold and silver mainly producing CO while copper can make a multitude of products, including CO. All of these catalyst are expected to reduce CO_2 to CO at a potential of -1 V vs. Ag/AgCl [36, 41, 47, 62]. We performed experiments with all three catalyst materials in CO_2-saturated aqueous 1 M $KHCO_3$ electrolyte spiked with 200 μM NCCA. Since the probe NCCA turns its fluorescence on in the presence of CO, it is anticipated that under operando CO_2R conditions, an enhanced fluorescent signal can be observed around the catalyst surface. As a control experiment, all measurements were repeated with argon-saturated aqueous $KHCO_3$ electrolyte. Since no CO_2 is present that could be reduced to CO, a fluorescent signal enhancement is expected for none of the catalysts investigated.

In contrast to the expectation, we observed a strong fluorescent turn-on under operando CO_2R conditions for all three catalyst materials in both CO_2- and argon-saturated electrolytes. Fig. 8.4 displays the average fluorescent signal observed at $\approx$20 μm above the electrode surface as a function of time for the three CO_2R catalyst materials copper, gold and silver in argon- as well as CO_2-saturated electrolytes.

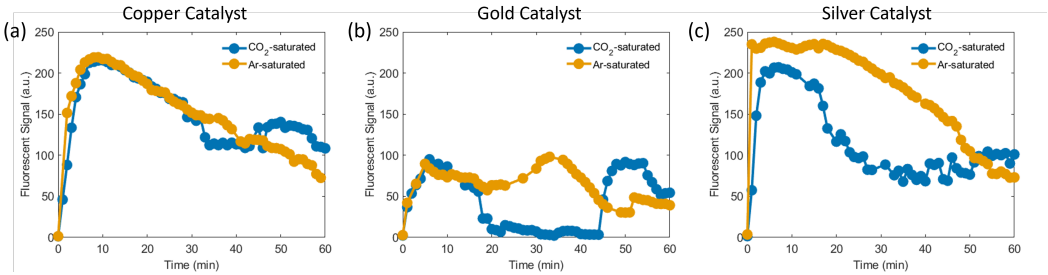

Figure 8.4: Fluorescent signal as a function of time at $\approx$20 μm above the electrode surface in CO_2- (blue) and argon- (orange) saturated 1 M $KHCO_3$ electrolytes with 200 μM NCCA at -1 V vs. Ag/AgCl for the catalysts (a) copper, (b) gold, and (c) silver.

Since no CO can be created at the catalyst surface for the experiments performed with argon-saturated electrolyte, there must be a different mechanism that causes NCCA to fluoresce. The sensing mechanism of NCCA relies on the reducing characteristics of CO and works via the reduction of a nitro- to an amino group [207]. We therefore propose that for all catalyst materials investigated, NCCA is directly being reduced at the cathode rather than by CO which leads to an uncontrolled fluorescence turn-on.

The direct reduction of NCCA at the cathode surface is responsible for the steep fluorescent signal increase within the first few minutes that can be observed for all curves in Fig. 8.4, both in the CO_2- and argon-saturated electrolytes. The fluorescent signal then peaks and slowly decreases again. This behavior can be seen especially well for the curves representing the copper and silver catalyst. For NCCA that is not reduced electrochemically but exposed to CO, the fluorescent signal is expected to increase and then plateau after 30 minutes [207]. The results in Fig. 8.4 differ significantly from this expectation. We hypothesize that within the first few minutes, NCCA molecules that are close to the cathode surface get collectively reduced, causing a quick fluorescent signal enhancement. A possible reason for the slow decrease of the fluorescent signal over the course of an hour could be the slow degradation of NCCA under a strong applied bias. In addition, an applied bias of -1 V vs. Ag/AgCl leads to the formation of gaseous hydrocarbon products as well as hydrogen and hence, to the formation of gas bubbles at the catalyst surface. Since

the fluorescent probe NCCA is not present inside gas bubbles, they cause noise as can be observed in the curves displayed in Fig. 8.4. The issue of gas bubbles is especially severe if the electrode surface is rough because surface roughness can prolong the residence time of bubbles [223] which leads to the accumulation of bubbles and hence, more noise. The gold foil used in these experiments exhibits a greater surface roughness than the other metal foils which explains the elevated noise levels that are observed for the gold catalyst and the close-to-zero fluorescent signal for the CO_2-saturated electrolyte over the course of several minutes.

The direct reduction of NCCA at the surface of all investigated catalysts makes it impossible to distinguish if an observed fluorescent signal originates from the reduction via a CO molecule or from the direct reduction at the cathode surface and therefore makes CO sensing around operating CO_2R electrodes very challenging.

Influence of the Potential on the Fluorescent Signal

In a next step, we investigated the influence of the potential on NCCA's fluorescent signal around a gold cathode, both in argon- and CO_2-saturated electrolyte. If the onset potential of the NCCA reduction is more negative than the onset potential for CO_2R on a given catalyst, a potential window exists within which CO_2R can proceed and create CO, but NCCA is not directly reduced by the cathode and can therefore be used to reliably detect local CO. This could present a possible solution to the problem of direct NCCA reduction at the cathode surface.

To determine the NCCA reduction onset potential on a gold foil cathode, we observed the fluorescent signal in argon-saturated electrolyte for various potentials between -0.60 V vs. Ag/AgCl and -0.78 V vs. Ag/AgCl, see Fig. 8.5 (a). Since no CO is expected at the cathode surface in that system, any observed fluorescence turn-on can be attributed to the direct NCCA reduction at the cathode. We observed a distinct enhancement of the fluorescent signal at -0.72 V vs. Ag/AgCl (orange curve) or more negative potentials. We conclude that the onset potential of NCCA reduction on a gold foil cathode is -0.72 V vs. Ag/AgCl.

We then repeated these experiments in CO_2-saturated electrolyte (Fig. 8.5 (b)) for potentials between -0.60 V vs. Ag/AgCl and -0.65 V vs. Ag/AgCl and observed a strong fluorescence turn-on already at a potential of -0.64 V vs. Ag/AgCl. The inset in Fig. 8.5 (a) shows the curves in Ag-saturated electrolyte for the same potential range and no increase in fluorescent signal can be observed. We conclude that the fluorescent signal observed between -0.64 V vs. Ag/AgCl and -0.72 V vs. Ag/AgCl

in CO_2R-saturated electrolyte originates not from direct NCCA reduction at the cathode but from CO molecules created via CO_2R.

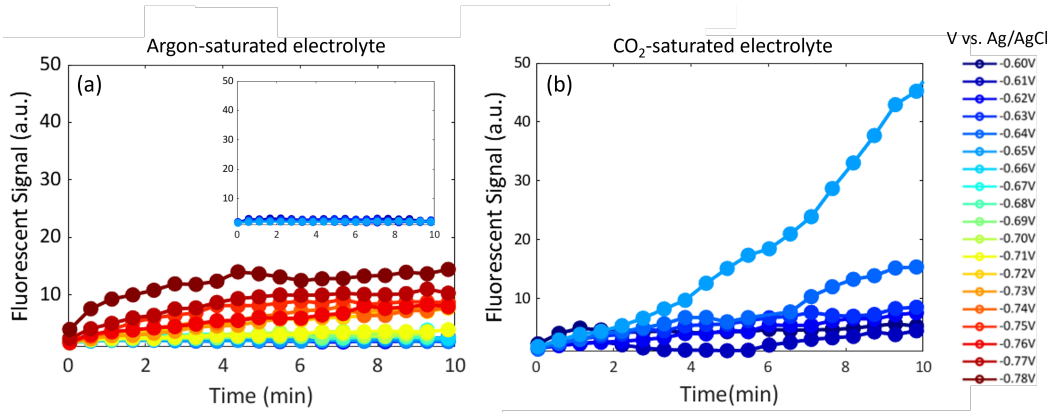

Figure 8.5: Fluorescent signal at 20 μm above the surface of a gold foil cathode as a function of time in (a) argon-saturated and (b) CO_2-saturated electrolyte with 200 μM NCCA for (a) potentials between -0.60 V vs. Ag/AgCl and -0.78 V vs. Ag/AgCl and (b) as well as (a) inset between -0.60 V vs. Ag/AgCl and -0.65 V vs. Ag/AgCl. The least negative potential in (a) for which a change in fluorescent signal can be observed is -0.72 V vs Ag/AgCl which is determined as the onset potential of NCCA. The least negative potential in (b) for which a change in fluorescent signal can be observed is -0.64 V vs Ag/AgCl which is determined as the onset potential of CO_2R.

Hence, NCCA could potentially be used to reliably image the local CO concentration around a gold foil $CO_2$2R electrode between -0.64 V vs. Ag/AgCl and -0.72 V vs. Ag/AgCl. However, it must be noted that this is a very narrow potential window and its reproducibility has not been verified. Further, the onset potential for both CO_2R and NCCA reduction can differ between catalysts, electrolytes, and experimental setups. It is therefore crucial to determine the onset potentials for both CO_2R and NCCA reduction individually for every experimental setup to take advantage of the potential window between CO_2R and NCCA reduction for CO concentration imaging.

Additive Coatings

As an alternative solution to the direct reduction of NCCA at a cathode, we tested the application of an additive coating that could prevent NCCA from getting into direct contact with the catalyst surface while still allowing the effective transport of CO_2 and its reduced products.

In a first test experiment, we applied the ionomer Nafion on a gold foil cathode via three-fold spin-coating and measured the fluorescent signal in argon-saturated electrolyte as a function of time for various potentials between -0.1 V vs Ag/AgCl and -1 V vs Ag/AgCl, see Fig. 8.6. We observed that a strong fluorescence turn-on persists despite the Nafion coating for potentials more negative than -0.7 V vs. Ag/AgCl. This result is in line with the observations made around a gold foil cathode without a coating in argon-saturated electrolyte, see Fig. 8.5 (a). We hypothesize that NCCA gets soaked up into the Nafion layer, leading to a counterproductive effect. Nafion is therefore not a suitable coating to prevent electrochemical NCCA reduction.

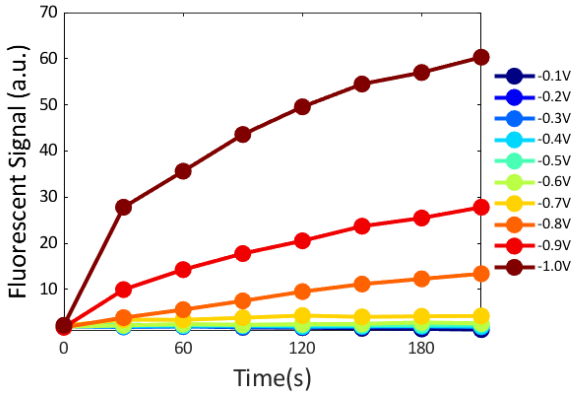

Figure 8.6: Fluorescent signal as a function of time at ≈20 μm above the electrode surface in argon-saturated electrolyte spiked with 200 μM NCCA for a gold catalyst with three layers of spin-coated Nafion for potentials between -0.1 V vs. Ag/AgCl and -1.0 V vs. Ag/AgCl. The fluorescent signal turn-on persists for potentials < -0.7 V vs. Ag/AgCl despite the Nafion coating.

Various alternative coating materials exists that could be used in the future to achieve the desired effect. Several additive coatings derived for example from N-tolyl pyridinium, phenyldiazonium or diphenyliodonium salts have been reported to suppress HER and boost the CO_2R performance [224–227]. It is possible that these films could prevent the reduction of NCCA at the cathode. Further, the capability to image the local CO concentration in and around these films could shine light onto the underlying working mechanisms of these films.

An alternative possible solution could be the use of molecular weight cutoff (MWCO) membranes that are permeable to small molecules but serve as a physical barrier towards molecules above a certain molecular weight [228, 229]. Since NCCA has a much larger molecular weight than CO_2 or its most prominent reduced products,

a wisely chosen membrane would not inhibit the transport of CO_2R but prevent the direct reduction of NCCA at the cathode surface.

To test the effect of alternative coatings or membranes as well as to refine and determine the feasibility of operating within a narrow potential window should be the object of future studies.

8.4 Fluorescent Probes Beyond Carbon Monoxide

Several fluorescent probes that can sense important CO_2R products beyond CO have been reported. This includes methanol, formic acid, or ethylene, see Table 8.2. The capability to sense the local concentration of these species in addition to CO with micrometer-scale spatial resolution could present a milestone in the understanding and improvement of CO_2R electrodes.

Table 8.2: Comparison of a selection of reported fluorescent probes that can sense CO_2R products other than CO. λ_{ex} is the excitation wavelength, λ_{em} the emission wavelength.

Probe	**Reference**	Sensing Capacity	λ_{ex} **(nm)**	λ_{em} **(nm)**	**Metal-mediated**	**Detection Range**	**Response Time**	**Ratiometric**	**Solvent**
TTO	[230]	Methanol	320	414	No	124 mM - 12 M	N/A	No	organic solvents
Receptor 1	[231]	Formic Acid	390	625	No	16 nM - 55 nM	N/A	No	Water
TH25	[232]	Formic Acid	365	414, 545	MOF	46 μM - 16 mM	0.5 min	Yes	DMF
FPRu	[233]	Ethylene	365	393	No	42 μM - 71 mM	60 min	No	BSA
BEP-4 & **BEP-5**	[234]	Ethylene	475	513	Ru	321 μM - 8 mM	6 hrs	No	Toluene/ PBS
Silver Complex I	[235]	Ethylene	353	394, 415	Ag complex	up to 62 mM	N/A	Yes	Chloro-form

Unfortunately, none of the probes presented in Table 8.2 fulfills all strictly required criteria for a fluorescent probe to be used in CO_2R applications as identified in the introduction. Since most confocal microscopes cannot excite molecules with λ_{ex} < 405 nm, many of the reported probes are not compatible with standard confocal microscopes. The probes that can be excited contain metals which is problematic in the context of CO_2R due to possible deposits that can promote HER as explained in previous sections. Consequentially, the employment of these probes for imaging around CO_2R electrodes presents a challenge.

8.5 Conclusion and Perspectives

We investigated the possibility to use an existing fluorescent CO probe to image the local CO concentration in CO_2R systems. While numerous fluorescent CO probes have been reported for the application in biological systems, no such probe

has been developed specifically for the electrochemistry community. We identified the requirements for such a probe and reviewed the existing literature. We chose the probe NCCA [207] as one of the most promising ones for CO_2R applications because it does not require the addition of heavy metal ions, has a wide CO detection span and is stable over a wide range of pH values.

We synthesized the dye NCCA and tested its feasibility under operando CO_2R conditions. We could show that NCCA does turn its fluorescence on upon the exposure to gaseous CO. However, we identified several challenges connected to the use of NCCA and existing CO probes in general in electrochemical systems.

1. The calibration process of fluorescent CO probes is very challenging. It requires to find the relation between a fluorescent signal and a known concentration of CO in solution. To make solutions with a controlled CO concentration, CO-releasing molecules like CORM-2 and CORM-3 had been widely applied in literature but recent reports have shown that they do not reliably release CO and posses a chemical activity of their own [213–216, 218–220]. CO gas on the other hand is a very reliable CO donor but much more difficult to handle and it is very challenging to control the CO concentration in solution using gaseous CO. A possible solution could be the careful use of CORMs with nucleophiles that trigger the release of CO [217] or the exploitation of chemical reactions that produce known amounts of CO [221, 222] but that is outside of the scope of this study.

2. While a small number of ratiometric CO probes have been reported (see Table 8.1), they all require the addition of heavy metal ions which renders them unsuitable in the context of CO_2R applications. All reported metal-free probes are not ratiometric. As a result, very careful attention must be paid to ensure that the probe concentration is constant throughout the whole system.

3. All reported CO probes are irreversible and have response times > 10 minutes. This makes both the data aquisition and interpretation difficult.

4. We observed that under operando CO_2R conditions, the probe NCCA is reduced directly at the cathode surface which leads to an uncontrolled fluorescence turn-on and makes signal deconvolution impossible. Initial attempts to prevent the probe reduction via coating the cathode with Nafion failed.

To the best of our knowledge, all fluorescent CO probes that have been reported to this date either rely on the addition of heavy metal ions or on the reduction of a nitro- to an amino group. The first impede the performance of a CO_2R system while the latter are prone to a direct reduction at the cathode surface in electrochemical systems. Consequently, it can be doubted that alternative CO probes that have been reported are less challenging to use in electrochemical systems than NCCA.

A possible solution to the challenge of the direct probe reduction at the cathode could be the operation within a potential window between the onset potential of NCCA reduction and the onset potential of CO_2R. For a gold catalyst, we determined the onset potential of NCCA reduction to be -0.64 V vs. Ag/AgCl and the onset potential of CO_2R to be -0.72 V vs. Ag/AgCl. This encouraging result suggests that such a potential window exists. However, it must be kept in mind that it is very narrow, the reproducibility has not been confirmed and it is expected that it differs between different experimental setups.

Alternative applications of NCCA or other fluorescent CO probes, e.g., in pulsed electrolysis or tandem catalysis systems present a challenge due to the irreversible characteristics of the probes. It could however be possible to apply NCCA in other chemical systems like thermochemical CO_2R setups [236].

While probes for CO_2R products beyond CO have been reported, they all have inherent problems like the required addition of metal species or incompatibility with commercially available confocal microscopes.

In conclusion, the application of existing fluorescent CO probes in electrochemical applications is extremely challenging and requires considerably more work that is beyond the scope of this work.

As a perspective, we believe that the most promising way forward is the development of novel fluorescent CO probes that are targeted for the use in electrochemical systems and fulfill the requirements listed in section 8.1. Specifically, the probe's sensing mechanism should not rely on a reduction process that can also be triggered electrochemically. It should further be reversible and ratiometric.

Chapter 9

CONCLUSION AND OUTLOOK

The central theme of this work is the interplay between a CO_2R electrode's microenvironment and its CO_2R performance. To this end, we performed operando fluorescent confocal laser-scanning microscopy measurements and combined the results with gas chromotography product detection and multiphysics simulations.

The first few chapters focus on the investigation of CO_2R GDEs with operando pH imaging with three-dimensional spatial resolution as well as time resolution. Chapter 2 demonstrates the three-dimensional imaging of the local operando pH value around copper CO_2R GDEs with the fluorescent probe DHPDS. We found that the pH increases as a function of current density and proximity to the GDE. Interestingly, we identified nonuniform hotspots of locally enhanced pH at relatively low overpotentials. We further observed that the pH is higher in trenches compared to the surrounding surface and that the local pH increases as the trench width decreases. Multiphysics simulations confirmed these results and further revealed the superior catalyst performance inside trenches. This presents the first systematic study of the influence of micrometer-scaled cavities in a GDE on CO_2R performance and inspired the following chapters.

In Chapter 3, we performed time-dependent confocal laser-scanning microscopy measurements to observe how CO_2 diffuses through an inhomogeneous GDE at open circuit. It was found that CO_2 reaches the electrolyte inside microcavities first before it diffuses to the bulk electrolyte. The circulation of electrolyte has a dramatic effect on the pOH and with it, the CO_2 concentration since OH^- is transported away via convection, leading to a concentration gradient with the highest CO_2 concentration confined to trenches. Both microcavities and large pore sizes can promote faster CO_2 transport through a GDE.

Chapter 4 provides more evidence for the close relation between a GDE's micrometer-scale morphology and the CO_2R performance. The pOH sensing capacity is extended with an additional fluorescent probe, APTS, that unlocks a broader measurable pOH range between 0 and 8 (pH 6 – 14). This study is the first demonstration of APTS as a pOH sensor. We confirmed the result reported in Chapter 2 that the pOH is lowest inside narrow trenches $\approx$5 μm wide. This phenomenon is connected

to the trapping of OH^- in confined spaces and to altered mass transport properties. Multiphysics simulations allow to find a correlation between the pOH and C_{2+} FE which suggests that the locally decreased pOH inside narrow trenches is connected to an elevated C_{2+} FE.

Based on the finding that narrow trenches can serve as local CO_2R hotspots with enhanced pH, we demonstrate the fabrication and operation of GDEs that exhibit tailored micromorphology patterns in Chapter 5. We systematically investigate the influence of a GDE's microcavity shape, width, depth and surface coverage with pH imaging, product detection and multiphysics simulations. We find is a close correlation between a GDE's micromorpholgy geometry, the local pH value and the C_{2+} FE that is dictated by an interplay between the effects of electrolyte confinement, surface-to-volume ratio, CO_2 transport and proximity to catalytic surfaces. Both trenches and holes can modestly boost the C_{2+} FE and the effect is most pronounced for features with a width of 5-10 μm, depth of 30 μm and surface coverage of 25% - 50%.

In Chapter 6, confocal pH imaging is applied to investigate how the tuning of a GDE's pore size impacts the CO_2R selectivity on the basis of silver PTFE GDEs. As expected, CO_2 transport is slower through smaller pores which causes a higher pH at the GDE surface. This effect can cause a switching of the reaction pathway for GDEs with small pores and promote the reduction of CO_2 to formate, even though silver is known to be a catalyst that predominantly generates CO. The GDE pore size is an important microenvironment factor that can be adjusted to control the product selectivity.

In Chapter 7, we turn our attention to CO_2R in acidic electrolytes. Using confocal microscopy pH measurements, we find a mechanistic correlation between the onset of CO_2R in acidic bulk electrolytes and a non-acidic microenvironment pH. The latter is created via the rapid depletion of H^+ for sufficiently high current density magnitudes. While the addition of M^+ is not necessary to enable CO_2R in acidic conditions, it can mitigate the H^+ transport and thereby increase and buffer the microenvironment pH. This suppresses HER and therefore promotes CO_2R. We show that a non-acidic microenvironment is the predominant requirement to perform CO_2R in acidic conditions.

Finally, we aim to expand the sensing capabilities of fluorescent confocal laser-scanning microscopy in Chapter 8 through the local detection of CO_2R products, specifically CO. We use the fluorescent CO probe NCCA that had previously been

reported for the use in life-science applications. While we could show that NCCA experiences a fluorescent signal enhancement upon exposure to gaseous CO, we identify various challenges. This mainly includes the direct reduction of NCCA at the catalyst under operando CO_2R conditions which leads to an uncontrolled fluorescence turn-on. Further, the calibration process is very challenging, most reported fluorescent CO probes are not ratiometric, they are irreversible and have long response times > 10 min. Further work is required to enable the imaging of local CO concentrations around CO_2R electrodes with fluorescent confocal laser-scanning microscopy.

As an outlook, we propose the application of the developed confocal pH imaging technique to alternative electrochemical systems. Initial attempts have been made to image the local pH value in and around bipolar membranes (BPMs) with promising results. This has the potential to resolve the internal structure of BPMs and to shed light on the reactions that proceed within and around an operating BPM. It could also provide information about the failure mechanisms of BPMs.

Another system that would benefit from spatially resolved pH imaging is tandem catalysis. Such devices consist of different catalyst materials that can in a first step reduce CO_2 to CO and subsequently reduce CO further to C_{2+} products. While this is a very promising approach, many questions about the working mechanism remain. The spatial resolution of confocal laser-scanning microscopy could answer some of them. Further, it would be very interesting to investigate the local pH value around photoelectrochemical CO_2R devices. This is a very appealing concept because it allows to directly harness solar energy to reduce CO_2. Spatially resolved pH imaging around such devices could answer important questions about the reduction mechanism. Additionally, additive electrode coatings have been developed that can suppress HER and boost the CO_2R FE and it is hypothesized that this is related to a steep pH gradient within the coating. pH imaging with confocal microscopy could be used confirm this theory.

Finally, future work should aim to complete the project presented in Chapter 8 and extend the sensing capabilities of confocal microscopy to CO_2R products. This could be possible via the operation within a narrow potential window or if appropriate electrode coatings are identified. We further suggest that novel fluorescent CO probes specifically for the application in electrochemical devices should be developed. In addition, fluorescent probes that can sense CO_2R products beyond CO should be investigated in more depth.

Overall, we developed and refined a technique to study CO_2R electrodes with three-dimensional sub-micrometer resolution. This work enabled to answer many questions related to the correlation between a CO_2R electrode's microenvironment, specifically the micrometer-scale morphology, and its CO_2R performance. Many exciting opportunities to employ the developed fluorescent confocal laser-scanning microscopy technique to other CO_2R and electrochemical applications remain.

BIBLIOGRAPHY

[1] H. Lee and J. Romero. *Climate Change 2023 Synthesis Report*. Geneva, Switzerland, 2023. DOI: 10.59327/IPCC/AR6-9789291691647.001.

[2] J.-C. Ciscar, A. Iglesias, L. Feyes, and A. Sorial. "Physical and Economic Consequences of Climate Change in Europe". In: *PNAS* 108 (2011), pp. 2678–2683. DOI: https://doi.org/10.1073/pnas.1011612108.

[3] J. E. Olesen and M. Bindil. "Consequences of Climate Change for European Agricultural Productivity, Land Use and Policy". In: *Eur. J. Agron.* 16 (4 2002), pp. 239–262. DOI: https://doi.org/10.1016/S1161-0301(02)00004-7.

[4] J. P. McCarty. "Ecological Consequences of Recent Climate Change". In: *Conserv. Biol.* 15 (2 2002), pp. 320–331. DOI: https://doi.org/10.1046/j.1523-1739.2001.015002320.x.

[5] E. A. Beever and J. L. Belant. *Ecological Consequences of Climate Change, Mechanisma, Conservation and Management*. Boca Raton, FL, USA: CRC Press, 2012.

[6] J. Chateau R. Dellink E. Lanzi. "The Sectoral and Regional Economic Consequences of Climate Change to 2060". In: *Environ. Resource Econ.* 72 (2019), pp. 309–363. DOI: https://doi.org/10.1007/s10640-017-0197-5.

[7] O. Edenhofer, R. Pichs-Madruga, Y. Sokona, E. Farahani, S. Kadner, K. Seyboth, A. Adler, I. Baum, S. Brunner, P. Eickemeier, B. Kriemann, J. Savolainen, S. Schloemer, C. von Stechow, T. Zwickel, and J.C. Minx. *Climate Change 2014: Mitigation of Climate Change. Contribution of Working Group III to the Fifth Assessment Report of the Intergovernmental Panel on Climate Change.* Cambridge, UK and New York, NY, USA: IPCC, Cambridge University Press, 2014.

[8] Engineering National Academies of Sciences and Medicine. *Carbon Dioxide Utilization Markets and Infrastructure: Status and Opportunities: A First Report.* Washington, DC: The National Academies Press., 2023.

[9] Our World in Data. *Greenhouse Gas Emissions*. 2021. URL: https://commons.wikimedia.org/wiki/File:Greenhouse-gas-emission-scenarios-01.png (visited on 09/28/2023).

[10] V. Masson-Delmotte, P. Zhai, H.-O. Poerter, D. Roberts, J. Skea, P. R. Shukla, and A. Pirani. *IPCC Report: Global Warming of 1.5° C*. Tech. rep. Cambridge, UK and New York, NY, USA: IPCC, 2018. DOI: https://doi.org/10.1017/9781009157940.001.

[11] C. Le Quere, R. M. Andrew, P. Friedlingstein, S. Sitch, and J. Hauck. "Global Carbon Budget". In: *Earth Syst. Sci. Data* 10 (4 2018), pp. 2141–2194. DOI: doi:10.5194/essd-10-2141-2018.

[12] U.S. Department of State. *The Long-Term Strategy of the United States: Pathways to Net-Zero Greenhouse Gas Emissions by 2050*. Washington, DC, USA, 2021. URL: https://whitehouse.gov/wp-content/uploads/2021/10/US-Long-Term-Strategy.pdf.

[13] A. Raza, R. Gholami, R. Razaee, V. Rasouli, and M. Rabiei. "Significant Aspects of Carbon Capture and Storage – A Review". In: *Petroleum* 5 (4 2019), pp. 335–340. DOI: https://doi.org/10.1016/j.petlm.2018.12.007.

[14] A. Al-Mamoori, A. Krishnamurthy, A. A. Rownaghi, and F. Rezaei. "Carbon Capture and Utilization Update". In: *Energy Technol.* 5 (6 2017), pp. 834–849. DOI: https://doi.org/10.1002/ente.201600747.

[15] A. Dubey and A. Arora. "Advancements in Carbon Capture Technologies: A Review". In: *J. Clen. Prod.* 373 (2022), p. 133932. DOI: https://doi.org/10.1016/j.jclepro.2022.133932.

[16] J. C. M. Pires, F. G. Martins, M. C. M. Alvim-Ferraz, and M. Simoes. "Recent Developments on Carbon Capture and Storage: An Overview". In: *Chem. Eng. Red. Des.* 89 (9 2011), pp. 1446–1460. DOI: https://doi.org/10.1016/j.cherd.2011.01.028.

[17] P. Aleta, A. Refaie, M. Afshari, A. Hassan, and M. Rahimi. "Direct Ocean Capture: the Emergence of Electrochemical Processes for Oceanic Carbon Removal". In: *Energy Environ. Sci.* 16 (2023), pp. 4944–4967. DOI: https://doi.org/10.1039/D3EE01471A.

[18] climeworks. *Remove to Zero*. 2024. URL: https://climeworks.com/ (visited on 01/04/2024).

[19] captura. *Harnessing the Ocean to Heal the Climate*. 2023. URL: https://capturacorp.com/ (visited on 01/04/2024).

[20] CarbonCapture. *Decarbonizing the Atmosphere with Direct Air Capture Technology*. 2024. URL: https://www.carboncapture.com/ (visited on 01/04/2024).

[21] Aker Carbon Capture. *Capturing Carbon for a Brighter Future*. 2024. URL: https://akercarboncapture.com/ (visited on 01/04/2024).

[22] Z. J. Schiffer and K. Manthiram. "Electrification and Decarbonization of the Chemical Industry". In: *Joule* 1 (2017), pp. 10–14. DOI: http://dx.doi.org/10.1016/j.joule.2017.07.008.

[23] D. Chiaramonti. "Sustainable Aviation Fuels: the Challenge of Decarbonization". In: *Energy Procedia* 158 (2019), pp. 1201–1207. DOI: https://doi.org/10.1016/j.egypro.2019.01.308.

[24] D. Timmons and R. Terwel. "Economics of Aviation Fuel Decarbonization: A Preliminary Assessment". In: *J. Clen. Prod.* 369 (2022), p. 133097. DOI: https://doi.org/10.1016/j.jclepro.2022.133097.

[25] F. Wang, Y. Li, W. Cai, Q. Chen, and M. Chen. "Metal–CO_2 Electrochemistry: From CO_2 Recycling to Energy Storage". In: *Adv. Energy Mater.* 11 (25 2021), p. 2100667. DOI: https://doi.org/10.1002/aenm.202100667.

[26] G. B. Stevens, T. Reda, and B. Raguse. "Energy Storage by the Electrochemical Reduction of CO_2 to CO at a Porous Au Film". In: *JEAC* 526 (1-2 2002), pp. 125–133. DOI: https://doi.org/10.1002/aenm.202100667.

[27] M. M. Rahman, A. O. Oni, E. Gemechu, and A. Kumar. "Assessment of Energy Storage Technologies: A Review". In: *Energy Convers. Manag.* 223 (2020), p. 113295. DOI: https://doi.org/10.1016/j.enconman.2020.113295.

[28] H. Ibrahim, A. Ilinca, and J. Perron. "Energy Storage Systems - Characteristics and Comparisons". In: *Renew. Sustain. Energy Rev.* 12 (5 2008), pp. 1221–1250. DOI: https://doi.org/10.1016/j.rser.2007.01.023.

[29] Y. K. Hori and S. Katsuhei Suzuki. "Production of CO and CH_4 in the Electrochemical Reduction of CO_2 at Metal Electrodes in Aqueous Hydrogencarbonate Solution". In: *Chem. Lett.* (1985), pp. 1695–1698. DOI: https://doi.org/10.1246/cl.1985.1695.

[30] S. Jin, Z. Hao, K. Zhang, Z. Yan, and J. Chen. "Advances and Challenges for the Electrochemical Reduction of CO_2 to CO: From Fundamentals to Industrialization". In: *Angew. Chem. Int. Ed.* 133 (2021), pp. 2–24. DOI: https://doi.org/10.1002/ange.202101818.

[31] M.-Y. Lee, K. T. Park, W. Lee, H. Lim, Y. Kwon, and S. Kang. "Current Achievements and the Future Direction of Electrochemical CO_2 Reduction: A Short Review". In: *Crit. Rev. Environ. Sci. Technol.* 50 (2020), pp. 769–815. DOI: https://doi.org/10.1080/10643389.2019.1631991.

[32] S. Wang, T. Kou, S. E. Baker, E. B. Duoss, and Y. Li. "Electrochemical Reduction of CO_2 to Alcohols: Current Understanding, Progress, and Challenges". In: *Adv. Energy Sustainibility Res.* 3 (2022), p. 2100131. DOI: https://doi.org/10.1002/aesr.202100131.

[33] D. J. G. Ives and G. J. Janz. *Reference Electrodes Theory and Practice*. New York, London: Academic Press., 1961.

[34] Alex J. Welch. "Understanding and Optimizing the Local Catalyst Environment in CO_2 Reduction Electrodes". PhD thesis. California Institute of Technology, 2022.

[35] L. C. Weng, A. T. Bell, and A. Z. Weber. "Modeling Gas-Diffusion Electrodes for CO_2 Reduction". In: *Phys. Chem. Chem. Phys.* 20 (25 2018), pp. 16973–16984. DOI: 10.1039c8cp01319e.

[36] Y. Hori. "Electrochemical CO_2 Reduction on Metal Electrodes". In: *Mod. Aspects Electrochem.* 42 (42 2008), pp. 89–189. DOI: https://doi.org/10.1007/978-0-387-49489-0-3.

[37] A. M. Appel, J. E. Bercaw, A. B. Bocarsly, H. Dobbek, D. L. Dubois, M. Dupuis, J. G. Aerry, E. Fujita, R. Hille, P. J. A. Kenis, C. A. Kerfeld, R. H. Morris, C. H. F. Peden, A. R. Portis, S. W. Ragsdale, T. B. Rauchfuss, J. N. H. Reek, L. C. Seefeldt, R. K. Thauer, and G. L. Waldrop. "Frontiers, Opportunities, and Challenges in Biochemical and Chemical Catalysis of CO_2 Fixation". In: *Chem. Rev.* 113 (8 2013), pp. 6621–6658. DOI: https://doi.org/10.1021/cr300463y.

[38] J. L. White, M. F. Baruch, J. E. Pander, Y. Hu, I. C. Fortmeyer, J. E. Park, T. Zhang, K. Liao, J. Gu, Y. Yan, T. W. Shaw, E. Abelev, and A. B. Bocarsly. "Light-Driven Heterogeneous Reduction of Carbon Dioxide: Photocatalysts and Photoelectrodes". In: *Chem. Rev.* 115 (23 2015), pp. 12888–12935. DOI: https://doi.org/10.1021/acs.chemrev.5b00370.

[39] M. Gattrell, N. Gupta, and A. Co. "A Review of the Aqueous Electrochemical Reduction of CO_2 to Hydrocarbons at Copper". In: *J. Electroanal. Chem.* 594 (1 2006), pp. 1–19. DOI: https://doi.org/10.1016/j.jelechem.2006.05.013.

[40] J. Qiao, Y. Liu, F. Hong, and J. Zhang. "A Review of Catalysts for the Electroreduction of Carbon Dioxide to Produce Low-Carbon Fuels". In: *Chem. Soc. Rev.* 43 (2 2014). DOI: https://doi.org/10.1039/C3CS60323G.

[41] R. Kortlever, J. Shen, K. J. P. Schouten, F. Calle-Vallejo, and M. T. M. Koper. "Catalysts and Reaction Pathways for the Electrochemical Reduction of Carbon Dioxide". In: *J. Phys. Chem. Lett.* 6 (20 2015), pp. 4073–4082. DOI: https://doi.org/10.1021/acs.jpclett.5b01559.

[42] A. Goyal, G. Marcandalli, V. A. Mints, and M. T. M. Koper. "Competition between CO_2 Reduction and Hydrogen Evolution on a Gold Electrode under Well-Defined Mass Transport Conditions". In: *J. Am. Chem. Soc.* 142 (9 2020), pp. 4154–4161. DOI: https://doi.org/10.1021/jacs.9b10061.

[43] Y.-J. Zhang, V. Sethuraman, R. Michalsky, and A. A. Peterson. "Competition between CO_2 Reduction and H_2 Evolution on Transition-Metal Electrocatalysts". In: *ACS Catal.* 4 (10 2014), pp. 3742–3748. DOI: https://doi.org/10.1021/cs5012298.

[44] M. C. O. Monteiro, F. Dattila, N. Lopez, and M. T. M. Koper. "The Role of Cation Acidity on the Competition between Hydrogen Evolution and

CO_2 Reduction on Gold Electrodes". In: *J. Am. Chem. Soc.* 144 (4 2022), pp. 1589–1602. DOI: https://doi.org/10.1021/jacs.1c10171.

[45] H. Dau, C. Limberg, T. Reier, M. Risch, S. Rognan, and P. Strasser. "The Mechanism of Water Oxidation: From Electrolysis via Homogeneous to Biological Catalysis". In: *ChemCatChem* 2 (7 2010), pp. 724–761. DOI: https://doi.org/10.1002/cctc.201000126.

[46] Y.-H. Li and T.-F. Tsui. "The Solubility of CO_2 in Water and Sea Water". In: *J. Geophys. Rev.* 76 (18 1971), pp. 4203–4207. DOI: https://doi.org/10.1029/JC076i018p04203.

[47] A. Bagger, W. Ju, A. S. Varela, P. Strasser, and J. Rossmeisl. *Electrochemical CO_2 Reduction: A Classification Problem*. 2017, pp. 3266–3273. DOI: https://doi.org/10.1002/cphc.201700736.

[48] K. P. Kuhl, T. Hatsukade, E. R. Cave, D. N. Abram, J. Kibsgaard, and T. F. Jaramillo. "Electrocatalytic Conversion of Carbon Dioxide to Methane and-Methanol on Transition Metal Surfaces". In: *JACS* 136 (2014), pp. 14107–14113. DOI: https://doi.org/10.1021/ja505791r.

[49] K. P. Kuhl, E. R. Cave, D. N. Abram, and T. F. Jaramillo. "New Insights Into the Electrochemical Reduction of Carbon Dioxide on Metallic Copper Surfaces". In: *Energy Environ. Sci.* 5 (5 2012), pp. 7050–7059. DOI: 10.1039/c2ee21234j.

[50] S. Nitopi, E. Bertheussen, S. B. Scott, X. Liu, A. K. Engstfeld, S. Horch, B. Seger, I. E. L. Stephens, K. Chan, C. Hahn, J. K. Nørskov, T. F. Jaramillo, and I. Chorkendorff. *Progress and Perspectives of Electrochemical CO_2 Reduction on Copper in Aqueous Electrolyte*. 2019. DOI: 10.1021/acs.chemrev.8b00705.

[51] M. R. Singh, E. L. Clark, and A. T. Bell. "Effects of Electrolyte, Catalyst, and Membrane Composition and Operating Conditions on the Performance of Solar-Driven Electrochemical Reduction of Carbon Dioxide". In: *Phys. Chem. Chem. Phys.* 17 (29 2015), pp. 18924–18936. DOI: https://doi.org/10.1039/C5CP03283K.

[52] A. Q. Fenwick, A. J. Welch, X. Li, I. Sullivan, J. S. DuChene, C. Xiang, and H. A. Atwater. "Probing the Catalytically Active Region in a Nanoporous Gold Gas Diffusion Electrode for Highly Selective Carbon Dioxide Reduction". In: *ACS Energy Lett.* 7 (2 2022), pp. 871–879. DOI: https://doi.org/10.1021/acsenergylett.1c02267.

[53] F. P. G. De Arquer, C.-T. Dinh, A. Ozden, J. Wicks, C. McCallum, A. R. Kirmani, D.-H. Nam, C. Gabardo, A. Seifitokaldani, X. Wang, Y. C. Li, F. Li, J. Edwards, L. J. Richter, S. T. Thorpe, D. Sinton, and E. H. Sargent. "CO_2 Electrolysis to Multicarbon Products at Activities Greater Than 1 A cm^{-2}". In: *Science* 367 (6478 2020), p. 661. DOI: https://doi.org/10.1126/science.aay4217.

[54] A. Botz, J. Clausmeyer, D. Öhl, T. Tarnev, D. Franzen, T. Turek, and W. Schuhmann. "Local Activities of Hydroxide and Water Determine the Operation of Silver-Based Oxygen Depolarized Cathodes". In: *Angew. Chem. Int. Ed.* 57 (38 2018), pp. 12285–12289. DOI: 10.1002/anie.201807798.

[55] S. Dieckhoefer, D. Oehl, J. R. C. Junqueira, T. Quast, T. Turek, and W. Schuhmann. "Probing the Local Reaction Environment During High Turnover Carbon Dioxide Reduction with Ag-Based Gas Diffusion Electrodes". In: *Nanoelectrochemistry* 27 (19 2021), pp. 5906–5912. DOI: https://doi.org/10.1002/chem.202100387.

[56] X. Lu, C. Zhu, Z. Wu, J. Xuan, J. S. Francisco, and H. Wang. "In Situ Observation of the pH Gradient near the Gas Diffusion Electrode of CO_2 Reduction in Alkaline Electrolyte". In: *J. Am. Chem. Soc.* 142 (36 2020), pp. 15438–15444. DOI: 10.1021/jacs.0c06779.

[57] N. Nesbitt and W. A. Smith. "Operando Topography and Mechanical Property Mapping of CO_2 Reduction Gas-Diffusion Electrodes Operating at High Current Densities". In: *J. Electrochem. Soc.* 168 (168 2021), p. 044505. DOI: 10.1149/1945-7111/abf183.

[58] K. Yang, R. Kas, and W. A. Smith. "In Situ Infrared Spectroscopy Reveals Persistent Alkalinity near Electrode Surfaces during CO_2 Electroreduction". In: *J. Am. Chem. Soc.* 141 (40 2019), pp. 15891–15900. DOI: 10.1021/jacs.9b07000.

[59] D. Kolb. "The pH Concept". In: *J. Chem. Educ.* 56 (1979), pp. 49–53.

[60] Z. Zhang, L. Melo, R. P. Jansonius, F. Habibzadeh, E. R. Grant, and C. P. Berlinguette. "pH Matters When Reducing CO_2 in an Electrochemical Flow Cell". In: *ACS Energy Lett.* 5 (10 2020), pp. 3101–3107. DOI: 10.1021/acsenergylett.0c01606.

[61] C. T. Dinh, T. Burdyny, G. Kibria, A. Seifitokaldani, C. M. Gabardo, F. P. García De Arquer, A. Kiani, J. P. Edwards, P. De Luna, O. S. Bushuyev, C. Zou, R. Quintero-Bermudez, Y. Pang, D. Sinton, and E. H. Sargent. "CO_2 Electroreduction to Ethylene via Hydroxide-Mediated Copper Catalysis at an Abrupt Interface". In: *Science* 360 (6390 2018), pp. 783–787. DOI: 10.1126/science.aas9100.

[62] X. Liu, P. Schlexer, J. Xiao, Y. Ji, L. Wang, R. B. Sandberg, M. Tang, K. S. Brown, H. Peng, S. Ringe, C. Hahn, T. F. Jaramillo, J. K. Norskov, and K. Chan. "pH Effects on the Electrochemical Reduction of $CO_{(2)}$ Towards C_2 Products on Stepped Copper". In: *Nat. Commun* 10 (32 2019), pp. 3101–3107. DOI: 10.1038/s41467-018-07970-9.

[63] L. Wang, S. A. Nitopi, E. Bertheussen, M. Orazov, C. G. Morales-Guio, X. Liu, D. C. Higgins, K. Chan, J. K. Nørskov, C. Hahn, and T. F. Jaramillo. "Electrochemical Carbon Monoxide Reduction on Polycrystalline Copper: Effects of Potential, Pressure, and pH on Selectivity toward Multicarbon

and Oxygenated Products". In: *ACS Catal.* 8 (8 2018), pp. 7445–7454. DOI: 10.1021/acscatal.8b01200.

[64] N. T. Nesbitt and W. A. Smith. "Water Activity Regulates CO_2 Reduction in Gas-Diffusion Electrodes". In: *ChemRxiv* (2021). DOI: 10.26434/chemrxiv.13571141.

[65] S. Suter and S. Haussener. "Optimizing Mesostructured Silver Catalysts for Selective Carbon Dioxide Conversion into Fuels". In: *Energy Environ. Sci.* 12 (5 2019), pp. 1668–1678. DOI: 10.1039/c9ee00656g.

[66] M. C. O. Monteiro and M. T. M. Koper. "Measuring Local pH in Electrochemistry". In: *Curr. Opin. Electrochem.* 25 (2021), p. 100649. DOI: 10.1016/j.coelec.2020.100649.

[67] A. J. Leenheer and H. A. Atwater. "Imaging Water-Splitting Electrocatalysts with pH-Sensing Confocal Fluorescence Microscopy". In: *JES* 159 (9 2012). DOI: 10.1149/2.022209jes.

[68] N. C. Rudd, S. Cannan, E. Bitziou, I. Ciani, A. L. Whitworth, and P. R. Unwin. "Fluorescence Confocal Laser Scanning Microscopy as a Probe of pH Gradients in Electrode Reactions and Surface Activity". In: *Anal. Chem.* 77 (19 2005), pp. 6205–6217. DOI: 10.1021/ac050800y.

[69] W. J. Bowyer, J. Xie, and R. C. Engstrom. *Fluorescence Imaging of the Heterogeneous Reduction of Oxygen*. 1996, pp. 2005–2009. DOI: https://doi.org/10.1021/ac9512259.

[70] J.C. O'Brien, J. Shumaker-Parry, and R.C. Engstrom. "Microelectrode Control of Surface-Bound Enzymatic Activity". In: *Anal. Chem.* 70 (1998), pp. 1307–1308. DOI: https://doi.org/10.1021/ac970957t.

[71] S. Cannan, I. Douglas Macklam, and P.R. Unwin. "Three-Dimensional Imaging of Proton Gradients at Microelectrode Surfaces Using Confocal Laser Scanning Microscopy". In: *Commun.* 4 (2002), pp. 886–892. DOI: https://doi.org/10.1016/S1388-2481(02)00482-4.

[72] J. T. Hou, W. X. Ren, K. Li, J. Seo, A. Sharma, X. Q. Yu, and J. S. Kim. "Fluorescent Bioimaging of pH: From Design to Applications". In: *Chem. Soc. Rev.* 46 (2017), pp. 2076–2090. DOI: https://doi.org/10.1039/C6CS00719H.

[73] B. Tassy, A.L. Dauphin, H.M. Man, H. Le Guenno, E. Lojou, L. Bouffier, and A. De Poulpiquet. "In Situ Fluorescence Tomography Enables a 3D Mapping of Enzymatic O_2 Reduction at the Electrochemical Interface". In: *Anal. Chem.* 92 (2020), pp. 7249–7256. DOI: https://doi.org/10.1021/acs.analchem.0c00844.

[74] A. Abou-Hassan, J. F. Dufrêchfer, O. Sandre, G. Mériguet, and V. Cabuil O. Bernard. "Fluorescence Confocal Laser Scanning Microscopy for pH Mapping in a Coaxial Flow Microreactor: Application in the Synthesis of Superparamagnetic Nanoparticles". In: *J. Phys. Chem. C* 113 (2009), pp. 18097–18105. DOI: https://doi.org/10.1021/jp9069459.

[75] B. Fuladpanjeh-Hojaghan, M. M. Elsutohy, V. Kabanov, B. Heyne, and M. Trifkovic adn E. P. L. Roberts. "In-Operando Mapping of pH Distribution in Electrochemical Processes". In: *Angew. Chem. Int. Ed.* 58 (2019), pp. 16815–16819. DOI: https://doi.org/10.1002/ange.201909238.

[76] N. Pande, S. K. Chandrasekar, D. Lohse, G. Mul, J. A. Wood, B. T. Mei, and D. Krug. "Electrochemically Induced pH Change: Time-Resolved Confocal Fluorescence Microscopy Measurements and Comparison with Numerical Model". In: *J. Phys. Chem. Lett.* 11 (17 2020), pp. 7042–7048. DOI: 10.1021/acs.jpclett.0c01575.

[77] A. J. Welch, A. Q. Fenwick, A. Boehme, H.-Y. Chen, I. Sullivan, X. Li, J. S. DuChene, C. Xiang, and H. A. Atwater. "Operando Local pH Measurement within Gas Diffusion Electrodes Performing Electrochemical Carbon Dioxide Reduction". In: *J. Phys. Chem. C* 125 (38 2021), pp. 20896–20904. DOI: https://doi.org/10.1021/acs.jpcc.1c06265.

[78] A. E. Boehme, J. C. Bui, A. Q. Fenwick, R. Bhide, C. N. Feltenberger, A. J. Welch, A. J. King, A. T. Bell, A. Z. Weber, S. Ardo, and H. A. Atwater. "Direct Observation of the Local Microenvironment in Inhomogeneous CO_2 Reduction Gas Diffusion Electrodes via Versatile pOH Imaging". In: *Energy Environ. Sci.* 16 (2023), pp. 1783–1795. DOI: https://doi.org/10.1039/D2EE02607D.

[79] S. Zhu, T. Li, W.-B. Cai, and M. Shaor. "CO_2 Electrochemical Reduction As Probed through Infrared Spectroscopy". In: *ACS Energ Lett.* 4 (3 2019), pp. 682–689. DOI: https://doi.org/10.1021/acsenergylett.8b02525.

[80] O. Ayemoba and A. Cuestar. "Spectroscopic Evidence of Size-Dependent Buffering of Interfacial pH by Cation Hydrolysis During CO_2 Electroreduction". In: *ACS Appl. Mater. Interfaces* 9 (2017), pp. 27377–27382. DOI: https://doi.org/10.1021/acsami.7b07351.

[81] A. Cuestar. "ATR-SEIRAS for Time-Resolved Studies of Electrode–Electrolyte Interfaces". In: *Curr. Opin. Electrochem.* 35 (2022), p. 101041. DOI: https://doi.org/10.1016/j.coelec.2022.101041.

[82] H. Shi, N. Poudel, B. Hou, L. Shen, J. Chen, A. V. Benderskii, and S. B. Cronin. "Sensing Local pH and Ion Concentration at Graphene Electrode Surfaces Using in Situ Raman Spectroscopy". In: *Nanoscale* 10 (2018), pp. 2398–2403. DOI: https://doi.org/10.1039/C7NR08294K.

[83] Z. Zhang, K. Bando, K. Mochizuki, A. Taguchi, K. Fujita, and S. Kawata. "Quantitative Evaluation of Surface-Enhanced Raman Scattering Nanoparticles for Intracellular pH Sensing at a Single Particle Level". In: *Anal. Chem.* 91 (5 2019), pp. 3254–3262. DOI: https://doi.org/10.1021/acs.analchem.8b03276.

[84] H. Wei, E. P. Vejerano, W. Leng, Q. Huang, M. R. Willner, L. C. Marr, and P. J. Vikesland. "Aerosol Microdroplets Exhibit a Stable pH Gradient". In: *Proc. Natl. Acad. Sci. USA* 115 (2018), pp. 7272–7277. DOI: https://doi.org/10.1073/pnas.1720488115.

[85] H. An, L. Wu, L. D. B. Mandemaker, S. Yang, J. de Ruiter, J. H. J. Wijten, J. C. L. Janssen, T. Hartman, W. van der Stam, and B. M. Weckhuysen. "Sub-Second Time-Resolved Surface-Enhanced Raman Spectroscopy Reveals Dynamic CO Intermediates during Electrochemical CO_2 Reduction on Copper". In: *Angew. Chem. Int. Edit.* 60 (30 2021), pp. 16576–16584. DOI: https://doi.org/10.1002/anie.202104114.

[86] M. C. O. Monteiro, L. Jacobse, and M. T. M. Koper. "Understanding the Voltammetry of Bulk CO Electrooxidation in Neutral Media through Combined SECM Measurements". In: *J. Phys. Chem. Lett.* 11 (22 2020), pp. 9708–9713. DOI: https://doi.org/10.1021/acs.jpclett.0c02779.

[87] Z. Zhu, Z. Ye, Q. Zhang, J. Zhang, and F. Cao. "Novel Dual Pt-Pt/IrOx Ultramicroelectrode for pH Imaging Using SECM in Both Potentiometric and Amperometric Modes". In: *Electrochem. Commun.* 88 (2018), pp. 47–51. DOI: https://doi.org/10.1016/j.elecom.2018.01.018.

[88] Y. Zhang, Y. Takahashi, S.P. Hong, F. Liu, J. Bednarska, P.S. Goff, P. Novak, A. Shevchuk, S. Gopal, I. Barozzi, L. Magnania, H. Sakai, Y. Suguru, T. Fujii, A. Erofeev, P. Gorelkin, A. Majouga, D.J. Weiss, C. Edwards, A.P. Ivanov, D. Klenerman, E.V. Sviderskaya, J.B. Edel, and Y. Korchev. "High-Resolution Label-Free 3D Mapping of Extracellular pH of Single Living Cells". In: *Nat. Commun.* 10 (2019), pp. 1–9. DOI: https://doi.org/10.1038/s41467-019-13535-1.

[89] B.P. Nadappuram, K. McKelvey, R. Al Botros, A.W. Colburn, and P.R. Unwin. "Fabrication and Characterization of Dual Function Nanoscale pH-Scanning Ion Conductance Microscopy (SICM) Probes for High Resolution pH Mapping". In: *Anal. Chem.* 85 (2013), pp. 8070–8074. DOI: https://doi.org/10.1021/ac401883n.

[90] C.A. Morris, C.C. Chen, T. Ito, and L.A. Baker. "Local pH Measurement with Scanning Ion Conductance Microscopy". In: *J. Electrochem. Soc.* 160 (2013), H430–H435. DOI: 10.1149/2.028308jes.

[91] W.J. Albery and E.J. Calvo. "Ring–Disc Electrodes. Part 21. pH Measurement with the Ring". In: *J. Chem. Soc.* 79 (1983), pp. 2583–2596. DOI: https://doi.org/10.1039/F19837902583.

[92] A.M. Zimer, M. Medina da Silva, E.G. Machado, H. Varela, L.H. Mascaro, and E.C. Pereira. "Development of a Versatile Rotating Ring-Disc Electrode for In Situ pH Measurements". In: *Anal. Chim. Acta* 897 (2015), pp. 17–23. DOI: https://doi.org/10.1016/j.aca.2015.09.047.

[93] F. Zhang and A.C. Co. "Direct Evidence of Local pH Change and the Role of Alkali Cation During CO_2 Electroreduction in Aqueous Media". In: *Angew. Chem. Int. Ed.* 59 (2020), pp. 1674–1681. DOI: https://doi.org/10.1002/anie.201912637.

[94] J. W. Lichtman and J.-A. Conchello. "Fluorescence Microscopy". In: *Nat. Methods* 2 (2005), pp. 910–919. DOI: https://doi.org/10.1038/nmeth817.

[95] proteintech. *IF Imaging: Widefield versus Confocal Microscopy*. 2022. URL: https://www.ptglab.com/news/blog/if-imaging-widefield-versus-confocal-microscopy/ (visited on 01/28/2024).

[96] A. Bigdeli, F. Ghasemi, S. Abbasi-Moayed, M. Shahrajabian, N. Fahimi-Kashani, S. Jafarinejad, M.A. Farahmand Nejad, and M.R. Hormozi-Nezhad. "Ratiometric Fluorescent Nanoprobes for Visual Detection: Design Principles and Recent Advances - a Review". In: *Anal. Chim. Acta* 1079 (2019), pp. 30–58. DOI: https://doi.org/10.1016/j.aca.2019.06.035.

[97] B. Fuladpanjeh-Hojaghan, M.M. Elsutohy, V. Kabanov, B. Heyne, M. Trifkovic, and E.P.L. Roberts. "In-Operando Mapping of pH Distribution in Electrochemical Processes". In: *Angew. Chem. Int. Ed.* 58 (2019), pp. 16815–16819. DOI: https://doi.org/10.1002/ange.201909238.

[98] W. Shi, X. Li, and H. Ma. "Fluorescent Probes and Nanoparticles for Intracellular Sensing of pH Values". In: *Methods Appl. Fluoresc.* 2 (2014), p. 042001. DOI: 10.1088/2050-6120/2/4/042001.

[99] J.-T. Hou, W. X. Ren, K. Li, J. Seo, A. Sharma, X.-Q. Yu, and J. S. Kim. "Fluorescent Bioimaging of pH: From Design to Applications". In: *Chem. Soc. Rev.* 46 (2017), pp. 2076–2090. DOI: https://doi.org/10.1039/C6CS00719H.

[100] A. Hakonen and S. Hulth. "A High-Performance Fluorosensor for pH Measurements Between 6 and 9". In: *Talanta* 80 (5 2010), pp. 1964–1969. DOI: 10.1016/j.talanta.2009.10.055.

[101] **A. E. Böhme**, A. J. Welch, R. Bhide, C. N. Feltenberger, S. Ardo, and H. A. Atwater. "Reversible Excited-State Photoacids and Photobases as Dynamic Fluorescence Sensors of Local pH". 63/332,540. California Institute of Technology. Non-provisional patent application. Apr. 19, 2023.

[102] R. Bhide, C. N. Feltenberger, G. S. Phun, G. Barton, D. Fishman, and S. Ardo. "Quantification of Excited-State Brønsted–Lowry Acidity of Weak Photoacids Using Steady-State Photoluminescence Spectroscopy and a Driving-Force-Dependent Kinetic Theory". In: *J. Am. Chem. Soc.* 144 (2022), pp. 14477–14488. DOI: https://doi.org/10.1021/jacs.2c00554.

[103] S. Eckert, M.-O. Winghart, C. Kleine, A. Banerjee, M. Ekimova, J. Ludwig, J. Harich, M. Fondell, R. Mitzner, E. Pines, N. Huse, P. Wernet, M. Odelius, and E. T. J. Nibbering. "Electronic Structure Changes of an Aromatic Amine Photoacid along the Förster Cycle". In: *Angew. Chem. Int. Ed.* 61 (27 2022), p. 202200709. DOI: https://doi.org/10.1002/anie.202200709.

[104] A. S. Hall, Y. Yoon, A. Wuttig, and Y. Surendranath. "Mesostructure-Induced Selectivity in CO_2 Reduction Catalysis". In: *J. Am. Chem. Soc.* 137 (47 2015), pp. 14834–14837. DOI: 10.1021/jacs.5b08259.

[105] D. Higgins, C. Hahn, C. Xiang, T. F. Jaramillo, and A. Z. Weber. "Gas-Diffusion Electrodes for Carbon Dioxide Reduction: A New Paradigm". In: *ACS Energy Lett.* 4 (1 2019), pp. 317–324. DOI: 10.1021/acsenergylett.8b02035.

[106] Y. Wang, H. Shen, K. J. T. Livi, D. Raciti, H. Zong, J. Gregg, M. Onadeko, Y. Wan, A. Watson, and C. Wang. "Copper Nanocubes for CO_2 Reduction in Gas Diffusion Electrodes". In: *Nano Lett.* 12 (19 2019), pp. 8461–8468. DOI: https://doi.org/10.1021/acs.nanolett.9b02748.

[107] T. N. Nguyen and C. T. Dinh. "Gas Diffusion Electrode Design for Electrochemical Carbon Dioxide Reduction". In: *Chem. Soc. Rev.* 49 (21 2020), pp. 7488–7504. DOI: 10.1039/d0cs00230e.

[108] D. S. Ripatti, T. R. Veltman, and M. W. Kanan. "Carbon Monoxide Gas Diffusion Electrolysis That Produces Concentrated C_2 Products with High Single-Pass Conversion". In: *Joule* 3 (2019), pp. 240–256. DOI: https://doi.org/10.1016/j.joule.2018.10.007.

[109] A. J. Welch, E. Dunn, J. S. Duchene, and H. A. Atwater. *Bicarbonate or Carbonate Processes for Coupling Carbon Dioxide Capture and Electrochemical Conversion*. 2020. DOI: 10.1021/acsenergylett.0c00234.

[110] K. G. Schulz, U. Riesesell, B. Rost, S. Thoms, and R. E. Zeebe. "Determination of the Rate Constants for the Carbon Dioxide to Bicarbonate Inter-Conversion in pH-Buffered Seawater Systems". In: *Mar. Geochem.* 100 (2006), pp. 53–65. DOI: https://doi.org/10.1016/j.marchem.2005.11.001.

[111] S. Nitopi, E. Bertheussen, S. B. Scott, X. Liu, A. K. Engstfeld, S. Horch, B. Seger, I. E.L. Stephens, K. Chan, C. Hahn, J. K. Nørskov, T. F. Jaramillo, and I. Chorkendorff. *Progress and Perspectives of Electrochemical CO_2 Reduction on Copper in Aqueous Electrolyte*. 2019. DOI: 10.1021/acs.chemrev.8b00705.

[112] A.J. Welch, J. S. Duchene, G. Tagliabu, A. Davoyan, W. H. Cheng, and H. A. Atwater. "Nanoporous Gold as a Highly Selective and Active Carbon Dioxide Reduction Catalyst". In: *ACS Appl. Energy Mater.* 2 (1 2019), pp. 164–170. DOI: https://doi.org/10.1021/acsaem.8b01570.

[113] A. S. Hall, Y. Yoon, A. Wuttig, and Y. Surendranath. "Mesostructure-Induced Selectivity in CO_2 Reduction Catalysis". In: *J. Am. Chem. Soc.* 137 (47 2015), pp. 14834–14837. DOI: 10.1021/jacs.5b08259.

[114] J. A. Gauthier, Z. Lin, M. Head-Gordon, and A. T. Bell. "Pathways for the Formation of C_{2+} Products under Alkaline Conditions during the Electrochemical Reduction of CO_2". In: *ACS Energy Lett.* 5 (2022), pp. 1679–1686. DOI: https://doi.org/10.1021/acsenergylett.2c00167.

[115] J. C. Bui, C. Kim, A. Z. Weber, and A. T. Bell. "Dynamic Boundary Layer Simulation of Pulsed CO_2 Electrolysis on a Copper Catalyst". In: *ACS Energy Lett.* 6 (2021), pp. 1181–1188. DOI: https://doi.org/10.1021/acsenergylett.1c00364.

[116] J. C. Bui, E. W. Lees, L. M. Pant, I. V. Zenyuk, A. T. Bell, and A. Z. Weber. "Continuum Modeling of Porous Electrodes for Electrochemical Synthesis". In: *Chem. Rev.* 122 (12 2022), pp. 11022–11084. DOI: https://doi.org/10.1021/acs.chemrev.1c00901.

[117] J. M. Spurgeon and B. Kumarl. "A Comparative Technoeconomic Analysis of Pathways for Commercial Electrochemical CO_2 Reduction to Liquid Products". In: *Energy Environ. Sci.* 11 (2018), pp. 1536–1551. DOI: https://doi.org/10.1039/C8EE00097B.

[118] M. G. Kibria, J. P. Edwards, C. M. Gabardo, C.-T. Dinh, A. Seifitokaldani, D. Sinton, and E. H. Sargent. "Electrochemical CO_2 Reduction into Chemical Feedstocks: From Mechanistic Electrocatalysis Models to System Design". In: *Adv. Mater.* 31 (2019), p. 1807166. DOI: https://doi.org/10.1002/adma.201807166.

[119] J. Newman and K. E. Thomas-Aleya. *Electrochemical Systems*. Hoboken: Wiley-Interscience, 2004.

[120] L. C. Weng, A. T. Bell, and A. Z. Weber. "A Systematic Analysis of Cu-Based Membrane-Electrode Assemblies for CO_2 Reduction through Multiphysics Simulation". In: *Energy Environ. Sci.* 13 (10 2020), pp. 3592–3606. DOI: https://doi.org/10.1039/D0EE01604G.

[121] L. C. Weng, A. T. Bell, and A. Z. Weber. "Towards Membrane-Electrode Assembly Systems for CO_2 Reduction: A Modeling Study". In: *Energy Environ. Sci.* 12 (6 2019), pp. 950–1968. DOI: https://doi.org/10.1039/C9EE00909D.

[122] K. Williams, N. Corbin, J. Zeng, N. Lazouski, D.-T. Yang, and K. Manthiram. "Protecting Effect of Mass Transport During Electrochemical Reduction of Oxygenated Carbon Dioxide Feedstocks". In: *Sustain. Energ. Fuels* 3 (2019), p. 1225. DOI: https://doi.org/10.1039/C9SE00024K.

[123] M. Moradzaman, C. S. Martinez, and G. Mul. "Effect of Partial Pressure on Product Selectivity in Cu- Catalyzed Electrochemical Reduction of CO_2". In: *Sustain. Energy Fuels* 4 (10 2020), pp. 5195–5202. DOI: https://doi.org/10.1039/D0SE00865F.

[124] A. S. Varela, M. Kroschel, T. Reier, and P. Strasser. "Controlling the Selectivity of CO_2 Electroreduction on Copper: The Effect of the Electrolyte Concentration and the Importance of the Local pH". In: *Catal. Today* 260 (2016), pp. 8–13. DOI: https://doi.org/10.1016/j.cattod.2015.06.009.

[125] G. Kastlunger, L. Wang, N. Govindajaran, H. H. Heenen, S. Ringe, T. Jaramillo, C. Hahn, and K. Chan. "Using pH Dependence to Understand Mechanisms in Electrochemical CO_2 Reduction". In: *ACS Catal.* 8 (2022), pp. 4344–4357. DOI: https://doi.org/10.1021/acscatal.1c05520.

[126] E. W. Lees, A. Liu, J. C. Bui, S. Ren, A. Z. Weber, and C. P. Berlinguette. "Electrolytic Methane Production from Reactive Carbon Solutions". In: *ACS Energy Lett.* 7 (5 2022), pp. 1712–1718. DOI: https://doi.org/10.1021/acsenergylett.2c00283.

[127] M. Sassenburg, R. de Rooji, N. T. Nessbitt, R. Kas, S. Chandrashekar, N. J. Firet, K. Yang, K. Liu, M. A. Blommaert, M. Kolen, D. Ripepi, W. A. Smith, and T. Burdyny. "Characterizing CO_2 Reduction Catalysts on Gas Diffusion Electrodes: Comparing Activity, Selectivity and Stability of Transition Metal Catalysts". In: *ACS Appl. Energy Mater.* 5 (2022), pp. 5983–5994. DOI: https://doi.org/10.1021/acsaem.2c00160.

[128] M. Eigen. "Proton Transfer, Acid–Base Catalysis, and Enzymatic Hydrolysis". In: *Angew. Chem., Int. Ed. Engl.* 3 (1 1964), pp. 1–19. DOI: https://doi.org/10.1002/anie.196400011.

[129] V. M. Ehlinger, A. R. Crothers, A. Kusoglu, and A. Z. Weber. "Modeling Proton-Exchange-Membrane Fuel Cell Performance/ Degradation Tradeoffs with Chemical Scavengers". In: *J. Phys. Energy* 2 (4 2020), p. 044006. DOI: 10.1088/2515-7655/abb194.

[130] C. Kim, J. C. Bui, X. Luo, J. K. Cooper, A. Kusoglu, A. Z. Weber, and A. T. Bell. "Tailored Catalyst Microenvironments for CO_2 Electroreduction to Multicarbon Products on Copper Using Bilayer Ionomer Coatings". In: *Nat. Energy* 6 (11 2021), pp. 1026–1034. DOI: https://doi.org/10.1038/s41560-021-00920-8.

[131] B. Kim, F. Hillman, M. Ariyoshi, S. Fujikawa, and P. J. A. Kenis. "Effects of Composition of the Microporous Layer and the Substrate on Performance in the Electrochemical Reduction of CO_2 to CO". In: *J. Power Sources* 312

(2016), pp. 192–198. DOI: https://doi.org/10.1016/j.jpowsour.2016.02.043.

[132] R. E. Vos and M. T. M. Koper. "The Effect of Temperature on the Cation Promoted Electrochemical CO_2 Reduction on Gold". In: *ChemElectroChem* 9 (2022), p. 13. DOI: https://doi.org/10.1002/celc.202200239.

[133] S. Ringe, E. L. Clark, J. Resasco, A. Walton, B. Seger, A.-T. Bell, and K. Chan. "Understanding Cation Effects in Electrochemical CO_2 Reduction". In: *Energy Environ. Sci.* 12 (10 2019), pp. 3001–3014. DOI: https://doi.org/10.1039/C9EE01341E.

[134] Millipore Sigma. *6,8-Dihydroxy-1,3-Pyrenedisulfonic Acid Disodium Salt*. 2024. URL: https://www.sigmaaldrich.com/US/en/product/sigma/37920 (visited on 02/16/2024).

[135] Fuel Cell Store. *Sigracet 28 BC Carbon Paper Property Sheet*. 2024. URL: https://www.fuelcellstore.com/spec-sheets/sigracet-22-28-36-39-properties-sheet.pdf (visited on 02/15/2024).

[136] J. A. Rabinowitz and M. W. Kanan. "The Future of Low-Temperature Carbon Dioxide Electrolysis Depends on Solving One Basic Problem". In: *Nat. Commun.* 11 (2020), p. 5231. DOI: https://doi.org/10.1038/s41467-020-19135-8.

[137] G. A. Mills and H. C. Urey. "The Kinetics of Isotropic Exchange between Carbon Dioxide, Bicarbonate Ion, Carbonate Ion and Water". In: *J. Am. Chem. Soc.* 62 (1940), pp. 1019–1026.

[138] Sterlitech. *PTFE Laminated Membrane Filters*. 2024. URL: https://www.sterlitech.com/ptfe-laminated-membrane-filters.html (visited on 02/15/2024).

[139] T. Hatsukade, K. P. Kuhl, E. R. Cave, D. N. Abram, and T. F. Jaramillo. "Insights Into the Electrocatalytic Reduction of CO_2 on Metallic Silver Surfaces". In: *Phys. Chem. Chem. Phys.* 16 (2020), pp. 13814–13819. DOI: https://doi.org/10.1039/C4CP00692E.

[140] H. Mistry, Y.-W. Choi, A. Bagger, F. Scholten, C. S. Bonifacio, I. Sinev, N. J. Divins, I. Zegkinoglou, H. S. Jeon, K. Kisslinger, E. A. Stach, J. C. Yang, J. Rossmeisl, and B. R. Cuenya. "Enhanced Carbon Dioxide Electroreduction to Carbon Monoxide over Defect-Rich Plasma-Activated Silver Catalysts". In: *Angew. Chem. Int. Ed.* 56 (2017), pp. 11394–11398. DOI: https://doi.org/10.1002/ange.201704613.

[141] M. Ma, B. J. Trzesniewski, J. Xie, and W. A. Smith. "Selective and Efficient Reduction of Carbon Dioxide to Carbon Monoxide on Oxide-Derived Nanostructured Silver Electrocatalysts". In: *Angew. Chem. Int. Ed.* 55 (2016), pp. 9748–9752. DOI: https://doi.org/10.1002/ange.201604654.

[142] M. R. Singh, J. D. Goodpaster, A. Z. Weber, M. Head-Gordon, and A. T. Bell. "Mechanistic Insights Into Electrochemical Reduction of CO_2 Over Ag Using Density Functional Theory and Transport Models". In: *Proc. Natl. Acad. Sci. U.S.A.* 114 (2017), E8812–E8821. DOI: https://doi.org/10.1073/pnas.1713164114.

[143] E. L. Clark, J. Resasco, A. Landers, J. Lin, L-T Chung, A. Walton, C. Hahn, T. F. Jaramillo, and A. T. Bell. "Standards and Protocols for Data Acquisition and Reporting for Studies of the Electrochemical Reduction of Carbon Dioxide". In: *ACS Catal.* 8 (7 2018), pp. 6560–6570. DOI: https://doi.org/10.1021/acscatal.8b01340.

[144] K. Liu, W. A. Smith, and T. Burdyny. "Introductory Guide to Assembling and Operating Gas Diffusion Electrodes for Electrochemical CO_2 Reduction". In: *ACS Energy Lett.* 4 (2019), pp. 639–643. DOI: https://doi.org/10.1021/acsenergylett.9b00137.

[145] A. Seifitokaldani, C. M. Gabardo, T. Burdyny, C.-T. Dinh, J. P. Edwards, M. G. Kibria, O. S. Bushuyev, S. O. Kelley, D. Sinton, and E. H. Sargent. "Hydronium-Induced Switching between CO_2 Electroreduction Pathways". In: *J.Am. Chem. Soc.* 140 (2018), pp. 3833–3837. DOI: https://doi.org/10.1021/jacs.7b13542.

[146] N. Gupta, M. Gattrell, and B. MacDougall. "Calculation for the Cathode Surface Concentrations in the Electrochemical Reduction of CO_2 in $KHCO_3$ Solutions". In: *J. Appl. Electrochem.* 36 (2006), pp. 161–172. DOI: https://doi.org/10.1007/s10800-005-9058-y.

[147] T. Moeller, T. N. Thanh, X. Wang, W. Ju, Z. Jovanov, and P. Strasser. "The Product Selectivity Zones in Gas Diffusion Electrodes During the Electrocatalytic Reduction of CO_2". In: *Energy Environ. Sci.* 14 (2021), pp. 5995–6006. DOI: https://doi.org/10.1039/D1EE01696B.

[148] Y. Lum, B. Yue, P. Lobaccaro, A. T. Bell, and J. W. Ager. "Optimizing C-C Coupling on Oxide-Derived Copper Catalysts for Electrochemical CO_2 Reduction". In: *J. Phys. Chem. C* 121 (2017), pp. 14191–14203. DOI: https://doi.org/10.1039/D1EE01696B.

[149] Y. Y. Birdja, E. Pérez-Gallent, M. C. Figueiredo, A. J. Göttle, F. Calle-Vallejo, and M. T. M. Koper. "Advances and Challenges in Understanding the Electrocatalytic Conversion of Carbon Dioxide to Fuels". In: *Nature Energy* 4 (2019), pp. 732–745. DOI: http://dx.doi.org/10.1038/s41560-019-0450-y.

[150] T. Alerte, J. P. Edwards, C. M. Gabardo, C. P. O'Brien, A. Gaona, J. Wicks, A. Obradović, A. Sarkar, S. A. Jaffer, H. L. MacLean, D. Sinton, and E. H. Sargent. "Downstream of the CO_2 Electrolyzer: Assessing the Energy Intensity of Product Separation". In: *ACS Energy Lett.* 6 (2021), pp. 4405–4412. DOI: http://dx.doi.org/10.1021/acsenergylett.1c02263.

[151] A. Perazio, C. E. Creissen, J. G. Rivera de la Cruz, M. W. Schreiber, and M. Fontecave. "Acidic Electroreduction of CO_2 to Multi-Carbon Products with CO_2 Recovery and Recycling from Carbonate". In: *ACS Energy Lett.* (2023), pp. 2979–2985. DOI: http://dx.doi.org/10.1021/acsenergylett.3c00901.

[152] Y. Xu, R. K. Miao, J. P. Edwards, S. Liu, C. P. O'Brien, C. M. Gabardo, M. Fan, J. E. Huang, A. Robb, E. H. Sargent, and D. Sinton. "A Microchanneled Solid Electrolyte for Carbon-Efficient CO_2". In: *Joule* 6 (2022), pp. 1333–1343. DOI: http://dx.doi.org/10.1016/j.joule.2022.04.023.

[153] J. Y. T. Kim, P. Zhu, F.-Y. Chen, Z.-Y. Wu, D. A. Cullen, and H. Wang. "Recovering Carbon Losses in CO_2 Electrolysis using a Solid Electrolyte Reactor". In: *Nat. Catalysis* 5 (2022), pp. 288–299. DOI: http://dx.doi.org/10.1038/s41929-022-00763-w.

[154] K. Xie, R. K. Miao, A. Ozden, S. Liu, Z. Chen, C.-T. Dinh, J. E. Huang, Q. Xu, C. M. Gabardo, G. Lee, J. P. Edwards, C. P. O'Brien, S. W. Boettcher, D. Sinton, and E. H. Sargent. "Bipolar Membrane Electrolyzers Enable High Single-Pass CO_2 Electroreduction to Multicarbon Products". In: *Nat. Communications* 13 (2022), p. 3609. DOI: http://dx.doi.org/10.1038/s41467-022-31295-3.

[155] J. Gu, S. Liu, W. Ni, W. Ren, S. Haussener, and X. Hu. "Modulating Electric Field Distribution by Alkali Cations for CO_2 Electroreduction in Strongly Acidic Medium". In: *Nature Catalysis* 5 (2022), pp. 268–276. DOI: http://dx.doi.org/10.1038/s41929-022-00761-y.

[156] J. E. Huang, F. Li, A. Ozden, A. Sedighian Rasouli, F. P. García de Arquer, S. Liu, S. Zhang, M. Luo, X. Wang, Y. Lum, Y. Xu, K. Bertens, R. K. Miao, C.-T. Dinh, D. Sinton, and E. H. Sargent. "CO_2 Electrolysis to Multicarbon Products in Strong Acid". In: *Science* 372 (2021), pp. 1074–1078. DOI: http://dx.doi.org/10.1126/science.abg6582.

[157] Y. Zhao, L. Hao, A. Ozden, S. Liu, R. K. Miao, P. Ou, T. Alkayyali, S. Zhang, J. Ning, Y. Liang, Y. Xu, M. Fan, Y. Chen, J. E. Huang, K. Xie, J. Zhang, C. P. O'Brien, F. Li, E. H. Sargent, and D. Sinton. "Conversion of CO_2 to Multicarbon Products in Strong Acid by Controlling the Catalyst Microenvironment". In: *Nat. Synthesis* 2 (2023), pp. 403–412. DOI: http://dx.doi.org/10.1038/s44160-022-00234-x.

[158] Z. Jiang, Z. Zhang, H. Li, Y. Tang, Y. Yuan, J. Zao, H. Zheng, and Y. Liang. "Molecular Catalyst with Near 100% Selectivity for CO_2 Reduction in Acidic Electrolytes". In: *Adv. Energy Mat.* 13 (2023), p. 2203603. DOI: http://dx.doi.org/https://doi.org/10.1002/aenm.202203603.

[159] W. Ren, A. Xu, K. Chan, and X. Hu. "A Cation Concentration Gradient Approach to Tune the Selectivity and Activity of CO_2 Electroreduction".

In: *Angew. Chem. Int. Ed.* 61 (2022), e202214173. DOI: http://dx.doi.org/https://doi.org/10.1002/anie.202214173.

[160] Y. Qiao, W. Lai, K. Huang, T. Yu, Q. Wang, L. Gao, Z. Yang, Z. Ma, T. Sun, M. Liu, C. Lian, and H. Huang. "Engineering the Local Microenvironment over Bi Nanosheets for Highly Selective Electrocatalytic Conversion of CO_2 to HCOOH in Strong Acid". In: *ACS Catal.* 12 (2022), pp. 2357–2364. DOI: http://dx.doi.org/10.1021/acscatal.1c05135.

[161] Z. Ma, Z. Yang, W. Lai, Q. Wang, Y. Qiao, H. Tao, C. Lian, M. Liu, C. Ma, A. Pan, and H. Huang. "CO_2 Electroreduction to Multicarbon Products in Strongly Acidic Electrolyte via Synergistically Modulating the Local Microenvironment". In: *Nature Commun.* 13 (2022), p. 7596. DOI: http://dx.doi.org/10.1038/s41467-022-35415-x.

[162] M. C. O. Monteiro, M. F. Philips, K. J. P. Schouten, and M. T. M. Koper. "Efficiency and Selectivity of CO_2 Reduction to CO on Gold Gas Diffusion Electrodes in Acidic Media". In: *Nature Commun.* 12 (2021), p. 4943. DOI: http://dx.doi.org/10.1038/s41467-021-24936-6.

[163] C. J. Bondue, M. Graf, A. Goyal, and M. T. M. Koper. "Suppression of Hydrogen Evolution in Acidic Electrolytes by Electrochemical CO_2 Reduction". In: *J. Am. Chem. Soc.* 143 (2021), pp. 279–285. DOI: http://dx.doi.org/10.1021/jacs.0c10397.

[164] H.-G. Qin, F.-Z. Li, Y.-F. Du, L.-F. Yang, H. Wang, Y.-Y. Bai, M. Lin, and J. Gu. "Quantitative Understanding of Cation Effects on the Electrochemical Reduction of CO_2 and H^+ in Acidic Solution". In: *ACS Catal.* (2022), pp. 916–926. DOI: http://dx.doi.org/10.1021/acscatal.2c04875.

[165] E. R. Cofell, U. O. Nwabara, S. S. Bhargava, D. E. Henckel, and P. J. A. Kenis. "Investigation of Electrolyte-Dependent Carbonate Formation on Gas Diffusion Electrodes for CO_2 Electrolysis". In: *ACS Appl. Mater. Inter.* 13 (2021), pp. 15132–15142. DOI: http://dx.doi.org/10.1021/acsami.0c21997.

[166] C. Chen, Y. Li, and P. Yang. "Address the "Alkalinity Problem" in CO_2 Electrolysis with Catalyst Design and Translation". In: *Joule* 5 (2021), pp. 737–742. DOI: http://dx.doi.org/https://doi.org/10.1016/j.joule.2021.02.008.

[167] M. S. Naughton, F. R. Brushett, and P. J. A. Kenis. "Carbonate Resilience of Flowing Electrolyte-Based Alkaline Fuel Cells". In: *J. Power Sources* 196 (2011), pp. 1762–1768. DOI: http://dx.doi.org/https://doi.org/10.1016/j.jpowsour.2010.09.114.

[168] K. Y. Leung and C. C. L. McCrory. "Effect and Prevention of Trace Ag^+ Contamination from Ag/AgCl Reference Electrodes on CO_2 Reduction Product Distributions at Polycrystalline Copper Electrodes". In: *ACS Appl. Energy*

Mat. 2 (2019), pp. 8283–8293. DOI: http://dx.doi.org/10.1021/acsaem.9b01759.

[169] A. Wuttig and Y. Surendranath. "Impurity Ion Complexation Enhances Carbon Dioxide Reduction Catalysis". In: *ACS Catal.* 5 (2015), pp. 4479–4484. DOI: http://dx.doi.org/10.1021/acscatal.5b00808.

[170] X. Qin, T. Vegge, and H. A. Hansen. "Cation-Coordinated Inner-Sphere CO_2 Electroreduction at Au–Water Interfaces". In: *J. Am. Chem. Soc.* 145 (2023), pp. 1897–1905. DOI: http://dx.doi.org/10.1021/jacs.2c11643.

[171] S.-J. Shin, H. Choi, S. Ringe, D. H. Won, H.-S. Oh, D. H. Kim, T. Lee, D.-H. Nam, H. Kim, and C. H. Choi. "A Unifying Mechanism for Cation Effect Modulating C_1 and C_2 Productions from CO_2 Electroreduction". In: *Nature Commun.* 13 (2022), p. 5482. DOI: http://dx.doi.org/10.1038/s41467-022-33199-8.

[172] J. Resasco, L. D. Chen, E. Clark, C. Tsai, C. Hahn, T. F. Jaramillo, K. Chan, and A. T. Bell. "Promoter Effects of Alkali Metal Cations on the Electrochemical Reduction of Carbon Dioxide". In: *J. Am. Chem. Soc.* 139 (2017), pp. 11277–11287. DOI: http://dx.doi.org/10.1021/jacs.7b06765.

[173] M. R. Singh, Y. Kwon, Y. Lum, J. W. Ager, and A. T. Bell. "Hydrolysis of Electrolyte Cations Enhances the Electrochemical Reduction of CO_2 over Ag and Cu". In: *J. Am. Chem. Soc.* 138 (2016), pp. 13006–13012. DOI: http://dx.doi.org/10.1021/jacs.6b07612.

[174] M. C. O. Monteiro, F. Dattila, B. Hagedoorn, R. García-Muelas, N. López, and M. T. M. Koper. "Absence of CO_2 Electroreduction on Copper, Gold and Silver Electrodes without Metal Cations in Solution". In: *Nature Catal.* 4 (2021), pp. 654–662. DOI: http://dx.doi.org/10.1038/s41929-021-00655-5.

[175] S. Weng, W. L. Toh, and Y. Surendranath. "Weakly Coordinating Organic Cations Are Intrinsically Capable of Supporting CO_2 Reduction Catalysis". In: *J. Am. Chem. Soc.* 145 (2023), pp. 16787–16795. DOI: http://dx.doi.org/10.1021/jacs.3c04769.

[176] H.-G. Qin, Y.-F. Du, Y.-Y. Bai, F.-Z. Li, X. Yue, H. Wang, J.-Z. Peng, and J. Gu. "Surface-Immobilized Cross-Linked Cationic Polyelectrolyte Enables CO_2 Reduction with Metal Cation-Free Acidic Electrolyte". In: *Nature Commun.* 14 (2023), p. 5640. DOI: http://dx.doi.org/10.1038/s41467-023-41396-2.

[177] S. Chandrashekar, H.-P. I. van Montfort, D. Bohra, G. Filonenko, H. Geerlings, T. Burdyny, and W. A. Smith. "Investigating the Role of Potassium Cations during Electrochemical CO_2 Reduction". In: *Nanoscale* 14 (2022), pp. 14185–14190. DOI: http://dx.doi.org/10.1039/D2NR03438G.

[178] M. C. O. Monteiro, A. Mirabal, L. Jacobse, K. Doblhoff-Dier, S. C. Barton, and M. T. M. Koper. "Time-Resolved Local pH Measurements during CO_2 Reduction Using Scanning Electrochemical Microscopy: Buffering and Tip Effects". In: *JACS Au* 1 (2021), pp. 1915–1924. DOI: http://dx.doi.org/10.1021/jacsau.1c00289.

[179] D. Bohra, J. H. Chaudhry, T. Burdyny, E. A. Pidko, and W. A. Smith. "Modeling the Electrical Double Layer to Understand the Reaction Environment in a CO_2 Electrocatalytic System". In: *Energy Environ. Sci.* 12 (2019), pp. 3380–3389. DOI: http://dx.doi.org/10.1039/C9EE02485A.

[180] H. Ooka, M. C. Figueiredo, and M. T. M. Koper. "Competition between Hydrogen Evolution and Carbon Dioxide Re-duction on Copper Electrodes in Mildly Acidic Media". In: *Langmuir* 33 (2017), pp. 9307–9313. DOI: http://dx.doi.org/10.1021/acs.langmuir.7b00696.

[181] W. Nie, G. P. Heim, N. B. Watkins, T. Agapie, and J. C. Peters. "Organic Additive-Derived Films on Cu Electrodes Promote Electrochemical CO_2 Reduction to C_{2+} Products Under Strongly Acidic Conditions". In: *Angew. Chem. Int. Ed.* 62 (2023), e202216102. DOI: http://dx.doi.org/https://doi.org/10.1002/anie.202216102.

[182] B. Cao, F. Z. Li, and J. Gu. "Designing Cu-Based Tandem Catalysts for CO_2 Electroreduction Based on Mass Transport of CO Intermediate". In: *ACS Catal.* 12 (15 2022), pp. 9735–9752. DOI: https://doi.org/10.1021/acscatal.2c02579.

[183] H. Zhang, X. Chang, J. G. Chen, W. A. Goddard III, B. Xu, M. J. Cheng, and Q. Lu. "Computational and Experimental Demonstrations of One-Pot Tandem Catalysis for Electrochemical Carbon Dioxide Reduction to Methane". In: *Nat. Commun.* 10 (2019), p. 3340. DOI: https://doi.org/10.1038/s41467-019-11292-9.

[184] A. He, Y. Yang, Q. Zhang, M. Yang, Q. Zou, J. Du, C. Tao, and Z. Liu. "The Enhanced Local CO Concentration for Efficient CO_2 Electrolysis Towards C_2 Products on Tandem Active Sites". In: *Chem. Eng. J.* 450 (2022), p. 138009. DOI: https://doi.org/10.1016/j.cej.2022.138009.

[185] M. Papasizza and A. Cuesta. "In Situ Monitoring Using ATR-SEIRAS of the Electrocatalytic Reduction of CO_2 on Au in an Ionic Liquid/Water Mixture". In: *ACS Catal.* 8 (7 2018), pp. 6345–6352. DOI: https://doi.org/10.1021/acscatal.8b00977.

[186] T. Smolinka, M. Heinen, Y.X. Chen, Z. Jusys, W. Lehnert, and R.J. Behm. "CO_2 Reduction on Pt Electrocatalysts and its Impact on H_2 Oxidation in CO_2 Containing Fuel Cell Feed Gas – A Combined in Situ Infrared Spectroscopy, Mass Spectrometry and Fuel Cell Performance Study". In: *Electrochem. Acta.* 50 (25 2005), pp. 5189–5199. DOI: https://doi.org/10.1016/j.electacta.2005.02.082.

[187] J. de Ruiter, H. An, L. Wu, Z. Gijsberg, S. Yang, T. Hartman, B. M. Weckhuysen, and W. van der Stam. "Probing the Dynamics of Low-Overpotential CO_2-to-CO Activation on Copper Electrodes with Time-Resolved Raman Spectroscopy". In: *J. Am. Chem. Soc.* 144 (33 2022), pp. 15047–15058. DOI: https://doi.org/10.1021/jacs.2c03172.

[188] P. Khanipour, M. Löffler, A. M. Reichert, F. T. Haase, K. J. J. Mayrhofer, and I. Katsounaros. "Electrochemical Real-Time Mass Spectrometry (EC-RTMS): Monitoring Electrochemical Reaction Products in Real Time". In: *Angew. Chem. Int. Ed.* 58 (2019), pp. 7273–7277. DOI: https://doi.org/10.1002/anie.201901923.

[189] M. Löffler, P. Khanipour, N. Kulyk, K. J.J. Mayrhofer, and I. Katsounaros. "Insights Into Liquid Product Formation During Carbon Dioxide Reduction on Copper and Oxide-Derived Copper from Quantitative Real-Time Measurements". In: *ACS Catal.* 10 (2020), pp. 6735–6740. DOI: https://doi.org/10.1021/acscatal.0c01388.

[190] V. L. Mahan. "Cardiac Function Dependence on Carbon Monoxide". In: *Med. Gas Res.* 10 (1 2020), pp. 37–46. DOI: https://doi.org/10.4103\%2F2045-9912.279982.

[191] K. Kashfi and K. K. Patel. "Carbon Monoxide and Its Role in Human Physiology: A Brief Historical Perspective". In: *Biochem. Pharm.* 204 (2022), p. 115230. DOI: https://doi.org/10.1016/j.bcp.2022.115230.

[192] Y.-S. Xia, L. Yan, G.-J. Mao, W.-L. Jiang, W.-X. Wang, Y. Li, Y.-Q. Jiang, and C.-Y. Li. "A Novel HPQ-Based Fluorescent Probe for the Visualization of Carbon Monoxide in Zebrafish". In: *Sens. Actuators B Chem.* 340 (2021), p. 129920. DOI: https://doi.org/10.1016/j.snb.2021.129920.

[193] J. Hong, Q. Xia, E. Zhou, and G. Feng. "A Novel HPQ-Based Fluorescent Probe for the Visualization of Carbon Monoxide in Zebrafish". In: *Talanta* 215 (2020), p. 120914. DOI: https://doi.org/10.1016/j.talanta.2020.120914.

[194] A. F. Tikum, W. Lim, M. M. Fortibui, S. Lee, S. Park, and J. Kim. "Palladium Probe Consisting of Naphthalimide and Ethylenediamine for Selective Turn-On Sensing of CO and Cell Imaging". In: *Inorg. Chem.* 60 (10 2021), pp. 7108–7114. DOI: https://doi.org/10.1021/acs.inorgchem.1c00091.

[195] Y. Deng, J. Hong, E. Zhou, and G. Feng. "Near-Infrared Fluorescent Probe with a Super Large Stokes Shift for Tracking CO in Living Systems Based on a Novel Coumarin-Dicyanoisophorone Hybrid". In: *Dyes Pigm.* 170 (2019), p. 107634. DOI: https://doi.org/10.1016/j.dyepig.2019.107634.

[196] W. Feng, D. Liu, S. Feng, and G. Feng. "Readily Available Fluorescent Probe for Carbon Monoxide Imaging in Living Cells". In: *Anal. Chem.* 88

(21 2016), pp. 1064–1065. DOI: https://doi.org/10.1021/acs.analchem.6b03073.

[197] W. Feng, J. Hong, and G. Feng. "Colorimetric and Ratiometric Fluorescent Detection of Carbon Monoxide in Air, Aqueous Solution, and Living Cells by a Naphthalimide-Based Probe". In: *Sensor. Actuat. B-Chem* 251 (2017), pp. 389–395. DOI: https://doi.org/10.1016/j.snb.2017.05.099.

[198] J. Wang, C. Li, Q. Chen, H. Li, L. Zhou, X. Jiang, M. Shi, P. Zhang, G. Jiang, and B. Z. Tang. "An Easily Available Ratiometric-Based AIE Probe for Carbon Monoxide Light-up Imaging". In: *Anal. Chem.* 91 (15 2019), pp. 9388–9392. DOI: https://doi.org/10.1021/acs.analchem.9b02691.

[199] Z. Wang, Z. Geng, Z. Zhao, W. Sheng, C. Liu, X. Lv, Q. He, and B. Zhu. "A Highly Specific and Sensitive Ratiometric Fluorescent Probe for Carbon Monoxide and its Bioimaging Applications". In: *New J. Chem.* 42 (2018), pp. 14417–14423. DOI: https://doi.org/10.1039/C8NJ03152E.

[200] S. Feng, D. Liu, W. Feng, and G. Feng. "Allyl Fluorescein Ethers as Promising Fluorescent Probes for Carbon Monoxide Imaging in Living Cells". In: *Anal. Chem.* 89 (2017), pp. 3754–3760. DOI: https://doi.org/10.1021/acs.analchem.7b00135.

[201] P. Zong, Y. Chen, K. Liu, J. Bi, M. Ren, S. Wang, and F. Kong. "Construction of a Unique Two-Photon Fluorescent Probe and the Application for Endogenous CO Detection in Live Organisms". In: *Talanta* 240 (2022), p. 123194. DOI: https://doi.org/10.1016/j.talanta.2021.123194.

[202] J. Wang, J. Karpus, B. S. Zhao, Z. Luo, P. R. Chen, and C. He. "A Selective Fluorescent Probe for Carbon Monoxide in Living Cells". In: *Angew. Chem. Int. Ed.* 57 (2012), pp. 9652–9656. DOI: https://doi.org/10.1002/anie.201203684.

[203] Z. Wang, C. Liu, X. Wang, Q. Duan, P. Jia, H. Zhu, Z. Li, X. Zhang, X. Ren, B. Zhu, and W. Sheng. "A Metal-Free Near-Infrared Fluorescent Probe for Tracking the Glucose-Induced Fluctuations of Carbon Monoxide in Living Cells and Zebrafish". In: *Sens. Actuators B.* 291 (2019), pp. 329–336. DOI: https://doi.org/10.1016/j.snb.2019.04.084.

[204] K. Dhara, S. Lohar, A. Patra, P. Roy, S. K. Saha, G. C. Sadhukhan, and P. Chattopadhyay. "A New Lysosome-Targetable Turn-On Fluorogenic Probe for Carbon Monoxide Imaging in Living Cells". In: *Anal. Chem.* 90 (4 2018), pp. 2933–2938. DOI: https://doi.org/10.1021/acs.analchem.7b05331.

[205] Z. Li, X. Jia, P. Zhang, Z. Guo, H. Zhao, X. Li, and C. Wei. "A Hepatocyte-Specific Fluorescent Probe for Imaging Endogenous Carbon Monoxide Release in Vitro and In Vivo". In: *Sensor. Actuat. B-Chem* 344 (2021), p. 130177. DOI: https://doi.org/10.1016/j.snb.2021.130177.

[206] L. Yue, Y. Tang, H. Huang, W. Song, and W. Lin. "A Fluorogenic Probe for Detecting CO with the Potential Integration of Diagnosis and Therapy (IDT) for Cancer". In: *Sensor. Actuat. B-Chem* 344 (2021), p. 130245. DOI: https://doi.org/10.1016/j.snb.2021.130245.

[207] S. Zhang, X. Mu, J. Zhu, and L. Yan. "A Metal-Free Coumarin-Based Fluorescent Probe for the Turn-On Monitoring of Carbon Monoxide in an Aqueous Solution and Living Cells". In: *Analyst* 146 (2021), p. 1289. DOI: https://doi.org/10.1039/D0AN02107E.

[208] A. Sarkar, C. Fouzder, S. Chakraborty, E. Ahmmed, R. Kundu, S. Dam, P. Chattopadhyay, and K. Dhara. "A Nuclear-Localized Naphthalimide-Based Fluorescent Light-Up Probe for Selective Detection of Carbon Monoxide in Living Cells". In: *Chem. Res. Toxicol.* 33 (2 2020), pp. 651–656. DOI: https://doi.org/10.1021/acs.chemrestox.9b00462.

[209] T. G. Kelly, S. T. Hunt, D. V. Esposito, and J. G. Chen. "Monolayer Palladium Supported on Molybdenum and Tungsten Carbide Substrates as Low-Cost Hydrogen Evolution Reaction (HER) Electrocatalysts". In: *Int. J. Hydrog. Energy* 38 (2013), pp. 5638–5644. DOI: https://doi.org/10.1016/j.ijhydene.2013.02.116.

[210] S. Sarkar and S. C. Peter. "An Overview on Pd-Based Electrocatalysts for the Hydrogen Evolution Reaction". In: *Inorg. Chem. Front.* 5 (2018), pp. 2060–2080. DOI: https://doi.org/10.1039/C8QI00042E.

[211] L. Zhang, Q. Chang, H. Chen, and M. Shao. "Recent Advances in Palladium-Based Electrocatalysts for Fuel Cell Reactions and Hydrogen Evolution Reaction". In: *Nano Energy* 29 (2016), pp. 198–219. DOI: https://doi.org/10.1016/j.nanoen.2016.02.044.

[212] A. Bilska-Wilkosz, M. Górny, and M. Iciek. "Biological and Pharmacological Properties of Carbon Monoxide: A General Overview". In: *Oxygen* 2 (2 2022), pp. 130–151. DOI: https://doi.org/10.3390/oxygen2020012.

[213] H. M. Southam, M. P. Williamson, J. A. Chapman, R. L. Lyon, C. R. Trevitt, P. J. F. Henderson, and R. K. Poole. "'Carbon-Monoxide-Releasing Molecule-2 (CORM-2)' Is a Misnomer: Ruthenium Toxicity, Not CO Release, Accounts for Its Antimicrobial Effects". In: *Antioxidants* 10 (6 2021), p. 915. DOI: https://doi.org/10.3390\%2Fantiox10060915.

[214] D. Liu, X. Yang, and B. Wang. "Sensing a CO-Releasing Molecule (CORM) Does Not Equate to Sensing CO: The Case of DPHP and CORM-3". In: *Anal. Chem.* 95 (2023), pp. 9083–9089. DOI: https://doi.org/10.1021/acs.analchem.3c01495.

[215] N. Bauer, Z. Yuan, X. Yang, and B. Wang. "Plight of CORMs: The Unreliability of Four Commercially Available CO-Releasing Molecules, CORM-2, CORM-3, CORM-A1, and CORM-401". In: *Biochem. Pharmacol.* 214

(2023), p. 115642. DOI: https://doi.org/10.1016/j.bcp.2023.115642.

[216] S. McLean, B. E. Mann, and R. K. Poole. "Sulfite Species Enhance Carbon Monoxide Release from CO-Releasing Molecules: Implications for the Deoxymyoglobin Assay of Activity". In: *Anal. Biochem.* 427 (2012), pp. 36–42. DOI: https://doi.org/10.1016/j.ab.2012.04.026.

[217] H. M. Southam, T. W. Smith, R. L. Lyon, C. Liao, C. R. Trevitt, L. A. Middlemiss, F. L. Cox, J. A. Chapman, S. F. El-Khamisy, M. Hippler, M. P. Willimason, P. J. F. Henderson, and R. K. Poole. "A Thiol-Reactive Ru(II) Ion, not CO Release, Underlies the Potent Antimicrobial and Cytotoxic Properties of CO-Releasing Molecule-3". In: *Redox Biol.* 18 (2018), pp. 114–123. DOI: https://doi.org/10.1016/j.redox.2018.06.008.

[218] Z. Yuan, X. Yang, and B. Wang. "Redox and Catalase-Like Activities of Four Widely Used Carbon Monoxide Releasing Molecules (CO-RMs)". In: *Chem. Sci. J.* 12 (39 2021), pp. 13013–13020. DOI: https://doi.org/10.1039/D1SC03832J25.

[219] Z. Yuan, X. Yang, Y. Ye, R. Tripathi, and B. Wang. "Chemical Reactivities of Two Widely Used Ruthenium-Based CO-Releasing Molecules with a Range of Biologically Important Reagents and Molecules". In: *Anal. Chem.* 93 (2021), pp. 5317–5326. DOI: https://doi.org/10.1021/acs.analchem.1c00533.

[220] T. Santos-Silva, A. Mukhopadhyay, J. D. Seixas, G. J. L. Bernardes, C. C. Romao, and M. J. Romao. "CORM-3 Reactivity Toward Proteins: The Crystal Structure of a Ru(II) Dicarbonyl-Lysozyme Complex". In: *J. Am. Chem. Soc.* 133 (2011), pp. 1192–1195. DOI: https://doi.org/10.1021/ja108820s28.

[221] H. Koch and W. Haaf. "1-Adamantanecarboxylic Acid". In: *Org. Synth.* 5 (1973), p. 20. DOI: https://doi.org/10.15227/orgsyn.044.0001.

[222] G. H. Coleman and D. Craig. "p-Tolualdehyde". In: *Org. Synth.* 12 (1932), p. 80. DOI: https://doi.org/10.15227/orgsyn.012.0080.

[223] Y. Sun, X. Bu, U. Ulusoy, O. Guven, B. V. Hassas, and X. Dong. "Sulfite Species Enhance Carbon Monoxide Release from CO-Releasing Molecules: Implications for the Deoxymyoglobin Assay of Activity". In: *Anal. Biochem.* 427 (2012), pp. 36–42. DOI: https://doi.org/10.1016/j.ab.2012.04.026.

[224] Y. Lai, N. B. Watkins, C. Muzzillo, M. Richter, K. Kan, L. Zhou, J. A. Haber, A. Zakutayev, J. C. Peters, T. Agapie, and J. M. Gregoire. "Molecular Coatings Improve the Selectivity and Durability of CO_2 Reduction Chalcogenide Photocathodes". In: *ACS Energy Lett.* 7 (3 2022), pp. 1195–1201. DOI: https://doi.org/10.1021/acsenergylett.1c02762.

[225] Y. Lai, N. B. Watkins, A. Rosas-Hernandez, A. Thevenon, G. P. Heim, L. Zhou, Y. Wu, J. C. Peters, J. M. Gregoire, and T. Agapie. "Breaking Scaling Relationships in CO_2 Reduction on Copper Alloys with Organic Additives". In: *ACS Cent. Sci.* 7 (10 2021), pp. 1756–1762. DOI: https://doi.org/10.1021/acscentsci.1c00860.

[226] N. B. Watkins, Y. Wu, W. Nie, J. C. Peters, and T. Agapie. "In Situ Deposited Polyaromatic Layer Generates Robust Copper Catalyst for Selective Electrochemical CO_2 Reduction at Variable pH". In: *ACS Energy Lett.* 8 (1 2023), pp. 189–195. DOI: https://doi.org/10.1021/acsenergylett.2c02002.

[227] W. Nie, G. P. Heim, N. B. Watkins, and T. Agapie. "In Situ Deposited Polyaromatic Layer Generates Robust Copper Catalyst for Selective Electrochemical CO_2 Reduction at Variable pH". In: *Angew. Chem. Inter. Edit.* 62 (12 2023). DOI: https://doi.org/10.1002/ange.202216102.

[228] Y. Du, B. K. Pramanik, Y. Zhang, and V. Jegatheesan. "Influence of Molecular Weight Cut-Off (MWCO) of Commercial Ultrafiltration Substrate on the Performance of Thin Film Composite Nanofiltration Membrane". In: *Desalination* 541 (2022), p. 116020. DOI: https://doi.org/10.1016/j.desal.2022.116020.

[229] M. Fadel, Y. Wyart, and P. Moulin. "An Efficient Method to Determine Membrane Molecular Weight Cut-Off Using Fluorescent Silica Nanoparticles". In: *Membranes* 10 (2020), p. 271. DOI: https://doi.org/10.3390/membranes10100271.

[230] Z. Wu, X. Fu, and Y. Wang. "Click Synthesis of a Triphenylamine-Based Fluorescent Methanol Probe with a Unique D-π-A Structure". In: *Sens. and Act. B: Chem.* 245 (2017), pp. 406–413. DOI: https://doi.org/10.1016/j.snb.2017.01.164.

[231] A. Kumar, A. Kumar, P. R. Sahoo, and S. Kumar. "A MC-Spiropyran for Smartphone Assisted Reversible, Selective and Nanomolar Level Detection of Formic Acid in Water and Gas Phase". In: *J. Mol. Struct.* 1223 (2021), p. 129249. DOI: https://doi.org/10.1016/j.molstruc.2020.129249.

[232] C.-W. Zhang, M.-L. Li, Y.-D. Chen, Q. Zhou, and W.-T. Yang. "Ratiometric Fluorescent Sensor Based on Tb(III) Functionalized Metal-Organic Framework for Formic Acid". In: *Molecules* 27 (24 2022), p. 8702. DOI: https://doi.org/10.3390/molecules27248702.

[233] M. Wu, C. Yin, L. Fu, T. Liu, M. Jiang, Q. Sun, L. Chen, and N. Niu. "Thermochemical CO_2 Hydrogenation to Single Carbon Products: Scientific and Technological Challenges". In: *ACS Energy Lett.* 3 (8 2018), pp. 1938–1966. DOI: https://doi.org/10.1021/acsenergylett.8b00740.

[234] S. N. W. Toussaint, R. T. Calkins, S. Lee, and B. W. Michel. "Olefin Metathesis-Based Fluorescent Probes for the Selective Detection of Ethylene in Live Cells". In: *J. Am. Chem. Soc.* 140 (41 2018), pp. 13151–13155. DOI: https://doi.org/10.1021/jacs.8b05191.

[235] Y. Hitomi, T. Nagaia, and M. Kodera. "A Silver Complex with an N,S,S-Macrocyclic Ligand Bearing an Anthracene Pendant Arm for Optical Ethylene Monitoring". In: *Chem. Commun.* 48 (2012), pp. 10392–10394. DOI: https://doi.org/10.1039/C2CC35277J.

[236] S. Roy, A. Cherevotan, and S. C. Peter. "Thermochemical CO_2 Hydrogenation to Single Carbon Products: Scientific and Technological Challenges". In: *ACS Energy Lett.* 3 (8 2018), pp. 1938–1966. DOI: https://doi.org/10.1021/acsenergylett.8b00740.

[237] R. A. Tufa, D. Chanda, M. Ma, D. Aili, T. B. Demissie, J. Vaes, Q. Li, S. Liu, and D. Pant. "Towards Highly Efficient Electrochemical CO_2 Reduction: Cell Designs, Membranes and Electrocatalysts". In: *Appl. Energy* 277 (2020), p. 115557. DOI: https://doi.org/10.1016/j.apenergy.2020.115557.

[238] S. Liang, N. Altaf, L. Huang, Y. Gao, and Q. Wang. "Electrolytic cell design for electrochemical CO_2 reduction". In: *J. CO_2 Util.* 35 (2020), pp. 90–105. DOI: https://doi.org/10.1016/j.jcou.2019.09.007.

[239] M. J. Aminoff and R. B. Daroff. *Encyclopedia of the Neurological Sciences*. Cambridge, MA: Academic Press, 2014.

[240] Millipore Sigma. *8-Aminopyrene-1,3,6-Trisulfonic Acid Trisodium Salt*. 2024. URL: https://www.sigmaaldrich.com/US/en/product/sigma/09341 (visited on 02/16/2024).

[241] Grainger. *WALTER TITEX Micro Drill Bit: 0.05 mm Drill Bit Size*. 2024. URL: https://www.grainger.com/product/WALTER-TITEX-Micro-Drill-Bit-0-05-mm-Drill-440P19 (visited on 02/21/2024).

[242] M. A. Saccone, R. A. Gallivan, K. Narita, D. W. Yee, and J. R. Greer. "Additive Manufacturing of Micro-Architected Metals via Hydrogel Infusion". In: *Nature* 612 (2022), pp. 685–690. DOI: https://doi.org/10.1038/s41586-022-05433-2.

[243] 3Dnatives. *What is the Current State of Microscale 3D Printing?* 2020. URL: https://www.3dnatives.com/en/what-is-the-current-state-of-microscale-3d-printing (visited on 02/21/2024).

[244] J. Wicks, M. L. Jue, V. A. Beck, J. S. Oakdale, N. A. Dudukovic, A. L. Clemens, S. Liang, M. E. Ellis, G. Lee, S. E. Baker, E. B. Duoss, and E. H. Sargent. "3D-Printable Fluoropolymer Gas Diffusion Layers for CO_2 Electroreduction". In: *Adv. Mater.* 33 (7 2021), p. 2003855. DOI: https://doi.org/10.1002/adma.202003855.

[245] V. Vedharathinam, Z. Qi, C. Horwood, B. Bourcier, M. Stadermann, J. Biener, and M. Biener. "Using a 3D Porous Flow-Through Electrode Geometry for High-Rate Electrochemical Reduction of CO_2 to CO in Ionic Liquid". In: *ACS Catal.* 9 (12 2019), pp. 10605–10611. DOI: https://doi.org/10.1021/acscatal.9b03201.

[246] A. Biswas, I. S. Bayer, A. S. Biris, T. Wang, E. Dervishi, and F. Faupel. "Advances in Top-Down and Bottom-Up Surface Nanofabrication: Techniques, Applications and Future Prospects". In: *Adv. Colloid Interface Sci.* 170 (1-2 2012), pp. 2–27. DOI: https://doi.org/10.1016/j.cis.2011.11.001.

[247] J. Melngailis. "Focused Ion Beam Lithography". In: *NIM-B* 80-81 (2 1993), pp. 1271–1280. DOI: https://doi.org/10.1016/0168-583X(93)90781-Z.

[248] Electronic Materials Microelectronic Technologies. *Microposit S1800 G2 Series Photoresists*. Marlborough, MA, 2006.

[249] MicroChemicals. *AZ P4000 Positive Resists*. 2024. URL: https://www.microchemicals.com/products/photoresists/az%5C_p4620.html (visited on 02/22/2024).

[250] MicroChemicals. *HMDS*. 2024. URL: https://www.microchemicals.com/products/adhesion%5C_promotion/hmds.htmll (visited on 02/22/2024).

Appendix A

LESSONS LEARNED

A.1 Electrochemical Cell Design

Various factors must be taken into consideration when designing an electrochemical cell and some of these are described in section 1.2.4. The design focus of electrochemical cells optimized for the use with confocal microscopy is not to maximize the CO_2R performance but to facilitate the operando characterization of the cathode.

Fig. A.1 shows schematic cross sections of two typical electrochemical cells used with confocal microscopy, (a) for a solid CO_2R cathode, e.g., a metal foil as used in Chapters 7 and 8 and (b) for a CO_2R GDE as used in Chapters 2, 3, 4, 5 and 6. The main difference between the two cell versions is that cell (a) has a gas inlet directly into the electrolyte chamber that allows the constant bubbling of the electrolyte to ensure its saturation while cell (a) exhibits a separate gas chamber through which CO_2 gas can be fed to the backside of the GDE.

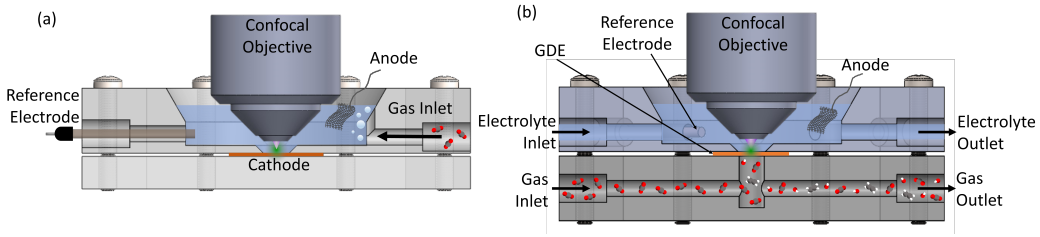

Figure A.1: Schematic drawings of electrochemical CO_2R cells designed for the use with confocal microscopy characterization, (a) for a solid cathode, e.g., a metal foil, and (b) for a CO_2R GDE. Typically, the reference electrode is a Ag/AgCl electrode and the anode a Pt mesh dipped into the electrolyte.

Typical electrochemical CO_2R cells that are used together with gas chromotography to analyze the product distribution are in the style of a parallel-plate compression cell with a cathode on one side, next to which is a catholyte chamber, then an ion exchange membrane, an anolyte chamber and finally, the anode. If a GDE is used, it is usually backed with a serpentine gas chamber through with gaseous CO_2 is fed. The cell orientation is vertical to facilitate the removal of gas bubbles [52, 237, 238]. In this work, a cell of that style was used to measure the product distribution of our GDE samples, see Chapters 2, 4 and 5. We altered and improved our cell design by

introducing tapered edges that prevent the buildup of gas bubbles in the catholyte and anolyte chambers as well as decreasing the GDE active surface area to 0.5 cm x 0.5 cm to reduce the size and therefore fabrication time of the GDE.

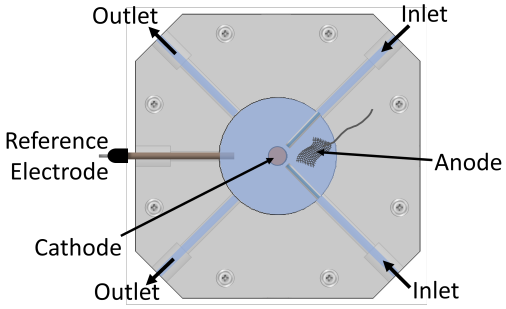

Figure A.2: Top view of an electrochemical CO_2R cell designed for confocal microscopy, exhibiting two perpendicular inlet tubes with straws leading directly to the cathode surface to facilitate the transport of fresh fluorescent dye molecules to the sample surface.

Compared to this more traditional CO_2R cell design, our novel cell design optimized for confocal microscopy exhibits several major differences. First, the cell orientation is horizontal and the electrolyte chamber is open at the top and exposed to air, see Fig. A.1. It is therefore unsuitable for the detection of gaseous products with gas chromotography since products are allowed to escape into the atmosphere. For the purpose of confocal microscopy however, this configuration enables a clear field of view for a water immersion confocal microscope objective. Water immersion objectives have several advantages in this context, one of them is the higher numerical aperture (NA) compared to air objectives due to the higher refractive index of water which leads to an improved resolution [239]. In addition, it facilitates the placement of the objective at working distance from the cathode without constraints on the size of the electrolyte chamber. One of the objectives used in this work is a Leica HC FLUOTAR L 25x/0,95 W VISIR, which has an NA of 0.95 and a working distance of 2.5 mm. Further, one of the main challenges for imaging purposes is the formation of gas bubbles because they can block the field of view. The open cell design with a water immersion objective makes the removal of accumulated gas bubbles easy. To further mitigate the issue of bubble formation, we decided to taper the rim around the cathode window to facilitate the release of gas bubbles.

Another design modifications that has proven to be useful is the introduction of a smaller active surface area and smaller electrolyte chamber to allow the use of a smaller GDE as well as limit the consumption of expensive fluorescent probes.

Finally, one design feature that is very important especially when probes like APTS that are prone to degradation (see Chapter A.2) are used is the inclusion of two perpendicular inlet and outlet tubes (Fig. A.2). Straws transport the electrolyte directly from the inlet to the cathode surface. This creates a turbulent flow pattern and ensures the effective transport of fresh, undegraded dye to the cathode. This ensures that a sufficient fluorescent signal from which the pH can be inferred ratiometrically can still be detected, even when high current densities that are detrimental for the probe, are applied.

A.2 Stability of the Fluorescent pH Probes DHPDS and APTS

It is important to verify the stability of fluorescent dyes under CO_2R operando conditions to make sure that experimental results obtained during CO_2R are accurate.

When performing measurements with the dye DHPDS in the current density range between 0 and -20 mA/cm^2, no significant decrease in photoluminescence intensity was observed. Some loss of fluorescent signal is observed for cathodic current densities of 100 mA/cm^2 in magnitude, or larger, but in our application the signal of DHPDS saturates for current densities larger in magnitude than 20 mA/cm^2 so this effect is not relevant herein.

In general, it can be said that DHPDS is a high-performing fluorescent pH dye owing to its stability under operando conditions but also because of its compatibility with standard confocal microscopes, ratiometric properties, wide accessible pH range, quick response time, reversibility, water-solubility, non-toxicity and commercial availability [100, 134].

APTS, too, is compatible with standard confocal microscopes, ratiometric, exhibits a quick response time and reversibility, is water-soluble, not toxic and commercially available [240]. Importantly, it allows to significantly expand the pH range that can be resolved by DHPDS. However, it is not as stable under operando CO_2R conditions.

First, we tested if APTS is sensitive to the concentration of potassium bicarbonate ($KHCO_3$) in solution, see Fig. A.3. This is important since the bicarbonate concentration can change over the course of an experiment and for different measurements. We dissolved different concentrations of $KHCO_3$ in an ammonia buffer solution to

keep the pH value constant and added NaCl to the test solution to ensure a constant ionic charge. We found that the ratio of emission that was detected from APTS was nearly independent of the $KHCO_3$ concentration which confirms that the signal is not influenced by dissolved inorganic carbon species.

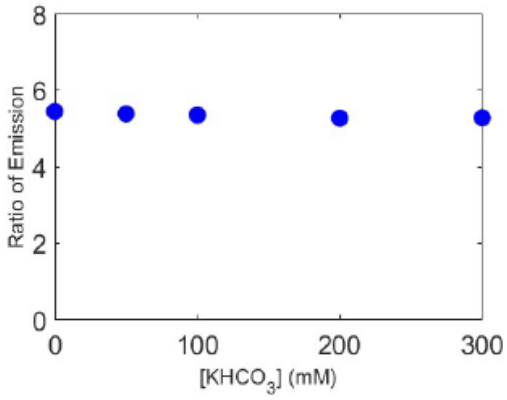

Figure A.3: Ratio of Emission of APTS as a function of $KHCO_3$ concentration. The experiment was carried out in an ammonia buffer solution to keep the pOH constant (it varied by less than 0.1 pOH units). The total amount of ionic charge was kept constant for all data points by adding NaCl to the test solutions. The ratio of emission from APTS is nearly independent of $KHCO_3$ concentration, indicating that aqueous dissolved inorganic carbon species insignificantly influence the sensing mechanism of APTS.

We then turned our attention to the stability of APTS upon the application of high current densities. We observed a decrease in photoluminescence intensity for current density magnitudes > 80 mA/cm^2 and we used APTS to investigate the operation of a GDE with current densities as high as 200 mA/cm^2 in magnitude. To understand this effect, we evaluated the stability of APTS under different conditions with UV-VIS spectroscopy (see Fig. A.4 (a), (b)). We observed a significant decrease in photoluminescence intensity from APTS with and without light and for solutions with pH 7.1 and pH 3, where the degradation effect was more pronounced for the pH 3 solution. Furthermore, we noticed a significant change in color of a 10 mM APTS stock solution that was exposed to -100 mA/cm^2 for 30 minutes, from bright green to brown (see Fig. A.4 (c)), that persisted for days without indication of reverting back to its original form. This suggests an irreversible chemical transformation and not a transient instability, such as formation of an excited-state triplet state or a metastable state. We observe the most significant and irreversible decrease in photoluminescence intensity from aqueous APTS under the following simultaneous conditions: (i) cathodic current densities >80 mA/cm^2 in magnitude, and (ii) closer

to the electrode surface and/or within trenches. The presence of illumination does not seem to play a role. In addition, we do not think that CO_2R products are resulting in observed degradation, because the steady state photoluminescence spectrum of APTS showed minimal change in intensity as concentration of dissolved inorganic carbon increased (see Fig. A.3). Hence, we suspect that APTS is being reduced at the electrode surface. Irrespective, calibration curves of fresh APTS solutions with different APTS concentrations, as well as a curve that was measured with an APTS stock solution that was exposed to -100 mA/cm^2 for 5 minutes, are nearly identical (see Fig. A.4 (d)), suggesting that APTS is suitable to use as a pOH sensor even in the presence of significant degradation to a less emissive product. This can be explained by the ratiometric nature of APTS as a pOH sensor.

It must be noted that even though APTS is still a reliable pOH sensor at high current density magnitudes, its degradation poses the challenge that even though the ratiometric signal remains mostly unchanged, the total signal decreases significantly. The consequence is a worse signal-to-noise ratio. This can be seen in Fig. 4.4 in the panels on the right hand side that represent high current density magnitudes that appear noisier than the panels on the left at lower current density magnitudes. Despite the noise, the images still exhibit a reasonable quality. Several measures were taken to make that possible. This includes a revised electrochemical cell design. We went from a design with one electrolyte inlet tube at the cell wall as was used in chapter 2 (see Fig. 2.1, only DHPDS was used) to a design with two perpendicular electrolye inlets with straws that lead directly to the GDE surface as used in chapters 3 and onward (see Fig. 3.2 (b)). The turbulent flow pattern ensures that fresh, undegraded APTS is constantly transported to the GDE surface. In addition, the APTS concentration in the electrolyte was increased, from initially 100 μM to 200 - 300 μM. Finally, the electrolyte in the whole cell is removed and replaced with electrolyte containing fresh APTS after every measurement under bias. A typical operando measurement in this work takes 30 - 45 seconds (see Chapters 4 and 6). As consequence, APTS can only be reduced at the electrode surface for less than a minute before fresh dye molecules are introduced.

A.3 CO_2 Reduction Gas Diffusion Electrodes with Flat Surfaces Deactivated by a SiO_2 Layer

In Chapter 4, we investigated the local influence of random trench patterns in a GDE on the CO_2R performance via operando pOH imaging in combination with multiphysics simulations. We were able to directly measure the local pOH

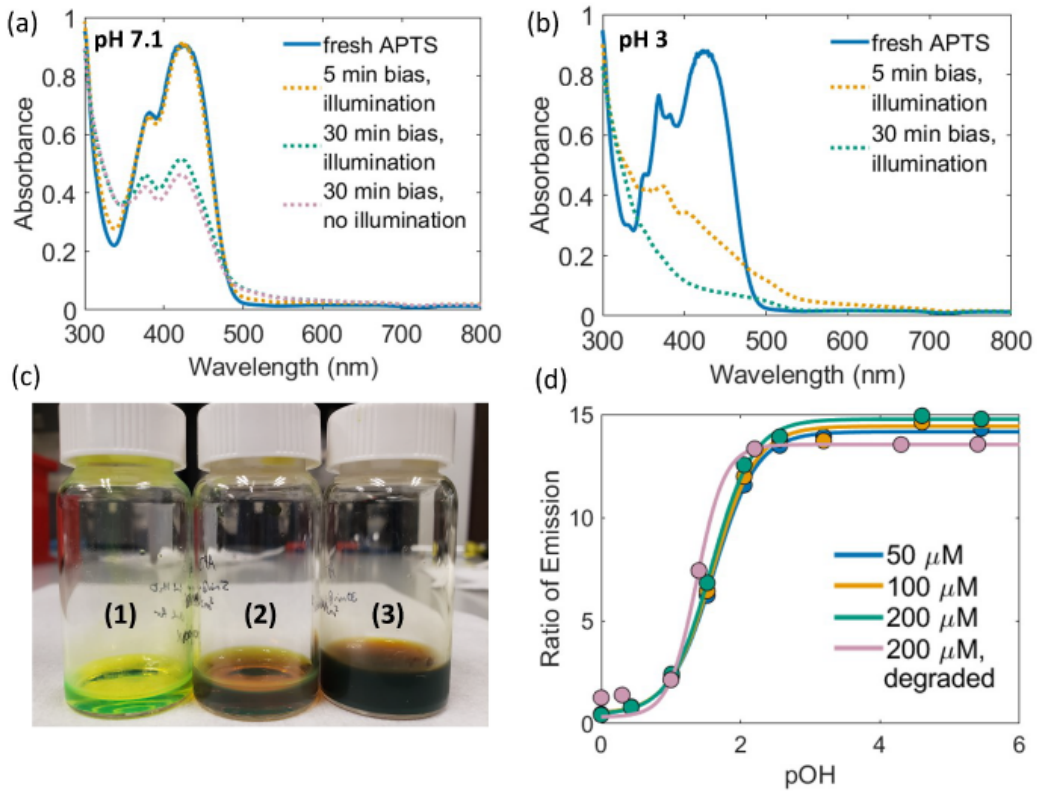

Figure A.4: UV-VIS spectra, photographs and calibration curves of fresh and degraded APTS. (a) UV-VIS spectra of 200 μM APTS in aqueous 100 mM $KHCO_3$, as freshly prepared, and exposed to a GDE operating at -100 mA/cm^2 for 5 minutes under laser illumination, and for 30 minutes, with and without laser illumination. (b) UV-VIS spectra of 200 μM APTS in an aqueous HCl pH 3 solution as freshly prepared and exposed to a GDE operating at -100 mA/cm^2 under laser illumination for 5 minutes and for 30 minutes. (c) Photographs of aqueous 10 mM APTS stock solutions: (1): fresh, (2): degraded by exposure to a GDE operating at -100 mA/cm^2 for 5 minutes, (3): degraded by exposure to a GDE operating at -100 mA/cm^2 for 30 minutes. (d) Calibration curves of APTS with the measured ratio of emission as a function of pOH together with best fit curves for different APTS concentrations between 50 μM and 200 μM and for 200 μM APTS that was degraded by exposure to a GDE operating at -100 mA/cm^2 for 5 minutes (solution (2) in panel (c)).

value inside trenches and from that, deduce the local selectivity inside trenches via simulations. However, we had no direct means to experimentally measure the local CO_2R product distributions inside trenches. The fabrication of tailored patterns of microstructures in GDEs as presented in Chapter 5 solves this issue. However, we also made an attempt to measure the local CO_2R selectivity inside the random trench patterns in Sigracet 38 BC carbon paper via the deactivation of surfaces outside trenches with the application of a dielectric silicon dioxide (SiO_2) layer.

We fabricated such samples by depositing 300 nm Cu on Sigracet 38 BC carbon paper with electron beam evaporation with the sample oriented at an angle of 90° in relation to the source, as described in Chapter 4. In a subsequent step, the sample was mounted on a custom-made, 3D-printed chuck that allows electron-beam deposition under an angle of 30° in relation to the source, see Fig. A.5 (e). The angled orientation allows to deposit SiO_2 on the Cu layer with only planar surfaces outside of trenches covered. The thickness of the SiO_2 layer was varied between 100 nm and 1000 nm. Fig. A.5 (a) – (d) shows SEM and EDS maps of a trench in the GDE surface. EDS measurements reveal that while Cu covers both flat surfaces and trench walls, SiO_2 can only be found on planar surfaces but not inside the trench owing to the angled deposition method. We used the same method of angled electron beam evaporation on a glass slide and measured the height thickness profile of the resulting film with profilometry. We found that the film is up to 100 nm thicker towards the end of the sample that was closer to the source during the deposition process. We therefore designed a better version of the sample holder chuck that, instead of one big angled plane, consists of four smaller angled planes next to each other. Profilometry reveals that the resulting film thickness with this updated sample holder version is much more uniform.

We then proceeded to perform electrochemical experiments with the novel samples. First, we performed pH imaging experiments with the pH probe DHPDS as described in Chapters 2, 4, 5 and 7. The experiments were performed in 100 mM $KHCO_3$ electrolyte spiked with 100 μM DHPDS, without electrolyte flow. This means that OH^- is only transported via diffusion. Since Cu is only exposed inside trenches and all other Cu surfaces are covered with a SiO_2 layer, it is expected that the pH value only increases locally inside trenches before enough time has passed to distribute OH^- via diffusive transport. Fig. A.5 (f) shows an exemplary pH map as a cross-section through a trench with flat surfaces covered with 100 nm SiO_2 within the first minute after the application of a current density of -5 mA/cm^2. The pH increases from the bulk pH 6.8 to >8 not only inside the trench, but also on the flat surfaces surrounding the trench. A similar observation was also made at a position on the GDE void of any trenches. This indicates that the 100 nm SiO_2 layer is not sufficient to disable the catalytic activity that causes the pH increase.

Further, we realized during chromopotetiometry measurements that the potential required to keep the current constant was not reproducible, it varied between different samples and also as a function of time. We hypothesized that this might be caused

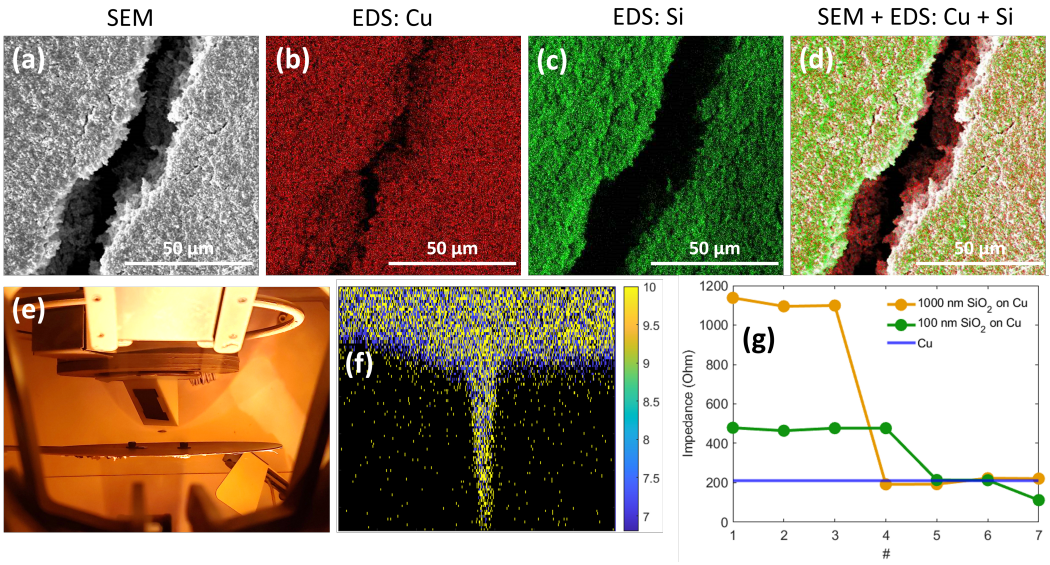

Figure A.5: Characterization of GDE samples with an SiO_2 layer deposited on flat surfaces. (a) SEM image of a trench in a Sigracet 38 BC carbon paper sample. (b) EDS map of the same trench with red color indicating the presence of Cu. Borh flat surfaces and trench walls are covered with Cu. (c) EDS map of the same trench with green color indicating the presence of silicon and hence, SiO_2. Only flat surfaces are covered while the trench remains free of SiO_2. (d) Overlay of SEM and EDS maps of both Cu and Si. (e) Photograph of the angled chuck that is used to deposit SiO_2 only on flat planes, mounted in the electron beam evaporator. (f) Operando pH map as a cross section through a trench for a sample with flat surfaces covered with 100 nm SiO_2 at a current density of -5 mA/cm^2. The pH increases from a bulk pH of 6.8 to >8 everywhere, also on surfaces that should be deactivated by SiO_2. The dimension of the map is 45 μm in y and 117 μm in x. (g) Impedance of samples with 1000 nm (yellow) or 100 nm (green) SiO_2, deposited at an angle of 90° as well as the impedance of a Cu on carbon paper sample without an SiO_2 layer (blue), as a function of the impedance spectroscopy run. The measurements are 1 minute apart.

by an insufficient and non-uniform SiO_2 surface coverage such that parts of the Cu on flat surfaces is still exposed for some of the samples. We hoped to mitigate this problem with the application of thicker SiO_2 layers up to 1000 nm but still observed the same inconsistencies.

To investigate the influence of an SiO_2 layer on a sample's electrochemical behavior more systematically, we fabricated samples with SiO_2 layers of varying thickness deposited onto the copper layer under an angle of 90° such that SiO_2 is deposited also inside trenches and should cover all Cu surfaces. The expectation is that resistance of these samples is significantly higher than that of a sample with pure copper owing

to the dielectric properties of SiO_2. To test this hypothesis, we performed impedance spectroscopy measurements for a sample covered with 1000 nm SiO_2, 100 nm SiO_2 and 0 nm SiO_2, see Fig. A.5 (g). This was repeated several times, approximately once every minute. The first impedance spectroscopy measurement fulfills the expectations: the impedance for the pure copper sample is 211 Ω, for the sample with 100 nm SiO_2 479 Ω and for the sample with 1000 nm SiO_2 1138 Ω. While the impedance remains constant over the course of several measurements for the pure copper sample, it drastically decreases for the other two samples. The impedance drops to the level of pure copper within the first four/ five impedance spectroscopy measurements. This shows that the ability of SiO_2 to shield the catalyst surface is highly unstable. We hypothesize that this is caused by small, unwanted pores in the SiO_2 layer that are unavoidable even if the thickness of the SiO_2 layer is increased to 1000 nm. The electrolyte slowly penetrates the pores during electrochemical experiments and reaches contact with more and more Cu surfaces. As a result, the SiO_2 layer fails to effectively and durably shield the catalytic surfaces outside on trenches.

We conclude that the application of a SiO_2 layer on the flat surfaces of a Cu GDE via angled electron beam evaporation is not suitable to measure the local product distribution inside trenches. While materials other than SiO_2 might exist that would be more fit for this purpose, we did not proceed with this route since the successful fabrication of controlled patterns of microstructures in GDEs provides a shortcut towards the direct measurement of the product distribution for various GDE micromorphology geometries, see Chapter 5.

A.4 Unsuccessful Attempts to Fabricate Gas Diffusion Electrodes with Tailored Microenvironments

In Chapter 5, the fabrication of CO_2R GDEs with tailored microtrenches with the method of laser ablation is described. However, in the first stages of the project, various other fabrication methods were tried. The aim of this section is to demonstrate why laser ablation was chosen as the most suitable fabrication pathway.

We know from the results in Chapters 2 – 5 that microcavities with feature sizes on the order of 5 μm are most beneficial to boost the CO_2R performance, it is therefore vital that geometries with that size can be fabricated.

A.4.1 Mechanical Milling

Because mechanical milling is very easy, requires only a single production step and very basic tools, it was the first fabrication method we tried.

As a very quick first test, a razor blade was used to cut a trench into a carbon paper substrate, see Fig. A.6. While this works well and is faster, easier and cheaper than any other method, it has three major drawbacks: (1) It is impossible to make intricate geometrical features like circular holes, (2) With a razor blade that is drawn across a substrate by hand, it is difficult to obtain a perfectly regular and controlled pattern and (3) The minimum trench width that can be obtained is 30 μm.

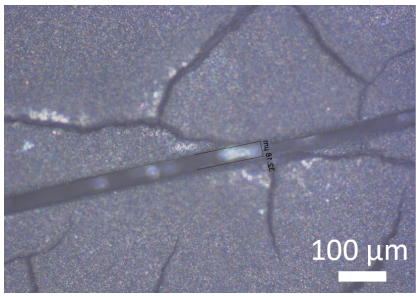

Figure A.6: Microscopic image of a Sigracet 22 BB carbon paper sample exhibiting a trench that was created with a razor blade. It is 30 μm wide.

Another mechanical patterning methods that was considered is the use of micro-drills. Drill bits with diameters as small as 50 μm are commercially available [241]. We purchased drill bits with diameters of 60 μm and 100 μm. While drills allow to easily make shapes like circular holes, careful engineering is required to control the depth of the holes or to create other pattern like trenches. Furthermore, the material that is removed from the hole tends to build up around the edges of the hole. The biggest drawback is the size of the drill bits, even the smallest ones are an order of magnitude above the desired 5 μm in size.

Despite these challenges, due to its simplicity, we performed some experiments using this method. To do so, we purchased a 125 μm thick polyester sheet and drilled holes through it with a 100 μm drill bit (see Fig. A.7(a) and (b)). We stacked this sheet on top of a PTFE (0.45 μm pore size, coated with 300 nm Cu) GDE and placed this stack in the electrochemical cell designed for confocal microscopy as described in Chapter 2. We used the fluorescent pH probe DHPDS (see section 1.5.1 and Chapters 4, 5 and 7), dissolved in CO_2-saturated 100 mM $KHCO_3$ electrolyte, to image the operando pH value inside the holes in the polyester sheet. It must be

noted that the sheet itself is neither conducting nor covered with catalyst, so it does not contribute to CO_2R, it only serves as a structuring mask on top of a Cu CO_2R GDE. Polyester is transparent in the visible range, which allows to see processes happening between the sheet and the GDE (see Fig. A.7 (c)). Since the GDE and the patterned polyester sheet are loosely stacked together, it is impossible to control if and how much electrolyte seeps in the volume in between.

Fig. A.7 (c) shows a pH map as a cross section through a hole in a polyester sheet upon the application of a current density <-4 mA/cm^2 (note that the exact determination of the current density is challenging since it is unknown to what extend electrolyte seeps between the polyester sheet and the GDE surface and therefore, the exact active surface area is unknown). The presence of fluorescence at the bottom left and bottom right of this panel indicates that some electrolyte containing fluorescent DHPDS enters the volume between the polyester sheet and the GDE. Further, we see that the local pH value increases locally close to the top of the hole. It is expected that the pH would be higher at the GDE surface and hence, at the bottom of the hole. We hypothesize that this discrepancy is connected to mass transfer limitations of the pH probe DHPDS.

Fig. A.7 (e) - (i) displays cross sectional pH maps in a hole as a function of time for a current density <-16 mA/cm^2. Such a high current density magnitude leads to the formation of large quantities of gaseous products that are confined to the holes in the polyester sheet. This leads to the formation of gas bubbles that slowly start to fill the entire channel in the polyester sheet. After 1.62 minutes (panel (e)), the bubble covers the bottom of the hole and slowly moves up until it reaches the surface after less than three minutes and then extends past the surface of the polyester sheet. Fig. A.7 (d) shows a microscopic image of such a gas bubble filling the channel in a polyester sheet stacked on top of a Cu GDE.

While this first attempt to perform experiments with deliberately structured GDEs was interesting, there are various problems. The first is the large size of achievable patterns. Further, it is challenging to control the depth of created structures or make patterns other than circular holes. In addition, covering a GDE with a foil that blocks most catalytic sites is not ideal, instead, the goal are structures in the microporous layer of the GDE itself. These challenges can be addressed with laser ablation as described in Chapter 5.

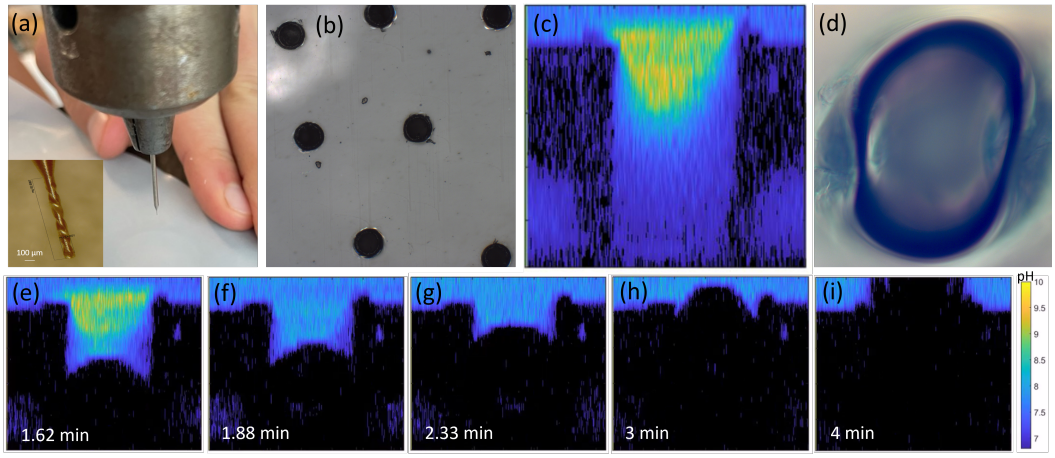

Figure A.7: Creation of structured GDEs with micro-drill bits and a polymer sheet stacked on a PTFE GDE. (a) Photograph of the drilling process with a drill press and a 100 μm drill bit. Inset: microscopic image of the drill bit. (b) Microscopic image of the resulting polymer foil with a pattern of drilled holes. (c) Cross-sectional pH map inside a hole in the polymer sheet stacked on top of a Cu/PTFE GDE at a current density <-4 mA/cm^2. (d) Microscopic image of a gas bubble that has formed inside the channel in the polymer sheet at a current density <-16 mA/cm^2. (e) - (i) Cross-sectional pH maps inside a hole for different times after turning on the bias. The evolution of a gas bubble (black) can be clearly followed. All pH maps have a size of x = 225 μm and y = 198 μm. The pH color bar is valid for all maps.

A.4.2 3D Printing

We considered 3D printing as a possible method to create GDEs with tailored micromorphology because it gives complete control over the printed structure and the freedom to print any shape.

Max Saccone, Julia Greer et al developed a 3D printing method including hydrogel infusion that allows to print materials from various different materials, including metals and alloys [242]. Using this technique, a carbon structure was printed with regular square pores of size 50 μm x 50 μm x 80 μm. This resolution is not suitable to print GDEs with geometrical features on the length scale of 5 μm. In theory, 3D printers that can print considerably smaller structures are commercially available [243]. However, is is critical to ensure that the printed material is suitable to be used as a CO_2R GDE and the resulting structure must be porous to allow the transport of CO_2 to the catalyst-electrolyte interface. It is a difficult balance to control both a GDE's pore size and hydrophobicity such that CO_2 transport is effective but at the same time the GDE is not flooded. It is very challenging to achieve these material properties with common 3D printing techniques.

J. Wicks et al. developed a 3D-printable fluoropolymer gas diffusion layer that enables the 3D printing of hydrophobic porous gas diffusion layers [244]. However, the described process is very complex and requires self-made materials and equipment. Additionally, printed features on the length scale of millimeters rather than micrometers were demonstrated.

As a consequence, we decided that 3D-printed structures as demonstrated in [242] could dhave the capability to be utilized as potent flow-through CO_2R electrodes [245]. However, considering the complex material requirements of a GDE, it is easier to carve into an existing commercially available GDE susbtrates rather than building an entire GDE via additive manufacturing.

A.4.3 Nanofabrication

Various very advanced and well-developed nanofabrication techniques exist that have a resolution well below the 5 μm required for this application [246].

We considered the use of focused ion beam lithography (FIB) [247] to create the desired structures. While this would be feasible and allow the creation of microcavities with controlled shape and the desired size, the technique is very slow. The fabrication of a single sample would require many hours or even days. Considering how many different samples are required for the project (see Chapter 5), this pathway is not feasible.

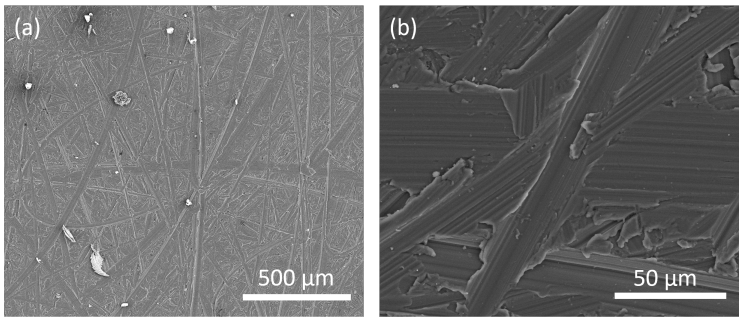

Figure A.8: SEM images at different length scales of Sigracet 38 BC carbon paper spin-coated with AZ4620 photoresist. The resist layer is non-uniform.

Another very common nanofabrication method is photolithography using a photoresist. We tried to spin-coat the photoresists S1813 [248] and AZ4620 [249], both without and with the photoresist adhesion HMDS [250] on a Sigracet 38 BC carbon paper substrate. The major problem with this approach is that the GDE substrate is porous and it is therefore very challenging to achieve a uniform photoresist coating

on the substrate surface. Fig. 1.9 shows SEM images of such a sample coated with photoresist at two different length scales. It is obvious that the resist layer is highly non-uniform. This presents a problem for the subsequent photolithography process.

Following all the tests and considerations presented in this chapter, we decided that for the study described in Chapter 5, laser ablation is the most suitable fabrication pathway. It allows to make features as small as 5 μm with controlled shape and size, it can be used to carve patterns directly into an existing GDE substrate, requires only one step to make patterns and is considerably faster than many nanofabrication techniques. Refer to Chapter 5 for details about the sample fabrication with laser ablation and the results of the study.